Luca Orefice, MSc.

Discrete Elements Method modelling of screw conveying and related processes

---

DOCTORAL THESIS

to achieve the university degree of
Doktor der Technischen Wissenschaften

submitted to
Graz University of Technology

Supervisor
Univ.-Prof. Dipl.-Ing. Dr. techn. Johannes G. Khinast
Institute for Process and Particle Engineering, Graz University of Technology
Research Center Pharmaceutical Engineering GmbH, Graz

Graz, June 2020

Luca Orefice
Discrete Elements Method modelling
of screw conveying and related processes
Dissertation

First assessor
Univ.-Prof. Dipl.-Ing. Dr. techn. Johannes G. Khinast
Institute for Process and Particle Engineering
Research Center Pharmaceutical Engineering GmbH
Graz University of Technology

Second assessor
Univ.-Prof. Dr. Jukka Rantanen
Department of Pharmacy
University of Copenhagen

Affidavit

I declare that I have authored this Thesis independently, that I have not used other than the declared sources/resources, and that I have explicitly indicated all material which has been quoted either literally or by content from the sources used. The text document uploaded to TUGRAZonline is identical to the present doctoral dissertation.

.....	.....
(Datum / Date)	(Unterschrift / Signature)

Caelum, non animum mutant
qui trans mare currunt.

Acknowledgments

To myself,
to my parents,
to everyone who supported me.

First and foremost I would like to thank my supervisor Prof. Johannes Khinast for giving me the opportunity to develop my skills as a researcher and pursuing a doctorate degree. His trust in my capabilities and his willingness to let me follow my "scientific inspirations" allowed me to study problems I was naturally curious about, therefore transforming work into a fascinating mental playground. I also want to acknowledge Prof. Jukka Rantanen for being the second assessor of my thesis.
Special thanks go to Anthony Thornton for the review of parts of this thesis, for all the scientific support and discussions, and for all the valuable time spent in University of Twente that is always extremely stimulating, and fertile soil for my ideas. Next to him my former PhD advisor and "attorney" Sebastian González, that, directly but mostly indirectly, contributed to teach me how to be independent when doing research.
To my parents I owe the opportunity I had to study, to develop myself and the luck to be able to decide which path to follow, among many, many other things. They are to me constant frame of reference and unconditioned support, and to them goes and will always go my unending, unbounded gratitude.
A special place here, as in my heart, is deserved by Đana, for all the love, the support and the motivation she gave me in these last years. The patience and the understanding she always shows me were a big help in my PhD journey, and I am grateful she accepted to accompany me, side by side, through this route I decided to travel.
Lastly I would like to thank everyone whom, in a smaller or bigger part, in a positive or negative way, was playing a role in the last years of my life. I believe that the person I am now, like a single of many grains, is also determined by the multitude of encounters and events I was taking part. For this reason everyone, being them relatives, friends, colleagues or random people met somewhere along the road, deserves to be mentioned here.

Graz, April 21, 2020
Luca Orefice

Abstract

Granular materials are well-known to humanity since its dawn and are ubiquitous in everyday lives. Huge amounts of energy and resources are spent daily for handling and manufacture of such materials. Numerical modelling of processes involving granular materials are widespread, their relevance in prediction and optimisation of the former well recognised by the scientific community. The aim of this thesis is to develop numerical models to replicate and study the behaviour of processes involving the manufacturing of granular materials, in particular screw conveying, relevant in the field of the pharmaceutical industry.
The first chapter is a thoroughly introduction to the three main components of this thesis: granular materials, screw conveyors and the numerical tools used here to model them. In the second chapter we model a section of screw conveyor and we study the particle flow inside. We show that, for certain operational parameters of the device, a consistent flow of particles against the direction of conveying is established for partially-filled conveyors, hindering the device transport efficiency. The critical fill level above which this backward flow begins is shown to be dependent on the screw geometry, while its magnitude depends on the fill level itself. The third chapter deals with a new approach in the modelling of roll compaction, where Discrete and Finite Element Methods are used in conjunction. By using the former to model powder conveying and the latter to model powder compaction, the particle flow entering the compaction region is modelled at the particle level, transformed into continuous fields and used as time-dependent inlet conditions for the compression model. Our approach exploits the strengths of both methods, since they are both applied to the region they are naturally suited to model, thus increasing the predictive capacity of roll compaction modelling if compared to the results of both methods independently. In the fourth chapter we develop a new framework to automatically calibrate a Discrete Element model of cohesive powders. The aim is to allow a more realistic modelling of systems involving cohesive materials manufacturing, such as most pharmaceutical processes related to solid dosage forms. The calibration consists of faithfully replicating powder rheology experiments to capture the bulk behaviour of the materials, the particle properties then used to model powder flow in manufacturing processes thus enabling a higher predictive model. We demonstrated that our automated iterative method, based on rational physical assumptions and a precise order of execution, can satisfactorily calibrate powders from free up to very badly flowing. The fifth chapter introduces our first steps in the modelling of plastic, deformable and breakable particle clusters. These clusters will be used in upcoming models to study complex particle behaviours such as attrition and agglomeration during feeding, or such as deformation and breakage during compression. The inter-particle interaction law used in the numerical model is exploited to obtain a highly precise analytical

model, enabling us to carefully craft particle clusters with desired size and porosity. One of many promising applications of this model, and the ability to create clusters with a precise structure, will be the realistic modelling of granules undergoing die compaction. Lastly, a conclusion with a short recapitulation of the main findings of the former studies is presented. The next steps in each of the topics presented, as well as the future research directions we would like to undertake, are explained and discussed.

Contents

List of Figures

List of Tables

Chapter 1

Introduction

"If you find yourself in the Valley of Despair,
try something new and different."

Sid Meyer

The key elements of this work are three: granular materials, screw conveyors and numerical particle models. Granular materials, like grain, sand and flour, are well-known to humanity since its dawn and are ubiquitous in everyday lives. On the other side screw conveyors are very simple devices known since millennia, and are among the simplest tools to exploit mechanical leverage as a mean of transporting materials. Finally, numerical models of particulate ensembles are a relatively recent field of study, especially when compared to the first two, and are aimed to study the physics of particle ensembles.
How could these elements "fit" together into a coherent research project? The answer is very simple: because physics of granular materials is "hard" and still poorly understood [27]. Not only does their physical behaviour lay somehow in between the ones of solids and fluids, but most of the times their dynamics is actually duplicitous. By nature they are also composed of a very high number of smaller elements, making the analysis of the ensemble very complicated. At some point in the evolution of granular systems the ensemble could not be described by average physical parameters, but the dynamics of every single element must be taken into account independently. For instance, the flow of corn through a funnel can stop if the elements, while converging towards the outlet, reach a stable configuration due to their shape and to friction. This phenomenon, known as *arching*, is very common, and is an example of a flow which state cannot be described statistically, since the sudden interruption of the flow is caused by a collective motion of discrete elements reaching a static equilibrium configuration. Now, if we model each element as a rigid body, the dynamics of each of the former is described by a set of 12 equations, hence the necessity of numerical techniques to cope with the astronomical amount of operations needed to solve the equations of motion and fully describe the system.
Handling and manufacturing of granular materials is the backbone of many processes, and each one involves a transport stage where they have to be moved from one point to another [93]. One of the most efficient and extensively used device is screw conveying [93]. By transforming mechanical torque into a longitudinal push these devices transport granular matter in many industrial applications. The ability to predict and optimise the outcome of

every stage of the production is of the upmost importance, and the feeding stage is not an exception. The material conveying stage is usually regarded as the "bottleneck" of every production line since the inflow of raw or partially manufactured materials sets the pace of every manufacturing process [93]. When the feeding stage involves granular materials it inherits the complicated nature of the latter, and becomes a natural candidate for being modelled numerically by means of particle simulations.
There are many ways to model granular ensembles, depending on which aspects one wants to investigate and on the scale of the phenomenon. Nevertheless, since for most phenomena the dynamics of single elements is essential in determining the collective behaviour of the ensemble, one of the most widespread numerical technique used to model such systems is by means of Discrete Elements Method (DEM). In such models the granular material is represented by a collection of solid rigid bodies, most of the times spheres, that interact with one-another via dissipative elastic forces upon collision. This method is simple yet very effective in modelling granular systems, since it can resolve the dynamics of single grains at the particle level including their main energy loss mechanism due to friction.
In essence, the study presented in this thesis work deals with numerical particle models applied to the study of manufacturing processes involving screw feeding of granular materials.

1.1 Granular matter

A granular material can be defined as matter composed of a high number of discrete, macroscopic and solid sub-components: the *grains*. These grains are not subject to dynamics driven by thermal fluctuations, and are characterised by dissipative interactions, the most common being friction forces. Therefore granular matter comprises materials which sub-components can vary in range from micrometres to several kilometres in size (figure 1.1), and is a quite peculiar state of matter since it can exhibit a broad range of behaviours with precise and distinctive features. According to the scales of the system and to the forces involved, granular materials can behave like solids, liquids or gases [5]. Tightly packed cobblestones can sustain the weight of pedestrians or vehicles for hundred of years, thus behaving like a solid. A frozen clump of snow detaching from a mountain summit will avalanche downstream, flowing like a fluid. Huge clouds composed of ice and debris of many sizes orbit around planets and form rings such as the ones around Saturn, their motion similar to gases.
Like fluids granular assemblies can exhibit phase transitions. Unlike the former they are not driven by temperature, but rather by differences in packing density, mobility or arrangement. In fact, for the granular systems studied in the work presented in this thesis, temperature is irrelevant in determining the physics of the system, and is therefore not included in the numerical models. Thermal effect such as kinetic energy dissipation due to collisions between grains are modelled instead by a viscous damping force proportional to their relative velocity upon collision. These kinetic energies and the grains inertia dictate the magnitude of the energy scales relevant for physically describe granular systems. Another dissipation mechanism is key to granular assemblies, and is due to frictional forces between the particles. When packed and at rest, the friction between each single component allows the ensemble to sustain a considerable amount of compressive force. Therefore

Figure 1.1: Examples of granular solids with different packing and particle size distributions: sand and pyramids. Both behave like solids and can sustain an incredible amount of weight, although the former is easier to fluidise. Source: *Wikipedia, the Free Encyclopedia.*

there are two main elements dominating the physics of granular matter: the inertia of its components and the dissipative interactions at play.

1.1.1 Why we do study granular systems

Granular matter is the second most manipulated material after water, which makes it an obvious subject of study. However, despite its ubiquitous appearance in everyday life, a comprehensive understanding of the behaviour of granular materials is still eluding us. The reasons behind our still incomplete knowledge are multiple and intertwined. First of all, most granular assemblies are composed of a large number of constituents: a single teaspoon full of usual granulated sugar (approximately 4 mg) contains, on average, up to 10^4 particles. Studying the dynamics of such ensembles requires a large amount of computational power, since the number of particles in commonly used systems is far above the millions. In the context of pharmaceuticals manufacturing, for instance, most of the raw solid dosage forms of the processed materials are in the form of powders with size well below the millimetre. Resorting to statistical approaches, like in thermodynamics, is not always possible since granular systems do not necessarily have local reference equilibrium states [7,22,43], making statistical averaging unsuitable. If we consider an enclosed volume of gas, there is a typical relaxation time after which, despite atoms still being in motion through the container, any random partition of the volume is equal to another. The same is not true for granular systems. First of all the only equilibrium state of a granular gas is the one with zero kinetic energy, and secondly a wide variety of instabilities will emerge

while reaching equilibrium. Each of these lead to local anisotropies such as clustering [7,32,60,152], and the system will be characterised by local transient states with respective characteristic times, making a definition of a local equilibrium state impossible. Similarly granular systems lack a universal separation scale: the typical transport mechanism of grains does not have a predefined relation with the average grain size, and the same is true for relevant fields [7, 43]. For example, when computing the average stress tensor in a granular flow, the result depends on both averaging volume and averaging interval. Certain particles can exhibit mean free paths macroscopically larger than the average, a feature not found in thermodynamic of fluid systems that are not in a critical state. Another element of complexity is given by the complicated interactions between particles. Frictional, dissipation, plastic and adhesive forces all contribute to a highly non-linear dynamics at the particle level. The picture is even more complicated if a fluid is present: even a small amount of fluid, leading to the formation of liquid bridges [162], completely changes the dynamics of the system [78, 121]. Collisions involving granular materials can also dissipate energy very fast: rubber balls do not bounce on sand. Finally, granular systems can exhibit different states of matter as previously mentioned, and different states can coexist in a single, relatively small system [32,60]. A simple example of such a system is a hourglass, where sand flows from an upper container into another below, passing through a funnel wide only a few particles size. The upmost layers, far from the funnel, and the downmost, below the flowing layers sedimenting at the bottom, are physically analogous to solids: the velocity fluctuations are negligible and they support the material above. When approaching the funnel the layers of sand progressively fluidise and start flowing downwards, their velocity dependent on their distance from the hourglass walls: material in contact with the former will flow slower and eventually stop, an aspect of dynamics that reminds laminar flow of fluids. Finally, once the sand grains overcome the funnel, they free-fall towards the bottom of the container, and during this motion they enter the kinetic regime dominated by single-particles collisions. Since the motion of the particles is not confined by the neighbouring ones, the stream tends to expand radially like gases and the dynamics is dominated by convection.

1.2 Screws and screw conveyors

Screws are simple mechanical devices aimed to transform a rotational motion into a linear one, by transforming rotational torque into a longitudinal force [93]. The invention of such devices dates back to Ancient Egypt before the third century BC, but there is no unequivocal historical source attributing their creation to a precise figure. In its first conception the screw was used as a water pumping device to lift water from the Nile or other water sources into irrigation ditches. Unlike modern conveyors these devices consisted of a continuous tube coiled around a middle axis, with their bottom edge submerged to allow the fluid to partially fill the lowermost sections. Gravity, in conjunction with the peculiar helical geometry, prevented the water trapped inside to flow back, and allowed a way more efficient transport than via bucket. When spun around its axis the parallel flights presents themselves to the material inside as independent contiguous containers moving towards the front end of the device, thus transporting the former in the same direction.
It was with the Greek mathematician Archimedes that the device was introduced into An-

cient Greece, after he described the tool at his return from a journey in Egypt. Archimedes also innovated its design, giving the screw conveyor its modern layout with a helicoidal flat surface wrapped around a middle shaft enclosed by a hollow cylinder (see figure 1.2). This renewed design would prove to be very efficient also in the transport of granular materials, but the application of screw conveyors for such usages had to wait until the 20th century. In fact, throughout history, screws as transport devices were only used for transporting fluids, besides their usage as simple machines for gaining mechanical advantage. The first application to the conveying of grains had to wait until 1945, when innovator Peter Pakosh invented the first prototype of modern grain augers. Since then the adoption of screw conveyors in transport of granular materials rose constantly and became one of the standard operations in handling of such substances.

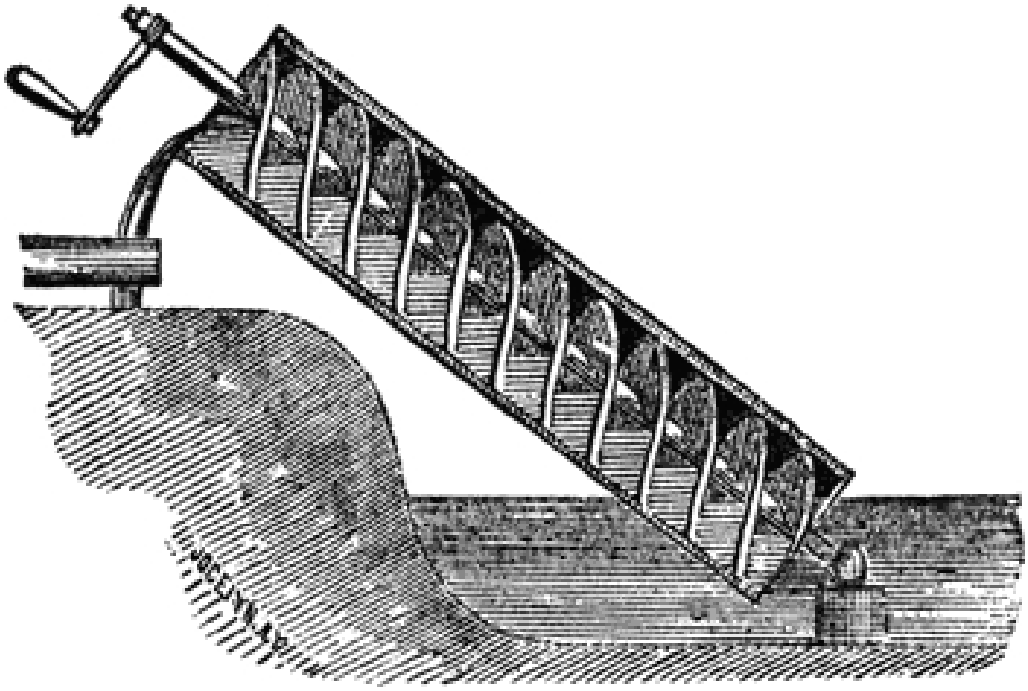

Figure 1.2: Archimedes' screw from Chambers's Encyclopedia (Philadelphia: J. B. Lippincott Company, 1875). Source: *Wikipedia, the Free Encyclopedia.*

1.2.1 Modern screw conveyors

Screw conveyors, interchangeably called screw feeders, saw numerous technological and design upgrades to answer precise and specific necessities of the systems they are part of, and are now very different from their ancestors [93]. First and foremost the geometry of the screw flight can differ depending on the material transported. The thickness of the flight is directly proportional to the amount of longitudinal back pressure the screw can sustain. If the material transported is dense and poorly flowing, it will oppose a considerable resistance when conveyed, and as a consequence the screw threads must be proportionally sturdier to overcome potential damage. The material composing the conveyor itself also depends on the specific application required. However, for the sake of simplicity we can

imagine screws built out of steel, since they are predominant in feeding processes. Also the pitch capacity can be changed to meet the necessary robustness, but is mainly related to performance [114, 151], wether it being related to amount of throughput, throughput periodicity, or power consumption. The former is defined as the amount of free volume per screw pitch, i.e. as the free space that can be occupied in a screw longitudinal section correspondent to a screw full revolution. The screw pitch length l, also referred to as screw lead (or simply lead), is the axial advance of a screw during one complete turn. Clearly, a wider free volume can host more material reflecting in a higher amount of stress acting on the flights, but also determines the maximum amount of material that can be conveyed per screw revolution. If we assume the content to behave like a perfectly flowing solid, halving the pitch length will result in half volumetric throughput per screw turn, and so on. However, since granular materials in motion do not behave like solids, the mechanics of granular material convection is way more complicated [113, 151]. For instance the screw clearance is defined as the space comprised between the screw flight tips and the inner surface of the external casing. Material occupying such region is not directly conveyed by the screw, but can be transported only by contact with neighbouring flowing elements. When transporting fluids the clearance should be kept as small as possible to avoid back-flowing, as much as viscosity and friction between mechanical parts allows. However, during handling of granular materials the clearance is an important parameter to account for, since a too small width can cause transported particles to remain trapped within, resulting in damaged products [109], increasing torque requirement, higher wear of the device and even jamming.

Another aspect to be considered is how much of the energy transferred by the screw to the conveyed material is translated into longitudinal push and how much into a rotation around the screw's axis [113]. To have an efficient device as much mechanical work spent as possible should be converted into the former. To quantify this ratio the screw *helix angle* γ is introduced. If we imagine a screw of fixed radius R (figure 1.3), increasing pitch length results in a more stretched helicoidal structure, i.e. the normal to the screw flight gets progressively less parallel to the screw axis and more pointing outward. The tangent of the helix angle is defined as the ratio between the longitudinal advance of one point on the screw and the circumference it travels during one revolution $\tan(\gamma) = l/2\pi R$. Clearly higher γ translates into a higher ratio of longitudinal versus rotational energy transfer, and therefore into a more efficient process. However, properties of the transported material and process characteristics usually pose a limit to both maximum helix angle and feeding efficiency.

Depending on the system screws can have a single or multiple flights, and conveyors can comprise multiple screws at once. Increasing the number of flights increases the robustness of the screws, but when conveying cohesive materials might lead to product accumulation between adjacent flights. To avoid such effect usually conveyors are designed to host two screws next to one another, especially when fine powders are involved in the process. In twin screw conveyors part of the active conveying volume of both screws overlap, creating a self-cleaning effect where one screw scoops away powder that might be adhering to the other. Active conveying volume comprises the free volume enclosed in a cylindrical shell circumscribed to the screw, i.e. the volume of material directly pushed by the flight motion.

The flight surface topology is yet another variable to be taken into consideration (figure

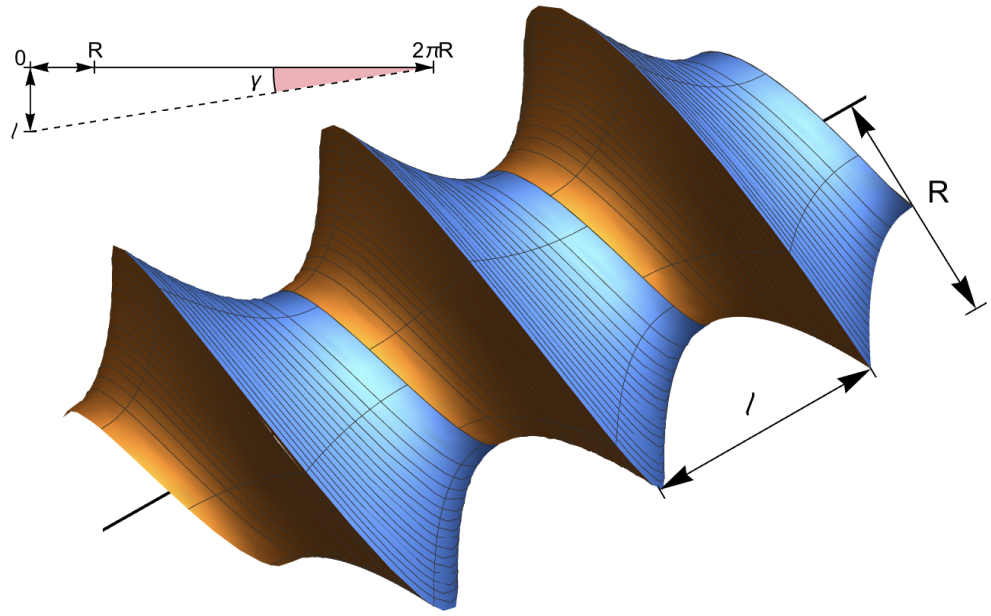

Figure 1.3: Mesh of coarse-concave screw section used in DEM simulations of powder feeding. In the inset a visualization of the helix angle and its dependence on the screw geometry. The flight slope reduce the powder compression during transport, especially relevant for cohesive powders.

1.3). The force exerted by the screw rotation is directed along the normal vector to its surface and determines the flow of the transported material. In case of cohesive powders the latter can be highly compressible, since the packing fraction of such materials is lower than others with same particle size distribution but lower cohesiveness. Since the screw is pushing the powder in a certain direction, the maximum pressure the former is exerting on the latter will be acting in the same orientation. Changing the shape of the screw flight can reduce not only the active conveying volume but also the pressure exerted, limiting the local compaction of the powder. In fact, when handling poorly flowing cohesive powders, it is often better practice to reduce the conveying efficiency in term of optimal helix angle and free volume to limit local powder agglomeration, that could lead to clogging or jamming. Most of the times, during handling of granular materials the inlet of screw conveyors is connected to a hopper. Hoppers are containers where grains or powders are deposited and temporarily stored with an open section on the bottom. From the latter the material can flow inside the conveyor and is dragged away towards its intended destination [65, 173]. The mass of powder contained also provides a certain pressure against the lower layers, enhancing the flow inside of the screw barrel. Since this pressure is proportional to the mass contained, during the emptying of the container the driving pressure steadily decreases, leading progressively less material inside the conveying region and a proportionally lower mass throughput. To avoid this steady decrease in throughput modern conveyors can be equipped with a controlling device monitoring the mass outflow in real time, and tuning the screw speed accordingly to keep a constant feeding rate. If, from one side, hoppers

and related instruments simplify the feeding process, removing the constant need to input materials into the conveyors, on the other they can significantly alter the feeding process. Components of granular matter can be very frictional, have high aspect ratios, exhibit cohesive behaviour and even charge electrostatically. All of these aspects can compromise the feeding performance even before the material reaches the screws by jamming the hopper. Consistent effort is regularly spent in improving and optimising hoppers connected to screw conveyors, such as reshaping their geometries and adding agitators to fluidise the powders inside. The latter consist of moving mechanical parts aimed to keep the material contained in the hopper in a flowing state, thus preventing local powder agglomeration that could eventually hinder or prevent it from entering the screw barrel. Given the tight connection between screw conveyors and hoppers in powder and grains processing, and given the extent of how the latter affect the performance of the former, they are usually regarded as unique systems. Thus referring to screw conveyors in the context of certain processes implies the presence of an inlet hopper, and pharmaceutical manufacturing is an example.
All of the elements enumerated above, while being only a simplified and reduced selection of the many aspects involved in screw feeding, can give a perspective of how complicated the study of such process is, despite the very simple principles behind it. The most important lesson to be learned is that conveyors are designed specifically to meet precise requirements in the context of selected manufacturing processes. For this reason material, process and device become intertwined, and it would be incorrect to focus a study on a single aspect aside from the other. This complicated dependency makes the formulation of mechanistic models of feeding very complicated, and usually valid for a very narrow range of material properties and screw operational parameters. The inability to formulate comprehensive mechanistic models motivated researchers to find different aims to study these systems. Among these, one of the most prominent is numerical models. Constant improvement in computational resources enables progressively more accurate and larger scale computer simulations of granular material manufacturing processes, and screw conveying is no exception. Not only the complexity of such systems makes numerical models an important tool of study in the field, but there are also two additional reasons that make numerical simulations an exceptionally valuable tool: the ability to "*see inside*" and the capacity to selectively tune and change single material parameters. These two aspects will be explained in detail in the upcoming section.

1.2.2 Feeding in pharmaceutical manufacturing

A substantial part of pharmaceutical industry's manufacturing is devoted to processing of solid dosage forms consisting of powder blends below 0.5 mm in size. Active Pharmaceutical Ingredients (APIs), i.e. the biologically active components of pharmaceutical formulations aimed to achieve a therapeutic effect, are predominantly poorly flowing particles with high cohesiveness, and as such pose a challenge for every manufacturing stage. Since they are very difficult to handle they are usually mixed with excipients into blends to greatly improve their manufacturability. Generally speaking pharmaceutical excipients are defined complementary to API, i.e. are all inert drug components that have no biological effects, but optimize formulations for manufacturing and delivery. Examples of excipients can be lubricants, disintegrants, carriers, and so forth.

In the context of feeding, APIs are mixed with lubricants to form blends with improved flowing capabilities. Achieving a precise, constant and reliable transport process is essential in pharmaceutical manufacturing [12] mainly for two reasons. Firstly: quality standards for pharmaceuticals are the strictest that can be found in industry. Drugs must be administered with great precision to guarantee the efficacy of a therapy, and the amount of API in each dosage form (i.e. the form in which a certain pharmaceutical is delivered and administered) usually don't exceed the order of milligrams. A too low dosage can compromise the effectiveness of a cure, a too high one can cause severe collateral effects, and both pose serious risks for patients' health. Therefore the high quality standards, and the necessity of strict and precise workflows at every stage of the manufacturing. Secondly API are among the most expensive substances on the market: drugs often exceed the 1000 €/g market value, making them 20 times more expensive than gold, priced around 50 €/g. Downtime and failures during drugs manufacturing entails a considerable cost, a factor that must be accounted for in the production stage.
The necessity of a stable, reliable and coherent pharmaceutical manufacturing process is the motivation behind the study of such systems. However, since most pharmaceutical solid dosage forms involve powders composed of small cohesive substances, handling and processing of these materials is very challenging. This makes the dynamics involved in the process very complicated, and led the scientific community to explore numerical models for their study aimed to a better understanding of the underlying physics. At the present time, a couple of decades after the dawn of this field of research, numerical models are a widespread tool for understanding such problems, and are well-established methods for process optimisation and design.

1.3 Discrete Element Method (DEM)

Discrete Element Method, also known as Distinct Element Method or Discrete Particle Method (DPM), is a widespread numerical technique for modelling granular ensembles. Firstly developed in 1979 as a tool to numerically study granular assemblies [23], DEM is now a well-known and unanimously recognized numerical technique to model and study systems comprised of many distinct independent components in mechanical interaction with one another. In this context DEM belongs to the subgroup of *"soft sphere"* models, where simulated particles are allowed to overlap with one another to mimic local deformations due to collisions. In reality, traditionally disregarding brittle breakage, local deformations between particles are very small, and therefore overlaps between DEM particles should be kept proportionally small. Each particle of the ensemble is modelled as an independent entity that can interact with others and with solid boundaries by means of prescribed physical laws, and can be subject to external force fields like gravity.
Given the complexity of granular systems numerical methods are frequently the best option available to gain scientific insight. Here discrete particle methods have the advantage on continuum numerical models since are naturally suited to simulate ensembles of elementary components [101]. Despite traditionally the latter cannot arbitrarily deform or break under pressure, but will be set in motion and forced to rearrange if allowed to. Local particle phenomena with macroscopic effect such as force chains are easily observed in discrete simulations, but are very hard to capture in continuum ones. Since complex rheologies are

not well-established, local particle-scale phenomena that are critical for the mechanics of granular ensembles cannot be captured with continuum models. Thus the dominance of DEM among numerical models applied to the study of granular systems.
DEM has an "edge" over real particle systems as well. In fact it is impossible to perform direct measurements on single grains of a large bulk, and is also extremely complicated to observe the internal structure of these systems despite its importance. This is the aforementioned advantage of being able to "look inside" and extract every needed information on the dynamics of each single particle, while most experiments can only gather informations at the bulk level. This means that the latter can only give information concerning macroscopic observables, like the material flow function, that are determined by statistical averages of phenomena acting at the particle scale, such as friction. How to observe the motion of lower layers of soil during a landslide? In DEM the dynamics of each particle is simulated continuously, and data such as forces acting on each particles, their position and their velocity at any moment in time are able to be accessed. Being able to "see what happens inside" paved the way for important understanding in the behaviour of granular matter, making DEM an invaluable research tool. Moreover, each material parameters modelled numerically can be arbitrarily changed to observe the impact of the former on the system under study. This ability is of extreme importance and has no equal in real experiments. For this reason DEM can be used for sensitivity analyses, where input parameters describing material characteristics are systematically varied and the consequent variations in the macroscopic behaviour of the system observed. For instance, let's imagine that one is interested in the angle of repose (i.e. the slope of the heap of a material let to fall under gravity onto a plane, as in figure 1.4) of a certain blend of granular materials. Experiments are performed, and the angle of repose measured, but the relative concentration of the blend components has to be changed to meet a certain requirement from the manufacturing. Now, instead of performing a new set of experiments, DEM can be used to guess the new value of the angle of repose for the new blend instead. This approach is not only faster, but also saves materials otherwise used to perform the experiments, thus reducing costs and wastes. The obvious caveat is that the numerical model must be reliable in simulating the physics of the system. The fitness of such models must therefore be ensured, and this is done via calibration and validation, as explained in the upcoming sections.

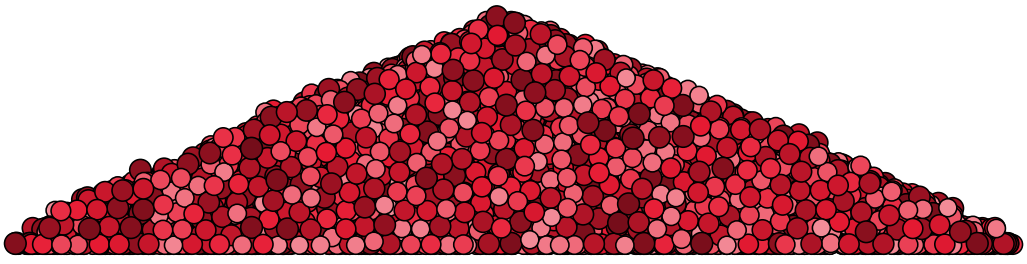

Figure 1.4: Piling of monomodal uniformly polydisperse frictional spheres under the effect of gravity. Colour gradient according to particle size.

1.3.1 Generalities on DEM

Exactly modelling real systems via DEM is unfeasible with modern technology: not only the number of particles in typical granular assemblies is extremely large, but also further complications due to shape, particle size distribution (PSD) and complex interaction modes can arise. Simplification is therefore necessary, and in many simulated systems particles can be modelled as perfect spheres without losing important predictive capabilities. The problem of the high particle number arises when considering that DEM models particles as single entities, and therefore the equations of motion for each one of the former must be solved at every integration step. From the dynamics of rigid bodies we know that in 3 dimensions there are 12 dynamic variables to be computed (position, velocity, orientation and angular velocity), resulting in 12 equations to be solved for each particle. This without considering the time required to search through all particles to determine which ones are in contact, such that overlaps and the resulting forces between the former can be computed. The only possible solution, without changing the simulation domain, is to upscale the particles, a technique also referred to as *coarse graining*. Considering the former teaspoon of sugar, if we are to simulate the system with particles of double the size, the number of particles required would decrease of a factor 8, i.e. a net $3 \cdot 10^4$ fewer equations to solve each integration step. When performing such approximations one must ensure that the increased size of the components are not altering the physics of the systems, and sometimes this is not straightforward to verify. Artefacts eventually introduced by scaling part of the modelled system go under the name of *finite size effects*, and must be avoided to grant a qualitative validity of the model.
Lastly, when considering dense granular flows the effect of air in the interstices between particles can usually be neglected if inertia dominates the particles motion, i.e. if particles are sufficiently packed or dense that eventual drag forces due to the air flow can be neglected. If this is the case, the inter-particle forces to be considered in the models can be reduced to simple inelastic binary collisions in the presence of gravity. This will not be the case in systems where gaseous flows or fluids determine important features of the flow, such as particles suspensions and fluidised beds. For all the systems studied presented in this work the effect of air between the particles can be neglected, and only interactions due to particle collisions will be considered.
With these simplifications, at each force integration time step all forces acting on every particle i in the ensemble will be computed, and will obey to Newton's second law:

$$m_i \frac{\mathrm{d}^2 \vec{r}_i}{\mathrm{d}t^2} = \vec{f}_i^{\,C} + \vec{f}_i^{\,NC} + \vec{f}_i^{\,B} \tag{1.1}$$

where $\vec{r}_i$ is the particle position, $\vec{v}_i$ its velocity and m_i its mass, $\vec{f}_i^{\,C}$ is the total contact force acting on the particle due to collisions with other bodies, $\vec{f}_i^{\,NC}$ is the total force due to non-contact interactions (like, for instance, electrostatic forces) and $\vec{f}_i^{\,B}$ is the resultant of all the body forces acting on the particles, such as its weight $m_i\vec{g}$. Now that the total force acting on each particle at a certain time t is known, both their new velocity and new position at the subsequent integration time $t + \mathrm{d}t$ are computed by solving the equations

of motion for every particle:

$$\vec{v}_i\left(t+\mathrm{d}t\right)=\vec{v}_i\left(t\right)+\frac{\mathrm{d}^2\vec{r}_i(t)}{\mathrm{d}t^2}\,\mathrm{d}t \tag{1.2}$$

$$\vec{r}_i\left(t+\mathrm{d}t\right)=\vec{r}_i\left(t\right)+\vec{v}_i\left(t\right)\mathrm{d}t+\frac{\mathrm{d}^2\vec{r}_i(t)}{\mathrm{d}t^2}\,\frac{\mathrm{d}t^2}{2} \tag{1.3}$$

where $\mathrm{d}t$ is the integration time step, and the accelerations are computed from equation (1.1). The latter is of great importance and should be chosen sufficiently small to avoid numerical instabilities. The usual rule-of-thumb is to choose $\mathrm{d}t$ such that the average particle collision time is 50 times bigger that the former. A detailed and thorough analysis of DEM would be out of the scope of this work, firstly because such numerical model is used by the scientific community since over 40 years [23] and is very well known and established, and secondly because there is already a substantial amount of literature published. We refer the interested reader to [84] and references therein for a more exhaustive overview of the method. The same set of equations as (1.2) and (1.3) for the rotation dynamics of a rigid body are also affecting the dynamics and are solved in a similar fashion, but are omitted here for sake of brevity.
The contact and non-contact forces $\vec{f}_i^{\,C}$ and $\vec{f}_i^{\,NC}$ are the terms of equation (1.1) that sees the most theoretical investigation when it comes to improving DEM models, since they are the ones that need to be improved or modified to include more complicated interactions between the particles. In this thesis, besides gravity, only contact forces $\vec{f}^{\,C}$ will be considered in the models presented, and will be the ones to be briefly described in some parts of the text. The most basic form of interactions used in DEM to mimic the contact dynamics between particles are of three kinds. Firstly there are repulsive forces, needed to prevent particles from collapsing into one another, and are proportional to the particles overlap during their collision. Secondly there are friction forces, that limit the tangential relative motion of particles against one another, thus limiting the local rearrangement of particles and allowing complex structures such as heaps to be modelled (figure 1.4). Lastly we encounter viscous interactions, adding a resistive force depending on the relative velocity of particles, aimed to mimic the energy dissipation of bodies due to thermal effects during collisions.

1.3.2 The link to reality: validation and calibration

Scientific theories must be validated by experiments and the same holds for numerical models. DEM validation is undertaken by preforming simulations of the same setups or scenarios as in experiments. Then parameters that can be measured in the experiments are then compared with the ones gathered from the simulations. The closer the agreement the better the model and the more reliable its predictions. Despite the conceptual simplicity validation of a DEM model is usually challenging.
First and foremost DEM parameters needed to describe particle behaviour are numerous, and most of them have great impact on the outcome of the simulations. Some parameters can be estimated via physical arguments or from experience, such as the particle restitution coefficient. Others parameters can be directly measured from experiments, such as the density of materials. All the remaining ones must then be determined via an expensive trial-and-error simulation procedure consisting of a sensitivity test. Here simulations are

repeated for different combinations of input material properties until a matching combination is found. This approach can be very time consuming since a whole DEM simulation must be carried out for each combination, when the first are very computationally expensive and the latter can be many.
Another difficulty that arises during such validations is due to multiple solutions of the validation simulations. Since many values are used as trial states, it can happen that more than one combination leads to the required results below a reasonably small error threshold. When this happens there is no way to choose among these multiple combinations unless via physical considerations. If none of the parameters are physically unplausible there is no unique solution, and more tests should be performed. This is also why experience and experiments should always be preferred to material parameters sensitivity tests, and are invaluable tools to complement numerical modelling.
Lastly a successful validation does not imply, a priori, that a validated model will be able to perform in an arbitrarily different setup. On the contrary, validation tests are relative to a certain material with precise properties in the context of a single device. This means that if the model is validated via a set of experiments employing a certain material, the former will not be able to predict the performance of the same device operated with a different substance. The same is true if the same material is used but in a different device. If either granular material or device are changed, the validation procedure must be repeated. The value of validated models resides in the former being able to predict the outcome processes ran with different operating conditions, albeit relatively close to the values used for model validation. For instance, let's assume that a screw feeding model has been validated for screw velocities of 10, 20 and 50 rpm, and each of the tested velocities led to results in agreement with the experiments. It is reasonably safe to assume that the model will be able to predict the performance of the same feeder loaded with the same powder for all screw velocities between 0 and 60 rpm. However this assumption becomes increasingly questionable the more we move from the tested range, and ceases to hold if macroscopic effects are expected to happen in between two tested values.
Validation involves the results of the numerical model, therefore happens after the model has been implemented and ran. Calibration, on the other hand, is a stage that comes before the implementation of the model itself, and is practically independent from it. As we have seen validation can be a prohibitively long stage, especially if processes involve a high amount of material or run for a long time. Calibration would, in principle, avoid this issue by finding the exact combination of particle properties that would allow to perfectly replicate the behaviour of the material numerically [20]. The key assumption is that even the experiments aimed to characterise the physical behaviour of granular materials are unable to test single particles, but only bulk properties. Therefore is pointless to focus on single particles behaviour, but the target should be to replicate flow and structural properties as measured in these *unit tests*. Assuming one is able to replicate the latter, particles calibrated in such way should in principle exhibit the same behaviour when used to model an actual process. Obviously the better the agreement between calibration experiments and simulations, the better should the modelled process agree with the real one.
These calibration experiments come in great variety, from compression (figure 1.5) to shear tests, from packing to air permeability tests, and so on. Tests performed to characterise the granular material for numerical calibration should cover every possible aspect of the physics implemented in the model. For instance, if cohesive powders are implemented, a

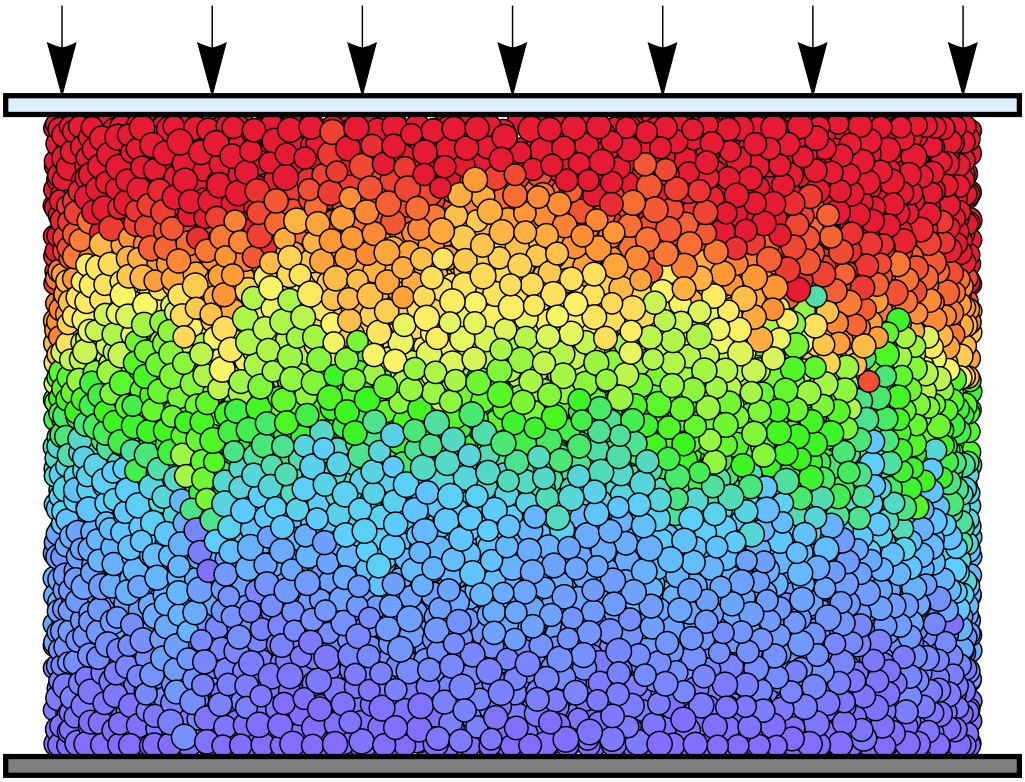

Figure 1.5: Snapshot of DEM compression test. Particles are contained inside a cylindrical casing (not shown) and compressed by displacing the top plate. Particles coloured according to vertical stress.

rheology test specifically aimed to measure the tendency of particles to adhere should be included in the calibration. The range of conditions tested for each parameter must also cover the material states occurring in the studied operations, since the range of validity of extrapolated parameters is not known beforehand, exactly as for numerical validation. Calibrating powders with compression tests where they are compacted up to 1kPa of pressure is completely useless if in the model they will be subject to stresses up to 10kPa.
As with validation, DEM powder calibration is a very complex and lengthy task, but the latter has three main advantages on the former: lower computational costs, intrinsic validated tests and reusable results. Lower costs are related to the size of the equipment. Rheology tests require an amount of material of the order of 1 to 100 grams, orders of magnitude smaller than the amount involved in actual processes. Secondly since the simulations are designed to match the experiments, the model is by definition validated. Same pros and cons of validation routines apply here. The real game changer is the reusability of calibration results. Since now flow and structure properties are matched by replicating rheology experiments, the fundamentals dynamics of a specific powder is assumed to be captured. The results are independent on the process one will end up modelling, and calibrated powders should in principle automatically replicate the correct outcome of the latter. Numerical calibration of a certain powder is then performed *once and for all*, and its results applied whenever this material needs to be modelled. As usual a special care must

be given to avoid finite size effects, since avoiding the former while performing numerical calibration tests does not imply they won't show up in the model of a different operation.

1.3.3 The problems in screw feeding modelling

DEM is a very powerful model for studying granular assemblies, but is a model nonetheless, and as such it comes with intrinsic limitations. Depending on the aspects of a problem at study one has to choose between scale or precision. For example both calipers and carpenter's rulers are instruments for measuring lengths, the first with greater precision and smaller scale, the opposite for the second. It really comes to what we want to measure and up to what precision that drives us in the choice of the instrument: a caliper is very precise in measuring the diameter of threaded bolts, but will be useless in measuring the length of a dining table. Vice versa a ruler might be able to measure the first with a higher measurement error, provided that its sensitivity allows it, but is more suited in measuring the second. DEM works in a similar way: if macroscopic bulk quantities are to be measured, and the local interactions between grains are not relevant, then a larger system with coarse grained particles can be the choice. However if the details of the particulate structure at a grain scale are the aim, then particles as close to real ones should be employed, and the physics modelled be as rich as possible, at the price of a smaller simulated domain. Clearly in both approaches any finite size effect introduced by either scaling must be avoided.
That being said, numerical modelling of screw feeders by means of particle-based methods face three main problems:

- *Common industrial feeders cannot be modelled without resorting to coarse graining.* If we imagine a common industrial feeder with mass throughputs of the order of kilograms per hour, the capacity of its hopper is of the order of decades of kilograms. Substances composing average pharmaceutical powders have a density laying around 1.5g/cm^3, and if we assume an average size of 100μm and particles perfectly spherical we would need an amount of particles of the order of 10^{13}. This astronomical number of particles cannot be modelled with any modern computer in a reasonably affordable time, thus forcing to resort to coarse graining and either upscaling the particles or modelling only a region of the device.

- *All parts of a feeder are intertwined, and cannot be separated without altering the system.* This point is key and has to do with the complexity of the feeding process. Feeders are complex systems and each section is in dynamic equilibrium with the neighbouring ones. Each of the latter can be imagined as a continuous flow of material through a system with inlet and outlet boundary conditions. Outlets of intermediate sections will serve as inlets for the following ones, and in a fluid dynamics fashion we can impose mass and momentum conservation between each section. Similarly local change in mass flow will cause a change in the stress fields and vice versa. For instance, the rate of fed material depends on the mass outflow from the hopper, but the screws exert a back pressure that constantly limit the former.

- *Aspects relevant to the macroscopic behaviour happen at the particle level.* This is a consequence of granular materials dynamics being governed by local single particles interactions. A practical example is the buildup of layers of particles inside the screw

casing. As mentioned a certain clearance between barrel and screw is necessary to avoid damage or jamming, and its width depends on the nature of the material transported. Cohesive materials will likely stick to the inner surface of the barrels and reducing the clearance, with two main effects: decrease of conveying capacity and increase of mean residence time. The first is simply a consequence of the reduced barrel cross-section available for particle flow and is connected to a systematic decrease of the mass throughput. The second is due to the first powder fed being the principal component of this stationary layer of particles. These will occupy the clearance and be compacted by the upcoming ones, thus being the first to enter the system but likely the last to exit. These so-called *dead flow zones* are characterised by stagnant material, responsible for long tails in the mean residence time distribution (RTD) of mass inside the device. This is an important issue during continuous manufacturing since makes the product hard to trace, which is a necessary feature in the production of drugs. Long tails in the RTD can negatively affect product quality, and makes tracing and control of products much harder.

It is evident that these issues cannot be addressed all at once since they are complementary to one another, therefore having a high fidelity numerical model capturing most of the physics at play is unfeasible with present-day computational tools. Nevertheless very important insights on the process can be obtained with such models, despite the inherent approximations, consistently increasing our understanding of the underlying physics. These all contribute to the global picture like small pieces of a puzzle, and allowed consistent optimisation and improvement of devices and operations, at the mere price of taking results *cum grano salis*.

1.4 Structure of the dissertation

The structure of this thesis work reflects both the practical needs in term of screw conveyors modelling in the context of pharmaceutical manufacturing and the current direction taken by the DEM community in terms of modelling of granular materials.
In the second chapter we study the dynamics of particle flow inside a screw conveyor section, and how screw geometry and friction affect the latter. We show that, for partially filled single screw conveyors, the screw shaft size plays a key role in the conveying efficiency of the device. The screw continuously lifts particles above the shaft while pushing them along the feeding direction, and if screw filling level and shaft size allow it, they might leap over the shaft and fall into the following screw pitch. This mechanism is shown to hinder the conveying efficiency since these particles experience a constant back flow against the conveying direction.
In the following chapter we present a methodology for modelling roll compaction by combining DEM with Finite Element Method (FEM). While FEM is most suited to numerically model compaction, it cannot model the flow of granular materials, and needs precise and realistic information about the material inflow inside the compaction region. During roll compaction powder is fed by a screw feeder towards the compacting rolls. The flow inherited by the former is inducing an non-isotropic powder bulk density leading to periodic density fluctuation in the compacted ribbon. The non-homogeneous periodic flow field was modelled via DEM and used as inlet boundary conditions for FEM, allowing to model the

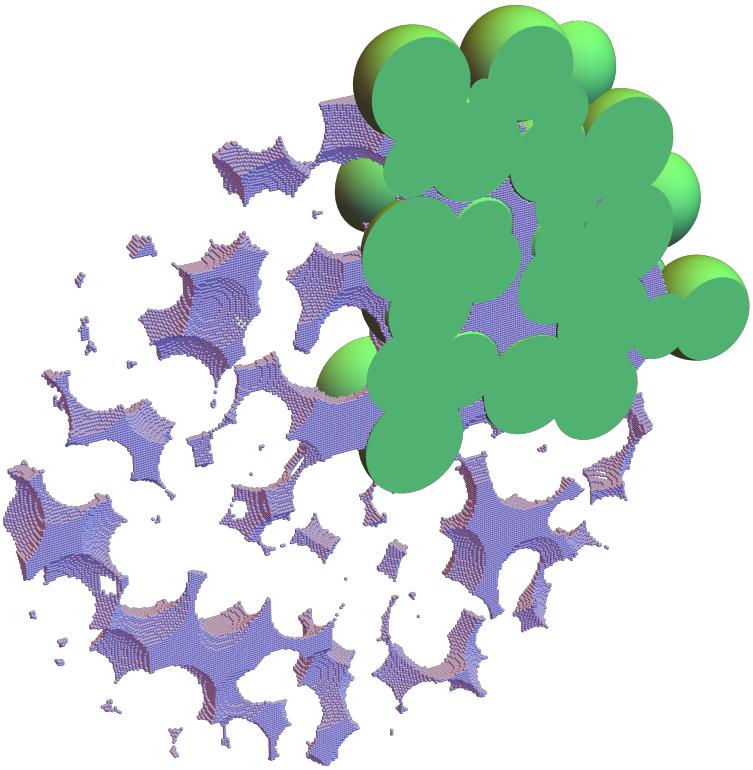

Figure 1.6: Vertical section of deformable and breakable particle cluster: the primary DEM particles (in green and only plotted in the top-left quadrant for sake of clarity) form a mechanically stable porous agglomerate. The interstitial space between the former (in blue) is highlighted by a regular cubical lattice of smaller particles.

periodic ribbon fluctuation observed in the experiments.
In the fourth chapter we describe a framework for automatic calibration of cohesive powders for use in DEM. Many processes involving granular materials frequently include manufacturing or handling cohesive powders. If DEM wants to reliably model such systems, numerical models with adhesive interactions must be adopted. The community is still lacking a standard, widely accepted method for the calibration of DEM particle properties of such materials, especially when it comes to pharmaceutical powders. We gave our contribution to this effort by developing an automatic powder calibration routine, validated with four increasingly cohesive powders of common pharmaceutical usage.
The fifth chapter introduces the next steps of our research efforts, presenting upcoming work concerning a DEM model of deformable and breakable particle clusters (figure 1.6). Initially this framework was conceived to model attrition, deformation and agglomeration of particles during feeding of granular material. However, while progressing with the devel-

opment, we realised that such model could be used to implement composite particle clusters to study, among other things, the dynamics of crushing, deformation and agglomeration of particles during die compaction. The current stage of the modelling, where structural properties of the clusters are predicted analytically, is presented and numerically validated. Future directions that we will like to investigate will be introduced as a conclusion of this chapter.
In the last chapter we present a short recapitulation of the main findings of the former studies. Future directions and topics for studies connected to the work presented are briefly introduced here as well.

Chapter 2

DEM study of granular transport in partially filled horizontal screw conveyors

Abstract[1]

A Discrete Element Methods model of a horizontal screw conveyor was developed and used to study the volume flow rate of granular materials. The volume throughput was monitored as a function of two operating parameters: the conveyor's filling level and the screw's rotating speed. For a steady flow, which is slow enough to avoid particle centrifuging, the volume throughput is linearly proportional to the screw velocity. However, the dependence on the relative filling level is non-linear. The particles, which are lifted laterally by the rotating blade, are often confined to one side, between the shaft and the casing. However, if the particle level is sufficiently high, the particles leap over the middle shaft into the previous screw thread (which is behind the original one), decreasing the throughput. These two major effects have strong impact on the particle levels to the left and the right side of the shaft and the relative velocity in relation to the screw's surface and geometry.
Our study aimed to investigate the relationship between the particle volume flow rate and the relative shaft size, as well as the influence of the friction coefficient between particles and walls on the efficiency of the device. The numerical results may be used for determining the optimal operating parameters in order to maximize the conveyor throughput efficiency based on the shaft's relative size.

[1]With minor corrections from: L. Orefice, J. G. Khinast, Powder Technology 305, 347-356 (2016).

2.1 Introduction

Screw conveyors are simple mechanical devices for transporting material. The mechanical components consist of an external shell (generally cylindrical) and a rotating helicoidal surface (screw) inside. Depending on the material that needs to be transported, the blade can be coiled around a cylindrical shaft (which is commonly the case) or can have multiple threads [127]. The rotational velocity of the spinning blade can be varied to achieve the desired material throughput. If necessary, the conveyor can be kept horizontal or inclined at any desired angle, which has impact on the back mixing [102]. Screw conveyors are widely employed in the industry to transport solid or semi-solid granular materials and their applications range from feeding apparatuses (typically from a filled hopper [30,65]) to lifting devices, such as grain augers [110, 113, 114] or water lifting pumps. In addition, materials may be de-watered or dried during transport. Despite the mechanical simplicity, the physics of the particle transport inside a screw conveyor is not trivial. As a consequence, the feeding (typically done with screw feeders) is often considered a bottleneck in many industrial processes since the dependence of the flow rate (in kg/h) on the material properties (and processing history) as well as on operating and design parameters is not explicitly known. Moreover, it is difficult to achieve a constant (non-pulsating) transport, especially at low throughput rates.

Many studies have been conducted to achieve a better understanding of the process. The first pioneering studies [114] concerning screw conveyors dealt with the volume flow rate of grains dragged vertically from a hopper by an inclined screw, and on how the inclination and the speed of the latter affects the volumetric efficiency of the device. The radial clearance between the screw blade edges and the cylindrical conveyor not only affect the volume throughput, but also can lead to grain damage during transportation, as pointed out in [109]. An analysis of the motion of the conveyed granular material is then analysed in [113], where the flow of the grains inherited by the screw rotation is related to the shape of the latter. Since screw feeders usually drag material from filled augers, part of the existing literature deals with the study of screw conveyor drag from those devices, aiming to relate the screw design to the drag uniformity [30, 65, 173]. The power consumption during feeding also poses important constraints in the design procedure, and thus the necessity to study the torque requirements, and the related power consumption, as a function of different process conditions and screw speeds [110, 114, 172]. With the development of computers and the corresponding increase in computational capacity, the conveying process begun to be modelled and studied numerically, mostly through Discrete Elements Method (DEM) modelling [23]. One example is [102], where the performance of screw conveyors is systematically studied for different screw inclinations, velocities and filling levels. Recent numerical studies also focus on screw design to achieve improved particle mixing [106] by studying how particle diffusion is affected by adding supplementary helices in the screw. Lastly, particle properties play a central role in the feeding process; in particular cohesive materials pose practical complications when moved by screw feeders because of both their lower flowability and their tendency to arch and jam. Numerical studies of this topic can be found in [57, 58].

Our paper aims to numerically investigate the volume throughput (flow rate) and the volume throughput efficiency of partially-filled horizontal screw conveyors, focusing on the wide variety of particle flow behaviour and its effects on the conveying process. Especially,

we tried to understand the granular flow dynamics in the rotating screw. Data gathered from systematic simulations of a horizontal screw feeder via DEM were used to study the volume throughput of spherical particles enclosed in a screw conveyor. By varying the two main operating conditions (the screw rotational speed and the particle filling level), we examined how the particle flow rate is affected by the size of the screw shaft relative to the screw casing and by the relative friction between the particles and the feeder's mechanical components.

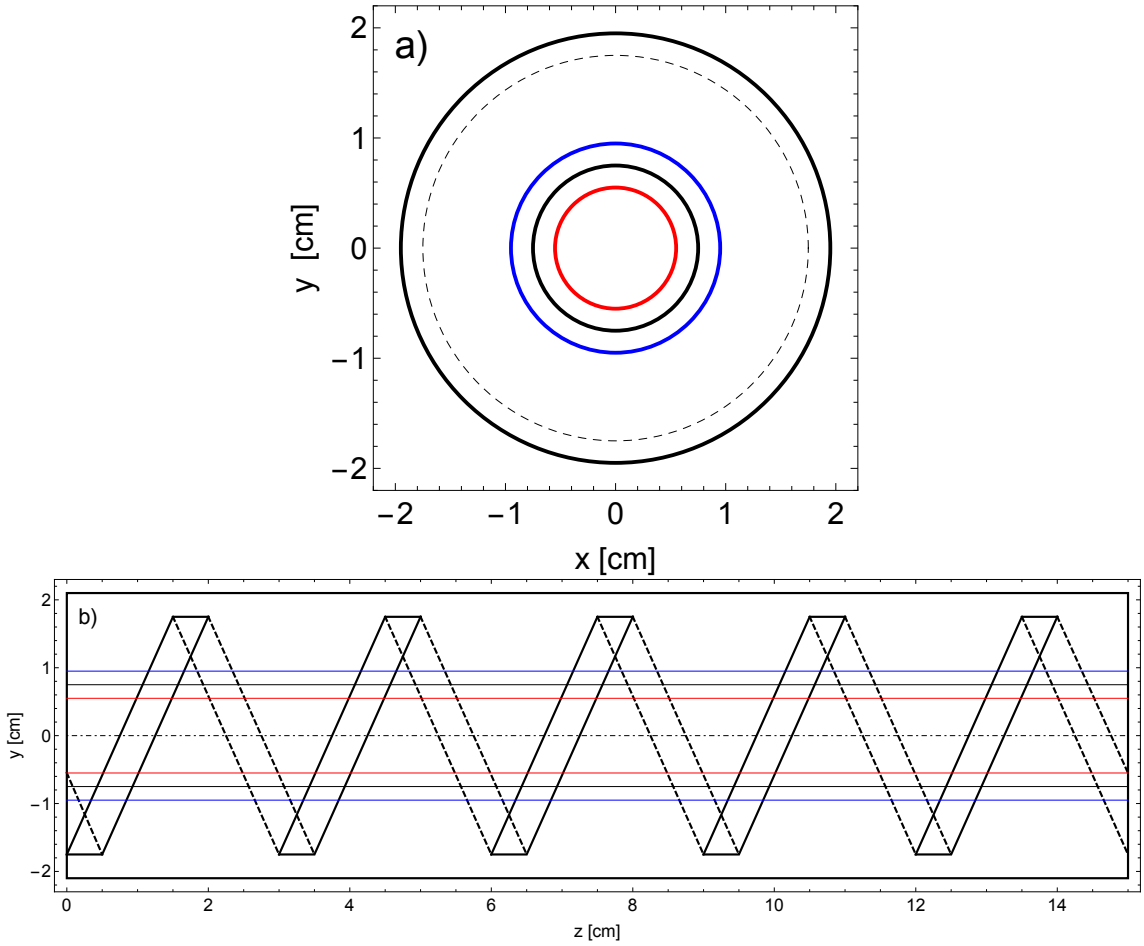

Figure 2.1: Screw conveyor schematics. Front view a): the external solid line represents the screw casing ($R_C = 1.95$ cm) while the dashed one the edge of the screw blade ($R_B = 1.75$ cm). The inner solid lines represent the 3 different screw shafts employed in the simulations (as explained further on): black ($R_S = 0.95$ cm), blue ($R_S = 1.15$ cm) and red ($R_S = 0.75$ cm). The blade section has been omitted for the sake of clarity. Side view b): the dot-dashed line represents the screw rotation axis, while the inner solid lines represents the 3 different shafts like in a).

In short, during forward transport in the screw the flowing particles continuously avalanche. The direction and profile of these avalanches are determined by the conveyor's geometry and the particle friction, as well as by interplay with the particle filling level. At screw speeds that prevent particles from centrifuging, with increasing filling level, the particles

are lifted by the screw blade and pushed to one side, according to the blade's surface geometry [113]. At certain filling ratios, the particles lifted and pushed aside can remain confined between the middle shaft and the external cylindrical wall of the conveyor. This phenomenon, hereinafter referred to as "side confining", is responsible for a highly efficient material transport. However, at higher filling ratios, the particles lifted while fed forward may cross over the middle shaft into the next thread of the screw. These dynamics, termed particle "back-flow", becomes systematic after a certain filling threshold, reducing the mass throughput of the device.
A better understanding of these processes can help to optimize the filling level of screw conveyors and may lead to higher transportation efficiency. It thus can have a practical application in the industrial sectors that apply those process conditions.

2.2 Model details

The data were gathered via DEM simulations of an infinitely-long enclosed screw conveyor. The screw blade was modeled as a helicoidal surface with a radius of $R_B = 1.75$cm, a thickness of $\delta = 0.5$cm and a pitch length of $l = 3$cm. The total screw length was $L = 15$cm, for an overall $n = 5$ screw turns. Periodic boundary conditions in axial direction were imposed, effectively yielding an infinitely long conveyor. The screw shaft and casing were concentric cylinders centered along the z-axis with radii $R_S = 0.95$cm and $R_C = 1.95$cm, respectively. Thus, there is a significant clearance between screw and housing in order to avoid too high shear rates. The screw schematics are showed in figure 2.1. In our simulations, the screw conveyor components are modelled by means of stereolitographical triangulation method (STL), the geometry been taken from a Komarek B050H horizontal lab press conveyor [94]. The particles are modeled as spheres with a uniformly distributed radius of $r_P = 0.1$cm $\pm 10\%$, whose interaction follow the Hertzian spring-dashpot model with Young's modulus $Y = 5$MPa and Poisson's ratio $\nu_{\text{Poisson}} = 0.45$ (roughly corresponding to rubber balls). Every 0.05s a snapshot of the particle positions and velocities was taken. The particle-particle and particle-conveyor coefficients of friction were set to $\mu_{PP} = 0.5$ and $\mu_{PC} = 0.25$, respectively. The simulations used for this study were performed using the *open source* DEM particle simulation code LIGGGHTS [1].
In each simulation, particles were loaded into the conveyor up to the full filling and were allowed to settle using the effect of gravity (pointing along the negative y-axis). Next, depending on the desired filling level ϵ (see figure 2.2), the particles were removed and the screw was set into motion. The screw rotation velocity ω ranged from 27 to 48 rpm and was low enough to prevent centrifuging on the particles. The filling level was defined as a dimensionless parameter, depending on the screw casing radius, as

$$\epsilon = \left.\frac{y}{R_C}\right|_{t=0} \tag{2.1}$$

where y is the height of the top layer of particles inside the conveyor. Thus, $-1 < \epsilon < 1$ by definition. The filling ratios analyzed ranged from 5% to 100% of the full loading capacity, in constant increments of 5% between subsequent simulation runs. Data gathering began when the system reached a steady state for 10s. Three sets of data were gathered: the particle mean velocity $\bar{v}$, the particle level on the screw axis h_L and h_R (figure 2.3a) and

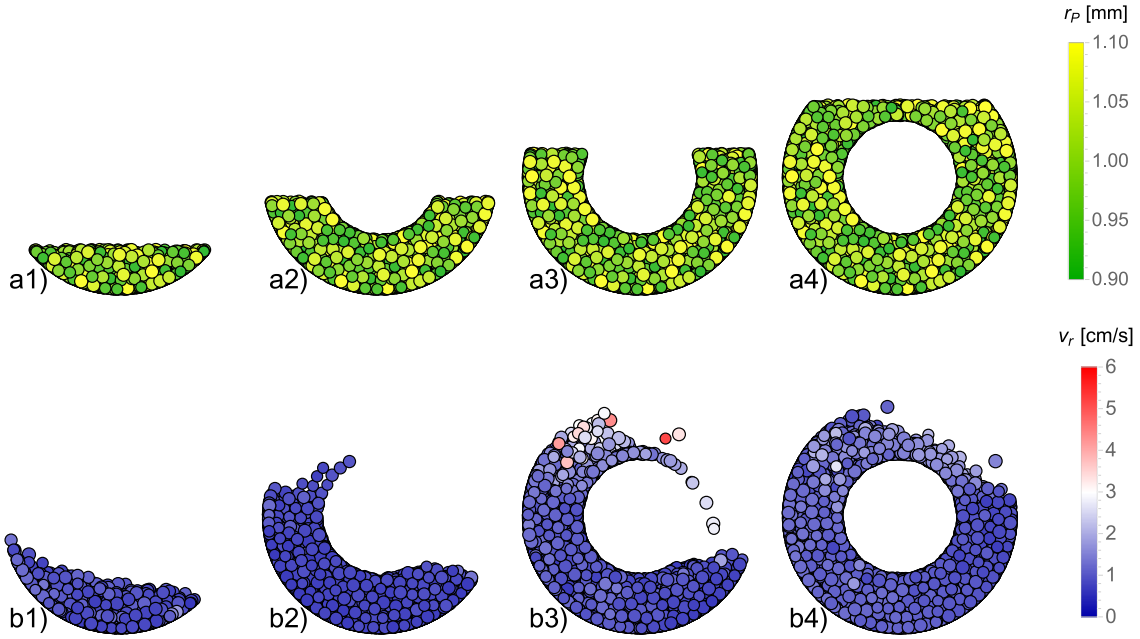

Figure 2.2: Snapshots of particles in the conveyor: projection on the plane normal to the rotation axis ($z = 0$ cm), rotation is in clock-wise direction. Top row: particles' position after loading, settling for four filling ratios (from left to right: a1) 20%, a2) 40%, a3) 60% and a4) 80%). The colour indicates the particles' radius, r_P, uniformly distributed around 1mm. Bottom row: Particle positions in the same systems after $t = 2.0$s of screw motion ($\omega = 48$rpm). The particles are coloured according to their radial velocity, v_r. Particles confined to one side are clearly visible in b2) and b3), while back-flowing particles are clearly noticeable cases b3) and b4). The mechanical components of the screw conveyor were omitted for clarity.

the mean volume throughput $\langle \dot{V} \rangle$.
The particles' mean velocity is obtained as a temporal average of the total particle velocity every 0.5s (i.e., over 10 snapshots). To compute the particle level, the conveyor was divided into 75 sections along its axis, each one $2r_P = 2$mm long, where the highest particle position was computed for the left and right sides of the screw axis. Subsequently, the mean maximum height was evaluated and averaged over time every 0.5s (same temporal average as the particles' velocities) for the left and right sides of conveyor to give h_L and h_R (see figure 2.3a). The particle height levels were rescaled to the dimensionless coordinate system based on the full filling of the screw. Finally, the mean volume throughput $\langle \dot{V} \rangle(\epsilon, \omega)$ was evaluated by computing the mean volume of particles crossing 5 axial sections of the system, located one screw thread length from one another (figure 2.3b) and then averaged in time.

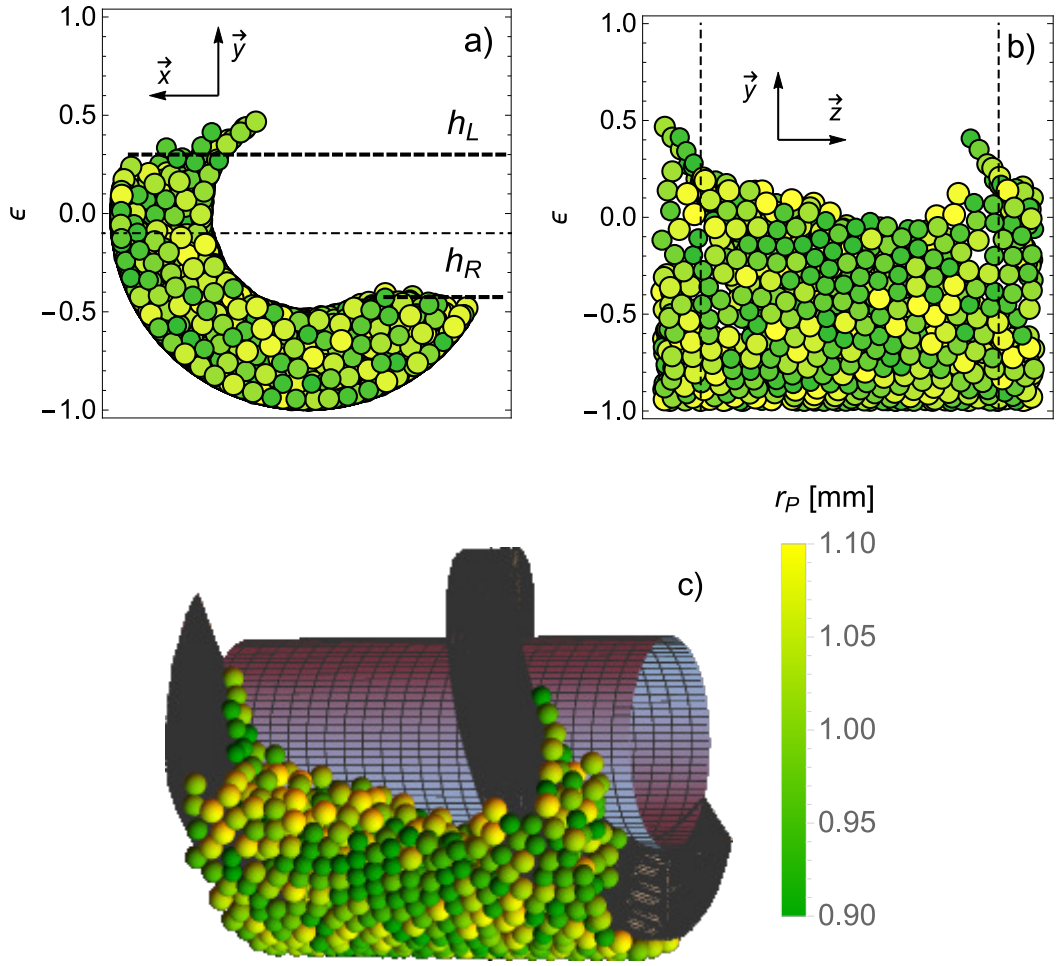

Figure 2.3: Snapshot of the system at $t = 2.0$s for filling level $\epsilon = -0.1$ and screw velocity $\omega = 48$rpm, with particles colour based on the size. Flowing direction is along the positive z semiaxis. a) projection on the x-y plane. The dashed lines represent the particles' height levels and the dot-dashed line is the initial level of particles. b) projection on the y-z plane of a section of the conveyor. The distance between dashed lines represent the length of one screw thread l. For the particles' level evaluation, for a better resolution of the top layer each one of these threads was divided into 15 slices. c) 3D view of the former section including the feeding screw elements. Both b) and c) are mirrored with respect to the y-z plane, to have the particles visually flow from left to right.

2.3 Results

2.3.1 Particle volume flow rate

We expected the volume throughput (flow rate) to be directly proportional to both the screw speed and the filling level. Since the velocity regimes studied in this paper are relatively low (to prevent the particles from centrifuging inside the conveyor), we expected the relation between the particle throughput and the screw velocity to be linear [124],

i.e., $\dot{V}(\epsilon, \omega) \propto \omega$. Moreover, neither the "particle side confining" nor the "back-flow" were expected to play any role at low fillings since these effects only occur when the particle height is roughly at the shaft level. The confining and back-flow have different filling thresholds, the former taking place before the latter. At high fillings, we expected the back-flow of particles to approach a constant value since the particles' level is constant above the screw shaft. Similarly, at high ϵ, the side confining should disappear since the leaping particles should fill the right side of the conveyor. Our simple considerations suggested a non-linear dependency of the throughput on the filling: $\dot{V}(\epsilon, \omega) \propto f(\epsilon)$.

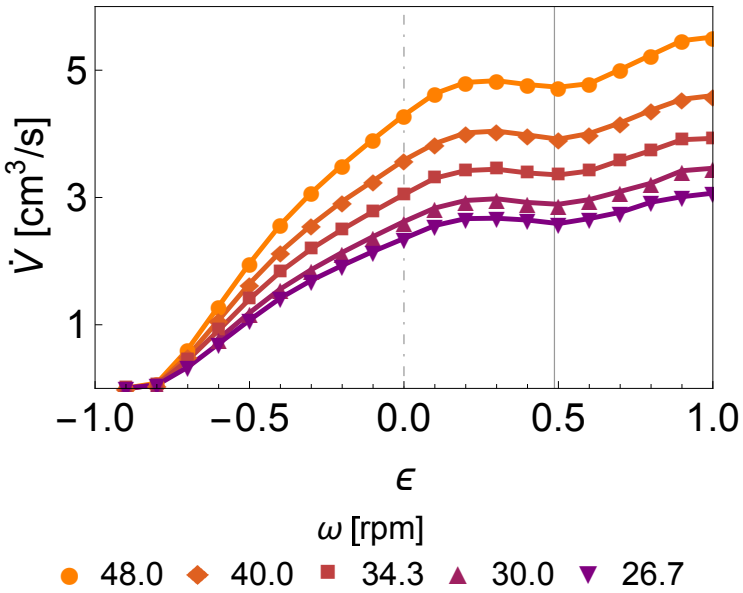

Figure 2.4: Mean volume throughput as a function of the filling level at various screw velocities (connecting lines provided as eye guide). The solid vertical line represents the shaft top edge position; the dot-dashed line is the screw axis.

Figure 2.4 shows the volume throughput as a function of the filling level for various angular velocities of the screw. Surprisingly, the throughput shows a maximum and a minimum for all rotation rates, and it is at a local minimum when ϵ is close to the shaft's top edge. The reasons for this are the following: the layer of particles on the conveyor's left side is not uniform along the screw axis and has a peak close to the screw's blade, which is constantly lifting the particles (see figure 2.3b and c). Because of this non-uniformity, the particles leap over the shaft at only a fraction of the length rather than along the entire length, for which it is required that the particle level ϵ be constantly higher than the shaft top edge level $\rho_S = R_S/R_C = 0.49$. Therefore, we expected to reach the minimum volume throughput when the back-flow acts along the entire length, which takes place when the initial filling level coincides with the shaft top level, i.e. $\epsilon = \rho_S$. For filling ratios higher than this threshold the contribution of the back-flow on the volume throughput becomes constant. In contrast, higher filling ratios imply a higher throughput for any given screw velocity. Therefore, we observe an increase in the throughput for $\epsilon > \rho_S$.
Note that in starve-fed conveyors the volume throughput is constant, corresponding to a horizontal line. Thus, in a certain range of throughputs, different fill ratios may be

achieved, since the horizontal line has three intersections, i.e., at low-, intermediate- and high-fill levels. This phenomenon is called multiplicity and can have significant impact on the control and processing of materials [70].

2.3.2 Effect of relative shaft size

In order to validate this assumption, the same set of simulations was repeated for two shaft sizes set at $R_S^{\pm} = R_S \pm 2\bar{r_P}$ (relative ratio of 0.59 and 0.38, respectively), i.e. one mean particle diameter bigger or smaller than the initial shaft.
The volume throughput normalised with respect to the screw angular velocity is shown in figure 2.5. The curves attributable to the same shaft size collapse into one, suggesting that the volume throughput is linearly proportional to ω as hypothesized. What is more, it was confirmed that the rescaled size ρ_S is a critical parameter for determining the slope of $\langle \dot{V} \rangle(\epsilon, \omega))$ and, in particular, its local extreme. For a smaller shaft (depicted in red in figure 2.5), since the threshold of the particle back-flowing along the entire pitch length is reached at lower fillings, the local minimum of the throughput is displaced towards the left. The opposite is true for a shaft with a bigger radius (blue curve).

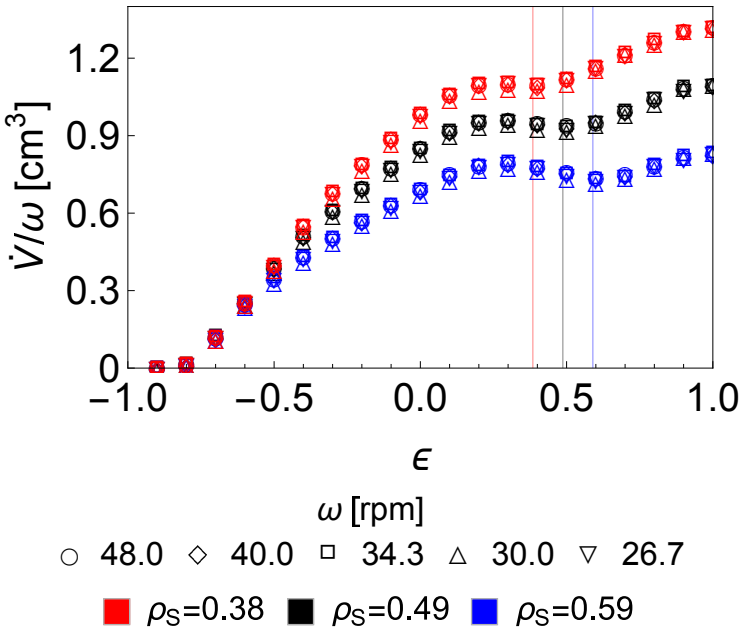

Figure 2.5: Mean volume throughput normalised with respect to screw velocity as a function of filling level for various shaft sizes. Curves for different rotation rates collapse (i.e., for 26.7 rpm, 30 rpm, 34.3 rpm, 40 rpm, 48 rpm). The continuous vertical lines represent the shaft top edge positions in the three cases. The colours refer to the three shaft sizes. The curves belonging to the same shaft ratio ρ_S coincide, which indicates the linear dependence of $\langle \dot{V} \rangle$ on ω.

Particle top layer height

Since we identified ρ_S as a key parameter for the particle back-flow, the next step was to study how the particles' top layer height changes with respect to the operating parameters ϵ and ω for different ρ_S ratios.

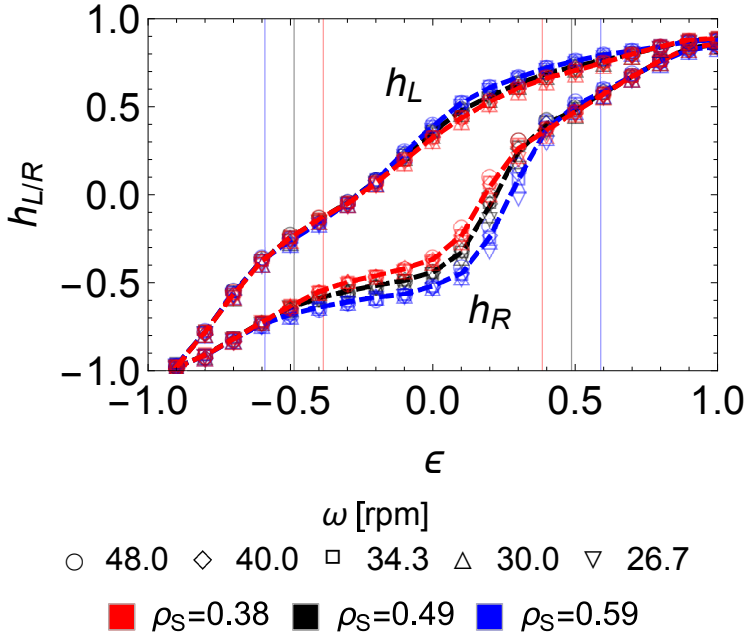

Figure 2.6: Particles' left h_L (upper branches) and right h_R (lower branches) levels as a function of filling level for the three shaft sizes. Data points for different velocities at the same ρ_S overlap. The vertical grid lines represent the top (right) and bottom (left) edges of the shaft $\epsilon = \pm\rho_S$, with different colours referring to the respective shaft sizes. (Note that for $\epsilon = 1$ the dimensionless height does not reach exactly 1, since particle levels are counted at the particle center and due to the initialization of the DEM simulation.)

Figure 2.6 shows the particles' left and right height levels as a function of the initial filling level. The results indicate a small deviation in the height at various screw velocities and the same ρ_S due to the low-velocity regime chosen for the simulations. The slope of h_L (upper branches in figure 2.6) indicates that the shaft size has no effect on the increment in height on the side of the conveyor, where the screw lifts the particles due to an interplay between the friction of the particles and the helix angle γ of the screw. This angle depends on the radial distance r between the measuring point and the screw axis and is defined as the angle between the projection of the blade on the y-z plane and the vertical y-axis:

$$\gamma = \tan^{-1}\left(\frac{l}{2\pi r}\right). \tag{2.2}$$

The value of γ is at its minimum near the external case and reaches the maximum approaching the middle shaft. The helix angle intrinsically determines the geometry of the screw blade and provides a measure of transport efficiency of the screw conveyor [113].

The height to which the screw can lift the particles is also affected by friction. Due to friction with the particles (particle-wall friction coefficient μ_{PC}) the blade drags the conveyed material higher up acting against gravity.
The higher the inter-particle friction μ_{PP} is, the more granular material can sustain itself. In our case, the difference between the various shafts, and consequently in the difference in the mean helix angle γ, is not enough to play an important role. In addition, the coefficient of friction does not depend on the relative velocity between the blade and the particles (provided it is non-zero). Therefore, h_L is dominated by friction effects and is not affected by either ρ_S or ω. The small differences observed around $\epsilon \simeq 0.1$ are due to the particle leaping, triggering the back-flow in the smaller shafts earlier than in bigger ones.
The situation is completely different for h_R. The initial slope of the curve is flatter compared to h_L due to the screw geometry, which continuously pushes the particles to the left, but still independent on ρ_S for $\epsilon < -\rho_S$. However, as soon as the filling level approaches ρ_S, the particles that are pushed to the left side remain between the left side of the conveyor and the shaft. This is due to the discrete size of particles in granular assemblies and the particles' friction coefficient. As a result, the slope of h_R clearly flattens once $\epsilon > -\rho_S$, especially for the bigger shaft (blue), until the particles begin to back-flow due to ϵ closing towards ρ_S. Thereafter, the particles that back-flow from the preceding screw section begin to fill the right side, and the height difference between h_L and h_R decreases. As soon as back-flow becomes uniform along l, the slope of h_R for $\epsilon > \rho_S$ returns to its former value.

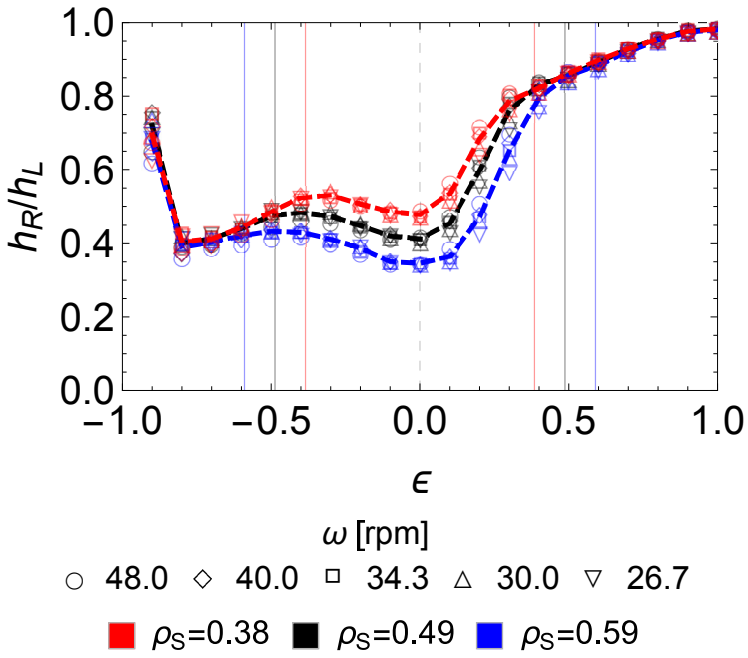

Figure 2.7: Ratio h_R/h_L of the particle levels at various velocities (data points) and their average (dashed lines) as a function of filling. Particles confined on the left side for $-\rho_S \leq \epsilon \leq 0$ are responsible for the slope change. The scatter of data at 5% filling ($\epsilon = -0.9$) is due to a high fraction of particles located below the screw bottom tips.

The amount of particles pushed from the right side to the left is determined by two factors: the screw helix angle γ and the particle friction coefficients μ_{PP} and μ_{PC}. These two parameters are also responsible for the slope of the particle's avalanche due to this transversal motion. The slope of the h_R/h_L curve in figure 2.7 confirms this. As soon as the shaft's presence does not interfere with particles' level (i.e., when $|\epsilon| > \rho_S$), the slope of h_R/h_L is the same regardless of the filling level, except for a small fluctuation due to the circular shape of the container. Investigating the particles' avalanches in this specific system is outside the scope of this paper and may be the topic of future studies.

Particle velocities

To achieve a better understanding of the particle flow, we examined the particle velocity. The component in the feeding direction v_z (hereinafter referred to as the axial velocity) is higher near the screw axis. The axial velocity is the component of the overall velocity that should be maximized since the closer it is to the screw's axial velocity v_z^{screw} (i.e., the velocity along z-direction at which the screw surface moves due to its rotation around its axis), the more efficient the feeding process is. The radial component of the velocity defined as $v_r = ||(v_x, v_y)||$ is responsible for the particle displacement through the circular ring enclosed between the shaft and the casing. Since the radial velocity does not contribute to the particle motion along the feeding direction, is irrelevant for conveying purposes.
As we observed, the screw blade lifts the particles at every transition, generating a continuous avalanche motion. Because of its shape, the direction of the avalanching particles is normal to the screw's surface and can be split into a longitudinal (along the z-direction) and a transversal (in the x-y plane) components. Their velocity components are v_z and v_r, respectively (depicted in figure 2.8a and b). Their time averages at the various operational parameters ω and ϵ are shown normalised by their respective screw component velocities defined as follows

$$v_z^{\text{screw}} = \omega \frac{l}{2\pi}, \qquad v_r^{\text{screw}} = \omega \frac{R_C + R_S}{2}. \tag{2.3}$$

The axial velocity increases along with the filling up to $\epsilon = -\rho_S$ and remains constant at higher filling levels as soon as $\epsilon > (\rho_S + 1)/2$. Figure 2.8c shows the ratio $\bar{v}_z/\bar{v}_r$ as a function of operating parameters. The slope of the curves reflects the trend of its components, exhibiting two plateaus for $-\rho_S \leq \epsilon \leq 0$ and $\epsilon > (\rho_S + 1)/2$. Although the data points are more scattered up for $\epsilon < 0$ (i.e., less than a half-filled screw) for various screw velocities, the mean ratio (dashed lines) clearly indicates that the smaller the shaft is, the more efficient the particles are conveyed, regardless of the filling level and of the screw velocity.

Conveying efficiency

Next, we aimed to establish how various shaft size ratios affect the particle levels and their velocities, since both aspects contribute to the volume throughput and its efficiency in different ways. First, there is a particle height difference, which is directly related to ρ_S. The higher ρ_S is, the later the particle back-flow begins and the longer side-confining continues, increasing the rate of axial transport. Secondly, the wider the shaft is, the further the particles remain from the screw axis, leading to a higher mean helix angle γ and a more inefficient particle conveying.

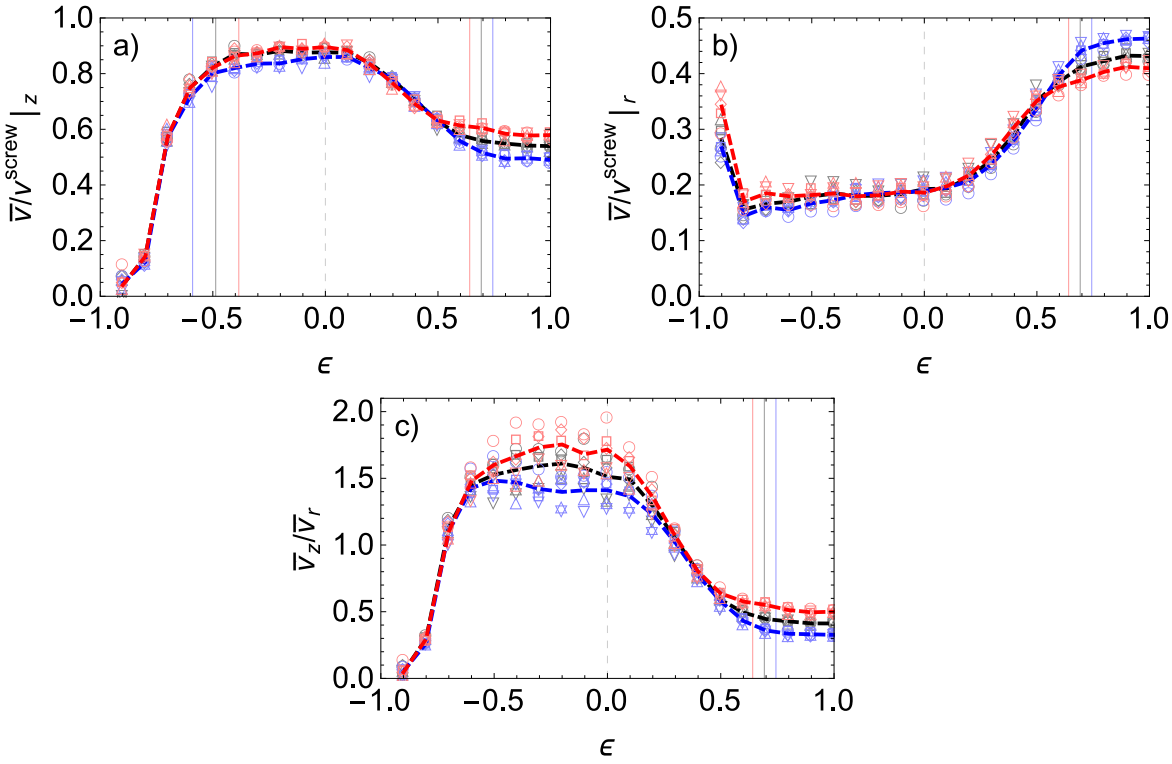

Figure 2.8: Particle mean velocities with respect to filling for various shaft size ratios (colours) and screw velocities (marker symbols). a) normalised mean axial component, b) normalised mean radial component, and c) mean axial versus mean radial velocity ratio. Differences at 5% filling ($\epsilon = -0.9$) in b) is for the same reason as in figure 2.7. The vertical grid lines are: bottom edge of the shaft (left), screw axis (middle dashed) and mean screw blade radius (right), with the color referring to the respective ρ_S-ratio.

To determine which configuration results in the most efficient process, we plotted the conveying efficiency defined as the ratio of the mean volume throughput to the mean maximum throughput:

$$\eta = \frac{\langle \dot{V} \rangle(\epsilon, \omega)}{\langle \dot{V}^{\max} \rangle(\epsilon, \omega)}. \tag{2.4}$$

The mean maximum throughput is defined as follows:

$$\langle \dot{V}^{\max} \rangle(\epsilon, \omega) \simeq \frac{\Delta V}{\Delta t}(\epsilon, \omega) = S(\epsilon) \cdot \frac{\Delta z}{\Delta t}(\omega) = S(\epsilon)\, v_z^{\text{screw}}(\omega) \tag{2.5}$$

where $S(\epsilon)$ is the screw cross section initially occupied by the particles (e.g. see figure 2.2a) and v_z^{screw} has been defined in equation (2.3), the first equality holding since the mean throughput is averaged over multiple screw turns. Note that the normalization in figure 2.9 was not performed with respect to full filling, since $\langle \dot{V}^{\max} \rangle$ is also a function of ϵ, and represents the maximum achievable volume throughput *for given initial filling level*. The shape of the curves in figure 2.9 is similar to the velocity ratio $\bar{v}_z/\bar{v}_r$ in figure 2.8c, with the same two plateaus. The data points represent the volume throughput efficiency

(equation (2.4)) while the dashed curves are rescaled taking into account the particles packing fraction, which was assumed to have a constant value of 0.63. The conveying efficiency η is always higher for smaller shafts, indicating that the back-flow of particles and the side confinement play a secondary role, compared to the mean axial velocity $\bar{v}_z$. The efficiency reaches its maximum at $-\rho_S \leq \epsilon \leq 0$, where it is $\eta \simeq 0.7$ for $\rho_S \simeq 0.5$, and decreases to $\eta \simeq 0.45$ at the full filling (taking into account the packing fraction).

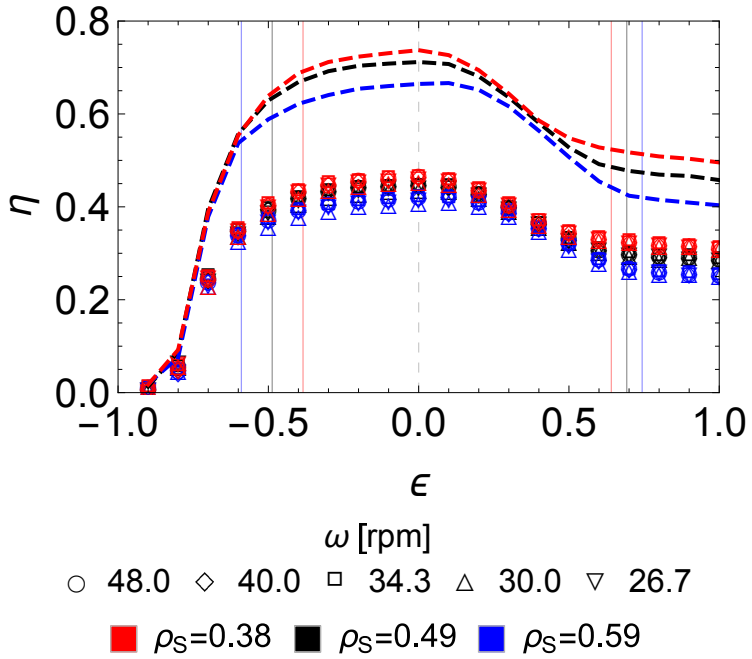

Figure 2.9: Screw-conveying efficiency with respect to operating parameters for the three shaft sizes (different colors). Data points represent the simple normalised volume throughput according to equation (2.4). The dashed curves are rescaled with a constant packing fraction of 0.63. The vertical grid lines are the same as in figure 2.8.

Partially-filled screw conveyors reach the maximum conveying efficiency within a precise filling interval, which is unaffected either by the screw velocity ω (provided that it is low enough to avoid particle centrifuging) or by the relative size of screw shaft relative to the external casing ρ_S. In addition, for given operating parameters (ϵ, ω), the most efficient device is the one with the lowest screw shaft-to-casing ratio ρ_S. This holds true if the mean size of the conveyed particulate is much smaller than the typical geometric parameters of the screw (pitch length, shaft diameter, blade radial length, casing diameter, etc.) to avoid finite size effects.

2.3.3 Effect of the particle-conveyor friction coefficient

As in every particle-based system and industrial process concerning mechanical components in motion, friction plays an important role. Its contribution affects the dynamics of the system and plays a major role with regard to the efficiency of the screw conveyor. As such, we investigated how the friction coefficient affects the throughput in the system and to

which extent.
In our case, there are three friction coefficients: the inter-particle friction μ_{PP}, the friction between the mechanical components of the conveyor and the particles μ_{PC} and the friction μ_{CC} between the various parts of conveyor. Since in practice we cannot change the friction between the conveyed material components and since in our model there is no contact between the rotating screw and the external casing (making the model de facto independent on μ_{CC}), we only investigated μ_{PC}. To that end, we applied the settings described in the previous section, except that the screw speed had a constant value of $\omega = 34.3$rpm, a constant shaft-casing size ratio of $\rho_S = 0.5$, and μ_{PC} varied in an interval of $[0.15, 0.55]$.

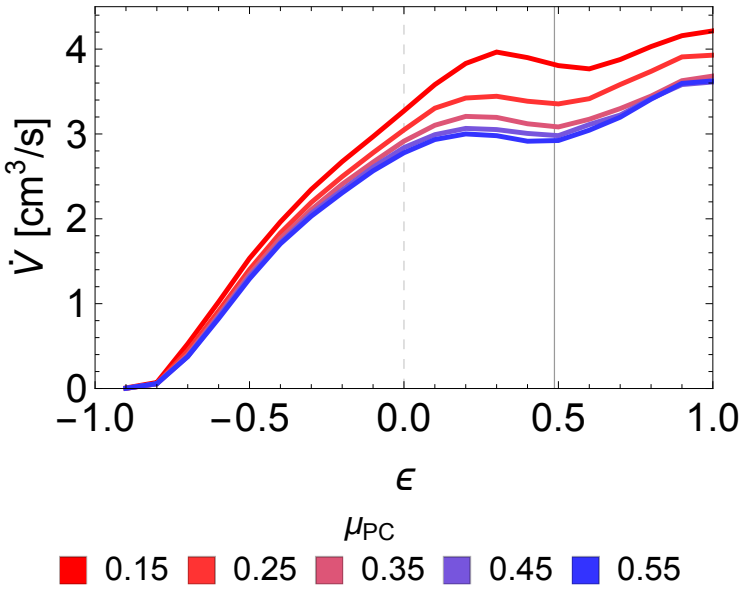

Figure 2.10: Mean volume throughput as a function of filling level for various particle-conveyor relative frictions μ_{PC} ($\rho_S = 0.5$). The continuous vertical line represents the shaft top edge position; the dot dashed line is the screw axis.

The volume throughput for various filling levels and various μ_{PC} is shown in figure 2.10. As expected, the volume throughput is inversely proportional to the relative friction coefficient. At higher friction, the curves converge to a lower limit, which is the least amount of volume throughput achievable under the system operating conditions. This value depends on the relative shaft size ρ_S and on the screw shape given by γ. The physical interpretation of having a lower-bounded volume throughput is simple: once the friction becomes higher, the relative tangential velocity of the particles with respect to the screw surface will tend to zero. Thus, for increasingly high friction coefficients, no further reduction in the volume throughput can occur (and the normal velocity stays constant as well). For lower friction coefficients, not only the volume throughput is higher, but the curve extrema are displaced toward higher fillings. The reason can be understood observing the particles levels.

Particle top layer height

As mentioned above, friction impacts the particle height. The higher the friction, the more strongly particles are dragged to the left side, leading to a higher h_L. The level cannot

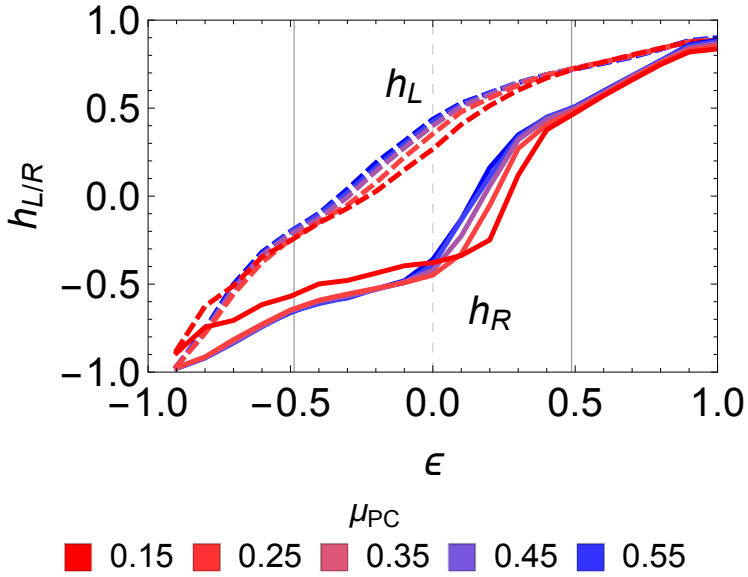

Figure 2.11: Particle left (dashed lines) and right (filled lines) heights as a function of filling level for various particle-conveyor relative frictions μ_{PC} ($\rho_S = 0.5$). The continuous vertical line represents the shaft edge position; the dashed line is the screw axis.

be raised arbitrarily high by friction, since frictional forces have an upper bound and act only tangentially relative to the blade surface. Therefore, h_L must be upper-bounded, the maximum value being reached after a certain μ_{PC} threshold for a given filling.
The relationship between the maximum h_L and μ_{PC} is complex. It depends on μ_{PP}, γ and the geometry of the system and, for the sake of brevity, we chose not to investigate it further. The minimum value of h_L is limited as well, since there is always a non-null lifting contribution from the screw determined by the normal component to the screw surface, being a function of γ. The same logic can be applied to the right level h_R. The higher the friction, the lower is the level, since the drag to the opposite side is higher. Both the higher and lower values of h_R are limited as well due to the aforementioned extremes in h_L.
The difference in the vertical drag due to friction with the blade can be observed in figure 2.11. Higher drags (and thus higher left levels) at a higher friction were observed for $-\rho_S \leq \epsilon \leq 0$, where the upper drag against gravity occurs and the particle side-confining mechanism dominates. The different slopes of h_L impact also h_R (filled lines) in the $0 \leq \epsilon \leq \rho_S$ region: the higher the level of particles dragged due to friction for a given filling, the earlier they will hop over the shaft and raise the right side level.
The slope of particle avalanches (i.e., the difference in height between left and right side) was also modified for low filling levels, as shown in figure 2.12. The vertical drag of the screw blade clearly depends on the geometry, given by γ, and the friction coefficient μ_{PC} and, indirectly, on the filling level. In fact, the lifting force exerted by the screw is a function of the angle γ which also depends on the relative position of the screw blade. The normal vector $\hat{n}(r, \phi)$ to the latter rotates in the x-y plane around the axis with the same period of the screw. While its component along the z axis depends on the radial position and is completely determined by γ, it is unaffected by the blade's relative

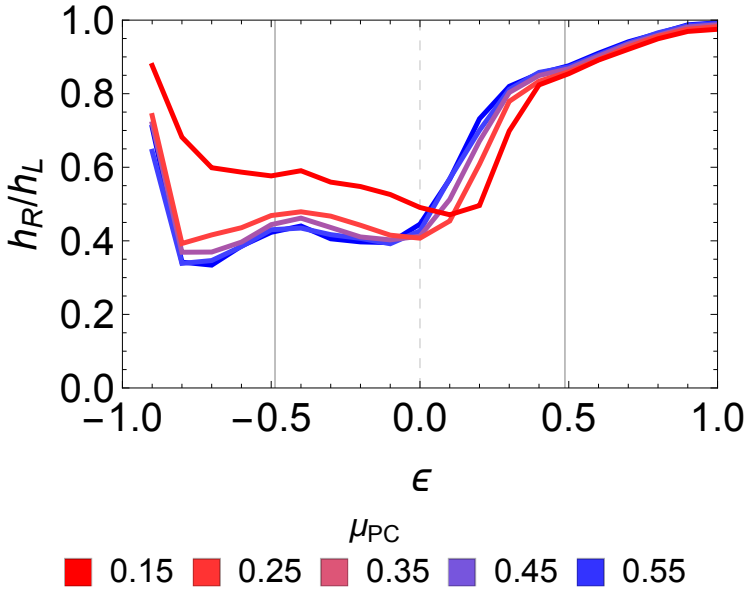

Figure 2.12: The ratio h_R/h_L for various relative friction coefficients μ_{PC} and $\rho_S = 0.5$ as a function of filling. For $\epsilon \leq -\rho_S$ the friction affects the transversal avalanche slope, while for $\epsilon > \rho_S$ the inter-particle friction μ_{PP} (constant) plays the major role. The scatter found at 5% filling is due to a high fraction of particles laying below the screw bottom tips.

position. On the contrary, the component along $\vec{y}$, which is the direction of gravity, is proportional to the angle ϕ between the blade projection on the x-y plane and the $-\vec{y}$ semiaxis: $\hat{n}_y \propto \sin\phi$. Similarly, the component normal to the blade along the $\vec{x}$ semiaxis has a $\pi/2$ phase shift from the former: $\hat{n}_x \propto \cos\phi$. Therefore, at low fillings $\epsilon \leq -\rho_S$, the transversal (perpendicular to axis) component $\hat{n}_x$, which is responsible for the height difference, is at its maximum. Consequently, the impact of the relative friction μ_{PC} on the height ratio h_R/h_L is higher for small filling levels (figure 2.12). At high filling levels, the avalanche is dominated by inter-particle collisions and the slope of the particle avalanche is affected by μ_{PP}. Since the latter was kept constant in this set of simulations, the h_R/h_L slope is the same for $\epsilon > \rho_S$, as confirmed by numerical data. The region $-\rho_S \leq \epsilon \leq 0$ has confining mechanics, while the leaping effect begins at $0 \leq \epsilon \leq \rho_S$. The threshold is slightly affected by the particle-conveyor friction for the reasons stated above.

Particle velocities

The plot of the components of the mean particle velocities normalised with respect to the factors in equation (2.3) are shown in figure 2.13. The behaviour of the velocity is the same as observed in the former set of simulations, in that the particles' mean axial $\bar{v}_z$ and radial $\bar{v}_r$ velocities have a plateau at $-\rho_s \leq \epsilon \leq 0$ and for $\epsilon > (\rho_S + 1)/2$, with the same underlying physics. Lower friction translates into lower heights (and thus in a more stable confining phenomenon), which results in a higher mean axial velocity (figure 2.13a). For reasons stated above, since the normal component of the screw is responsible for the axial velocity, there is a lower limit to $\bar{v}_z$ at higher friction coefficients.
The most notable effect of lower friction is its extension to higher fillings of the upper

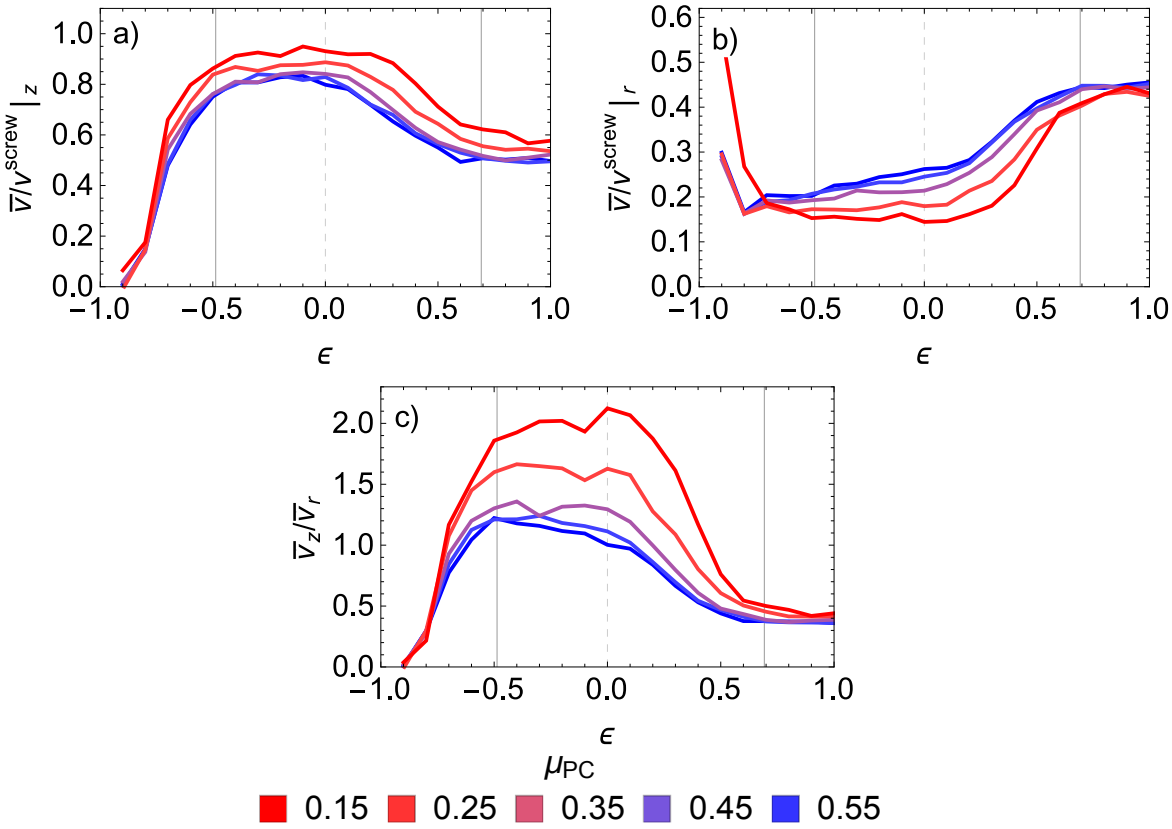

Figure 2.13: Particles' mean velocities with respect to the filling level for various particle-conveyor relative frictions and $\rho_S = 0.5$. a) normalised mean axial component, b) normalised mean radial component and c) mean axial versus mean radial velocity ratio. Fluctuation at 5% filling in b) due to a high fraction of particles below the screw bottom tips. The vertical grid lines are: bottom edge of the shaft (left solid), screw axis (middle dashed) and mean screw blade radius (right solid).

threshold that are responsible for the plateau due to the side confinement. This happens due to a flatter profile of particles in the x-y plane, and the leaping state is reached for higher ϵ the lower the friction. In fact, the lower the friction, the less the particles will be dragged against gravity when in contact with the screw blade. Therefore, the particle profile along the axis will be flatter. Because of this, the maximum height is lower due to mass conservation, and the leap-over will be triggered at higher filling ratios for lower friction coefficients. The radial velocity component is inversely proportional to the axial one, as described above (the closer the particles are to the shaft, the faster they move along the z-axis and the lower the radial velocity is), with a longer plateau in the side confinement region ($-\rho_s \leq \epsilon \leq 0$) at lower friction coefficients.
With regard to the velocity components ratio $\bar{v}_z/\bar{v}_r$ (figure 2.13c), the effect of friction appears to be significant. In the $-\rho_s \leq \epsilon \leq 0$ region, the ratio doubles when μ_{PC} is within the range of $0.15 - 0.55$, and the optimal conveying region further extends to values of $\epsilon > 0$. As stated above, the velocity ratio is lower for higher particle-conveyor friction coefficients, the latter being almost non-influential under the lower plateau regimes for

$\epsilon > (\rho_S + 1)/2$ (since μ_{PP} dominates the frictional effects rather than μ_{PC}).

Conveying efficiency

Finally, we considered the effect of friction on the conveying efficiency (figure 2.14). The axial profiles in figure 2.13 are very close in shape to the particle volume conveying efficiency in figure 2.14. The top-plateau extension to higher ϵ values is as also observed for lower particle-conveyor friction coefficients, since the threshold typically found around $\epsilon = 0$ for the particle height levels and velocities is shifted towards a higher filling level.
The maximum of the volume conveying efficiency is still found in the region $-\rho_S \leq \epsilon \leq C$, where $C \in [0, \rho_S]$ and is reduced to 0 at high μ_{PC}, while tending to ρ_S when $\mu_{PC} \to 0$. The value of the efficiency ranges from $\eta \simeq 0.65$ for $\mu_{PC} = 0.55$ to $\eta \simeq 0.75$ for $\mu_{PC} = 0.15$ (with a constant packing fraction of 0.63). For higher relative friction coefficients, the efficiency collapse to the same curve, as seen for the particle volume throughput in figure 2.10.

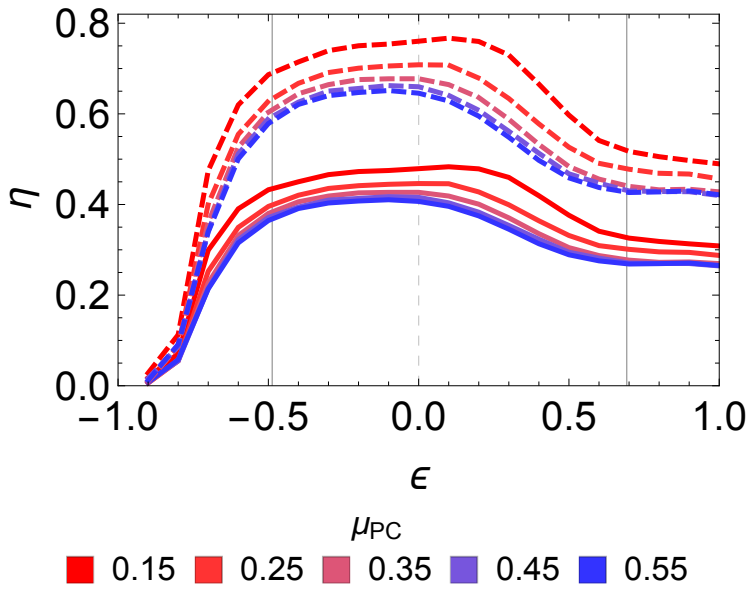

Figure 2.14: Screw conveying efficiency with respect to operating parameters for various particle-conveyor components friction coefficients ($\rho_S = 0.5$). Solid lines represent the simple normalised volume throughput according to equation (2.4), the dashed lines rescale the latter with a constant packing fraction of 0.63. The vertical grid lines are the same as in figure 2.13.

2.4 Discussion

Despite the mechanical simplicity of screw conveyors, a detailed analysis of the granular material motion in such devices is complex. The screw's geometry makes it impossible to reduce it to a quasi-2D system, which is, for instance, possible for rotating tumblers and inclined chutes. The horizontal inclination of the conveyor disrupts the cylindrical symmetry of the system since gravity pushes the particles in the preferred direction. Moreover,

the behaviour of dynamic granular systems has to be considered, making the conveying process strongly dependent on the particles' relative friction coefficients, particle size distribution and finite size effects.
As sketched in figure 2.5, the volume throughput is linearly proportional to the screw rotating speed; therefore the velocity ω has no effect on the conveying efficiency as defined in equation (2.4). This result is valid in the assumption of a reasonably low screw velocity to avoid particle cataracting or centrifuging. The interaction between particles and screw shaft determines a characteristic particle motion, which manifests itself in a non-linear dependence of the throughput on the filling level (figure 2.4). There are 4 main filling ranges, within which the particles have systematic behaviours, depending on the geometry of the screw through the parameter ρ_S:

- $\epsilon \leq \rho_S$: the particles do not interact with the screw's middle shaft. Blade-casing clearance adds systematic fluctuations to the particles' levels and velocities. Friction and screw shape play a major role in determining the particles' avalanching and their dynamics.

- $-\rho_S \leq \epsilon \leq C, C \in [0, \rho_S]$: the particles are confined to one side, between the external casing and the shaft. The friction determines the constant C and is inversely proportional to it. Axial avalanching is enhanced. The conveying efficiency reaches its maximum and remains roughly constant.

- $C \leq \epsilon \leq (\rho_S + 1)/2$: the confined particles are lifted and leap over the middle shaft, falling into the next screw thread and contributing to the transversal avalanching. The particle back-flow is characteristic to this region. Volume throughput and efficiency are significantly reduced, the former reaching the local minimum.

- $(\rho_S + 1)/2 \leq \epsilon \leq 1$: the particles back-flow is uniform along the entire screw section length, and the transversal avalanching reaches the maximum. The conveying efficiency reaches its minimum and becomes constant.

The relative shaft size and friction between the particles and the mechanical components of the conveyor directly affect throughput and efficiency. Moreover, they determine the thresholds of the filling regions. We established that, regardless of the operating parameters, both the volume throughput and the conveying efficiency are inversely proportional to the shaft's relative size compared to the conveyor as well as to the particle-conveyor friction coefficient. Thus, highly-polished steels will increase conveying efficiency compared to rougher materials.
Our work provided the following insights, which can be useful for screw conveyor design and operating parameters tuning:

- At screw speeds that prevent particle cataracting or centrifuging, the volume throughput linearly depends on the screw rotating velocity, while the efficiency does not depend on it.

- The conveying efficiency is maximized at a filling ratio around 50%, with this value being shifted due to particle-screw relative friction.

- The friction between the conveyor components and the transported material should be minimized to improve both throughput and efficiency.

- Regardless the operating parameters, a smaller shaft always translates into a higher throughput and efficiency.
- In a certain range of throughputs, multiple fill levels can result in the same volume throughputs (i.e., the system exhibits multiplicity).

2.5 Conclusions

In this study we performed a set of Discrete Element Method simulations, modelling the transport of a granular material by a screw conveyor. The screw rotation velocity and the initial particle filling level are used as operating parameters to study the mean volume throughput of the device. Different screw shaft radii were employed in this numerical study to show how the shaft size compared to the conveyor one is a determinant factor for the flow of the conveyed material. The conveyor operating parameters directly affected the particles' height levels and relative velocities with respect to the screw blade, both of which are key aspects with regard to throughput and efficiency. Because of the peculiar frictional properties of granular materials, we identified four different filling intervals where the flow exhibits typical patterns, such as a *side-confining* and a *back-flow* mechanisms. The extension of those filling regions is unaffected by the screw velocity, but is modified by the friction coefficient.
Our work can provide useful insights in both the design and the operational parameter tuning of starved-fed screw conveyors, widely employed, among others, in grain transport devices and mining.
Future work will address the numerical study of transport properties of such a system for a bi-disperse particle mixture, and the interplay between the particle dynamics dependent on the filling ratio and size segregation. Moreover, it is intended to perform an experimental validation of the proposed model, relating the particle and design properties to the particle flow rate. Since the setup of the experiment is not straightforward, and the validation requires a high number of experimental data points, the experimental validation of the results presented in this paper will be a separate study and will be the topic of future publications.

Acknowledgements

This work was supported by the IPROCOM Marie Curie initial training network, funded through the People Programme (Marie Curie Actions) of the European Union's Seventh Framework Programme FP7/2007-2013/ under REA grant agreement No. 316555. Research Center Pharmaceutical Engineering is funded by the Austrian COMET Program under the auspices of the Austrian Federal Ministry of Transport, Innovation and Technology (BMVIT), the Austrian Federal Ministry of Economy, Family and Youth (BMWFJ) and by the Province of Styria (Styrian Business Promotion Agency, SFG). COMET is managed by the Austrian Research Promotion Agency, FFG.

Chapter 3

A combined DEM & FEM approach for modelling roll compaction process

Abstract[1]

Roll compaction is a continuous manufacturing process aiming to produce particulate granules from powders. A Roll press typically consists of a screw feeding system, two rolls and a side sealing. Despite its conceptual simplicity, numerical modelling of the process is challenging due to the complexity involving two different mechanisms: feeding by the screw and powder compaction between the rolls.

To represent the materials' behaviour both in the feeding zone and in the compaction area, a combined three-dimensional Discrete Elements Method (DEM) and Finite Elements Method (FEM) is developed in this work. The DEM, which is a more suitable method to describe the flow of granular material, is used to model the motion of particles in the feeding zone. As the granular material deforms under high pressure between rolls, FEM offers a more versatile approach to represent the powder behaviour and frictional conditions. In the proposed approach the DEM and FEM are treated as complementary methods, enabling us to take advantages of the strengths of both.

In this proposed approach, the time dependent velocity field of the particles at the end of the screw feeder is evaluated as a continuous field using the Coarse Graining (CG) framework, which was used as input data for the FEM model. FEM is then used to simulate the powder compaction in between the rolls, and the resultant roll pressure and ribbon relative density are obtained.

[1]With minor corrections from: A. Mazor, L. Orefice, A. Michrafy, A. de Rycka, J. G. Khinast, Powder Technology 337, 3–16 (2018).

3.1 Introduction

Roll compaction is a process designed to compact fine powders to produce particulate granules, and it pertains to continuous manufacturing procedures. During the process, powder is subjected to high pressure from the rolls, leading to the formation of compacted ribbons, which are later milled into granules. The ribbon's relative density largely influences the compactibility of granules and subsequently the final solid dosage form (i.e., compacted tablets) properties. Therefore, relative density is commonly used as a critical quality parameter of the roll compaction process. In order to ensure the consistency, repeatability and quality of the final dosage form, it is important to avoid heterogeneity of the produced ribbon.
A typical roll compactor consists of a single rotating screw, which feeds the material into a gap between two counter-rotating rolls and cheek plates on the sides to avoid leakage. The conveying of powder towards the rolls have a large influence on the roll compaction process. Experimental work showed that the delivery of powder by a screw feed is linearly related to the screw speed [48,130]. An appropriate compaction is reached and maintained with a screw to roll speed ratio laying in a specific range. Simon and Guigon [48] also showed that by using a single feed screw, the compacted ribbon was neither homogeneous along the ribbon's width nor in time. Moreover, these fluctuations have the same period of the screw rotation. The impact of the screw motion on the compaction process is relevant for the ribbon properties, albeit not in a trival way. Not only does the screw design affect particle flow [113] and mixing [106], but also powder properties play an important role [57, 58, 130]. In addition, the behaviour of simple screw feeders will differ as soon as they are coupled with other devices, which will alter the flow properties and the pressure distributions inside. A numerical example can be found in [97].
Numerous studies investigated analytically the roll compaction process. The most well-known analytical model is the Johanson model [63], which is able to determine the pressure along the roll surface, torque and separating force of the rolls, based on the physical characteristics of the powder and dimensions of the press. The main limitation of the classical Johanson model is that it does not include the important process parameters of roll and screw speeds, which led to the extension of this model by Reynolds et al. [111]. However, these models are only one-dimensional and do not take into account the non-uniformity of the conveying of powder and as a result the non uniform roll pressure and ribbon's density distribution. Bi et al. [10] attempted to overcome this limitation by extending Johanson's model to account for a non-uniform powder velocity in the nip region. However, their result is of little experimental use because the model developed introduces a high variability in the predicted pressure peak, and because the estimation of a key parameter of the model cannot be measured experimentally.
To resolve this, Finite Elements Method (FEM) modelling was adopted to simulate the roll compaction process, starting with plane strain two-dimensional cases [24, 28, 95, 98], followed by the development of three-dimensional models to provide greater insight into the pressure and density distribution during the roll compaction processes [25, 90, 94, 99]. In these models, the effect of the screw feeder is approximately represented by a uniform or oscillatory inlet feeding pressure at the entry angle. Liu and Wassgren [80] implemented a mass-corrected version of Johanson's model analogous to [10] in a two-dimensional FEM model, yet based on two experimentally-determined fitting parameters. The results show

a better agreement with the experimental pressure profile when compared to the original Johanson's model. However, the model still relies on experimental data, and only uses an arbitrary constant feed pressure, which does not account for the complex pressure pattern created by the screw conveyor. Michrafy et al. [94] investigated the effect of a constant inlet feeding velocity on the roll compaction process using cheek plates, which resulted in higher pressure and relative density in the middle of the ribbon compared to the edges. Cunningham et al. [25] compared a uniform inlet feeding velocity to a linearly decreasing velocity from the centre to the edges, where both cases have no friction between powder and cheek plates. In the case of uniform inlet feeding velocity, the maximum roll pressure and relative density were the same along the ribbon's width. Using a non-uniform inlet feeding velocity, the powder is fed rather in the middle than at the edges, and consequently results in higher maximum roll pressure, shear stresses and relative density in the middle of the ribbon. These results are comparable with experiments only with the understanding that the conveying of powder in between rolls have a direct effect of the process. In conclusion, in all of the previous FEM models of roll compaction the inlet velocity or feed pressure values are chosen arbitrarily and do not represent the effect of screw feeding. Therefore, features associated to the periodic feeding, such as a non-uniform conveying in both space and time, are still unaccounted for.
The numerical modelling of the roll compaction process remains challenging due to the complexity involving two different mechanisms: the feeding by the screw conveyor and the powder compaction between the rolls. On one side, the incoming particle flow is a key parameter strongly influencing the compaction process, since it dictates the pace of the process and affects the homogeneity of the compacted ribbon. On the other hand, the material deformation under high stress, and the frictional conditions in the compaction region, are the fundamental quantities needed to model the system.
In order to address these issues, we developed a combined three-dimensional Discrete Elements Method (DEM) and FEM methodology. DEM is naturally suited to model the conveying process and will be used to study the particle flow in the feeding zone. The results will be used as boundary inlet conditions for the FEM modelling of the compaction process, which is the best approach to study the compaction of porous materials under high pressure. In our work, the DEM and FEM are treated as complementary methods: combining them in the study of roll compaction enables us to take advantage of their strengths in the regions where they are respectively best suited. The aim of our study is therefore to improve the existing numerical models, leading to a more realistic description of the process which will head us to a better prediction of the final ribbon quality.

3.2 Materials and methods

3.2.1 Roll compaction design and process parameters

This work is based on the Komarek B050H Laboratory Press (K.R. Komarek Inc., Wood Dale, IL, USA) shown in figure 3.1. The Komarek roll compactor is constructed with a horizontal screw conveyor and two counter-rotating rolls with fixed side seals (i.e. cheek plates) in between. The process parameters of minimum gap width between rolls, rolls speed and screw speed were set to $\delta_{\min} = 0.2$cm, $\omega_R = 6$rpm and $\omega_S = 48$rpm, respectively. Further details about the roll press dimensions can be found in table 3.1.

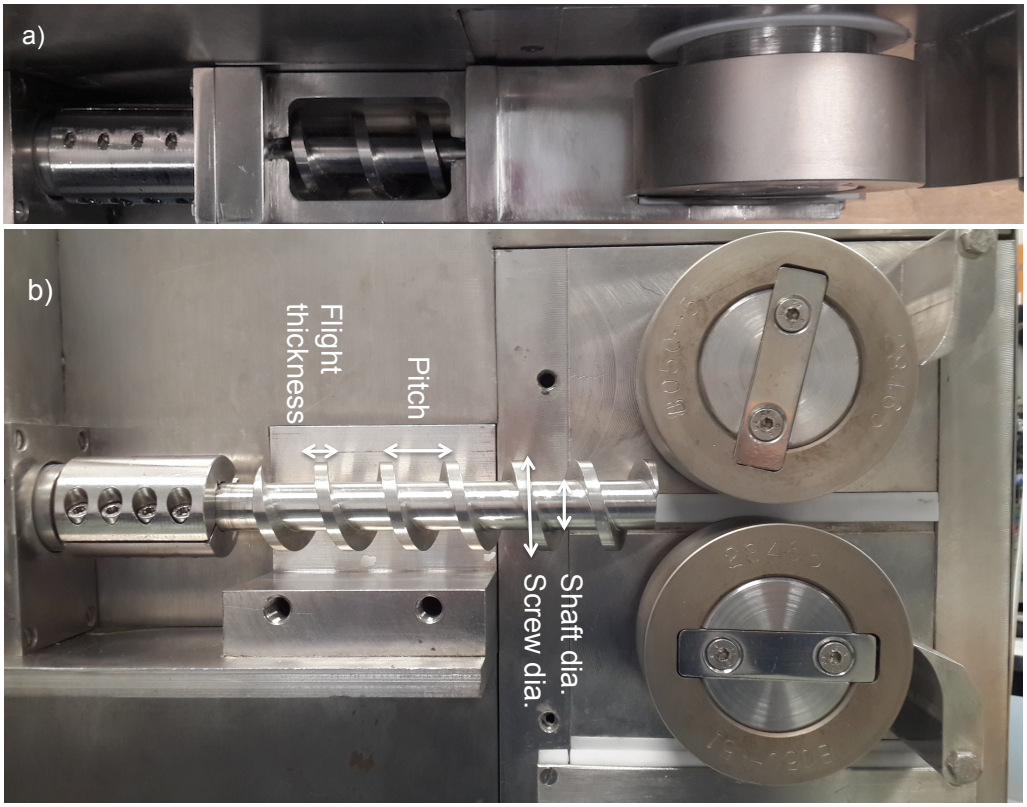

Figure 3.1: Komarek B050H roll compactor; a) Top view and b) Side view (w/o feed barrel and side seals)

3.2.2 Powder

The powder used in this work is microcrystalline cellulose (MCC) (Avicel PH 101, FMC BioPolymer, Philadelphia, PA, USA). MCC is one of the most important and widely employed excipients in the pharmaceutical industry. It has excellent compressibility properties and is used as diluent for drug formulations in the tableting process [18, 56]. The true density of the powder blend was determined using a helium pycnometer (Accupyc 1330, Micromeritics Instrument Corp., Norcross, GA, USA) as ρ_{true}=1.56 g/cm^3.

3.2.3 Discrete Element Method

The Discrete Element Method [23] is a numerical method for computing the dynamics of a large ensemble of small components, typically spherical particles. Particles interact with each other according to a special interaction law and can be influenced by external force fields, such as gravity. In addition, they interact with geometrical objects, which are generally located inside the simulation domain (e.g., walls or pipes) and may affect their movement. The interaction law governing the forces experienced by objects upon collision commonly accounts for an elastic repulsive term (due to the rigidity of the bodies) and a dissipative term (due to friction). In a DEM simulation, contacts between the objects at each time step and forces generated by the collisions are computed. Next, the dynamics of

Table 3.1: Komarek B050H roll compactor dimensions.

Part	Symbol	Size [cm]
Screw feeder		
Screw length	l_s	15
Pitch length	l_p	1.95
Flight thickness	t_{sf}	0.5
Flight diameter	d_{sf}	3.5
Shaft diameter	d_{ss}	1.9
Casing diameter	d_c	3.8
Roll press		
Rolls diameter	d_R	10
Rolls width	w_R	3.8
Minimum gap width	δ_{min}	0.2

the components are evaluated and the equations of motion are integrated, with the position and velocity of objects being updated accordingly. This is repeated at each time step for the entire duration of the simulation.
Discrete Element modelling is suitable for studying the flow of solid particulate materials since the detailed dynamics of every single particle are determined at any moment and the physics of the macroscopic medium is based on it. However, the results greatly depend on the interaction laws between the objects. For instance, accounting for the particle deformation or breakage caused by high pressure is difficult as is the modelling of a (realistically) large ensemble of particles due to very high computational cost. As such, although the DEM model in this study is unsuitable for modelling the compaction process, it can be employed to model the particle flow transported by the screw conveyor inside the compaction region.

Contact model and parameters

In DEM simulations, objects interact according to the well-known Hertzian spring-dashpot contact model [14, 55]. We used rigid, frictional, non deformable spheres of uniformly distributed poly-disperse radius in the range $r_P \pm 10\%$ to model the powder particles and for the compactor components we employed frictional, non-deformable *stereolitographical* (STL) meshes. The mean particle radius was chosen such that every particle could fit through the gap of 0.2cm between the screw blade and the conveyor casing (see table 3.1), with the polydispersity eliminating crystallisation effects between particles that may affect the flow [123, 154]. A common practice in DEM is to use mesoscopic particles in the simulations, i.e., much bigger than the ones in the experiment. We observed that the particle size is not affecting the velocity profile of the particles inside of the screw, and therefore the size chosen is the biggest possible one fitting through the screw clearance (the distance between the screw blade and the casing) to reduce the computational expense. However, we monitored the forces acting on the particles and their overlap to guarantee that no jamming occurred. The interactions account for sliding and rolling friction. In our model, the particles were composed of *Micro-Crystalline Cellulose* (MCC) and the compactor's

Table 3.2: Parameters used in the DEM simulations.

Parameters and material properties	Symbol	Value
Particle mass density [g/cm^3]	ρ_P	1.56
Particle mean radius [cm]	r_P	0.09
Particle Young's modulus [Pa]	Y_P	$1.0 \cdot 10^{10}$
Conveyor Young's modulus [Pa]	Y_C	$1.8 \cdot 10^{11}$
Particle Poisson ratio [−]	ν_P	0.30
Conveyor Poisson ratio [−]	ν_C	0.30
Particle-particle restitution coeff. [−]	e_{PP}	0.83
Particle-conveyor restitution coeff. [−]	e_{PC}	0.80
Particle-particle sliding friction coeff. [−]	$\mu_{PP}^{\text{sliding}}$	0.53
Particle-conveyor sliding friction coeff. [−]	$\mu_{PC}^{\text{sliding}}$	0.20
Particle-particle rolling friction coeff. [−]	$\mu_{PP}^{\text{rolling}}$	0.25
Particle-conveyor rolling friction coeff. [−]	$\mu_{PC}^{\text{rolling}}$	0.10
Screw operational velocity [rpm]	ω_S	48
Rolls operational velocity [rpm]	ω_R	6
Gap width [cm]	δ	0.36
Time step [s]	δt	$5.0 \cdot 10^{-6}$
Data output interval [s]	Δt	0.01

components material was steel, material properties taken from [52, 75, 76, 116, 176]. We recorded the DEM simulation data every $2 \cdot 10^3$ time steps of length δt, resulting in a time interval of duration Δt between the monitored snapshots. The simulation parameters and the material properties are reported in table 3.2. The simulations used for this study were performed using the *open source* DEM particle simulation code LIGGGHTS [71].

Discrete Element Model

A schematic representation of the DEM model of the compactor is shown in figure 3.2, all the geometry parameters being listed in table 3.1. Each simulation is composed of 3 distinct phases: loading, transient and steady flow.
During the loading phase, the system is filled with particles. To this end, 7500 particles were loaded into a parallelepipedal volume inside the hopper (A) every second of physical time. As soon as they reached the bottom, the screw (B) dragged them towards the compaction region (D) that gradually began to fill. The screw velocity during this phase was a fraction of the one used at full speed during the compaction process, and the rolls speed was set to zero. A wall prevented the particles from exiting the compaction region through the inter-rollers gap. The loading phase continued until both the compaction region and the hopper were completely filled with particles.
Once the desired fill level was achieved, the transient phase began and the wall blocking the exit through the gap between the rolls (E) was removed. Both the screw and the roll velocities were set to their operational values of ω_S and ω_R respectively, and the particles began to flow through the gap. The particle loading in the hopper remained unchanged in order to keep it constantly full and to preserve the overall number of particles in the

system at around $8 \cdot 10^4$. The purpose of this phase is a transition from the static loading phase to the steady state phase.
The steady-state regime is reached when there are negligible fluctuations both in the mean volumetric flow and in the mean axial velocity of the particles measured along certain planes normal to the axis. A snapshot of the steady-state system is illustrated in figure 3.3. As it can be seen, the axial velocity of the particles, which is almost uniform inside the screw barrel, quickly drops as soon as they approach the compaction region inlet, where they experience a considerable back-pressure due to a high density in this area. Regions of low velocity are located against the back wall of the compaction chamber. The particles' velocity rises as they approach the gap, where they are compacted (in reality) and are expelled. In this flowing regime, the data of interest were recorded along the inlet plane (C) between the screw conveyor and the compaction region and averaged, as explained below.

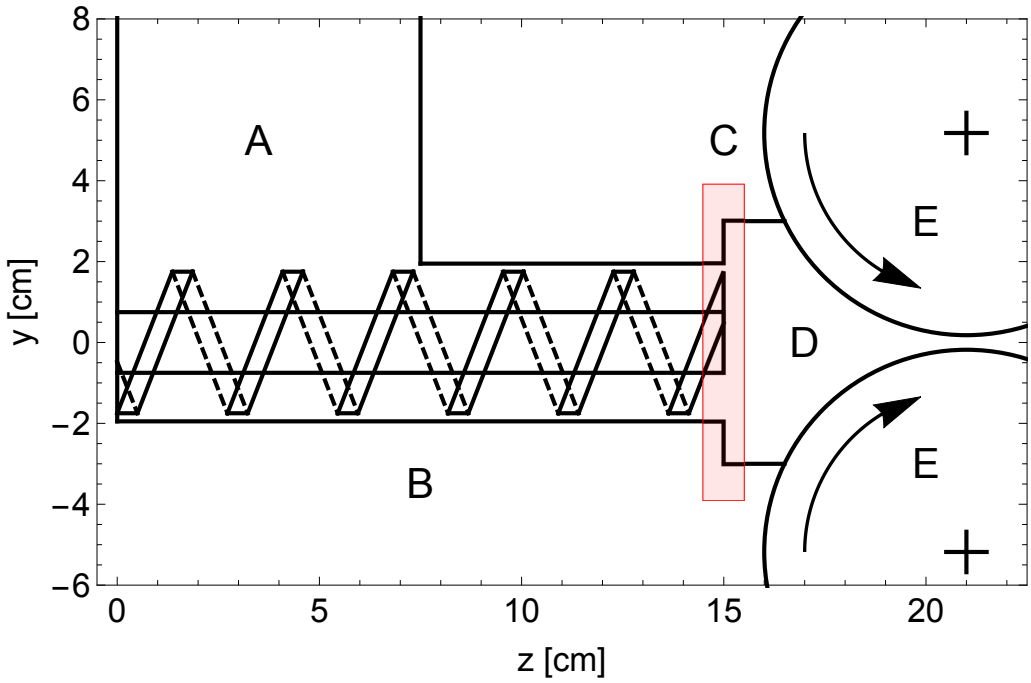

Figure 3.2: Schematics of the RC implemented in the DEM model. A: hopper. B: screw conveyor. C: compaction region inlet (transition area from DEM to FEM modelling). D: compaction region. E: counter-rotating compaction rolls (the rotation direction is indicated by the arrows).

The purpose of the DEM model is to simulate the particle flow at the inlet of the compaction region, and not other quantities of central importance for the compaction process, such as the pressure. This is due to the fact that the interaction laws are not suitable for the modelling of this aspect. Moreover, FEM is the natural tool to approach a study of the pressure distribution. For this reason, to avoid too high particle overlap in the neighbourhood of the screw tip, and consequent unphysical behaviour of the particle dynamics, the gap size in DEM is much bigger than the respective FEM and experimental counterparts. A bigger gap allows the particles to easily flow out from the compaction chamber, prevent-

ing them from overlapping under the pressure exerted by the screw rotation. In addition, the gap has to be small enough to avoid the compaction chamber to empty which would lead to an inhomogeneous packing of the inflowing particles. Similar constricted outflow conditions have been already used in the literature, e.g., in [97].
Because of this artefact the particles in the inflow region are densely packed but still in a free-flow condition, granting the applicability of the Hertz-Mindilin interaction law. As a consequence, the powder density at the inlet corresponds to tapped MCC, which justifies the FEM inlet density assumption. Lastly, since both the geometry of the inlet and the density of the powder are the same in both DEM and FEM, and the velocity field, by definition, coincides, both volumetric and mass throughputs at the inlet of the different models match.

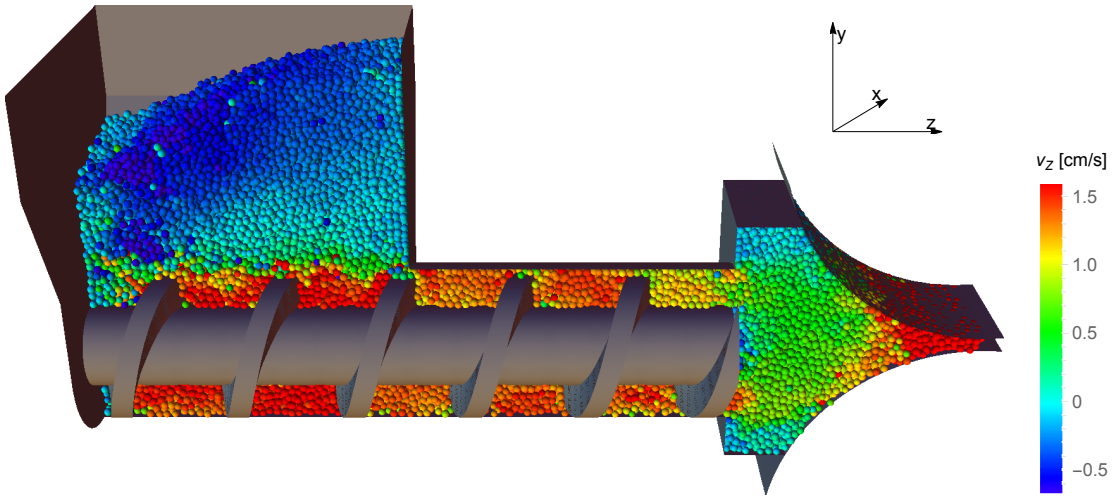

Figure 3.3: Vertical section of one snapshot of the system at steady-state, the particles are coloured according to their axial velocity v_z.

3.2.4 Finite Element Method (FEM)

In this work, FEM is used to investigate the effect of screw feeding velocity on the roll compaction process by obtaining the magnitudes and directions of stresses and strains. The FEM model was solved as a steady-sate problem using the Arbitrary Lagrangian-Eulerian (ALE) adaptive meshing in Abaqus/Explicit v6.14. The ALE adaptive mesh domain for steady-state problems is used to model material flowing through the mesh, and consist of two Eulerian boundary regions (inflow and outflow), connected by a Lagrangian or Sliding boundary region [26].

FEM model

The FEM model is based on the geometry of the desired roll compactor. In the case of the Komarek press, the roll's diameter and width are $d_R = 10$cm and $w_R = 3.8$cm respectively, and defined as analytic rigid surfaces. The minimum gap width between the rolls remains fixed during FEM modelling, having a value of $\delta_{min} = 0.2$cm. Once sketching

the press dimensions, the region between the rolls is discretized and meshed by 80,000 C3D8R three-dimensional continuum reduced integration elements. The FEM model of the roll compactor can be visualized in figure 3.4. It is important to mention that due to the non symmetric feeding velocity, the model was constructed fully without taking into account symmetry conditions, which are usually applied to reduce computational costs.

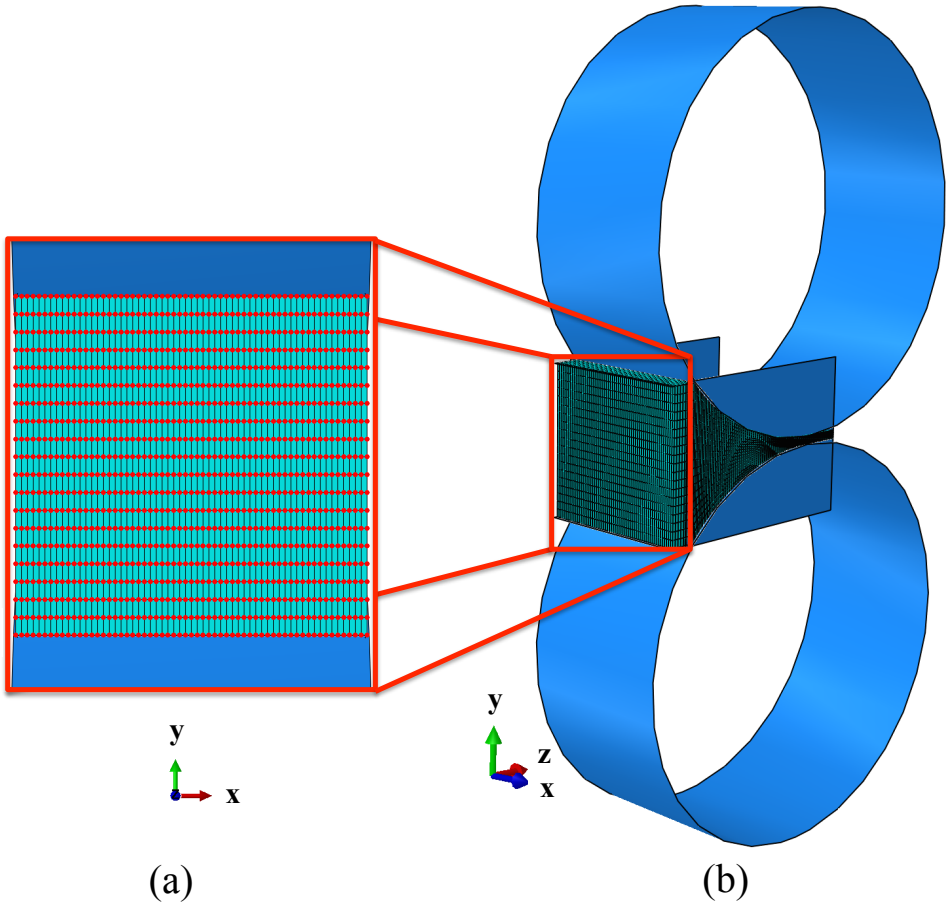

Figure 3.4: Visualisation of the (a) Back inlet nodes and (b) Entire FEM model.

Boundary conditions

In FEM, introducing the powder into the roll compaction system is possible by two different boundary conditions: either pressure or velocity inlet. Applying a non-uniform pressure on each element face in an ALE adaptive mesh domain causes a separate Lagrangian boundary region. Since Lagrangian corners are formed where Lagrangian edges meet, all nodes will follow the material in every direction, and each region becomes nonadaptive [26]. On the other hand, by assigning a non-uniform nodal velocity boundary condition to the inlet Eulerian region (figure 3.4), there is no alteration of the nodes to be nonadaptive and therefore was the approach chosen for this work. The inlet material density was set to be the tapped powder density as a result of the screw feeding. The MCC Avicel PH 101 tapped density ρ_{tapped} is about 0.47 g/cm^3, which corresponds to an initial relative density

ρ_{rel} of 0.3. In addition, the rolls rotational boundary condition of ± 0.63rad/s about the x-axis was defined to represent ω_R.
As mentioned previously, the ALE method enables working both with the advantages of Lagrangian and Eulerian elements in the same part [9]. While the inlet and outlet surfaces are defined as Eulerian regions, the surfaces that are in contact with the rolls are defined as sliding surfaces. The contact between the powder mesh and the outer surfaces representing the sealing and rolls is defined as surface-to-surface with Coulomb friction coefficient for a non lubricant case of $\mu = 0.4$ [90, 95, 99].

Constitutive model for continuum modelling

In our FEM modelling, the behaviour of the powder, considered as a continuous, porous, compressible material, is described using the density-dependent Drucker-Prager Cap (DPC) model [51, 54] and implemented by an external user-defined VUSDFLD Fortran subroutine.

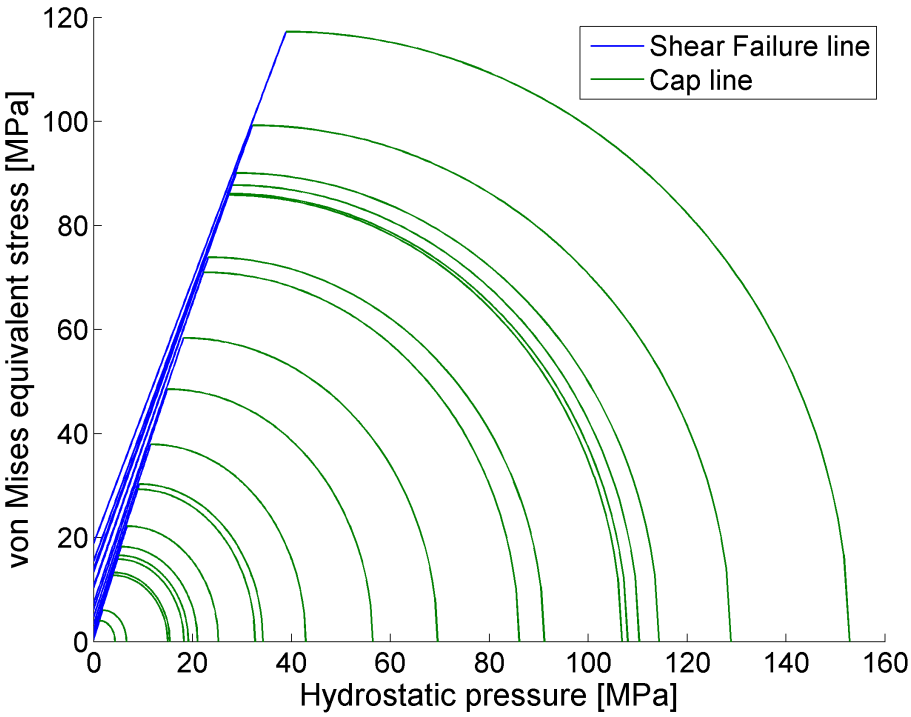

Figure 3.5: Density-dependant Drucker-Prager Cap model [90].

Assuming the material is isotropic, the model consists of three different parts: a shear failure surface F_s representing shearing flow, a cap surface F_c representing an inelastic hardening for plastic compaction and a transition zone F_t between the two surfaces, providing smooth surface to avoid singularities in the modelling. The shear failure is simply described by a straight line on the p-q plane and defined as:

$$F_s = q - d - p \tan \beta = 0 \tag{3.1}$$

The slope of the line represents the friction angle β, and the intersection with the q axis represents the cohesion, d. Here p represents the hydrostatic pressure (i.e. negative mean stress) and q the Von Mises equivalent stress. They are both obtained from the stress tensor σ as follows:

$$p = \frac{1}{3} tr\left(\sigma\right) \tag{3.2}$$

$$q = \sqrt{\frac{1}{2}\left[\left(\sigma_1 - \sigma_2\right)^2 + \left(\sigma_2 - \sigma_3\right)^2 \left(\sigma_3 - \sigma_1\right)^2\right]} \tag{3.3}$$

The cap yield surface is obtained by analyzing the stress state of the loading and unloading path in die compaction and written as:

$$F_c = \sqrt{\left(p - P_a\right)^2 + \left(\frac{Rq}{1 + \alpha - \alpha/\cos\beta}\right)^2} - R\left(d + P_a \tan\beta\right) \tag{3.4}$$

Where P_a is the evolution parameter representing the material hardening and softening, R is the cap eccentricity, and α is the smoothing transition constant that is used to define the smooth transition between the shear failure surface and the cap. In this work, an arbitrary transition parameter of α=0.01 was chosen (typically 0.01< α <0.05) to avoid numerical singularities.
As mentioned previously, a transition surface F_t should be applied and defined as follows:

$$F_t = \sqrt{\left(p - P_a\right)^2 + \left[q - \left(1 - \frac{\alpha}{\cos\beta}\right)\left(d + P_a \tan\beta\right)\right]^2} - \alpha\left(d + P_a \tan\beta\right) \tag{3.5}$$

Based on standard calibration method, the density-dependent DPC model (figure 3.5) was obtained. Further information regarding the DPC model and an extended detail on the calibration method used in this work can be found in a previous study [90].

3.2.5 Coarse graining

Information gathered via DEM modelling of the system is, by definition, discretised (e.g., every particle has a specific velocity computed at every time step). However, for the data to be used as an inlet condition for FEM modelling of the compaction region, every discrete physical quantity of interest has to be transformed into a continuous 3D field. We chose to obtain continuous data from a discrete set via *Coarse Graining (CG)* [44, 158].
Let us assume we have L particles in our domain, labelled with an integer subscript $j = 1, 2, \ldots, L$. According to the definition, at every point $\mathbf{r} = (x, y, z)$ of the system and at any time t, we can define a coarse grained density field $\bar{q}(\mathbf{r}, \Delta; t)$ of a physical observable of interest (e.g., velocity) $q(\mathbf{r}; t)$ as:

$$\bar{q}(\mathbf{r}, \Delta; t) = \sum_{j=1}^{L} q_j(t)\, \phi(\mathbf{r} - \mathbf{r}_j, \Delta) \tag{3.6}$$

where ϕ is the coarse graining function, which depends on the coarse graining length $\Delta > 0$, and $\mathbf{r}_j$ is the position of particle j.
The function $\phi(\mathbf{r}, \Delta)$ is defined as a continuous symmetric even function, centred in $\mathbf{r}$, with

Table 3.3: Axial positions for volumetric throughput evaluation (also compare with figure 3.2 for the sake of clarity).

Description	Axial position [cm]
Inside the screw barrel	$z_0 = 12.00$
Compaction region inlet	$z_1 = 15.00$
Rolls-compaction walls contact point	$z_2 = 16.50$
Mid point between z_2 and z_4	$z_3 = 18.75$
Rolls gap	$z_4 = 21.00$

finite support and normalized to unity. The suitable choices for such a function can be a Heaviside, a Gaussian or a Lucy function [82]. The choice of graining function does not significantly affect the fields, provided it is not highly anisotropic or singular. However, the value of the coarse graining scale, dictated by the choice of Δ, is the main parameter of interest of the framework, determining the spatial resolution of the averaging process and the related fields. As smoothing function, we used a Lucy polynomial, so that in $3D$ we obtain:

$$\phi(\mathbf{r}, \Delta) = \frac{105}{16\pi\,\Delta^3}\,\chi(\|\mathbf{r}\|, \Delta)\left(1 + 3\frac{\|\mathbf{r}\|}{\Delta}\right)\left(1 - \frac{\|\mathbf{r}\|}{\Delta}\right)^3. \tag{3.7}$$

Here $\chi(\|\mathbf{r}\|, \Delta)$ is the support of the function, i.e., $\chi(\|\mathbf{r}\|, \Delta) = 1$ for $\|\mathbf{r}\| \leq \Delta$ and $\chi(\|\mathbf{r}\|, \Delta) = 0$ elsewhere.
In this paper, the main quantity of interest for the DEM model is the particle velocity field $\mathbf{v}(\mathbf{r}; t)$, which in the CG framework is defined as

$$\bar{\mathbf{v}}(\mathbf{r}; t) = \frac{\bar{\mathbf{p}}(\mathbf{r}; t)}{\bar{\rho}(\mathbf{r}; t)} = \frac{\sum_{j=1}^{L} \mathbf{v}_j m_j\,\phi(\mathbf{r} - \mathbf{r}_j, \Delta)}{\sum_{k=1}^{L} m_k\,\phi(\mathbf{r} - \mathbf{r}_k, \Delta)}. \tag{3.8}$$

The numerator of equation (3.8) is the coarse grained momentum density field $\bar{\mathbf{p}}(\mathbf{r}; t)$ and the denominator $\bar{\rho}(\mathbf{r}; t)$ is the mass density field. It has been shown in [44, 158] that for mass and momentum densities defined according to equation (3.6), defining a coarse grained velocity such as equation (3.8) guarantees both mass and momentum conservation. Hereinafter, coarse grained quantities are indicated with a bar on the top, while their explicit dependence on the coarse graining length Δ is omitted for the sake of brevity.

3.3 DEM results

As stated above, to obtain a general result, data gathering from DEM simulations has to be performed when the system is in steady state. To this extent we need to choose a quantity which behaviour and evolution in time is able to determine the state of the system. Let us define $\dot{V}(z; t)$ as the volumetric throughput at time t across a planar section of the system normal to the screw axis in the axial position z. Analogously let's define the mean volumetric throughput across the same plane averaged along 10 seconds of steady state as $\dot{V}^{\text{steady}}(z)$. The volumetric throughput $\dot{V}(z; t)$ at time t is computed by summing the volume of particles crossing these sections in between the two subsequent time steps t and $t + \Delta t$.

At $t = 10.0$s the velocities of screw and rolls are set to their operational value (transient state), but the system needs some time to self-adjust before it reaches a steady state. We defined the system to be in steady state when the relative deviation of the volumetric throughput from the steady state value

$$\Sigma(\dot{V}(z;t)) = \frac{\left|\dot{V}(z;t) - \dot{V}^{\text{steady}}(z)\right|}{\dot{V}^{\text{steady}}(z)} \tag{3.9}$$

tends to zero across the whole domain.
The quantity $\Sigma(\dot{V}(z;t))$ is computed across 5 different planes perpendicular to the flow direction, enumerated in table 3.3, and plotted as a function of time in figure 3.6. Since the volumetric throughput linearly depends on the mean axial component of the velocity, the latter follows the same trend. Both of them reach steady state with variations $\Sigma(\dot{V}(z;t))$ being negligible after 10s of transient state (i.e. after $t \simeq 20.0$s). Data collection and coarse graining occur during 5 screw turns (highlighted in red in figure 3.6), corresponding to a data gathering period of $5\frac{2\pi}{\omega_S} = 6.25$s, beginning at $t = 23.75$s.

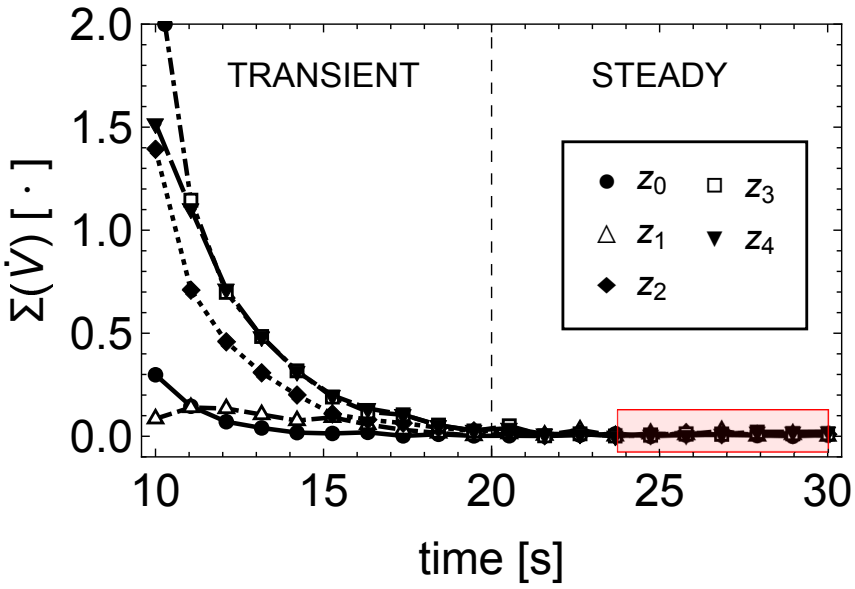

Figure 3.6: Relative deviation $\Sigma(\dot{V}(z;t))$ of the volumetric throughput across a section of the system as a function of time. The values are computed in 5 different axial planes explained in table 3.3. When $\Sigma(\dot{V}(z;t)) \simeq 0$ the system is considered to be in steady state, which was reached after 20s in this case. The data gathering time interval is highlighted in red.

3.3.1 From discrete to continuum (coarse graining and time averaging)

For the purpose of our study, we computed the particle velocity field as a function of time via coarse graining of the DEM data that corresponds to the plane perpendicular to the screw axis located at the tip of the screw conveyor (at $z = z_1$). In this area the particles flowed from a cylindrical casing of radius $R_C = 1.95$cm into the compaction region with a

square section of width $w = 6$cm.
A planar cut perpendicular to the screw axis is taken at time $t = 28.0$s and shown in figure 3.7a, the particles being coloured according to their inflow velocity v_z. The blade components and the chamber walls have been omitted for the sake of clarity, but their presence is hinted by the particles with a smaller cross section (since the latter can only be in contact with the former and not passing through). For instance, the particles around the inflow ring are in contact with the chamber wall, the ones along the circle in the middle are in contact with the middle shaft, and the ones enclosed in the circular sector on the top right are in contact with the blade flat edge. The particles in those regions are almost stagnant, since they are not directly pushed forward by the inflowing ones. The velocity along the feeding direction exhibits a broad range of values, varying from around 1.5cm/s close to the screw blade to -0.5cm/s occasionally throughout the domain. In the annular inflow area v_z is not constant, but peaks under the blade (on the right side) and decreases steadily as moving clockwise to a minimum value of 0.5cm/s. This happens because in the figure the screw rotation direction in clockwise, and the particles directly in contact with the blade have a higher velocity. These "faster" particles should, in reality, undergo a pre-compaction process driven by the screw pressure, as assumed by the most common analytical models [63,111]. However, this feature cannot be replicated by our model due to the inter-particle interaction used. Finally, because of their discrete nature, and because of the back pressure experienced, the inflowing particles naturally rearrange their position with respect to one another, which is the reason why some of them are moving slightly backward (depicted in dark blue). Nevertheless, on average, the net inflow of particles into the compaction region is positive, as shown below.
Once the DEM flow data were obtained, we defined a spatial grid where the CG fields were evaluated. Two factors have to be accounted for when choosing the extension of grid: spatial resolution and avoidance of boundary effects. To obtain a better resolution of the fields, the inter-nodal distances in the grid dx and dy have to be reasonably smaller than the CG length Δ. At the same time, the grid size l has to be small enough (with respect to the compaction section w) for the presence of external wall not to affect the velocity field. To that end, we restricted the CG region such that the particles in contact with the cheek plates were at least at distance Δ from the edge of the grid. Therefore, to account for both conditions, CG length Δ and grid length l need to satisfy

$$\max\big(dx, dy\big) < \Delta < \frac{w}{2} - \frac{l}{2} - \max\big(r_j\big) \tag{3.10}$$

where r_j is the radius of the j-th particle.
The velocity field was evaluated along a planar grid composed of $N_X = 39$ and $N_Y = 25$ nodes along the x and y directions, respectively. For the coarse graining region we chose a square of side $l = 5$cm to obtain an inter-nodal distance of $dx = l/(N_X + 1) = 0.125$cm and $dy = l/(N_Y + 1) \simeq 0.192$cm in the two directions and set $\Delta = 2.5 r_P = 0.225$. These values satisfy both sides of Equation 3.10. Such a choice for the CG length prevents scale dependencies of the velocity fields on the particle scale, as reported in [156]. The chosen grid illustrated in figure 3.7b is superimposed on the DEM data slice, where the red boundary outlines the region within which the particles contribute to the average over the selected grid. The resulting velocity field can be seen in figure 3.7c: after coarse graining, all information about the discrete components of the system is lost.

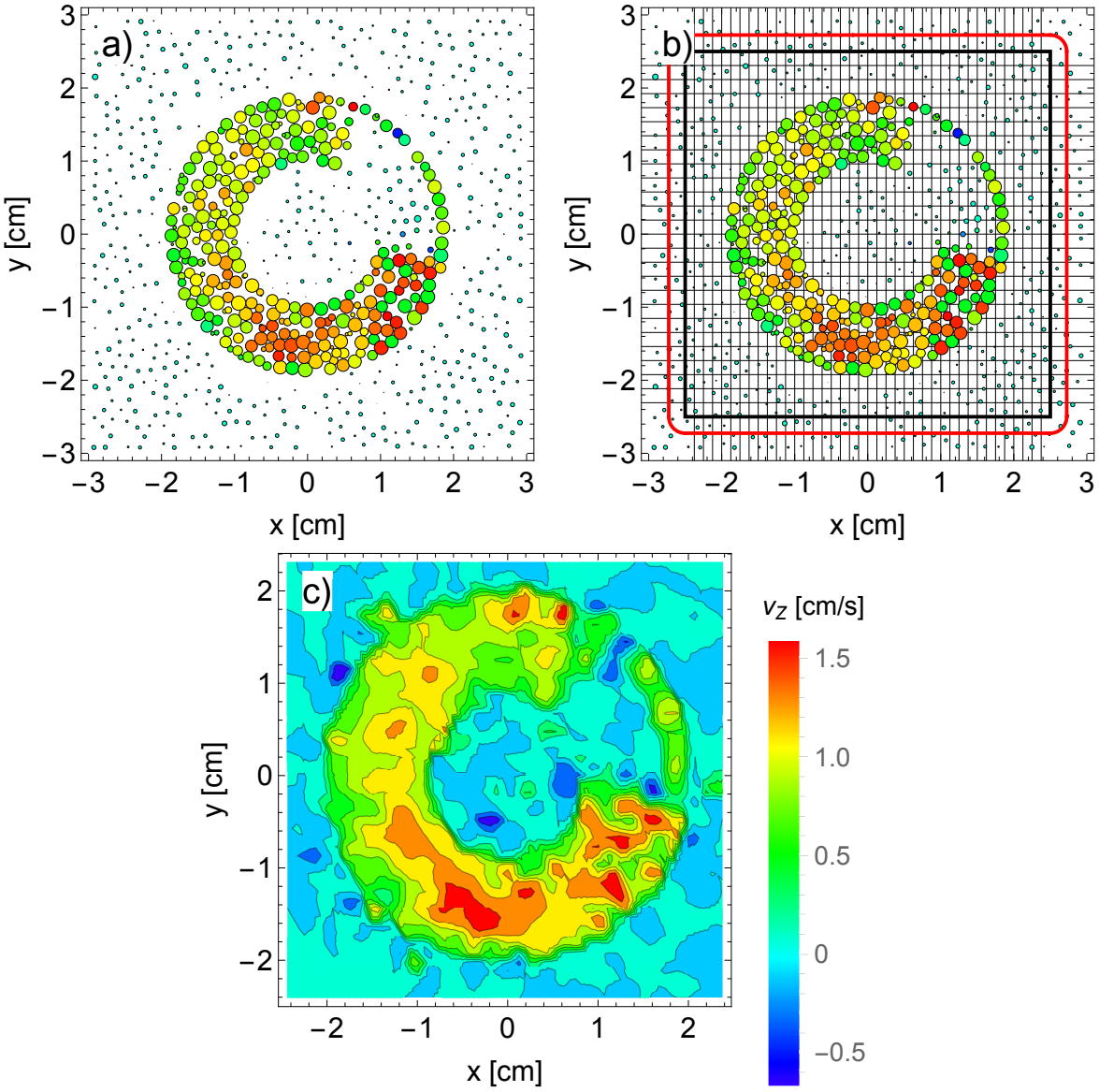

Figure 3.7: Schematic illustration of the coarse graining process along the plane $z = z_1$ for one snapshot of DEM simulation, with the particle direction of flow towards the reader and the screw rotating clockwise. Here a snapshot of the system has been taken at $t = 28.0$s, particles and field are coloured according to the axial component of the velocity v_z. a) Slice of the system as modelled via DEM. The plotted region is the entire section of the compaction region of width w at the tip of the screw. b) Superimposition of the grid where the fields are computed, the thick black square being the coarse graining region of side l. The red line represents the boundary around the plane within which the particles contribute to graining. c) Contour plot of the 3D field based on data coarse graining.

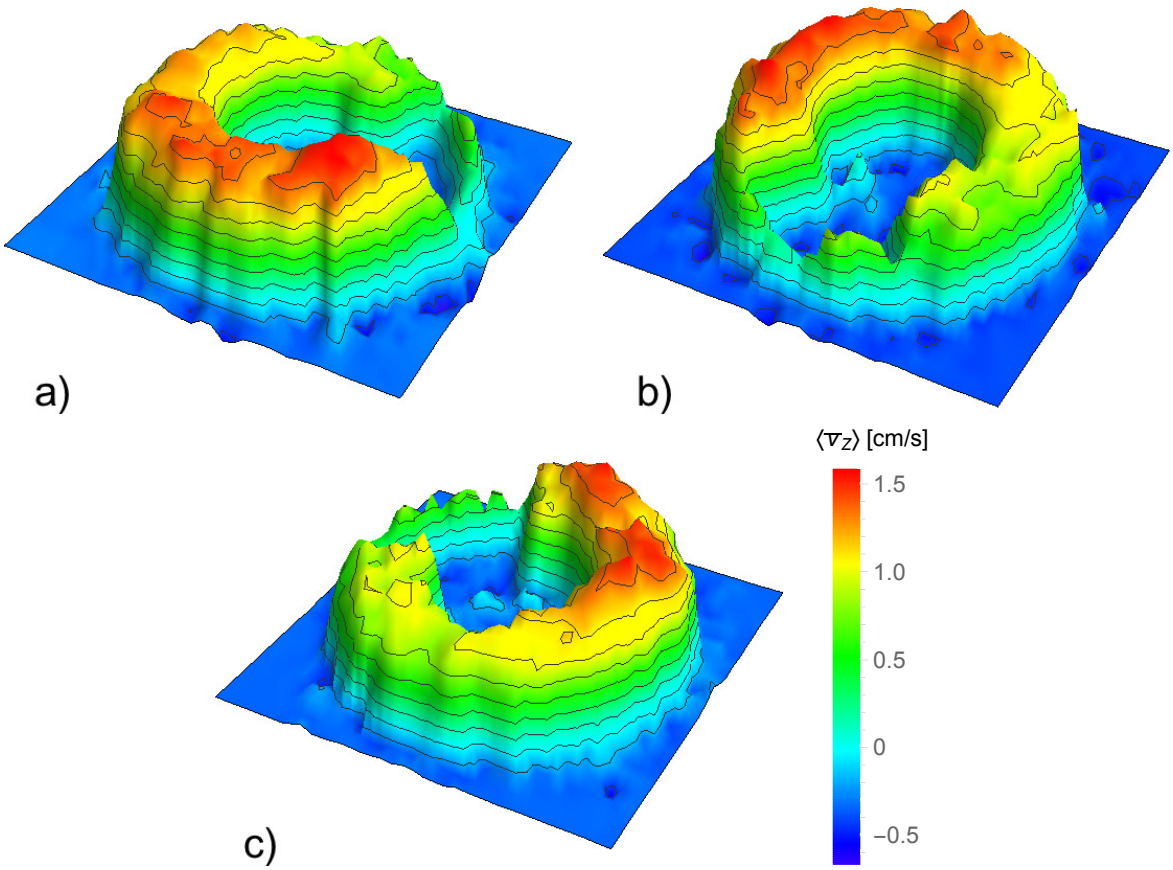

Figure 3.8: 3D plots of time-averaged CG axial velocity component computed for 3 screw positions. The absolute time corresponding to each snapshot is: a) $t^* = 0$, b) $t^* = T_S/3$ and c) $t^* = 2T_S/3$.

Nevertheless, even if the velocity field is spatially averaged, it still depends on the particular configurations of discrete components from which it originated: the effect of their distribution prior to graining is reflected in the averaged fields. For example, a gradient of the velocity field due to a particle with a higher (or lower) speed is located around the position of the former (see the red and blue peaks on the top-right of figure 3.7c and compare it to figure 3.7a). Generally, the velocity field should be as unaffected by a particular realisation of the system as possible. For this purpose, the spatially averaged fields can be further averaged in time, exploiting the periodicity of the flow due to the screw rotation. Assuming that the velocity field at reference time t_0 should be the same at all other times $t_0 + kT_S$ ($T_S = 2\pi/\omega_S$ being the rotation period of the screw and k any positive integer), the time averaged CG velocity field is computed as follows:

$$\langle \bar{\mathbf{v}}\,(\mathbf{r};\, t_0)\rangle = \frac{1}{N}\sum_{n=1}^{N} \bar{\mathbf{v}}\,(\mathbf{r};\, t_0 + (n-1)T_S). \tag{3.11}$$

In our study we averaged in time over $N = 5$ screw turns. The final result was the particle flow during a single screw rotation split into $T_S/\Delta t - 1 = 124$ snapshots. In the remainder of this paper, quantities averaged over time in this way are indicated with angular brackets $\langle\,\cdot\,\rangle$. Figure 3.8 shows the time-averaged CG axial velocity component $\langle \bar{v_z}\,(\mathbf{r};\, t^*)\rangle$ for three screw positions at inlet location z_1, where $t^* \in [0; T_S[$ is the absolute time of a screw rotation. It is clear that the localised gradients in a single CG snapshot (figure 3.7c) were completely smoothed out by time averaging.

3.3.2 Results and discussion

In our study, we paid particular attention to two main aspects of the particle flow: the mean of the velocity components, indicating in which flow directions the particles generally move and with which magnitude, and their periodicity, showing to which extent the flow is affected by the periodic screw motion and how deeply into the compaction region this effect extends.
Since the contact law is unsuitable for modelling the high-pressure region close to the gap, we considered data up to point z_2. For the mean velocity we exploited the cylindrical symmetry of the system, still undisturbed by the presence of the rolls, and observed the cylindrical components of the former defined as

$$v_r(\mathbf{r};t) = \frac{v_x\,x + v_y\,y}{\sqrt{x^2+y^2}} \quad v_\phi(\mathbf{r};t) = \frac{v_x\,y - v_y\,x}{\sqrt{x^2+y^2}}. \tag{3.12}$$

According to our definition, the angular component of the velocity $v_\phi(\mathbf{r};t)$ has a positive sign when it is concurrent with the screw rotation. In figure 3.9 we plotted the time average of the particles velocity components as a function of their position along the $\vec{z}$ axis.
The mean radial component of the velocity is roughly zero both inside the conveyor case and in the first part of the compaction region up to z_2 (in yellow in figure 3.9). From this point onwards, its value is constantly negative, even if its magnitude is much smaller than the axial component, due to the pressure exerted by the rolls pushing the particles towards the $\vec{y} = 0$ plane. The angular component has a constant value inside of the screw barrel, as expected (e.g., at z_0 highlighted in blue). Its value starts to rapidly decrease

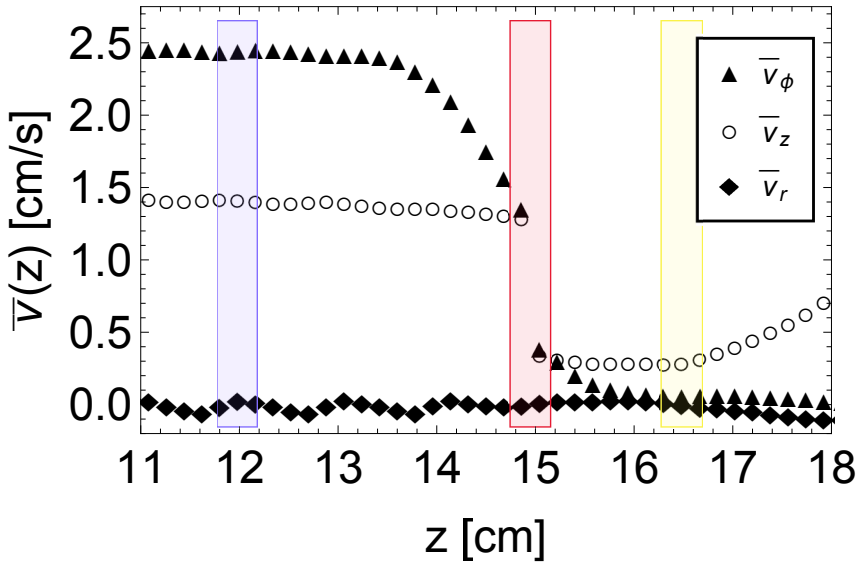

Figure 3.9: Time averaged cylindrical components of the particle velocity as a function of the axial position. The 3 highlighted sections correspond to the first 3 positions of table 3.3: z_0 in blue, z_1 in red and z_2 in yellow.

close to the inlet region z_1 (in red in figure 3.9) and approaches zero at $z > z_2$. Although the mean velocity along the feeding direction is constant along the entire screw length, it decays abruptly as soon as the particles are affected by back pressure due to the bulk effect in the first section of compaction region $z_1 < z < z_2$. From z_2 onwards, the mean axial velocity constantly increases due to the combined effect of the pressure on particles exited by the conveyor and the rolls drag. Therefore, on average, the axial component of velocity is dominant inside the compaction region, while inside the screw barrel, far enough from the inlet, the flow is uniform with no net transport in the radial direction. The flow in the screw barrel can be compared with the experimental findings in [150] by means of x-ray penetration. The axial flow of the tracer particles observed in [150] is constant along the screw length, with small oscillations when the powder meets the screw blade edge. These oscillations are factored out in our analysis because we averaged along the whole screw section. The radial motion of the tracer particles observed in the referenced paper is also shown to be almost negligible, and concentrated mainly around the screw blade edge. This is also consistent with our model, predicting an almost negligible mean radial velocity inside the barrel.

A much more detailed picture emerges if we analyze the flow as a function of time. To monitor the particle movement, we observed the cartesian components of the mean velocity along the planes z_0, z_1 and z_2. While the axial component of velocity evaluated as such is roughly constant, the movement of particles coplanar to these sections is periodic in time. The velocity component $v_x(t)$ as a function of time along 5 screw rotations is plotted in figure 3.10. The velocity $v_x(t)$ oscillates simultaneously with the same period T_S of the screw. Interestingly, this oscillation also persists inside of the compaction region (yellow data points) and is likely to be responsible for the inhomogeneity of the powder bulk prior to compaction. The same oscillatory behaviour of the particles inside of the compacted

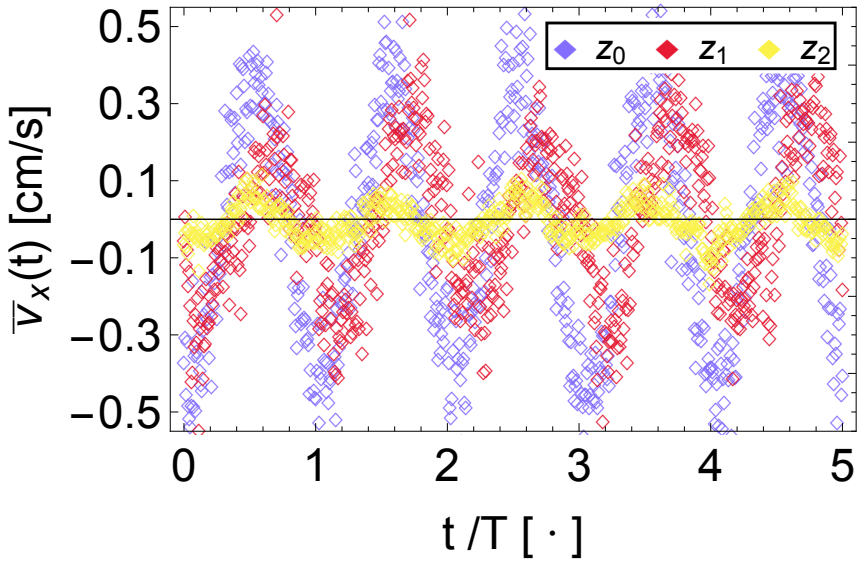

Figure 3.10: Mean cartesian component $v_x(\mathbf{r};t)$ of the particle velocity along 3 axial sections as a function of time. The data correspond to the axial positions highlighted in figure 3.9 with the same color code. The component $v_y(\mathbf{r};t)$ has the same periodic behaviour, with a phase difference of $\pi/2$.

region has been observed experimentally in [48]. It is this inhomogeneity that leads to the observed anisotropy in the compacted ribbon, as the following sections explain with the help of Finite Element modelling.

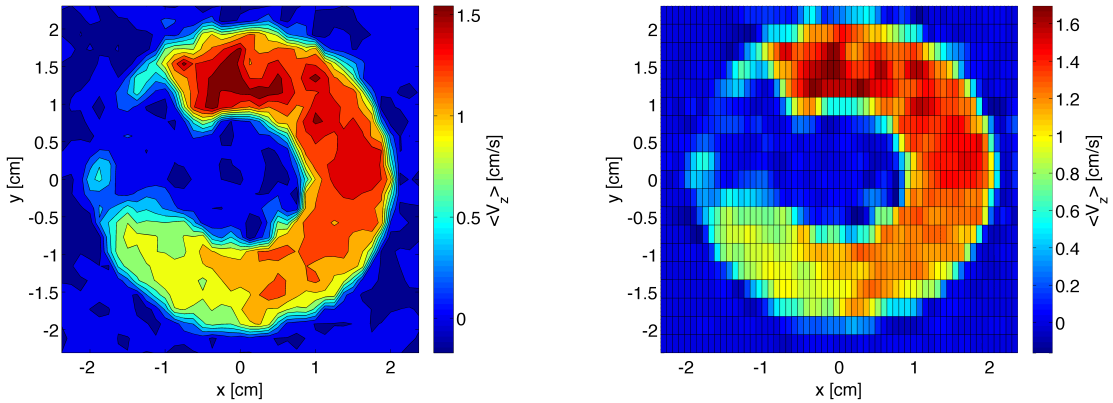

Figure 3.11: Plot of velocity field and the transition from CG result to FEM inlet boundary condition for $t^* = 0$. Axial velocity component $\bar{v_z}$ values for a) DEM coarse graining result and b) Corresponding FEM inlet nodes.

3.4 From CG to FEM

In order to implement DEM results into the FEM model, several step are performed using MATLAB®. First, the function "ndgrid" is being called in order to define a new rectangular grid in N-D space, which represents the FEM inlet mesh.
In the output $[x, y] = \text{ndgrid}\,(x_{min} : hx : x_{max}, y_{min} : hy : y_{max})$, the coordinates of the (i, j)-th node are $(x_i, y_i) = (x_{min} + (i-1)\,hx, y_{min} + (j-1)\,hy)$. Now that the new grid is formed to represent the FEM mesh, the DEM data is transferred. This is done via the "Interp2" function, which returns interpolated values of the DEM grid into the new FEM grid. The interpolated value at a query point is based on a cubic interpolation of the values at neighbouring grid points in each respective dimension.
For an equally spaced data, most interpolation functions are in the following form:

$$g(x) = \sum_k c_k u(x - x_k) \tag{3.13}$$

where the sampled data is described as $c_k = f(x_k)$ for a given sampled function f at an interpolation node x_k and u is the cubic interpolation kernel. For convenient reasons, the distance between the point to be interpolated and the grid point being considered is defined as $s = (x - x_k)$.

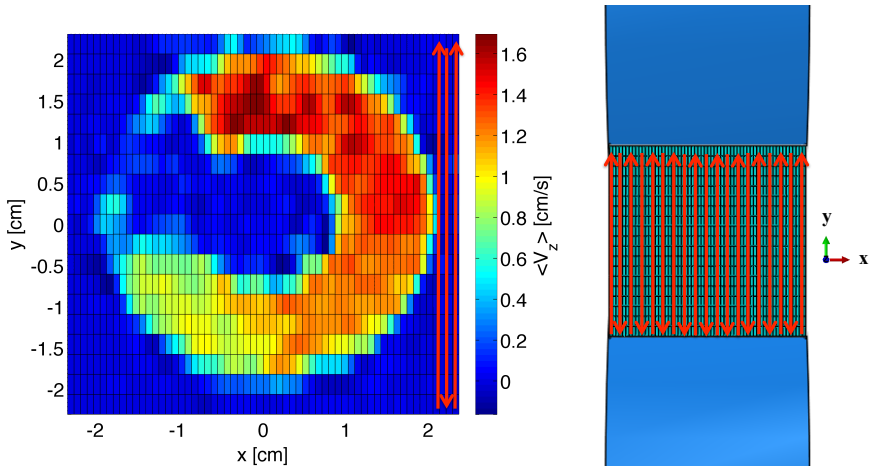

Figure 3.12: Schematic illustration of the procedure assigning axial inlet velocity interpolated values into the FEM model. The red arrows shows the direction in which values are read in the data file and being assigned into the FEM back nodes.

The following cubic convolution interpolation kernel (equation (3.14)), proposed by R.Keys [68], is symmetric and defined by piecewise cubic polynomials in the intervals $|s| \leq 1$ and $1 < |s| \leq 2$. For $|s| > 2$, the kernel is zero. This kernel offers a third-order convergence and guaranteed superiority to nearest-neighbor (first order) and linear interpolation (second order) [104].

$$u(s) = \begin{cases} \frac{3}{2}|s|^3 - \frac{5}{2}|s|^2 + 1 & |s| \leq 1 \\ -\frac{1}{2}|s|^3 + \frac{5}{2}|s|^2 - 4|s| + 2 & 1 < |s| \leq 2 \\ 0 & |s| > 2 \end{cases} \tag{3.14}$$

The kernel function $u(s)$ is centered at point x, the location of the point to be interpolated. The interpolated value $g(x)$ is the weighted sum of the discrete neighboring points (2 to the left and 2 to the right) scaled by the value of interpolation function at those points.
For two-dimensional interpolation (i.e., Bicubic interpolation), the one-dimensional function is applied in both directions. It is a separable extension of the one-dimensional interpolation function. The Bicubic interpolation algorithms interpolate from the nearest sixteen mapped source pixels. Obtaining an interpolated value for a given point is done in two steps. First an interpolation is done along the x-direction using the 16 grid samples. The following step is interpolating along the y-direction using the interpolated points from the previous step.

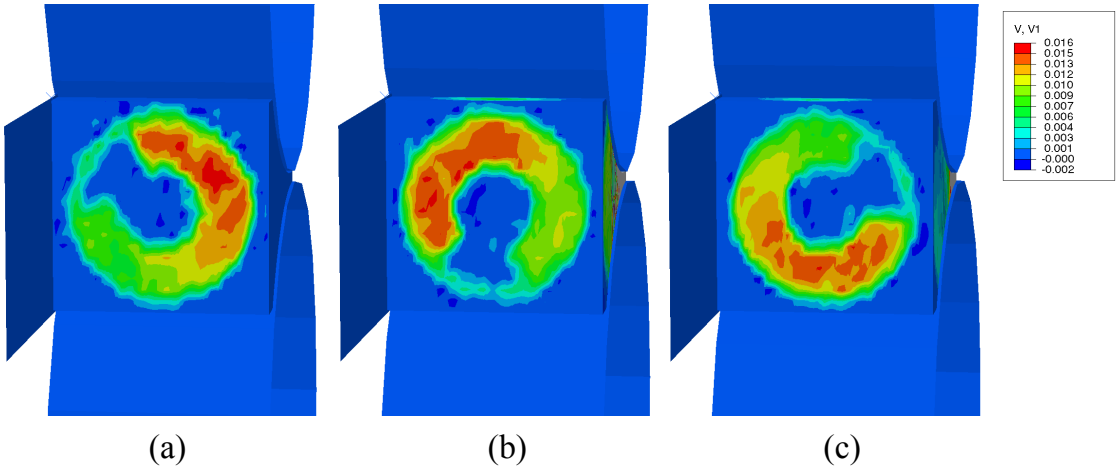

Figure 3.13: 3D plots of the axial velocity component $\bar{v_z}$ in the FEM model (right seal removed for better visualisation) for 3 screw positions, with a counter-clockwise rotation. The absolute time corresponding to each snapshot is: a) $t^* = 0$, b) $t^* = T_S/3$ and c) $t^* = 2T_S/3$.

The above algorithm is applied to the DEM CG data at each time interval Δt during a screw period, resulting in a total of 124 matrices of 61x20 (i.e., 1220 elements) corresponding to the FEM inlet nodes (figure 3.4b). The velocity values for each absolute time t^* are then represented as an array in a separate file. Figure 3.11 illustrates the previously described steps of constructing a new grid, which correlates to the FEM mesh and interpolates the values from the DEM results.
The new interpolated data is then implemented as a FEM nodal velocity boundary condition in Abaqus/Explicit using an external user-defined VDISP Fortran subroutine. At each absolute time t^*, the VDISP subroutine is being called and assigns the corresponding interpolated velocity values from the previously saved data file into the FEM model in a chronological order to the predefined inlet nodes (figure 3.12).

3.5 Results and discussion

Results obtained by DEM simulation (section 3.3), showed that the flow of powder being conveyed to the rolls, varies in velocity due to the oscillation of the screw. This is in fact

the main cause attributed to the inhomogeneity of the compacted ribbon, resulting in a "snake-wise" light transmission pattern [48]. Our results demonstrates the importance of combining DEM & FEM methods to obtain a more realistic model of the process.

3.5.1 Transition From DEM (CG) to FEM

In the previous section, the multi-scale approach was described in order to investigate the behaviour of granular material in roll compaction, by combining DEM at the micro scale into the FEM macro scale level. Figure 3.13 visualizes the result of the numerical transition method, which was used to gap between the different scales and used as input data in FEM modelling. By comparing the axial velocity component $\bar{v_z}$ in the FEM inlet nodes (figure 3.13) with the CG results (figure 3.8), it can be seen that feeding velocity field values and pattern are almost identical with some discrepancies due to the counter pressure from the rolls (except for $t^* = 0$ in figure 3.13a). Therefore, it is possible to successfully implement the DEM data into the FEM, and to represent the velocity of the powder entering the compaction region.

3.5.2 DEM & FEM combined simulation

By implementing the CG DEM results into the FEM, a numerical study on the effect of the screw blade position and the inhomogeneous inlet feeding velocity on the roll compaction process was conducted. The resulting contact pressure and relative density (figure 3.14) are distributed non-homogeneously in the minimum gap region and vary with time as a result of the inlet feeding velocity. The maximum contact roll pressure and relative density positions in the minimum gap region vary with simulation time along the ribbon's width. It can be noted that the 3D axial velocity plot does not correspond to the pressure and density values at the minimum gap due to the fact that the influence of the inlet velocity takes effect only at a later stage. This means that, due to the distance between the inlet region and the minimum gap region, there is a certain phase shift between the sinusoidal pattern of the inlet velocity and the contact roll pressure and relative density.
In order to evaluate and quantify this variation during the process and consequently on a compacted ribbon, the values were monitored at two different positions with a distance of 5 mm from the left and right side seals. Initially, the values of relative density and contact pressure are increasing gradually as powder is being delivered in between the rolls. At around $t^* = 3s$, the roll compaction reaches a steady-state condition, where the mean values of the relative density and of the roll pressure at the minimum gap region remain constant. Results obtained with our combined approach showed that the inlet feeding velocity has a direct effect on the resulting pressure and density distribution. For a specific time, the contact pressure and relative density values at one side of the ribbon are higher with respect to the other. Moreover, a sinusoidal pattern of the roll pressure and relative density during compaction is observed, having a period equal to the screw rotation period. Due to numerical reasons, the results are obtained and plotted only for the material which is still in contact with the roll, up to the narrowest gap region [99]. Therefore, in order to illustrate the resultant roll compacted ribbon, multiple sliced snapshot at the gap region were taken at intervals of $\Delta t = 0.05s$ and assembled together. As can be seen clearly in figure 3.15, higher powder feeding rate in one side resulted in higher contact pressure and

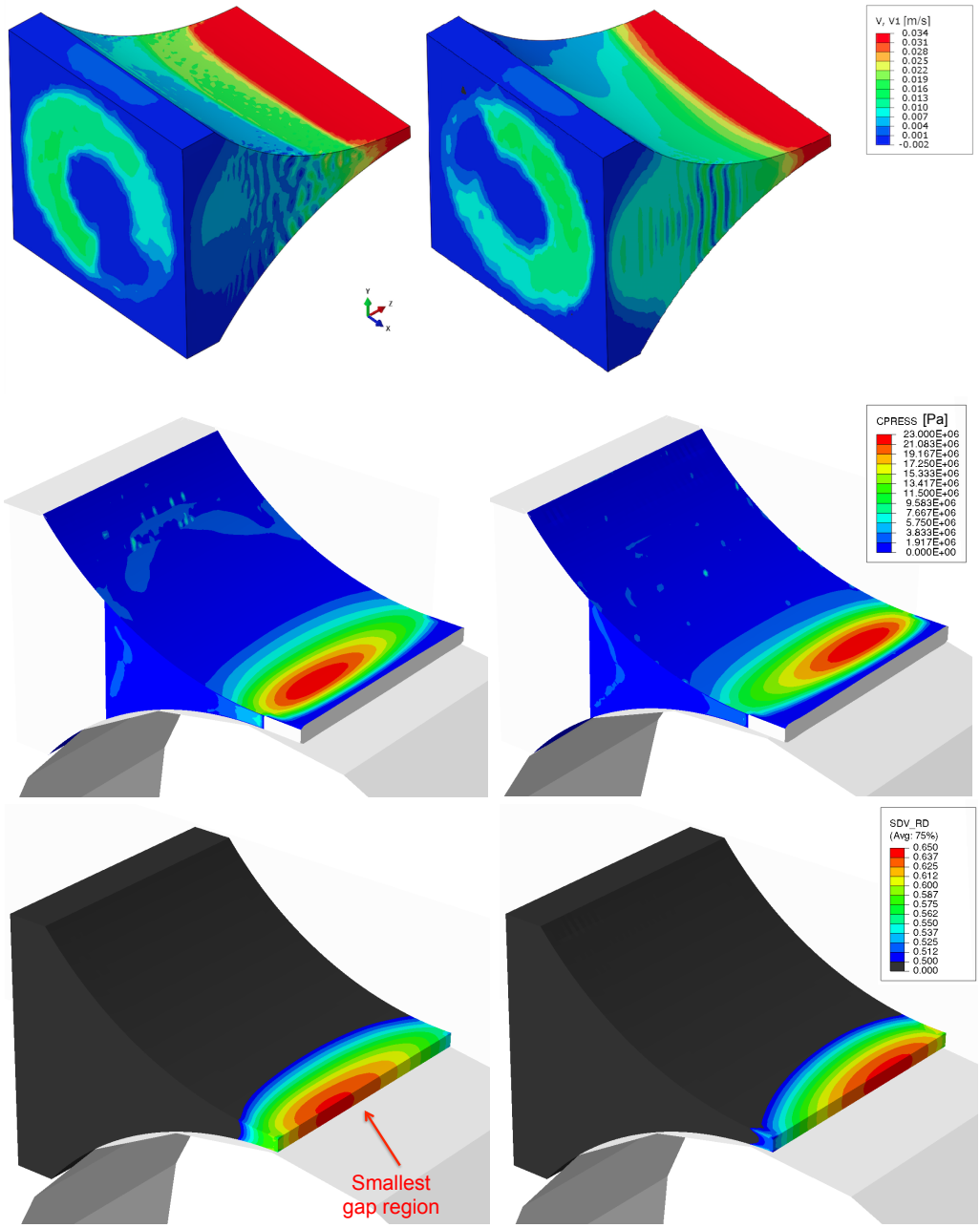

Figure 3.14: 3D plots of FEM modelled parameters for 2 time steps: $t^* = 2.35s$ (left column) and $t^* = 2.9s$ (right column). The depicted values are: powder axial velocity (top row), contact pressure (middle row) and relative density (bottom row) at the outlet of the compaction region.

relative density on the same side under the rolls. This can be explain by transporting higher amount of mass into one side, thus increasing the nip angle which will ultimately result in higher compaction force and density.

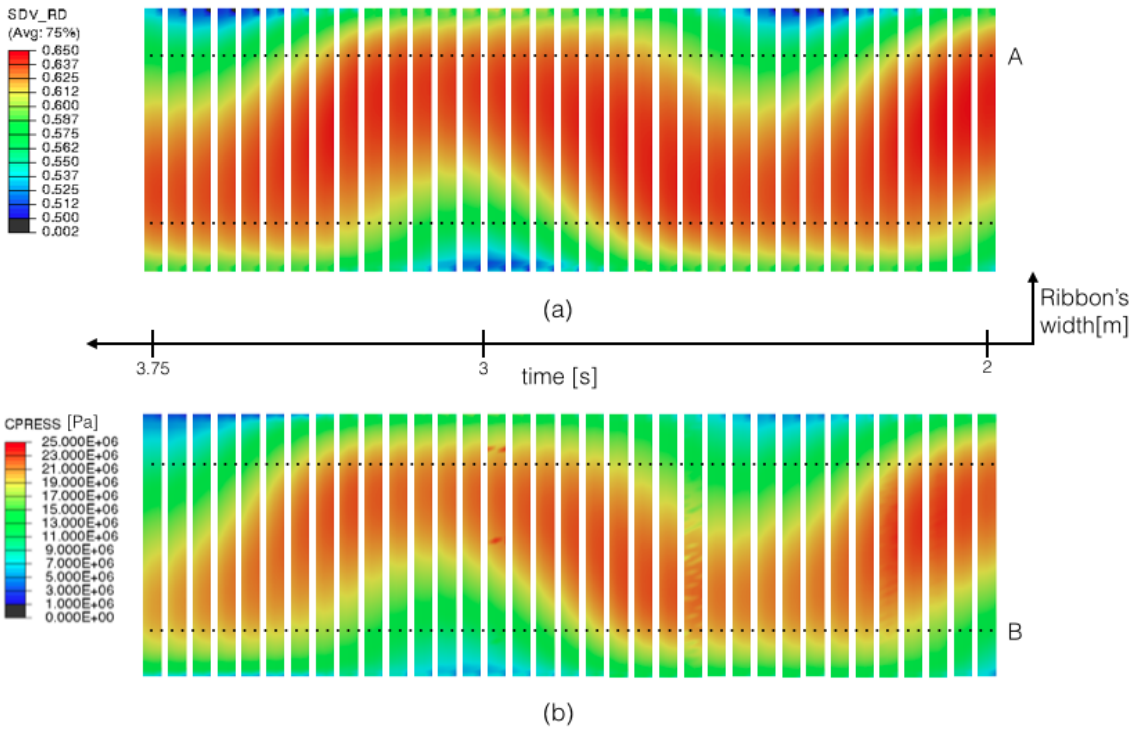

Figure 3.15: Multiple sliced snapshots of the a) relative density and b) contact pressure values obtained by the combined DEM-FEM simulations at the minimum gap region between $t = 2.00$s and $t = 3.75$s. The two highlighted positions A and B are the positions at 5 mm from the side seals and where the values are evaluated.

3.6 Conclusions

Roll compaction is a complex process involving two main parts, powder conveying using a screw feeder and compaction between two counter rotating rolls, where the powder undergoes large deformation. In this work, a combined DEM-FEM multi-scale approach was developed in order to investigate the behaviour of granular material in roll compaction. DEM was used to model the flow of granular material through the screw conveyor into the compaction zone. The DEM simulation was successfully used to model the behaviour of particles in a screw feeder and to obtain the highly inhomogeneous (although periodic in time) velocity field at the interface between the screw feeder and the compaction region. Then, FEM was applied to simulate the powder compaction in between the rolls and to study the effect of the inhomogeneous inlet feeding velocity due to the screw feeder. The combined DEM-FEM methodology clearly shows the resultant inhomogeneous roll contact pressure and relative density over the rolls width, resulting in a "snake-wise" pattern over time. This behaviour is reflected in an inhomogeneously compacted ribbon. Moreover, the sinusoidal pattern of the roll pressure and relative density during roll compaction has a period equal to the screw rotation time.
Combining both DEM and FEM methods to model the roll compaction process allows us to take advantage of the strength of both methods in order to describe complex processes,

and enables us to achieve a more realistic model of both the process itself and of the final product quality. The methodology proposed can be used to study how process parameters, such as screw and roll speeds, will likely affect the ribbon density and homogeneity. In addition, this coupled approach can be a useful tool to guide future design optimisations, with the aim to diminish the effect of the screw driven flow on the compaction final product.

Acknowledgements

This project has received funding from the European Union's Seventh Framework Programme for research, technological development and demonstration under grant agreement No. 316555.

Chapter 4

A novel framework for a rational, fully-automatised calibration routine for DEM models of cohesive powders

Abstract[1]

A new framework for calibration of DEM models of cohesive materials is presented. DEM simulations are a widespread numerical tool for modelling granular assemblies and related processes, but require careful calibration to give realistic predictive results. To this aim routine small-scale laboratory tests are used to investigate powders rheology while limiting resource investment, in conjunction with a rational approach to reduce computational costs as well. A specific order in numerical tests and calibrated variables is defined, enabling the implementation of an automatic iterative routine to calibrate material parameters from a given dataset. This method is successfully applied to calibrate four common increasingly cohesive powders of pharmaceutical relevance. Our framework saves an important amount of computational expense when compared to traditional parameters design space approaches, and proved to be able to calibrate very cohesive powder exhibiting plastic bulk volume loss of up to 25% *(after uniaxial consolidation up to* $10kPa$*).*

[1]With minor corrections from: L. Orefice, J. G. Khinast, Powder Technology 361, 687-703 (2020).

4.1 Introduction

Powders and granular materials are ubiquitous in everyday life, as well as in industry and manufacturing processes. Granular materials greatly range in size according to the products and the respective processes. Mining and rock industries, for instance, deal mainly with particles of size ranging from centimetre to metre, food industry mainly processes particles ranging from millimetres (grains) to several tens of micrometers (food additives and powders), while pharmaceutical processes involve powders typically below the 100 μm size as well as larger granules and pellets.
The last decades have seen a progressively growing application of numerical methods to model the behaviour of granular materials and processes in which they are involved; among all of modelling approaches, the Discrete Element Method [23] (DEM) is one of the most commonly used. With growing computational capacity DEM has been successfully employed to tackle problems of increasing magnitude and complexity. First and foremost, modern computers can handle simulations with orders of magnitude of over a million particles [13, 19, 45, 73, 108, 128, 149]: the possibility to handle such a high number of particles enabled the study of systems composed of many particles without resorting to scaling, consequently achieving unprecedented resolutions. By nature, spheres are the tridimensional objects easiest to model, and their intrinsic symmetry allow predicting reciprocal collision in a straightforward way by simply computing their relative distance. However granular materials exist in a broad variety of shapes, and approximating the former by means of spheres [160] can, in many cases, completely alter the physics of the system under consideration. If that is the case, the simpler solution is to model particles by means of a clumped ensemble of spheres [62], to mimic the shape of real particles in more detail. The previous method, despite being efficient, cannot be used for every application, displaying intrinsic limitations as the sphericity of the granules under study decreases [87]. The only solution here is to use particles which faithfully replicate the true shapes [13, 46, 73, 133, 167], at the price of computational costs. Originally, the interaction models of particles in DEM, despite being slightly different [74, 84], were purely repulsive: upon contact the particles experience a force that will tend to separate them, proportional to the relative overlap due to the undergoing collision. These simple models have been extended to include adhesive interactions, both on contact and at short range, that can arise due to van der Waals or electrostatic forces, liquid bridges, etc. [64, 83, 126, 139].
For certain problems pure DEM is not able to correctly predict the behaviour of the particles; exemplary cases are whenever the interaction with fluids surrounding particles cannot be neglected but must be accounted for [61, 120], or when thermal effects and heat exchange are relevant to the process [164]. All of the former refinements to the original DEM implementation are not mutually exclusive, but can be combined to model processes and granular assemblies increasingly rich and diversified in physical phenomena.
However, despite the variety of models, all DEM implementations share the same necessity for both proper calibration and validation [86]: a numerical method is considered to be reliable only if it can replicate the real behaviour of the granular material up to an arbitrary extent. Model calibration consists of the careful choice of the (many) material input parameters needed to reflect the real behaviour of the particles in the numerical simulation, and happens before the actual modelling of the process under study. In contrast, model validation is performed by comparing a set of experimentally studied *test cases* to their

simulated counterpart to evaluate if both match. Since this step needs data from the model itself it is carried out after a certain set of simulation runs. Although equally important, in many circumstances it is either impracticable or impossible to validate a modelled process, especially if the latter involves a very large amount of expensive material. An example comes from the pharmaceutical industry [103]: processes at industrial scale frequently involve kilograms of powder that can be extremely expensive (> 1000€/g). Therefore, an experimental *test case* specifically aimed to model validation is unfeasible. However, calibration of the modelled powder is affordable even for pharmaceutical applications, since the amount of material needed is of the order of magnitude of dozens of grams [153].
There is plenty of literature concerning DEM calibration [15, 20, 21, 117, 118, 171]. Because of the large number of material attributes to be set, and the experimental challenge of measuring certain properties independently [34], calibration techniques focus only on selected parameters, while others have to be chosen reasonably a priori. These parameters also depend on which interaction model is chosen, as briefly explained earlier. Additionally, since it is often impossible to measure single particle properties, experimental data used for the model calibration mainly refers to bulk particle properties (a technique known as *bulk-calibration approach*). Use of statistical tools for the calibration procedure is widespread [107, 161, 165].
Despite the extensive usage of DEM in the pharmaceutical context, there is no standardised calibration technique for pharmaceutical blends. Moreover, a framework capable of successfully calibrating cohesive powders from small and relatively inexpensive laboratory measurements is not in place.
The ambition of this study is to develop a new calibration procedure based on routine small-scale laboratory experiment, to successfully calibrate both cohesive and non-cohesive single-component powders of pharmaceutical relevance. The idea is use only small amounts of material that are typically available during early development phases. Additionally, this procedure must be able to correctly capture the complex rheology without reliance on the particle shape, using only simple sphere models to represent the actual particles. This necessity arises since the calibrated powders will be used in the modelling of industrial-scale processes, where ensembles of the order of $> 10^6$ particles are required. Therefore, at the current state of computational capacity, only spherical particles can ensure reasonable particle numbers beyond a million particles. Our method will thus focus on the numerical calibration of the most relevant parameters involved in the experiments, such as friction coefficients and internal spring stiffnesses, while other quantities, such as particle size and plasticity, will be carefully estimated via physical arguments based on packing structures and relative properties. After the relative relevance is assigned to the calibrated variables, the order of the tests composing the numerical routine will be determined. Of key importance in this work will be to completely automatise the whole calibration process, consequently minimising computational effort and avoiding both a systematic parameter study and trial and error procedures. This framework will constitute the backbone of future developments, where multi-component pharmaceutical blends, and perhaps non-spherical elements can be considered. This will be included in the procedure.
In the first part of the study the experimental setup and the relevant tests will be briefly described. The adhesive elasto-plastic interaction model will be shortly introduced, mainly focusing on its main features. The second part will explain and motivate the choice of the material properties calibrated in our framework. Some of the former will be inferred

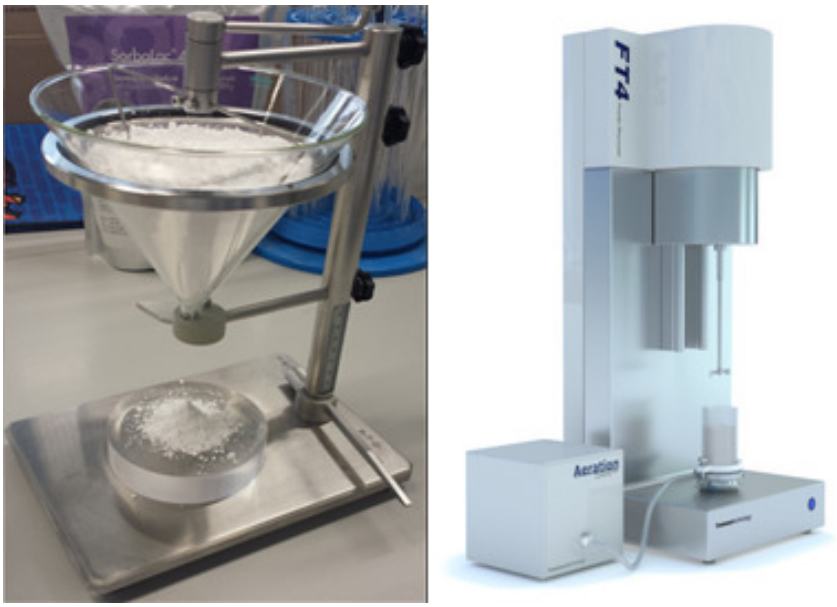

Figure 4.1: Small-scale laboratory devices used for powder characterisation experiments: the AoR tester (left) and the FT4 Powder Rheometer (right).

before the actual numerical calibration procedure has begun via physical arguments. Subsequently, the precise order to follow in performing the numerical tests is explained, determining the order in which the parameters are calibrated. The results of the experiments will be presented in the fourth part, while in the last part the results from the numerical calibration tests will be presented and compared with the experiments.

4.2 Experimental setup

Two experimental devices will be used for the small-scale routine rheological characterisation of the pharmaceutical powders: an *angle of repose (AoR) tester* and a *FT4 Powder Rheometer* [33]. These are standard tools employed for powder characterisation in the pharmaceutical industry, and are used in this study to maximise its usability. The usage of these specific instruments does not affect the proposed framework, which remains valid as long as the tools used for the experiments are faithfully replicated in the numerical models.
The AoR tester consists of a glass funnel that will be filled with the powder to test and an underlying circular glass plate, with a radius of 5cm. During the filling phase the outlet is closed to prevent the powder from escaping the container. Once the latter is full, the small shutter closing the outlet is removed and the powder let to settle above the glass plate. To enhance the powder flow and prevent arching an agitator is slowly moved in a circular motion. When all the powder exited the container and piled underneath, the height of the powder pile is measured and compared with the size of the underlying plate to get an estimation of the angle of static repose α.
The FT4 powder rheometer can perform compression and shear tests. The toolset used is composed of a fixed cylindrical casing of height $H_0 = 1.90$cm and radius $R = 1.25$cm,

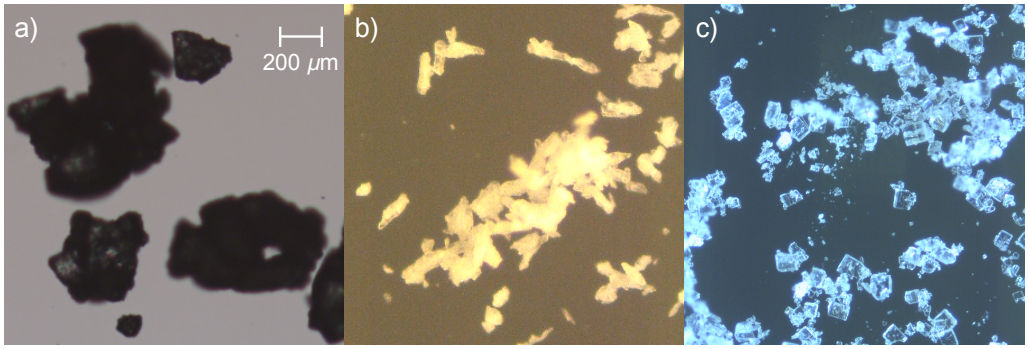

Figure 4.2: Optical microscope images of the commonly employed powders used for laboratory testing: a) lactose monohydrate (LAC), b) microcrystalline cellulose (MCC) and c) ascorbic acid (ASA).

containing the powder bed, and of a piston, located on top of the powder bed, able of moving along the axial direction and of rotating in the plane normal to its axis. Sensors connected to the latter measure the pressure P exerted by the piston on the powder, its position H (or compression $\Delta = H_0 - H$) and the torque τ at any time. Both experimental devices are shown in figure 4.1.
Four different powders of pharmaceutical interest have been used to obtain experimental data to test our numerical calibration method: engineered mannitol Pearlitol® 160 C for (MAN) from *Roquette Frères*, lactose monohydrate Capsulac® 60 (LAC) from *Molkerei Meggle Wasserburg GmbH & Co. KG*, microcrystalline cellulose Avicel® PH-102 (MCC) from *FMC BioPolymer* and ascorbic acid (ASA) from *Mühlenchemie GmbH & Co. KG*. Engineering on mannitol powder was performed to achieve a better flowability of the particles. All particles besides the latter are illustrated in figure 4.2. The powders were selected to have different flowability, regardless of other properties: the first two can be considered free-flowing, while the last two are progressively more cohesive. The reason behind this selection is the problem we want to precisely tackle: the calibration of cohesive powders to be used in numerical models based on a spherical particle geometry, via DEM. Shape and size distribution were not considered here, as the aim was to create a consistent, industrially-relevant workflow from small-scale testing to prediction of in-process powder performance. Therefore, for our approach a detailed characterisation of the powders is not relevant, and will be omitted for sake of brevity. Since the materials used are standard ingredients of pharmaceutical manufacturing, we refer readers to examine the extensive literature, including [119].

4.3 DEM model and interaction parameters

The numerical simulations were carried out using the open source discrete element code Mercury DPM [2, 140, 159]. General aspects of DEM are well-known [84], and we refer the reader to the hefty literature. The tangential sliding friction interaction and the viscous damping implemented are the standard used in DEM linear spring-dashpot models, and are not discussed here for the sake of brevity. The rolling resistance model used here is the

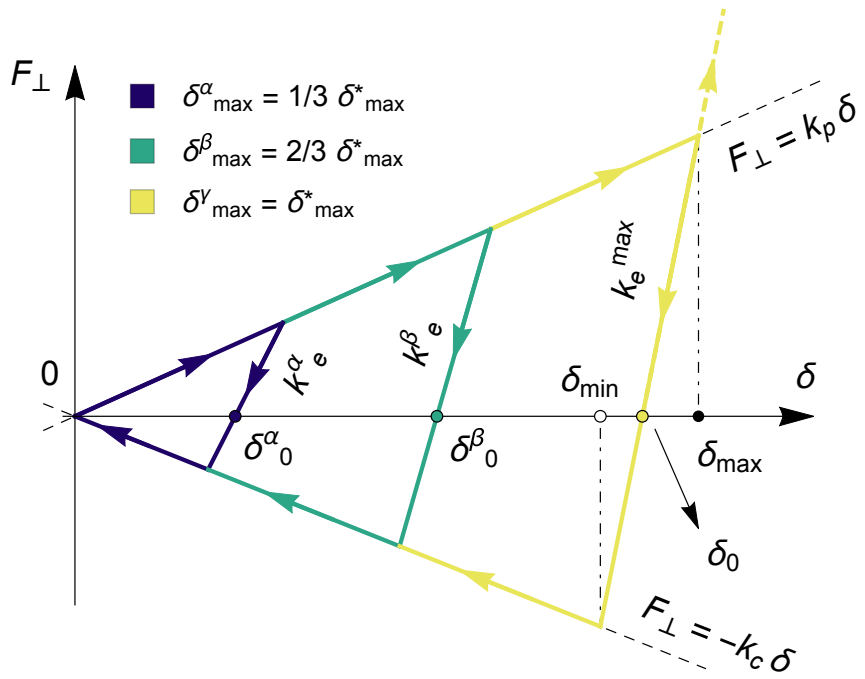

Figure 4.3: Schematic graph of the normal piecewise hysteretic force $F_\perp$ as a function of the overlap δ for two colliding particles. Different colours indicate different $\delta_{\max}/\delta^*_{\max}$ ratios, which lead to different values of k_e, δ_0 and $\delta_{\min}$.

same reported in [83, 84]. It is however worth to briefly introduce the interaction law used in our simulations, since it is key to understand the calibration procedure.
The discrete particles modelled are interacting via an adhesive elasto-plastic model, presented in [83], which is a linearised version of the more complicated constitutive model that can be found in [146, 147]. Despite some concern has been expressed regarding the asymptotic response of the model [142], the latter has valuable predictive capacity [58], and its simplicity made it the constitutive model of choice for this work. The main feature of this inter-particle interaction is to add an adhesive (attractive) interaction to the particles upon collision. The strength of the attractive force is hysteretic in nature, depending on the particle overlap during the collision: the higher the relative particles overlap, the stronger the resulting cohesive bond. When two particles collide, the normal force acting between them is given by

$$F_\perp = \vec{F} \cdot \vec{n} = \begin{cases} k_p\,\delta & \text{if } k_e\left(\delta - \delta_0\right) \geq k_p\,\delta \\ k_e\left(\delta - \delta_0\right) & \text{if } k_p\,\delta > k_e\left(\delta - \delta_0\right) > -k_c\,\delta \\ -k_c\,\delta & \text{if } -k_c\,\delta \geq k_e\left(\delta - \delta_0\right) \end{cases} \tag{4.1}$$

where δ is the overlap between the colliding particles and $\vec{n}$ is the normal vector, i.e. the vector along which the collision occurs. With k_p we indicated the plastic stiffness, i.e. the elastic constant during the force loading phase leading to plastic deformations, with k_e the elastic stiffness, i.e. the stiffness of the elastic spring during the initial particle detachment, and with k_c the cohesive stiffness, i.e. the proportionality constant of the attractive branch of the force. The hysteretic normal force described by equation (5.1) is sketched in figure

5.1. (We point out that our notation for the spring stiffnesses slightly differs from the original one [83]; choice made for the sake of clarity).
Upon contact the overlap between the colliding particle δ is growing, and the particles experience a normal repulsive force of magnitude $k_p\delta$ (coloured line of slope k_p). At a certain point a maximum penetration depth $\delta_{\max}$ is reached, and the distance between the particles starts to increase. The maximum overlap is stored in memory as a history parameter, and is necessary for the computation of the maximum attractive normal force. The unloading force acting on the particles follows a steeper slope k_e until the overlap $\delta_{\min} = (k_e - k_p)\delta_{\max}/(k_e + k_c)$ is reached. The inter-particle force becomes attractive during the unloading phase, for overlaps smaller than δ_0 as indicated in figure. The maximum cohesive force, of magnitude $k_c\delta_{\min}$, is reached at $\delta = \delta_{\min}$, and decreases for smaller overlaps. Other forces can start acting on the particles during the collision, for instance due to contacts with a third particle, and change the overlap of the former pair. If this is the case, the hysteretic normal force will move along a reloading branch of slope k_e. In our model we only considered contributions to the hysteretic force from inter-particle collisions, neglecting non-contact interactions at negative overlaps (e.g., from liquid bridges).
If no other forces are acting on the two colliding particles, there is a point $\delta_0 = (1 - k_p/k_e)\,\delta_{\max}$ where the unloading branch intersects the abscissae axis for which $F_\perp = 0$, i.e., the particles are in equilibrium. This behaviour is analogous to a plastic contact deformation, where the particles irreversibly deform and stick to one another forming a stable bond. The equilibrium point depends linearly on the history parameter $\delta_{\max}$, and increases accordingly. However, real particles undergoing plastic deformations have a more complicated behaviour, e.g. they can become stiffer the more they are compressed, and reaching the plastic equilibrium at proportionally smaller overlaps δ_0. A refinement of the model, accounting for a stiffness k_e depending on the maximum overlap, is therefore needed. For this reason an additional model parameter, the dimensionless plasticity depth ϕ, is introduced and a maximum penetration depth $\delta^*_{\max}$ is defined as

$$\delta^*_{\max}(\phi) = \frac{k_e^{\max}}{k_e^{\max} - k_p}\,\phi\,\frac{2r_i r_j}{r_i + r_j}. \tag{4.2}$$

Here r_i and r_j are the radii of the colliding particles and $k_e^{\max}$ is the maximum elastic stiffness, used as a model parameter instead of k_e. The latter is instead defined as a function of the history parameter as

$$k_e\big(\delta_{\max}\big) = \begin{cases} k_p + \big(k_e^{\max} - k_p\big)\,\frac{\delta_{\max}}{\delta^*_{\max}} & \delta_{\max} < \delta^*_{\max} \\ k_e^{\max} & \delta_{\max} \geq \delta^*_{\max} \end{cases} \tag{4.3}$$

providing a stiffer "hard core" for deformations larger than $\delta^*_{\max}$. The effect that the introduction of ϕ has on k_e, δ_0 and $\delta_{\min}$ are clearly visible in figure 5.1. This refinement makes the collision behaviour more realistic but relies on an additional parameter, increasing the hysteretic normal force model parameters count to four: k_p, $k_e^{\max}$, k_c and ϕ.

4.4 DEM parameters and calibrated variables

The calibration of meso-scale particles to faithfully replicate the physics of real powders is extremely complicated, both practically and conceptually. The reason behind this is

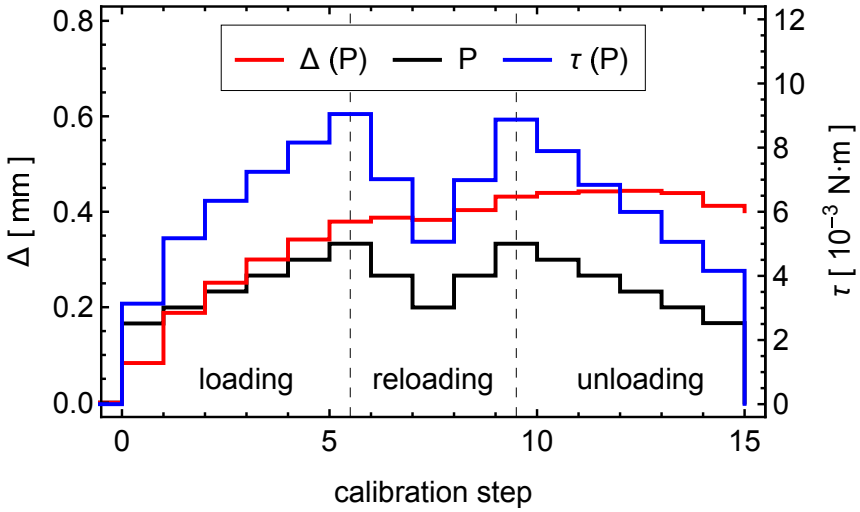

Figure 4.4: Illustrative example of prescribed pressure steps P (black) used during powder rheology tests. In this figure the former is provided only as eye-guide for comparison with the rest (the actual values used are explained in the upcoming sections, and are the same for all materials). During compression tests the compression height Δ (red) is measured, while during shear tests the piston torque τ (blue) is measured instead. The data plotted were gathered during rheology tests on MAN, and will constitute the target values for the calibration simulations. Because of hysteresis the slope of both Δ and τ does not exhibit the same symmetry and regularity of the prescribed P.

complex and is related to the nature of granular materials. Firstly, the results of small-scale laboratory tests aimed to measure the powders' bulk behaviour always depend on a high number of particle properties, each one of the latter affecting the measurements. For example, when performing shear testing, not only the friction parameters are important to determine the torque acting on the rotating shell, but also the particle shape and size distribution, the ensemble arrangement and configuration inside of the container, the inter-particle cohesion forces, the aeration of the particle bulk, and so on.
Though experiments can be designed and performed to limit the number of particle properties affecting the measurements (i.e., to allow for a clearer understanding on how single particle properties affect the bulk behaviour), macroscopic behaviour will always be determined by a combination of microscopic quantities. Secondly, granular materials have an intrinsic hysteretic nature, i.e., the status of a granular system depends on its history. For example, a granular material will behave differently after subsequent compression cycles, a property that is well-known and exploited, for instance, during the making of snowballs or die compaction processes. For this reason, when calibrating the meso-scale particles via a compression experiment, it is not enough to measure the pressure after a single compression instance, but measurements should be done after subsequent compression steps to carefully capture the elastic response of the bulk [137]. To explore the plastic behaviour, data gathering has to be performed while the piston is decompressing or shearing the particle bed, since plastic adhesive interactions can only be observed during tensile tests.
Ideally, during uniaxial compression a discrete set of points $\mathcal{P}_i = \left(P_i, \Delta_i\right)$ should be measured while loading, reloading and unloading the powder. An example of such an ideal

test is depicted in figure 4.4, where target pressure steps are predefined and the piston displacements measured when cycling through the former. During pressure increase repulsive inter-particle interactions are dominant, while cohesive effects can be neglected. The same is not true while the pressure is decreased: cohesive interactions allow the system to reach mechanical equilibrium before the particles detach, further separation leading to an attractive force. During uniaxial compression only repulsive forces $F_\perp \geq 0$ can be measured because the piston, while retracting, cannot exert a pulling force. To test the attractive branch $F_\perp < 0$ a shear test has to be performed, where the traction applied is sufficient for the particles to detach above the point of plastic equilibrium (the point δ_0 in figure 5.1). During a shear test, the measured points $\mathcal{T}_i = (\tau_i,\, P_i)$ are distributed in analogy with their counterparts $\mathcal{P}_i$, as indicated in figure 4.4. As previously, a set of target pressures is set, but the torque experienced during shearing is measured instead.
The particle properties needed to set up a DEM model are numerous:

- particle shape, average size and size distribution;
- particle density;
- four interaction parameters, i.e., three spring stiffnesses and the dimensionless plasticity depth;
- sliding, rolling and torsional friction coefficients;
- restitution and damping coefficients

For sake of simplicity the particle shape is assumed to be perfectly spherical, while the particle size follows a uniform distribution of mean r and extrema $r \pm 10\%$. Even if the distribution is mono-modal, polydispersity is needed to avoid long-range crystallisation effects arising from mono-dispersed particle ensembles [123, 154], which would alter the physics of the system.
Of the remaining 11 parameters only 10 are independent, due to contact dynamics of DEM: particle mass, spring stiffness, restitution coefficient and damping parameter are all related by a constitutive equation [84], therefore limiting the number of independent variables between the former to three. In our model we fixed particle mass (through size and density) and restitution coefficient, while keeping the spring stiffness as independent variable to be calibrated. Because of our choice, the damping viscous coefficient is implicitly determined by the former parameters and does not need to be explicitly chosen.
The 10 independent parameters left needed for the DEM model have to be either measured, calibrated or estimated. Particle density ρ is obtained by direct experimental measure (in our case we used values specified by suppliers), while particle average size is chosen to be the highest possible to limit the simulation time, provided the particles to be small enough to prevent the system from exhibiting finite-size effects. Details will be provided in the upcoming sections. Maximum elastic spring stiffness $k_e^{\max}$ and restitution coefficient e are fixed a priori to limit the minimum collision time t_c and, with it, the overall computation time. The time step dt chosen for the integration of the equations of motion satisfies the usual DEM requirement $dt \leq t_c/50$ necessary for granting numerical stability. The collision time is obtained by solving the dynamics equations of a damped harmonic oscillator [84] of spring stiffness $k_e^{\max}$. Rolling friction coefficient μ_R has to be calibrated, but is regarded

as a less-impactful parameter when compared to sliding friction. Its initial value is fixed to 0.10, and will only be changed if the first iteration of the calibration of μ_S will not converge, as explained later. Since we model spherical particles, the resistance these oppose to torsion can be negligible when compared to the resistance exhibited versus either rolling or sliding [34]. For this reason the torsion friction coefficient is neglected and set to zero.
All the remaining four variables have to be calibrated: plastic k_p and cohesive k_c spring stiffnesses, dimensionless plasticity depth ϕ and coefficient of sliding friction μ_S. A list of the former DEM parameters is provided in table 5.1 (the values reported for the calibrated parameters, highlighted in brackets, are the ones chosen prior to calibration, and are updated on-the-run). Since $k_e^{\max}$ is fixed, from now on the other spring constants will be expressed in dimensionless form as $\hat{k} = k/k_e^{\max}$.
An important note regarding the choice of the friction coefficients has to be made: in our study the friction coefficients of the walls have been set equal to particles' counterparts. This assumption, albeit not accurate [107], does not force us to guess what the friction between particles and walls might be, therefore not affecting the final calibration results with variables chosen a priori. In teh context of our framework, the only case when this might play a role is during the modelling of the FT4 rheometer. This device, however, is naturally designed to limit the effect due to direct contact between its elements and the powder, and the tests performed are dominated by particle-particle interactions. For instance, during compaction and shear experiments, there is always a layer of powder in the interstice between casing and the powder directly displaced by the piston motion. For this reason the impact of neglecting a detailed particle-wall friction model is greatly reduced. Clearly, when calibrated DEM particles will be used for modelling other devices, the relative friction coefficient between the former and the materials composing the latter should be separately determined as well.

4.5 Preliminary parameter estimation

DEM simulations are computationally expensive, and the amount of simulations needed for the calibration grows with the number of parameters to be estimated. To optimise the procedure, it would be ideal to rely on constitutive laws according to which calibrated parameters are connected, or to limit the range of parameter values spanned by the former. In addition, parameters such as the average particle radius r, can be chosen through physical considerations involving a specific set of simulations, independent from the calibration simulations routine, that have to be performed as a first step. This first part of the calibration procedure is independent on the specific material to be calibrated, relying only on physical considerations, and can therefore be regarded as a general first step for every future calibration following this same framework.
From this point onward both particle deformation (or overlap) δ and piston displacement Δ will be expressed in dimensionless form as $\hat{\delta} = \delta/r$ and $\hat{\Delta} = \Delta/H_0$ respectively.

4.5.1 Particle size and particle number

The total number of particles N used in the simulation of the powder rheometer is determined by the average particle size r and by the cylindrical casing volume $V_{\text{cyl}} = \pi R^2 H_0$, and is of high practical interest, since it affects the computational expense of the simu-

Table 4.1: List of DEM parameters used in the simulations.

Parameter	Symbol	Unit	Source	Value
Average radius	r	cm	Inferred	$3.125 \cdot 10^{-2}$
True density	ρ	g/cm^3	Measured	[1.44; 1.69]
Max elastic stiffness	$k_e^{\max}$	N/m	Set	$5 \cdot 10^3$
Restitution coefficient	e	—	Set	0.50
Dim.less plastic stiffness	$\hat{k_p}$	—	Calibrated	(0.1)
Dim.less cohesive stiffness	$\hat{k_c}$	—	Calibrated	(10^{-3})
Sliding friction coefficient	μ_S	—	Calibrated	(0.5)
Rolling friction coefficient	μ_R	—	Calibrated	(0.1)
Dim.less plasticity depth	ϕ	—	Inferred	—

lations. We determine the particle size from the rheometer setup because, as it will be explained in the subsequent sections, the numerical model for the AoR test does not impose any constraint on the particle size.
Since the particle size distribution is uniform, we can approximate the total volume of particle V_p^{tot} as

$$V_p^{\text{tot}} = \sum_{i=1}^{N} V_i \approx N\,\overline{V_p} = \zeta_{3D}\,V_{\text{cyl}} \tag{4.4}$$

where N is the total number of particles of average volume $\overline{V_p}$ and ζ_{3D} is the 3-dimensional packing fraction of the particle ensemble inside the cylindrical casing of volume V_{cyl}. Inverting the previous relation, and introducing the dimensionless cylinder-to-particle size ratio $\lambda = R/r$, the total number of particles needed to fill the cylindrical casing is

$$N = \frac{3H_0}{4R}\,\zeta_{3D}\,\lambda^3. \tag{4.5}$$

The number of particles scales with a power law $N \propto \lambda^3$, therefore being very sensitive to variations of the average particle radius, and linearly with the casing volume.
To save computational time we chose r to be as big as possible provided that the system does not exhibit finite size effects. The 3-dimensional packing fraction is the bulk quantity we investigated to determine if the system is affected by the latter: ζ_{3D} should not depend on the particle size. To this avail we performed different simulations where the FT4 casing was filled with non-cohesive particle ensembles of different ratios λ, and compared the 3D packing fractions obtained in this way. In every numerical test performed, particles are loaded into the geometry in random positions, providing them from being in contact with any previously inserted object. They then settle due to gravity, rearranging in a configuration analogous to particles poured inside a container. The other interaction parameters used are the ones presented in table 5.1. We explored a broad range of integer values of λ, the resulting packing fraction measured after the particle settled is plotted in figure 4.5 along with the total number of particles.
The value of ζ_{3D} reaches a plateau for $\lambda \geq \lambda_{\text{t}} = 40$, the latter being the threshold above which the system is scale-invariant. Above λ_{t} the packing fraction becomes constants and very close to 0.60. This threshold on λ is the maximum particle radius we can use for our

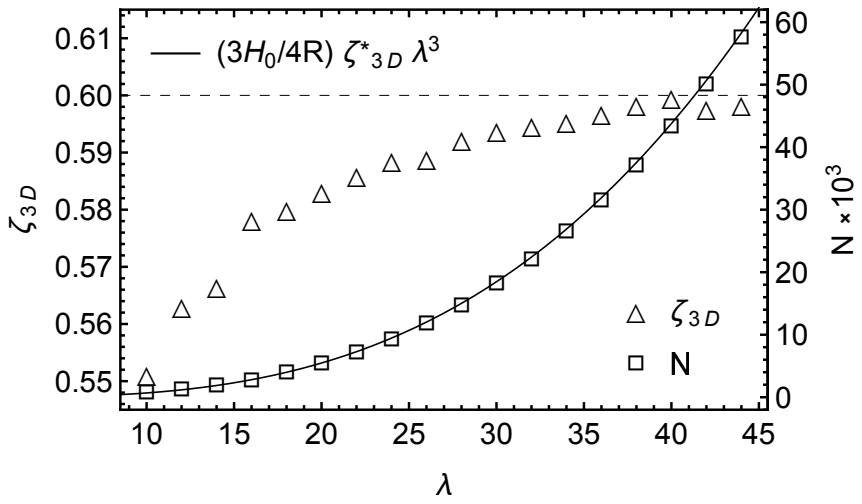

Figure 4.5: Numerically computed packing fraction ζ_{3D} (triangle markers) and total number of particles N (square markers) as a function of the ratio λ. ζ_{3D} reaches a plateau for $\lambda \geq \lambda_\mathrm{t} = 40$ where $\zeta_{3D} = 0.60$ (indicated by the dashed line). The total number of particles follows the power law $N \propto \lambda^3$; the solid line depicts equation (4.5) for a packing fraction $\zeta^*_{3D} = 0.60$.

simulation, i.e., $r_\mathrm{max} = R/\lambda_\mathrm{t} = 3.125 \cdot 10^{-2}$cm. To save computational time we then set the average particle radius for the future numerical calibration to $r = r_\mathrm{max}$, leading to a total number of particles $N \approx 4.2 \cdot 10^4$.

4.5.2 Plasticity depth and linear scale-invariant approximation

The dimensionless plasticity depth ϕ is central in determining the behaviour of the material since it is related to the penetration threshold $\hat{\delta}^*_\mathrm{max}$: for smaller particle overlaps they behave plastically, elastically otherwise. In addition to the threshold, it also affects how the plastic branch k_p is interpolated to the elastic one k_e due to equation (5.3). Besides its importance in determining the particle dynamics at the microscopic level, ϕ plays an even more important role in determining the macroscopic behaviour of the bulk. To understand the macroscopic behaviour, we need to relate the local particle deformation $\hat{\delta}$ to the deformation of the ensemble $\hat{\Delta}$.
Since the particle deformation is related to the piston displacement, we can reasonably assume the maximum average particle deformation $\langle\hat{\delta}\rangle_\mathrm{max}$ to be proportional to the maximum the piston displacement $\hat{\Delta}_\mathrm{max}$. If we consider the simplest arrangement of particles inside the casing, a crystalline configuration where identical particles are perfectly piled on top of one another (see figure 4.6), they will form N_h vertical layers of particles of height $2r$ each. Assuming $r \ll H_0$, the number of vertical layers is deduced from the cylinder height as $N_h \approx H_0/2r$. Assuming a homogeneous deformation of the particle bed upon compression, every particle will endure a maximum relative deformation given by $\Delta_\mathrm{max} \approx 2N_h \langle\delta\rangle_\mathrm{max} = H_0\langle\delta\rangle_\mathrm{max}/r$, which implies $\langle\hat{\delta}\rangle_\mathrm{max} \approx \hat{\Delta}_\mathrm{max}$. Plugging this relationship into (5.3), imposing $\langle\hat{\delta}\rangle_\mathrm{max} \leq \hat{\delta}^*_\mathrm{max}$ and solving for ϕ we obtain

$$\phi \geq \phi_\mathrm{min} = \left(1 - \hat{k_p}\right) \hat{\Delta}_\mathrm{max}. \tag{4.6}$$

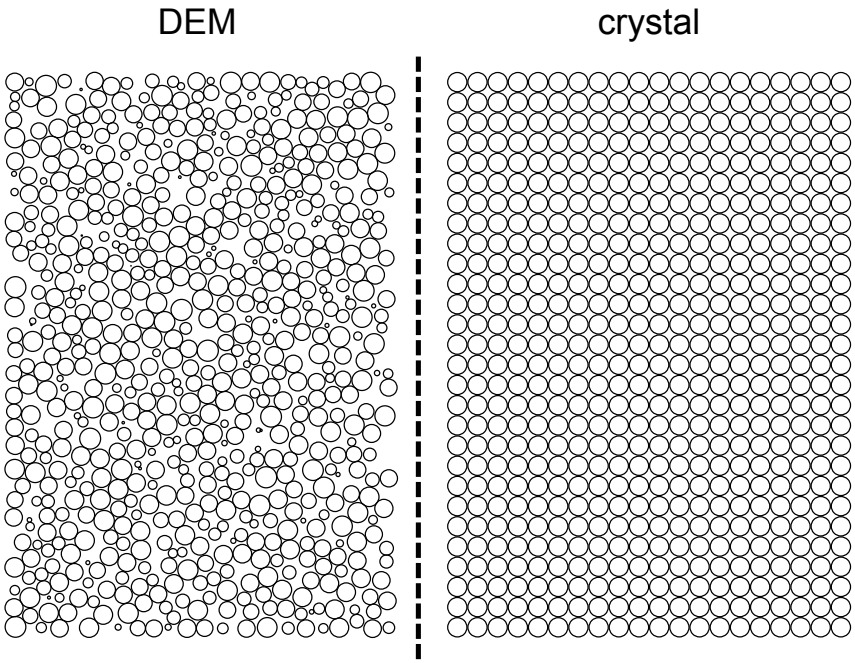

Figure 4.6: Visual comparison between the cross-section of a region inside non-cohesive particle bulk after settling (left) and an ideal ordered crystal configuration (right). The particles involved have the same radius, the variability of the cross-section on the left being due to the 3D arrangement of the spheres.

The physical meaning of the former inequality is the following: to have, on average, a plastic behaviour at the particle level, the plasticity depth has to be set greater than a minimum threshold value $\phi_{\min}$, which in turn only depends on the rescaled plastic stiffness $\hat{k_p}$ and on the maximum relative piston compression $\hat{\Delta}_{\max}$.
For small bulk compressions like the ones performed in our small-scale rheological experiments ($P \leq 10$kPa) we can assume, for $\phi \geq \phi_{\min}$, $\lambda \geq \lambda_t$ and a tightly packed bed, the linearity between microscopic and bulk deformations to hold for every step of the particle bed compression

$$\langle \hat{\delta} \rangle \approx \hat{\Delta}. \tag{4.7}$$

This can be used to relate the microscopic interaction force parameters F and $\hat{\delta}$ to the macroscopic ones P and $\hat{\Delta}$ measured experimentally. Because of the interaction law used the inter-particle force is piecewise linear, and such will be the relation between pressure and piston displacement for any point

$$\mathcal{F}\big(F, \langle \hat{\delta} \rangle\big) \sim \mathcal{P}\big(P, \hat{\Delta}\big). \tag{4.8}$$

During loading, if we consider the pressure between piston and the upmost particle layer we can write

$$P = \frac{F}{S} = \frac{\sum_{i=0}^{N_S} k_p \delta_i}{S} \approx \frac{N_S \, k_p \, \langle \delta \rangle_{N_S}}{S} \tag{4.9}$$

where $\langle \delta \rangle_{N_S}$ is the average deformation of the N_S particles composing the upmost layers and S is the cylindrical casing cross-section. At the maximum compression pressure $P_{\max}$

we have that $\langle\delta\rangle_{N_S} \approx \delta_{\max}$, and we can use relation (4.7) to obtain

$$P_{\max} \approx \frac{N_S\, k_p r\, \hat{\Delta}_{\max}}{S}. \tag{4.10}$$

The pressure can oscillate and have a non-linear behaviour in the initial stage of the compression due to small particle rearrangement. However, once the latter interlock into a stable structure, for pressure values small enough not to alter the physical properties of the material (e.g., like during sintering or extrusion), the pressure can be considered to be a linear function of the piston displacement.
Because of hysteresis, the mechanical equilibrium point $\mathcal{F}_0 = \big(0,\, \langle\hat{\delta}_0\rangle\big) \sim \mathcal{P}_0 = \big(0,\, \hat{\Delta}_0\big)$ is met for $\langle\hat{\delta}_0\rangle > 0$ (see figure 5.1); therefore under the aforementioned conditions we can expect a similar behaviour macroscopically. This is exactly what is observed in reality during compression of granular materials. Since both loading and unloading branches intersect at point $\mathcal{P}_{\max} = \big(P_{\max},\, \hat{\Delta}_{\max}\big)$ we can assume

$$\hat{k_p}\, \hat{\Delta}_{\max} \approx \frac{S\, P_{\max}}{N_S\, k_e^{\max}\, r} \approx \hat{k_e}\, \big(\hat{\Delta}_{\max} - \hat{\Delta}_0\big). \tag{4.11}$$

This last equation enables us to guess which elastic spring stiffness $\hat{k_e}$ is needed to completely unload the piston at a displacement $\hat{\Delta}_0$ after the particle bed was compressed down to $\hat{\Delta}_{\max}$ with a plastic stiffness $\hat{k_p}$, and will be of great help during the interaction parameters calibration. Since $\hat{k_e}$ is determined by equation (5.3), we actually have a closure relation between $\hat{k_p}$ and ϕ. Substituting (5.4) into (5.3) and using the linear relation (4.7) gives:

$$\hat{k_e} = \hat{k_p} + \big(1 - \hat{k_p}\big)^2\, \frac{\hat{\Delta}_{\max}}{\phi}. \tag{4.12}$$

Now solving for ϕ gives us

$$\phi^* = \frac{\big(1 - \hat{k_p}\big)^2}{\hat{k_e} - \hat{k_p}}\, \hat{\Delta}_{\max} = \frac{\big(1 - \hat{k_p}\big)^2\, \hat{\Delta}_{\max}}{(C-1)\, \hat{k_p}} \tag{4.13}$$

where we defined the proportionality constant $C = \hat{k_e}/\hat{k_p} = \hat{\Delta}_{\max}/\big(\hat{\Delta}_{\max} - \hat{\Delta}_0\big)$ from equation (4.11). Simply put, ϕ^* is the value of the dimensionless plasticity depth needed to totally unload the piston at a displacement $\hat{\Delta}_0$ after a compression down to $\hat{\Delta}_{\max} > \hat{\Delta}_0$ of particles of stiffness $\hat{k_p}$. Because of this relation we can manipulate the local deformations in response to a compressive force to control the bulk compressibility by simply tuning ϕ. 4.7.

4.6 Calibration procedure

Once we fix the dimensionless plasticity depth ϕ according to equation (4.13) there are only 3 variables left to be calibrated, namely sliding friction coefficient μ_S, plastic spring stiffness $\hat{k_p}$ and cohesive spring stiffness $\hat{k_c}$. Since the parameters to be calibrated affect the numerical simulations in different ways and magnitude, the simulations need to be performed in a precise order. This procedure will limit the effect of parameters yet to

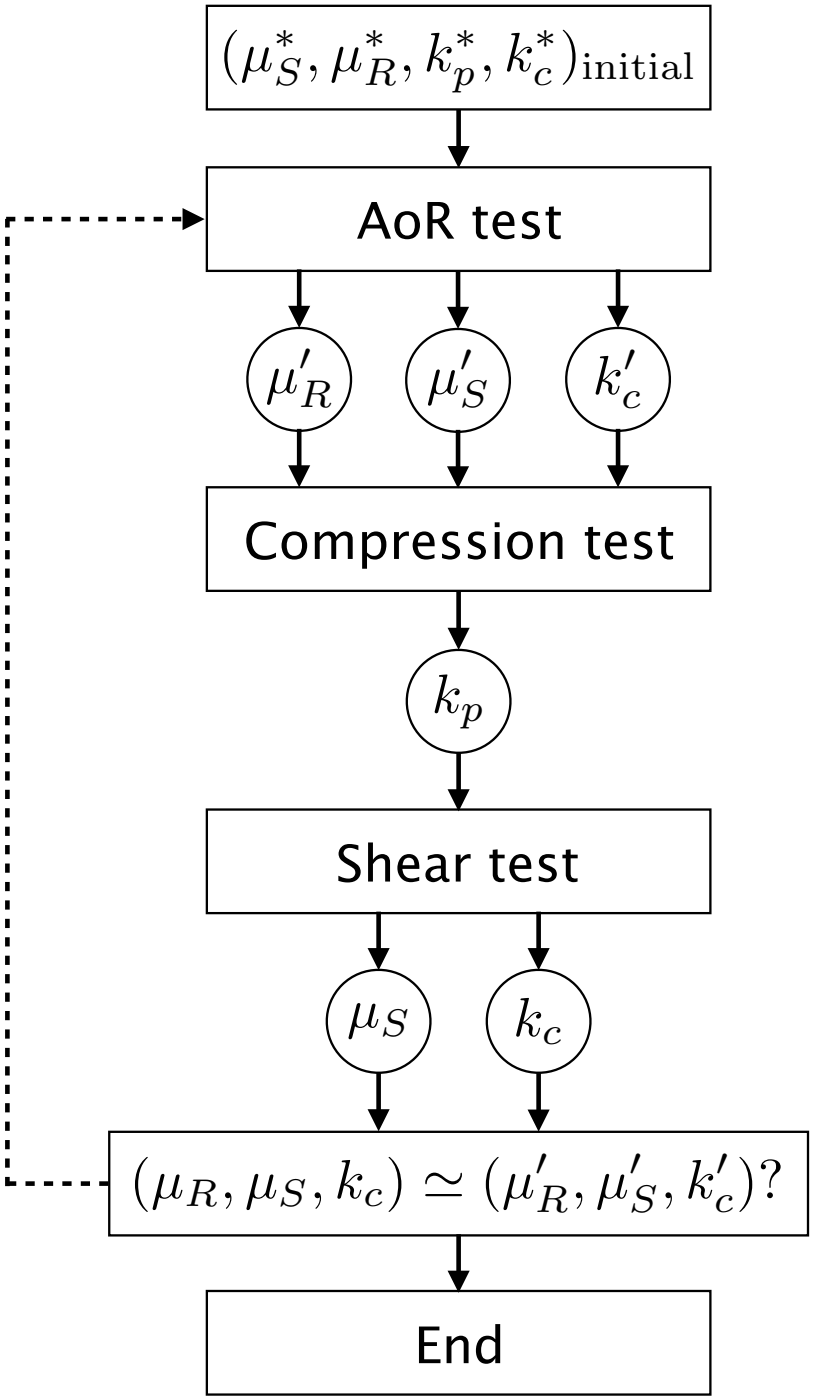

Figure 4.7: Diagram of the numerical calibration procedure. The boxes represent the main calibration steps, while the calibrated variables are encircled; the first box is for defining an initial set of uncalibrated variables, denoted by an asterisk. If a calibration step is successful the flow follows the solid arrow, while if the calibration step fails, the flow goes back to a previous step following the dotted line.

Table 4.2: Sensitivity of numerical calibration tests on calibrated parameters.

Calibration Test	μ_S	$\hat{k_p}$	$\hat{k_c}$
Angle of repose	Yes	No	Yes
Compression	Yes	Yes	No
Shear	Yes	Yes	Yes

be calibrated on the current calibration routine focusing on a specific variable, and will allow calibrating variables in a selective way. Which calibrated parameter affects which calibration test is noted in table 4.2.
Since the granular material is in a state of tight packing during each calibration test, the static friction coefficient μ_S is strongly affecting the system in every single one. Both compression and shear tests are performed on particles enclosed in a cylindrical casing and subject to compressive forces. In this state the pressure exerted on the particle naturally builds up, and the plastic spring stiffness $\hat{k_p}$ plays an important role. On the contrary, during the static angle of repose test the powder is let to settle on top of a horizontal plate, and is therefore in a free-surface state, where $\hat{k_p}$ plays a secondary role when compared to friction [20, 47, 81, 125, 168]. The importance of cohesion forces in this test depends on the nature of the powder tested, while friction strongly affects the results independently of the cohesiveness of the particles. The cohesive branch of the force is activated when the particles are subjected to tension. By definition, a compression test cannot exert tensile forces: after compression the particle bed will recover part of its initial volume until a final equilibrium state is reached, but the cohesive branch determined by $\hat{k_c}$ will not play any role. For this reason the cohesive stiffness $\hat{k_c}$ cannot, according to the model, be calibrated via compression tests. However, since the slope of the reloading branch is instrumental in determining the mechanical equilibrium point $\mathcal{P}_0$, the compression test simulation has to be executed before the shear test. Because of the variability of the AoR test dependency upon $\hat{k_c}$, this test will be the first to be performed, followed by compression and shear tests respectively. The main stages of the numerical calibration framework are sketched in figure

4.7 Results and discussion

4.7.1 Laboratory tests

The experimental measurement of the angle of repose is done by measuring both the powder heap height, formed by the powder bulk falling through the tester, and the radius of the powder pile; the angle of repose α_{exp} is computed by taking the arc tangent of their ratio. Measurements have been repeated 3 times, and the results are reported in table 4.3. Pictures of the powder testing phase are shown in figure 4.8 for LAC and ASA to highlight the extreme slopes of the heaps obtained due to the effects of friction and cohesion.
For the uniaxial compression test a set of 16 data points with prescribed pressures were defined, distributed as in figure 4.4. The data points from the experiments $\mathcal{P}_{\text{exp}}$ used to calibrate the model are taken at each plateau, where both pressure and piston displacement are measured. The initial target pressure was set to 5kPa, followed by steps of 1kPa increases up to a total of 10kPa; afterwards two decompression steps followed, both de-

Table 4.3: Angle of repose test, experiment results.

n. test	MAN	LAC	MCC	ASA
Test 1	24.57°	28.37°	36.50°	53.67°
Test 2	25.51°	29.25°	37.23°	54.07°
Test 3	24.20°	28.81°	36.50°	53.67°
Average	24.76°	28.81°	36.75°	53.81°

Figure 4.8: Pictures of the AoR testing phase for LAC (left) and ASA (right). The high cohesiveness of the latter makes its slope steep and craggy, especially when compared to the broad smooth surface of the LAC pile.

creasing the pressure by 2kPa. The bulk is then re-compressed and de-compressed following the same pattern reversed: two compression steps of 2kPa and five smaller de-compression steps of 1kPa each. At this point the piston is unloaded until zero pressure is measured, where the last data point $\mathcal{P}_0$ is taken. The pressure-deformation curves obtained from the experimental data are depicted on the top row in figure 4.9. The final objective of the compression test calibration is to reproduce how the bulk deformation is related to the applied pressure. Since the materials tested have different rheology and packing configurations, the initial piston height, below which the pressure starts to steadily increase, is likely to differ. For this reason the experimental data points are all shifted to have an initial pressure of $0.05P_{\max}$ at $\hat{\Delta} = 0$. This approach does not alter the outcome of the test since the rheology depends on the link between P and Δ and not on the initial powder height, but allows to use the same initial particle bed height H_0 for every simulation.
The shear cell test is aimed to measure the magnitude of the resistive forces while the granular ensemble is subject to shear, and the mechanical measure is the torque needed to rotate the upper layers of the powder. In the model the resistive forces experienced are due to both inter-particle friction and cohesion, the first activating when particles move

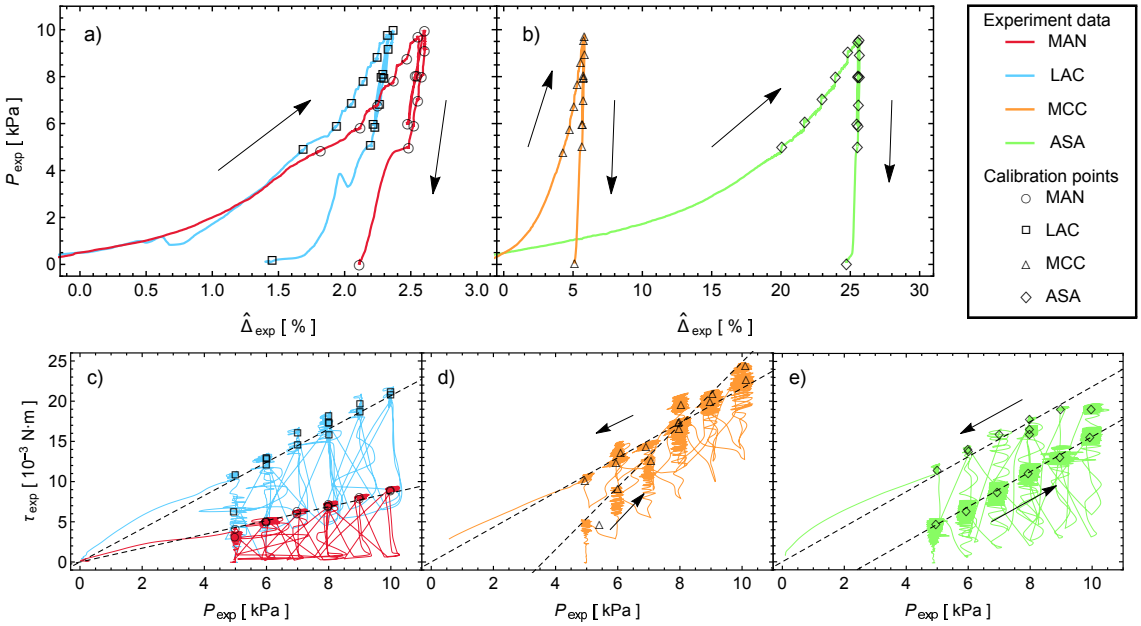

Figure 4.9: Top row: experimentally measured $\mathcal{P}_{\text{exp}}$ curve for a) free-flowing and b) cohesive materials, the arrows indicating the compression test cycle. Note the different scale of the powder deformation with a) (maximum deformation $\sim 1.5 - 2.0\%$) and b) (around 25%). The difference in the tested powders' volume loss is due to their diverse compressibility, while the different slope between loading and unloading branches is a clear indication of hysteresis. Bottom row: experimentally measured $\mathcal{T}_{\text{exp}}$ curve for c) free-flowing, d) moderately cohesive and e) very cohesive powders, the arrows indicating the shear test cycle. The slope of the curve connecting the data points collected during the piston rotation (dashed lines) is linear, and can be interpreted as the macroscopic friction coefficient μ_{MS}. A different offset is instead dependent on the macroscopic cohesiveness of the material, denoted by the displacement of $\mathcal{T}_{\text{exp}}$ during decompression.

along their contact plane, the second when their relative distance increases due to the flow of the neighbouring bulk. The torque measurement is made in the same casing where the uniaxial compression test was carried out. The same target pressure steps are defined but in addition, once they are reached, the piston tip is rotated at a constant angular velocity of $\omega_{\text{exp}} = 0.3°/\text{s}$ until it spans an angle of $\theta_{\text{exp}} = 60°$. During this circular motion the torque τ_{exp} experienced by the piston is measured, and is plotted in the bottom row of figure 4.9 as a function of the piston measured pressure P_{exp}. To calibrate the model both sliding friction μ_S and cohesive stiffness $\hat{k_c}$ are tuned to reproduce the behaviour of the torque-pressure curve $\mathcal{T}(\tau, P)$ at the selected data points.

4.7.2 Numerical calibration I — angle of repose

The AoR measurement was performed via a funnel tester (figure 4.1), but a numerical counterpart cannot be implemented due to the particles being too cohesive and jamming the funnel. In the experiment the powder is forced to flow through by rotating an impeller, but the same experiment would not work numerically and make the model unstable. For this

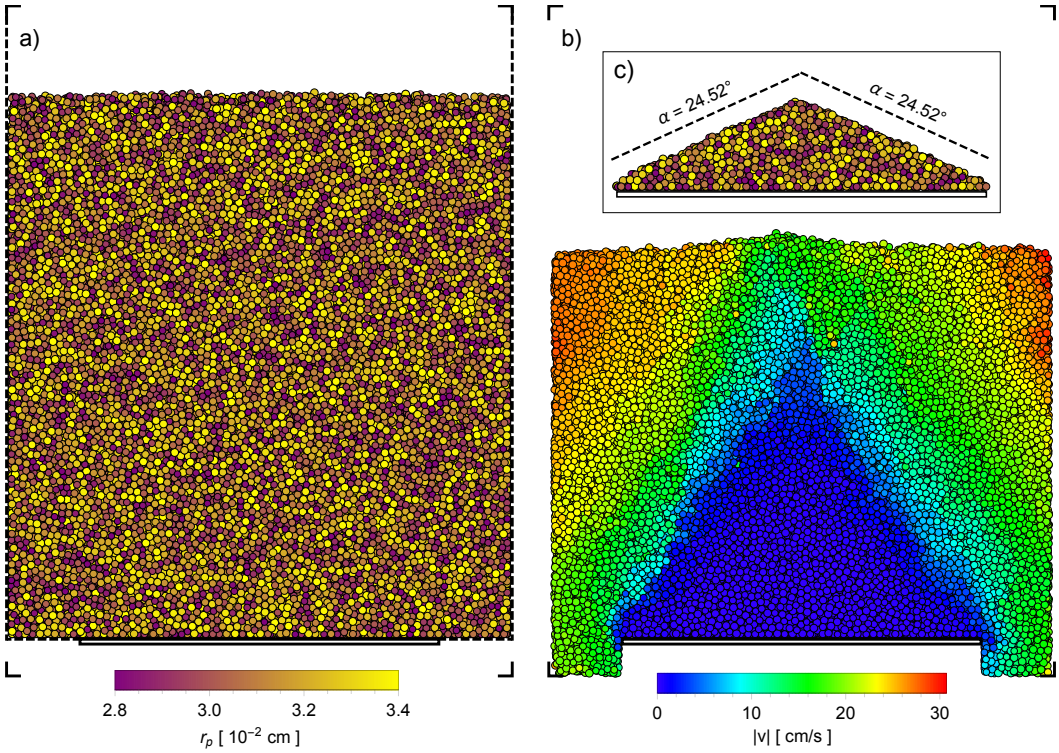

Figure 4.10: Front view of the DEM angle of repose simulation snapshots after particle loading a) and during discharge b) with starting particle properties $\hat{k}_c^0 = 10^{-2}$, $\mu_S = 0.50$ and $\mu_R = 0.10$. The solid lines in the middle represent the fixed base to support the final particle heap. The dashed lines in a) represent the removable walls that will allow the particles to fall, the latter being deleted if crossing the simulation boundaries indicated by the corners at the edges. The inset c) is a snapshot of the final pile after discharge during the last AoR iteration for the calibration of MAN ($\hat{k}_c^0 = 10^{-3}$, $\mu_S = 0.20$ and $\mu_R = 0.10$ leading to an angle of repose $\alpha_{\text{final}} = 24.52°$), the dashed lines indicating the average experimental value of the angle for visual comparison. On the left and in the inset particles are coloured according to size, on the right according to speed.

reason, instead of using a funnel tester, we implemented a draw down test. We are aware of the possible discrepancies between angles of repose measured in different tests [8, 118], but this eventual discrepancy is going to be averted by re-calibrating the friction coefficients during the shear test. In this framework the angle of repose test is used to find a preliminary value of the friction coefficients, that are later adjusted via shear test. The step of finding a preliminary friction coefficient is necessary since it affects the compression tests.

The geometry implemented for the DEM simulation of the AoR test consists of a rectangular box inside of which the particles are loaded, similar to the device used in [177]. The size of the system depends on the average particle size: the length of the box $L_{\text{box}} = 140r$ and its width $W_{\text{box}} = 20r$ are all defined as a function of r. Periodic boundary conditions are imposed along the width direction, to prevent the particles from interacting with

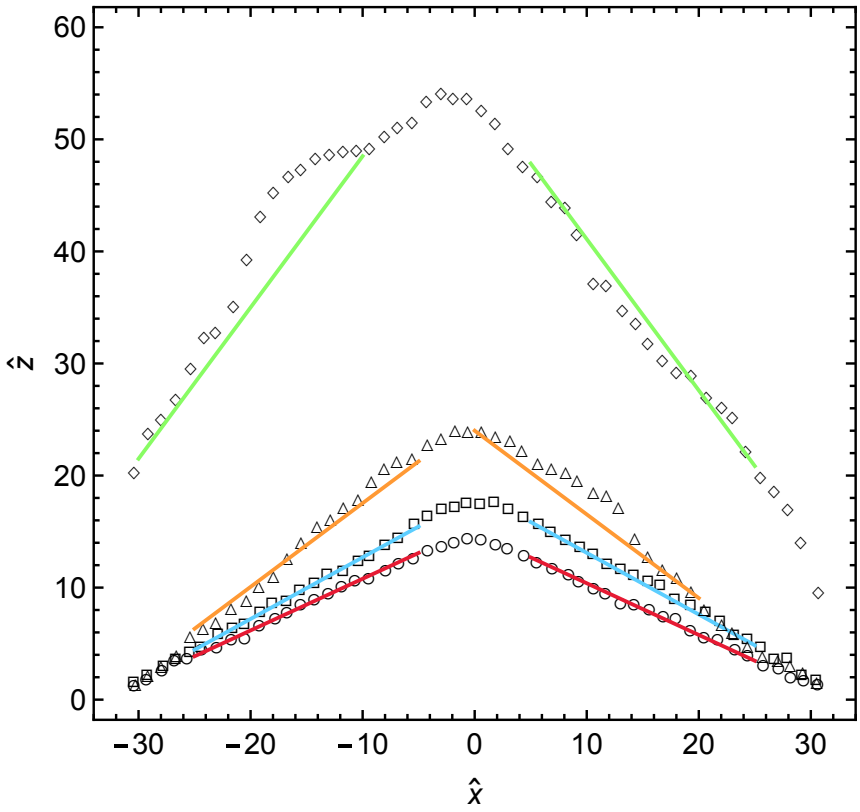

Figure 4.11: Profiles of the surface of the formed powder heaps for each material. Last iteration of the numerical AoR test routine is shown. Each point represents the position of the highest particle in each bin, averaged along the whole width of the system. The solid lines represent α_{exp} for each powder as reported in table 4.3. For colour coding and plot markers refer to the legend in figure 4.9.

side walls during the discharge leading to a non-uniform particle bed slope across the box width. The bottom of the box is composed of a fixed plate in the middle, covering the whole width but only $L_{\text{plate}} = 100r$ long, and of two removable shutters on both sides of length $L_{\text{shutter}} = 20r$. The amount of particles loaded is chosen to have a particle bed height $H_{\text{AoR}} \approx 120r$, leading to around $5.3 \cdot 10^4$ spheres. Since the geometry of the system scales directly with the particle size, the number of particles needed in the AoR test simulation is constant and independent on the particle size.
A front view of the setup after the initial particle loading is shown in figure 4.10a. The removable walls are indicated by dashed lines, while the solid lines in the middle represent the fixed plate, the simulation domain being indicated by the corners on the sides. Once the particles are loaded and settled, the shutters and the side walls are removed letting the particles fall under the effect of gravity. Particles are removed as soon as they cross the simulation domain to save computational time. A snapshot of the discharge process, taken 0.1s after the walls removal, is shown in figure 4.10b. The time the particles need to form a stable pile depends on their cohesiveness, therefore the simulation is stopped only when every particle is still after which the slope of the heap can be measured. In the inset

Table 4.4: Angle of repose test, numerical results.

	MAN	LAC	MCC	ASA
α_{exp}	24.76°	28.81°	36.75°	53.81°
α_{final}	24.52°	28.56°	36.95°	53.47°
$\varepsilon_{\text{final}}$	0.96 %	0.86 %	0.54 %	0.63 %
$n_{\text{iterations}}$	7	3	11	19
μ_R	0.10	0.10	0.10	0.30
$\hat{k_c^0}$	10^{-3}	10^{-3}	10^{-2}	$3.0 \cdot 10^{-2}$
$\mu_S^{\text{calibrated}}$	0.20	0.28	0.25	0.24

the final configuration of the particles is depicted for the last iteration of the test during calibration of MAN, to be compared with the AoR value from the experiment indicated by dashed lines.

As discussed previously $\hat{k_p}$ plays no important role in the determination of α, but the same is not true for $\hat{k_c}$. Therefore, we need to decide what value to use for the cohesion stiffness, knowing that it will affect the value of the calibrated μ_S by altering the angle of repose [4, 41]. To define the initial cohesion stiffness $\hat{k_c^0}$ to use, we assumed an inverse relationship between the former and the angle of repose. Three different cases are provided: for $\alpha \leq 30°$ we set $\hat{k_c^0} = 10^{-3}$, for $30° < \alpha \leq 50°$ we have $\hat{k_c^0} = 5 \cdot 10^{-3}$ and finally for $\alpha \geq 50°$ the initial stiffness is set to $\hat{k_c^0} = 10^{-2}$. The initial rolling friction coefficient μ_R^0 is instead kept the same for each case. These are only starting values to allow a faster convergence to a solution, since they will be modified as well if a solution is not met, as we will soon explain.

The calibration procedure for the AoR test exploits the monotonic dependence of α on μ_S [20,77,81,168], and is carried out as follows: the first two simulations are run with fixed friction coefficients $\mu_S^1 = 0.50$ and $\mu_S^2 = 0.05$, leading to the angles of repose α_1 and α_2, respectively. The initial value of the following computation is then set to $\mu_S^3 = \left(\mu_S^1 + \mu_S^2\right)/2$ resulting in an AoR α_3, satisfying $\alpha_1 \geq \alpha_3 \geq \alpha_2$. Now for every computed angle α_i, given $i \geq 3$, the relative deviation

$$\varepsilon_i\left(\alpha_i\right) = \frac{|\alpha_i - \alpha_{\text{exp}}|}{\alpha_{\text{exp}}} \tag{4.14}$$

between the AoR obtained and the target α_{exp} is computed. If $\varepsilon_i\left(\alpha_i\right) < \sigma_\alpha$, the latter being an user defined tolerance, the calibration is considered successful, and μ_S^i is used as static friction coefficient in the subsequent simulations. If this is not the case the cycle is iterated, and the new friction coefficient tested chosen via the bisection method: $\mu_S^i = \left(\mu_S^{i-1} + \mu_S^{i-2}\right)/2$. This procedure is repeated until the desired convergence is met. Being this test the first of the set, we chose the very stringent threshold $\sigma_\alpha = 0.01$. Since cohesion affects the AoR in a complicated manner, especially for poorly flowing powders, it can happen that the first guess μ_S^1 leads to a value α_1 smaller than the target one. If this is the case, the rolling friction coefficient is increased by an amount μ_R^0 and the simulations are repeated. In case convergence is still not met, μ_R is increased by the same amount until either the former reached the maximum allowed value of 0.50 or the angle of repose converged to the desired value. If this is not the case, then μ_R is re-set to its initial value μ_R^0 while the cohesion stiffness is increased by an amount $\hat{k_c^0}$, and so on. The rolling fric-

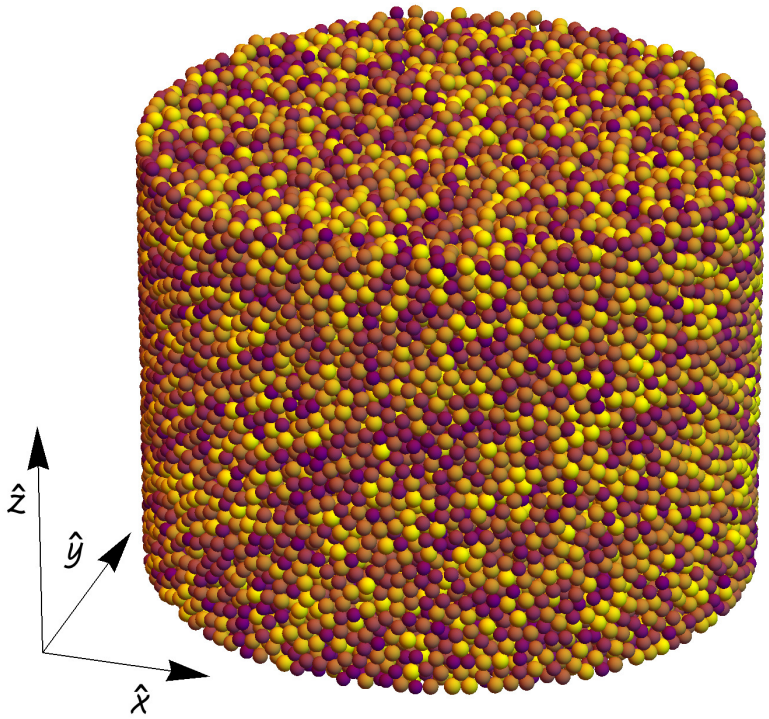

Figure 4.12: Snapshot of the settled powder bed prior to a compression test. The confining walls (bottom base, top piston and enclosing cylindrical wall) are not shown for the sake of clarity. Particles are coloured according to size as in figure 4.10a.

tion coefficient is then progressively increased before the cohesion stiffness is changed, until $\alpha_1 \geq \alpha_{\text{exp}}$. This situation occurred, for instance, in the cases of both cohesive powders. To evaluate α all particles after the discharge are binned according to their position inside a grid along the xy plane, x being the longitudinal direction and y the transversal. The grid meshes are squares of size $2r$, for a total of 50 and 10 bins along the x and y directions respectively. Inside of these the position of the highest particle is computed, and α is calculated by considering the average height difference of the highest particles in neighbouring bins along the x direction. The height profile of each powder bed at the end of each respective final calibration routine is plotted in figure 4.11, where the $(\hat{x}, \hat{z})$ coordinates of the particles on top are averaged across neighbouring bins along the y direction. The results of the numerical AoR tests are summarised in table 4.4. Calibrated values of the sliding friction coefficient $\mu_S^{\text{calibrated}}$ are different for each material as expected, rolling friction and cohesion differing as well in case of more cohesive materials. We reported as well the number of iterations $n_{\text{iterations}}$ of the AoR calibration cycle necessary to satisfy $\varepsilon(\alpha) < \sigma_\alpha$ for every powder tested, including the runs leading to an increase of either μ_R^0 or $\hat{k}_c^0$.

4.7.3 Numerical calibration II — powder rheometer

Powder rheometer simulations are substantially different from the former: not only they are considerably lengthier, but also various experiment data points must be met at once. The DEM model of the cylindrical casing for powder rheometer simulations is a faithful representation of the experimental counterpart described previously. Particles are loaded inside a cylindrical casing of radius R and let to settle, the ones laying above the powder bed heigh H_0 subsequently removed. An image of the settled powder bed before tests are performed is provided in figure 4.12. The topology of the piston surface depends on the test ran: flat for compression tests, with blades protruding perpendicularly to the surface for shear tests. Both geometries are faithful representations of the real pistons used in the experiments. During both tests, the velocity of the piston along its axis is set to $10^{-4} r_{\min}/dt$, $r_{\min}$ being the smallest particle in the system, to ensure numerical stability and a quasi-static compression regime.
During each rheometer calibration cycle every selected experiment data points has to be met, and to do so the relevant DEM parameters can be tuned several times. These tunings are performed very slowly, by an amount equal to 10^{-3} times the actual calibrated variable every 5 time steps, to ensure the system stability. In case of compression tests the plastic stiffness $\hat{k_p}$ is tuned to match the pressure P^i_{exp} at each compression height Δ^i_{exp}. During shear tests, both sliding friction μ_S and cohesive stiffness $\hat{k_c}$ are tuned to match the torque τ^i_{exp} at each piston pressure P^i_{exp}. At the end of each cycle, to determine if the parameters are successfully calibrated, both the mean relative deviation of calibrated variables, and the deviation of their mean from their starting value are computed. For a certain calibrated variable x the former are respectively expressed as follows:

$$\varepsilon(x) = \frac{1}{L} \frac{\sum_{i=1}^{L} |x^i - \langle x \rangle|}{\langle x \rangle} \tag{4.15}$$

$$\iota(x) = \frac{|\langle x \rangle - x^0|}{x^0} \tag{4.16}$$

where L is the number of calibration points (in our case $L = 15$). If the routine does not converge, a new numerical calibration cycle is performed from a new starting value $x^0|_{\text{new}} = \langle x \rangle$ of the calibrated variable. Calibration cycles are iterated until one of the following progressively less-stringent criteria is met:

- both $\varepsilon < \sigma_x$ and $\iota < \sigma_x$, where σ_x is a user-define threshold, meaning that calibration is successfully achieved within the defined desired tolerance

- $\iota < 10^{-3}$, since further iterations will be pointless given that $x^0|_{\text{new}}$ will always coincide with x^0 for every subsequent run

- a defined maximum number of iterations n_I is met.

In practice, if convergence within the threshold $\varepsilon < \sigma_x$ cannot be met, the routine can either stop because of the condition $\iota < 10^{-3}$, signifying that the cycle successfully settled to an average value of x albeit not being able to satisfy the desired precision, or exit after

n_I unsuccessful calibration trials. These multiple conditions ensure the robustness of our calibration method while, at the same time, reducing the computational costs as much as possible. In this work we set $n_I = 5$ and we chose $\sigma_x = 0.05$, a suitable compromise between speed and precision.
A dynamic, albeit slow, tuning of material properties will impact the loading history of the system since it will change the bulk properties of the material. When increasing $\hat{k_p}$ the granular solid becomes stiffer, when increasing μ_S or $\hat{k_c}$ the powder bulk becomes more consolidated. The precise effect on the bulk properties is out of the scope of this paper, but it could work similarly to a sintering process [85]. To contrast the artefacts that the dynamic calibration might have had on the bulk is important to follow two steps. First: a new settling phase must be executed at the beginning of each calibration step. Different material properties lead to different packings properties of the particles, and the latter affect bulk and flow behaviour. For this reason loading a previously settled particle bed but with new parameters to save computation time should be avoided. Second: the final validation test case, where the numerical calibration test are run without material parameters tuning, is a necessary step to ensure that the calibrated model behaves properly without any eventual disturbance due to parameters dynamic tuning.

Uniaxial compression

The compression test simulation is height driven, meaning that the piston is moved until it reaches a prescribed compression $\hat{\Delta}_i$ data point, the pressure being monitored at every time step and computed according to

$$P = \frac{1}{S} \sum_{i \in \mathcal{M}} \vec{F_i} \cdot \hat{z} \tag{4.17}$$

where the sum runs over the set $\mathcal{M}$ of all particles i exerting a force $\vec{F_i}$ against the piston. Once the latter reaches the desired height, if the pressure P^i is below the target pressure P^i_{exp}, the plastic stiffness $\hat{k_p}$ is increased until the former reaches the target value. On the contrary, if $P^i > P^i_{\text{exp}}$, $\hat{k_p}$ is decreased accordingly. Figure 4.13a shows the numerical data from the last performed calibration cycle for each powder (i.e., $\hat{k_p}$ is still dynamically varied if needed). Marked data points are the ones to be matched during the calibration, and are the same highlighted in figure 4.9 (the whole data from the compression experiment are shown as well for comparison). It is of particular importance to match the correct overall powder plastic deformation after compression, which by definition determines the powder elastic recovery as well. In order to do so, the calibration curve must intercept the $P = 0$ axis of figure 4.13a at the same point where the experiment data curve does. As it can be observed, both the behaviour along most of the calibrated data range and the final powder plastic deformation are in excellent agreement with the experiment. Numerical results differ from the experiments mostly during the loading phase, but this must not surprise: real particles have different shape and broader size distribution, resulting in a different packing state. However, when they interlock under the piston pressure, the elasto-plastic behaviour is almost perfectly captured by the numerical model.
A front snapshot of the powder bed is also shown on the left of figure 4.13 to visualise the overall plastic deformation of the powder bed: the uncoloured particles in the background

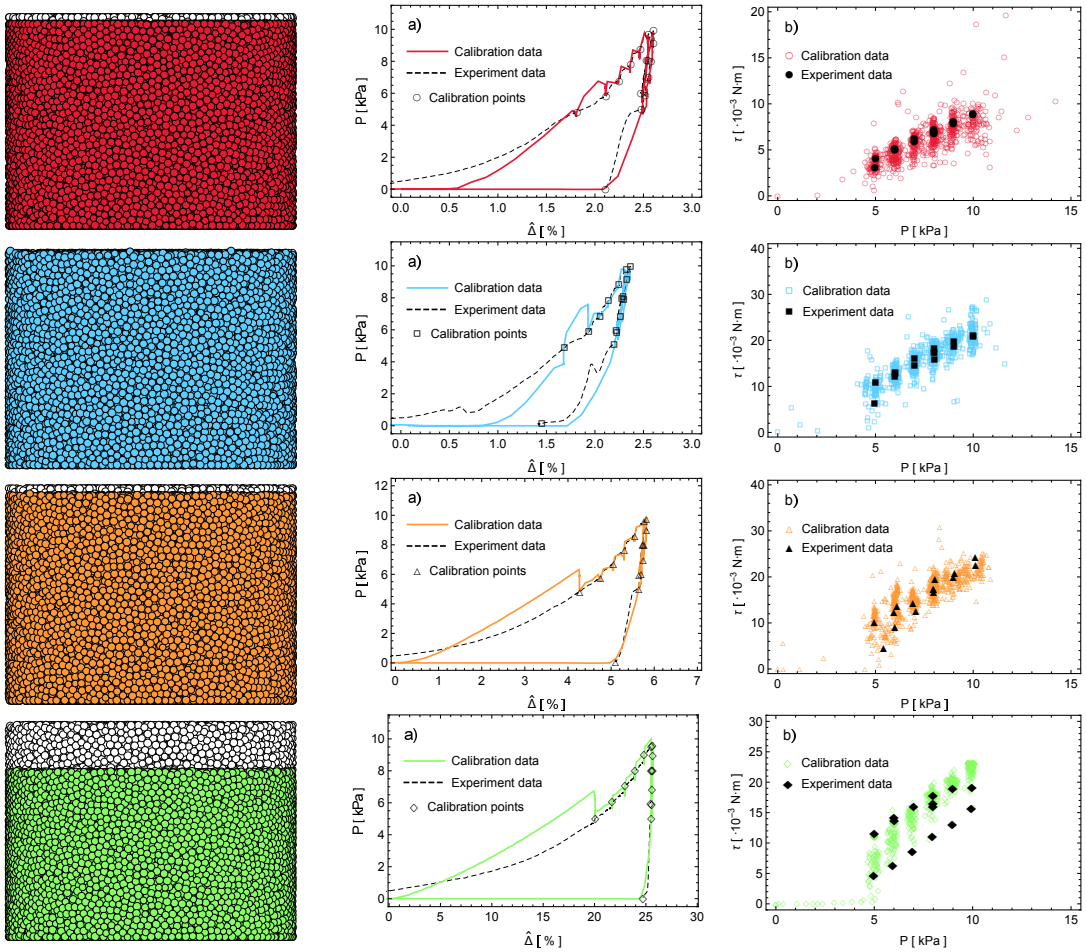

Figure 4.13: Numerical data from the last iteration of rheology calibration cycles for each powder tested (from top to bottom, MAN, LAC, MCC and ASA). To the left is a frontal snapshot of the system before (white particles in the back) and after (coloured according to material, in front) the compression test as a visual proof of the powder permanent plastic deformation. In the middle columns a) is plotted the piston pressure P as a function of bed relative deformation $\hat{\Delta}$ from initial bed height H_0 (solid coloured lines represent numerical data, dashed black ones represent experiments). The rightmost columns b) show the torque τ measured during shearing as a function of pressure P (experiment data omitted for sake of clarity). For colour coding, plot markers, and data points used for the calibration in a) and b) refer to figure 4.9.

represent the modelled particles before the last compression cycle, while the superimposed coloured ones are the mechanically stable configuration after the piston is released after the calibration. The accurate prediction of the piston unloading point validates equation (4.13) and the theoretical framework of section 4.5.

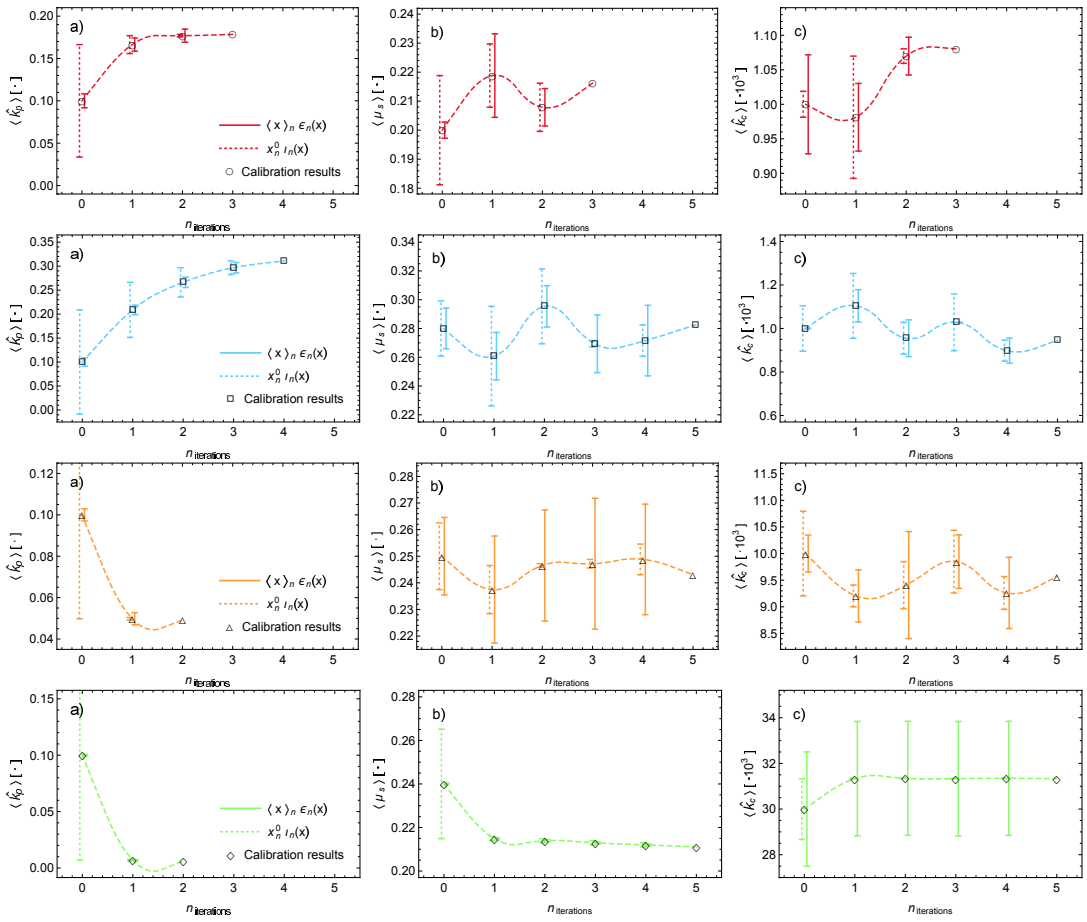

Figure 4.14: Mean calibrated parameters as a function of the number of calibration cycles iterations (from top to bottom, MAN, LAC, MCC and ASA). From left to right: a) $\langle \hat{k_p} \rangle$ calibrated during compression tests, b) $\langle \mu_S \rangle$ and c) $\langle \hat{k_c} \rangle$ both calibrated at the same time via shear tests (dashed lines connecting calibration points displayed as eye-guide). The initial values $\left(\hat{k_p^0}, \mu_S^0, \hat{k_c^0}\right)$ are used for $n_{\text{iteration}} = 0$, while for subsequent iterations the averages of the calibrated values from the previous one are used instead. The vertical error bars represent the absolute calibration errors $\langle x \rangle_n \varepsilon\left(x_n\right)$ (solid) and $x_n^0 \iota\left(x_n\right)$ (dotted) for every calibration iteration n relative to each respective calibrated variable, as defined in equations (4.15) and (4.16). Colour coding and markers style are the same of figure 4.9.

Results from the performed compression calibration routines are plotted in figure 4.14a for each material tested. The initial value for the plastic spring stiffness is set to $\hat{k_p^0}$ and the calibration routine ran. Both calibration errors $\varepsilon(\hat{k_p})$ and $\iota(\hat{k_p})$ computed from the 15 different stiffnesses $\hat{k_p^i}$ are obtained for each data point are plotted as error bars on top of each initial stiffness value. The mean value $\langle \hat{k_p} \rangle$ converges to a stable value where both

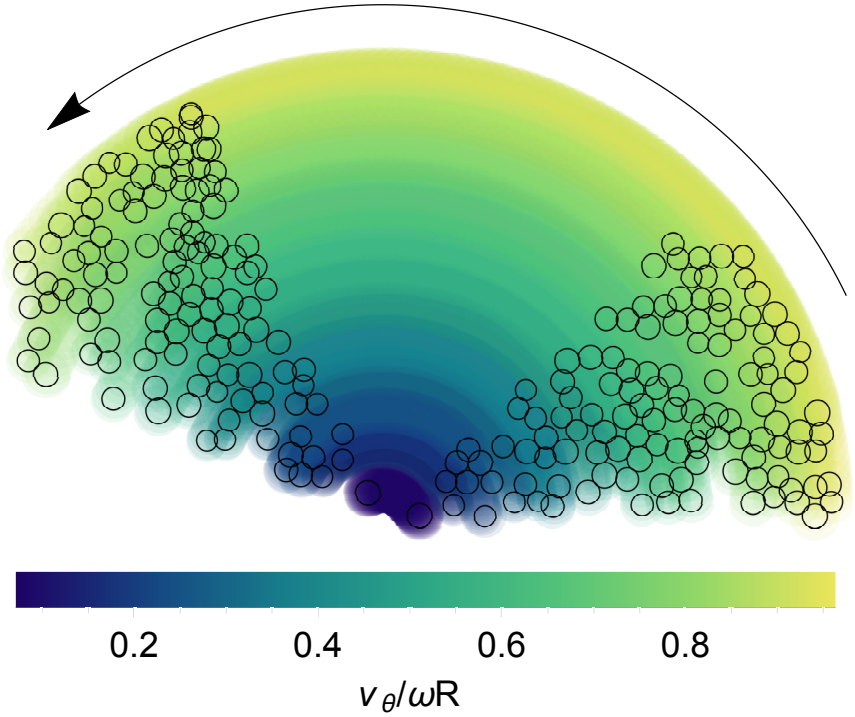

Figure 4.15: Particle tangential velocity v_θ normalised by ωR from a small sample of angular width $\pi/4$ when sheared by an angle $2\pi/3$ immediately after the rearrangement stage, during the last numerical shear test of ASA. The particle sample is generated by selecting all the ones contained in a slice $2r$ thick and them following their path for a time $t = 2\pi/3\omega$, where their projection on the rotation plane is indicated for first and last tracing time step. The shearing direction is indicated by the arrow, the colouring is given by applying a semi-transparent circular tracer of radius $2r$ over every particle at each time step, indicating their normalised tangential velocity.

$\varepsilon(\hat{k_p}) < \sigma_{\hat{k_p}}$ and $\iota(\hat{k_p}) < \sigma_{\hat{k_p}}$ for $n_I < 5$ for each material. Usually most of the displacement from $\hat{k_p^0}$ towards the final value is covered in the first calibration cycle, as can be seen by the rapid decrease of $\iota(\hat{k_p})$ (dotted error bars) in the first couple of cycle iterations. Since values of $\hat{k_p^i}$ can still differ from one another, although oscillating around the progressively more accurate estimation $\langle\hat{k_p}\rangle$, the first error measure $\varepsilon(\hat{k_p})$ (indicated by dashed error bars) usually decreases slower than $\iota(\hat{k_p})$, and is responsible for most cycle iterations. This is also why the condition $\varepsilon(\hat{k_p}) < \sigma_{\hat{k_p}} \implies \iota(\hat{k_p}) < \sigma_{\hat{k_p}}$ but not vice-versa.
The final values of the variables involved in the calibration routines, as well as the number of iterations $n_{\text{iterations}}$ needed for the algorithm to converge, are reported in table 4.5 (the plasticity depth used is calculated via equation (4.13)). In both non-cohesive materials the convergence criterion met was the most stringent $\varepsilon(\hat{k_p})$, while for the cohesive powders tested a condition $\sigma_{\hat{k_p}} = 0.05$ is too strict, and therefore, only the condition on $\iota(\hat{k_p})$ was met. Nevertheless an agreement of $\varepsilon(\hat{k_p}) < 0.10$ was obtained in both cohesive cases, even if compression of ASA led to a significant change in volume of up to 25%.

Shear test

During the shearing phase of this test we used a piston angular velocity $\omega = 10\,\omega_{\text{exp}} = \pi/60$ rad/s, a value higher than the experimental counterpart to considerably reduce the computation time. This choice does not alter the outcome of the test since the inertial number $\mathcal{I}$ is anyway small enough to ensure a quasi-static flow [36, 72] (for the parameters range of this study $\mathcal{I} \approx 4.0 \cdot 10^{-5}$). In addition, numerical tests were ran with smaller rotational speeds for comparison and no relevant difference was observed.
Unlike the previous, this test is pressure driven: the piston is displaced downwards until the prescribed pressure point is met, and kept constant until the desired torque is achieved. The piston is then rotated at a constant velocity ω_{exp} and the torque along its axis computed according to

$$\tau = \left(\sum_{i \in \mathcal{M}} \vec{R_i} \times \vec{F_i} \right) \cdot \hat{z} \tag{4.18}$$

where $\vec{R_i}$ is the position of the particle with respect to the piston axis. Before tuning either μ_S or $\hat{k_c}$ a particle rearrangement phase is performed, where the piston is let to rotate for a time $T = 2r/v_\theta(l)$ while keeping the pressure constant. Here $v_\theta(l) = \omega l$ is the tangential velocity of the piston at some point l along its radius. To fix the latter, we chose $l = R/\sqrt{2}$, i.e., the point on the radius that, via its circumference, divides the piston surface in a smaller circle and a concentric ring of equal surface. By doing so, after a time $T = 2\sqrt{2}/\omega\lambda$, on average at least half of the particles directly sheared by the piston were displaced by at least a distance $2r$. This measure is taken to ensure that most of the powder bed rearranged due to the piston motion before the parameters tuning is started. Despite this, for the most cohesive powder, particles still redistribute during the first stages of the calibration, as shown in figure 4.15 for ASA.
Like with compression, each experimental data point must be met during each cycle leading to multiple tunings of the same variable, but this time μ_S is calibrated only during compression while $\hat{k_c}$ only during decompression. It is important to tune the former separately since they both proportionally contribute to τ. In addition, since two variables are responsible for the calibration, the range of values they can assume each cycle must be restricted around their initial value, to prevent them for diverging. For instance, let's assume that μ_S was temporarily set to 0 during the ongoing cycle, and anyway $\tau^i > \tau^i_{\text{exp}}$. If now $\hat{k_c}$ happens to be tuned for the data point $j+1$, it can happen that, since $\mu_S = 0$, $\tau^{i+1} < \tau^{i+1}_{\text{exp}}$, so the routine will try to reach the target data point by increasing $\hat{k_c}$. In the next cycle, since $\hat{k_c}$ was increased, the torque cannot be possibly met when tuning μ_S since the stiffness was increased from the previous iteration, and so on. To avoid this artefact both μ_S and $\hat{k_c}$ are allowed to vary only up to 10% from their respective initial calibration cycle value μ_S^0 and $\hat{k_c^0}$. This strategy is not biasing the calibration scheme since on one side the intervals of allowed values follow the trend of $\langle \mu_S \rangle$ and $\langle \hat{k_c} \rangle$; on the other side it is not affecting the computation of neither ε nor ι, which are the defining quality parameters for the shear calibration.
Numerical data from the last performed shear calibration cycle are shown in figure 4.13b for each tested powder. The simulated results are in good agreement with the whole range of experiment data (indicated by solid markers) for MAN, LAC and MCC. For the most cohesive ASA, τ is overestimated during the compressive phase of the shear test, but is in

Table 4.5: Numerical results of rheology calibration routines for a chosen $k_e^{\max} = 5.0 \cdot 10^3$ N/m.

	MAN	LAC	MCC	ASA
$\langle \hat{k_p} \rangle$	$1.78 \cdot 10^{-1}$	$3.11 \cdot 10^{-1}$	$4.92 \cdot 10^{-2}$	$6.20 \cdot 10^{-3}$
ϕ	0.020	0.021	0.137	1.360
$\varepsilon_{\text{final}}(\hat{k_p})$ [%]	4.32	3.50	5.95	8.99
$\iota_{\text{final}}(\hat{k_p})$ [%]	0.86	4.80	0.01	0.03
$n_{\text{iterations}}$	3	4	2	2
Exit condition	ε	ε	ι	ι
$\langle \mu_S \rangle$	0.216	0.283	0.243	0.211
$\langle \hat{k_c} \rangle$	$1.08 \cdot 10^{-3}$	$9.46 \cdot 10^{-4}$	$9.57 \cdot 10^{-3}$	$3.13 \cdot 10^{-2}$
$\varepsilon_{\text{final}}(\mu_S)$ [%]	2.98	8.67	9.54	0.20
$\iota_{\text{final}}(\mu_S)$ [%]	3.99	4.03	2.31	0.45
$\varepsilon_{\text{final}}(\hat{k_c})$ [%]	2.53	6.12	6.98	7.97
$\iota_{\text{final}}(\hat{k_c})$ [%]	0.98	5.38	3.32	0.04
$n_{\text{iterations}}$	3	5	5	5
Exit condition	ε	n_I	n_I	n_I

good agreement along the whole second phase when P is decreased. How the calibrated averages $\langle \mu_S \rangle$ and $\langle \hat{k_c} \rangle$ evolve through different iterations of the calibration cycle is shown in figure 4.14b and 4.14c respectively. It can be noticed how the previously explained interplay between tuning of μ_S and $\hat{k_c}$ still affect the simulations in the case of low-cohesive powders, albeit in a minor part due to the variation limitation: an increase in μ_S is usually followed by a decrease in $\hat{k_c}$ and vice-versa. Calibration of MAN converges the fastest satisfying both $\varepsilon^{\text{MAN}}(\mu_S) < 0.05$ and $\varepsilon^{\text{MAN}}(\hat{k_c}) < 0.05$ after 3 iterations. The stiffer LAC shows a converging behaviour, but does not manage to successfully overcome the stringent threshold of $\sigma = 0.05$ while $n_{\text{iterations}} < 5$, and therefore, the cycle is interrupted by hitting the n_I exit condition. The slope of the calibrated averages hints at a likely convergence for $n_I > 5$. MCC showed the least accurate results, probably due to the needle shape of the real particles (see figure 4.2) that assume different packing configurations, while under shear, from spheres, and can easily suffer fracture when subjected to shear and high pressure. In this case, as well as for ASA, the exit condition met was on n_I. For the latter the condition $\varepsilon^{\text{ASA}}(\mu_S) < 0.05$ is surprisingly met after the first iteration, albeit the initial high value of $\iota^{\text{ASA}}(\mu_S)$. However, due to a constant high variability in $\langle \hat{k_c} \rangle^{\text{ASA}}$ throughout each iteration, convergence could not be met with the chosen threshold.
The final calibrated values are reported in table 4.5. The numbers show that, despite 3 powders not converging below $\sigma = 0.05$, the relative error associated to calibrated variables was never above 10%, which is a proof of the capabilities of such a calibration procedure.

4.8 Numerical validation

A numerical validation of the model constitutes the last step of this work. Instead of using a third device to compare the behaviour of calibrated powder to experiments, which would introduce additional variables to be calibrated such as the friction coefficients between

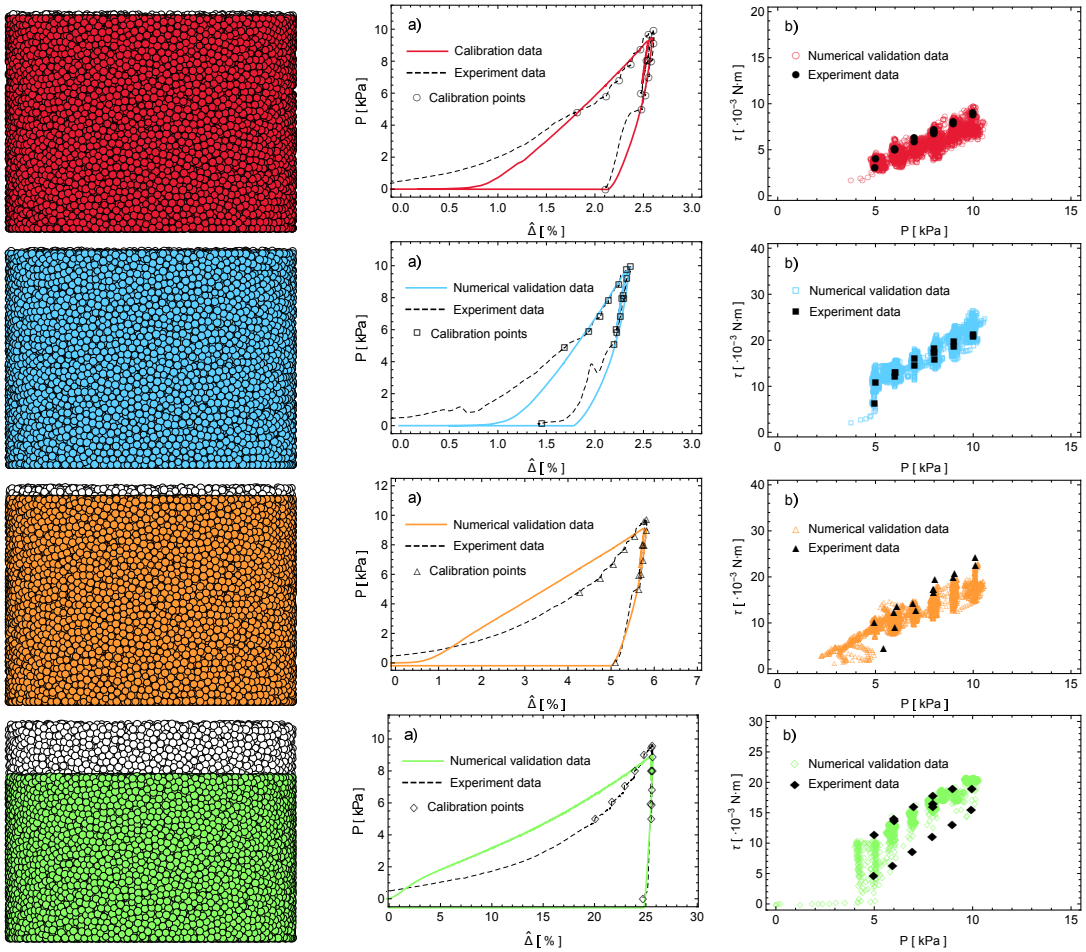

Figure 4.16: Numerical data from the validation simulations for each powder tested (from top to bottom, MAN, LAC, MCC and ASA). Colours and structure are the same of figure 4.13 and data comes from single simulation runs where material parameters (reported in table 4.5) are not tuned but are kept fixed. The former constitute the validation of this calibration framework.

powders and the device's material, we chose a faster and simpler way to test the calibration results. Such approach will also limit time and resources expenses and material waste. Since the powder rheometer tests constitute the backbone of the calibration procedure, a last simulation of both compression and shear tests is ran with the calibrated powders. This time powder properties are not dynamically adjusted to meet the required data points, but they are left with their original calibrated values of table 4.5 throughout the processes. Target piston heights are met and the pressure measured; comparing the latter to the values measured in the experiments (figure 4.9) will constitute the validation of the calibration process.

Data from the set of validation simulations is plotted in figure 4.16 on top of the experiments results. The model shows a very good prediction of both compression and shear behaviours for non-cohesive particles along the whole experiment data range. In case of cohesive

Table 4.6: Relative errors between numerical validation rheology tests of calibrated powders and experiment data.

	MAN	LAC	MCC	ASA
$\chi(P)$ [%]	8.04	3.26	8.48	12.95
$\chi_{\text{l}}(P)$ [%]	4.80	4.61	13.79	11.18
$\chi_{\text{r-u}}(P)$ [%]	10.20	2.36	4.95	14.13
$\chi(\tau)$ [%]	13.65	14.31	26.49	34.64
$\chi_{\text{l}}(\tau)$ [%]	17.38	19.66	31.93	69.30
$\chi_{\text{r-u}}(\tau)$ [%]	11.16	10.75	22.86	11.53

powders the compression simulation manages to capture very well the behaviour of real materials, especially in the reloading and unloading regions, and gives a very accurate prediction of the final plastic deformation of the powder bed. Since we are using a linear interaction model, the loading branch of the curve is naturally becoming a straight line, which might differ from the first measured points at lower compressive pressures. The same behaviour is found in the shear cell, where the rheology is better captured during the unloading and re-loading phases, especially for the most cohesive material tested. The relative error

$$\chi(x) = \frac{1}{L} \sum_{i=1}^{L} \frac{|x_i^{\text{DEM}} - x_i^{\text{exp}}|}{x_i^{\text{exp}}} \tag{4.19}$$

is used to quantify the how good pressure and torque match their counterparts in the compression and shear tests respectively, and are reported in table 4.6. Since the biggest discrepancy is found during the loading phase, the relative error evaluated only during loading $\chi_{\text{l}}(x)$ and only during reloading and unloading $\chi_{\text{r-u}}(x)$ are reported as well. As expected cohesive powders are the toughest to calibrate, and after the validation run carry the highest relative error. The validation of the compression tests shows a good agreement with the experiments since $\chi(P) < 10\%$ for each powder besides ASA, which behaviour $\chi_{\text{ASA}}(P) < 13\%$ is still in acceptable range. Shear tests show a good qualitative agreement but a worse quantitative one, and are the most affected by the discrepancy during the loading phase. The whole data range gives $\chi(\tau) < 15\%$ for non cohesive powders, which drops at $\chi_{\text{r-u}}(\tau) < 11\%$ if we remove the loading branch from the error computation. MCC is the worst behaving of the tested materials under shear, mainly due to its shape and probably due to breakage during testing (as seen by the different slopes in the shear test experiment in figure 4.9), and the relative error ranges around 26%. Finally, the most cohesive ASA powder shows a high relative error $\chi_{\text{ASA}}(\tau) < 35\%$, that is however greatly reduced below 12% when disregarding the loading branch.
The systematic discrepancy in the loading behaviour was likely introduced by the requirement to meet the correct permanent plastic deformation of the bed, which led to tuning ϕ alongside with k_p. This artefact cannot be avoided if a linear interaction model is used. A refinement of the model to address this will be the topic of future studies, but such behaviour demonstrates that using many calibration points for each test is necessary to capture the complex rheology of powder materials. For instance, simply matching the maximum compression point and the final powder bed height from a compression test will likely lead to an oversight of the initial plastic behaviour, especially for cohesive materials.

Moreover effect due to particle shape and electrostatic forces, altering the packing configuration of the powders and its response to compression and shear, are also very likely to affect the tests during the loading stages. These aspects cannot be neglected if a more faithful representation of the experiment has to be achieved.

4.9 Conclusions

A new, robust, rational and fully-automatised method for the calibration of DEM parameters for modelling cohesive powders is developed and presented. These parameters are calibrated by performing numerical models of routine small-scale laboratory experiments, such as angle of repose, compressibility and shear tests, that must replicate the outcome of their real counterparts, and are specifically designed to capture the complex hysteretic behaviour of granular materials.
To be considered successful each calibration routine must converge towards each of the 15 data points selected from each rheology tests. For testing and validating this new approach four powders of pharmaceutical relevance are used for the laboratory tests, ranging from free-flowing to highly cohesive.
Certain parameters, such as particle average size and plasticity, rather than being calibrated, are selected according to physical arguments, and are intimately connected to calibrated variables and the geometry of the testing devices. Others, such as maximum elastic stiffness and restitution coefficient, are chosen a priori to limit the computational cost of the procedure, but in a range of values physically meaningful. The four parameters directly calibrated, sliding and rolling friction and plastic and cohesive stiffness, are then related to their relative impact on the calibration tests, leading to a precise order according to which the simulations of the latter have to be performed.
The automatic calibration routine then intends to iteratively converge to a solution within a chosen maximum number of iterations, with two possible positive outcomes: either all the selected quality attributes, such as the absolute mean deviation of calibrated parameters, are below the user-defined acceptance threshold, or the former still stabilise to a constant value, albeit outside the desired boundaries. This second mode enables the algorithm to continue with the subsequent tests in case the variables are distributed around a stable mean value, which can be important, since the desired precision might sometimes be too high to be achieved. The routine ends successfully when every numerical test converged, and then returns the calibrated values found with the associated statistical deviations. In case convergence is not met within the allowed numbers of iterations, the last calibrated value is chosen and the procedure goes on until all parameters are calibrated.
In our study we managed to successfully calibrate all four materials tested, including the highly cohesive powder exhibiting a compressibility of up to 25%, which is at the boundary of the validity of DEM modelling capabilities. Despite certain tests not converging within the chosen numbers of iterations, every calibrated variable at the end of the cycles had an associated relative error below 10%, proving the potential of this framework. Our new approach is more physically sound when compared to a traditional parameter space partition type of calibration, and calibrated parameters are univocally determined (no multiplicity in the solution that can instead occur in the latter). On top of this, our method converges faster, making it an ideal candidate to become a standard procedure for bulk calibration

approaches in this field of study.
An additional validation of this approach will constitute the next step of our study: the behaviour of a DEM model of a manufacturing process will be compared with the experiment, after the powder has been calibrated with this framework. The extension of this calibration technique to the calibration of blends, including mixtures with different average particle size, will be the topic of upcoming studies. Inclusion of non-spherical particles to the model is also planned.

Acknowledgements

The authors would like to thank M. Piller and S. Fathollahi for performing the experiments needed to validate our calibration framework. The Research Center Pharmaceutical Engineering is funded by the Austrian COMET program under the auspices of the Austrian Federal Ministry of Transport, Innovation and Technology (bmvit), the Austrian Federal Ministry of Economy, Family and Youth (bmwfj) and by the State of Styria (Styrian Funding Agency SFG). COMET is managed by the Austrian Research Promotion Agency FFG.

Chapter 5

Deformable and breakable DEM particle clusters for modelling compression of plastic and brittle porous materials — model and structure properties

Abstract[1]

A new framework for DEM modelling of deformable and breakable particles is presented. In our approach, real-life particles are modelled as agglomerates (or clusters) of many DEM particles forming spherical clumps and interacting via a linear elasto-plastic force. Such interaction provides a finite equilibrium overlap, resulting in mechanically stable clusters after agglomeration. Since inter-particles bonds are elastic, clusters can be used to model particles or structures that can deform elastically, plastically or break. Different clusters can bond as well, providing the basis for modelling complex particle agglomeration. The framework is described, and key structural properties of clusters are defined and analytically related to DEM components packing and their material properties. These relations are numerically validated showing a very good agreement, enabling clusters to be designed with a precise structure. Applications of this model range from particle deformation and breakage to porous structures, from soil mechanics to die compaction and tableting.

[1]With minor corrections from: L. Orefice, J. G. Khinast, Powder Technology, in press.

5.1 Introduction

Many physical systems are comprised of granular materials. Upon compression, materials deform either elastically, plastically or via brittle fracture, i.e., breakage. For example, during pharmaceutical manufacturing [3,105,115,131] or in the study of soil mechanics [50,163], the behaviour of individual particles has significant impact on the final product or the mechanical responses of the macroscopic system [59]. In many cases the ability to deform before breaking constitutes the main factor leading to final product quality [105, 131, 138]. For instance, during die compaction of pharmaceutical powders or granules, the individual components deform plastically to occupy the neighbouring interstices left in the bulk, before potentially fracturing, and eventually forming a bond with neighbouring particles. Both deformation and breakage are thus equally important when modelling such systems, and neither should be neglected.
The numerical techniques mainly used for modelling deforming bodies, such as Finite Elements Method, are unable to model their breakage without relying on complex couplings with other numerical techniques. Thus the computational expense of modelling a large collection of bodies is unfeasible. To address these limitations the deformable and breakable particles are here modelled as composite entities comprising many cohering elementary components. These composite particles, interchangeably labelled here as *clusters* or *agglomerates*, can be used to model grains with either a simple or a compound structure, such as a sand pebble or a pharmaceutical granule, respectively. The constitutive smaller elements, modelled via Discrete Elements Method (DEM), will be the fundamental independent, spherical "bricks" these bodies are composed of, their interaction determining hardness and plasticity of the clusters.
Modelling of composite particles undergoing impact or uniaxial compression breakage is a relevant approach in the literature, among which DEM has an important role especially in the latest years [6, 16, 17, 29, 35, 42, 49, 69, 79, 88, 91, 96, 122, 134, 141, 143, 148, 155, 174]. The ability to access dynamic variables and stress configuration of every particle constituting each cluster is a key factor in understanding their deformation and breakage behaviour. The discrete nature of these agglomerates gives DEM an advantage on finite methods in studying brittle breakage, since crack propagation and fragment distributions derive naturally from particle and material properties and their configuration [17, 29, 35, 49, 79, 88, 96, 134, 141, 148, 174]. For these reasons DEM simulations have been broadly used to study breakage problems in the past.
Given the flexibility of DEM, many properties of the original (composite) particles can be designed, such as shape and size distributions of the components [29, 69, 134, 143, 155, 174]. These have been shown to play a fundamental role in describing the breakage dynamics, but inevitably introduce additional complexity to the model. For instance, the effect of multi-modal elementary particle size distribution on breakage patterns is non-trivial and adds an additional complication since the spatial arrangement of the biggest particles within the agglomerates will affect the fracture as well [69, 134, 155]. The same goes for the clusters shape. Clearly high aspect ratios or fractal configurations are altering hardness and breakage patterns, but precise descriptors of these quantities must be defined and controlled, and the decreasing symmetry makes the problem dependent on the clusters orientation [29, 143, 174].
One of the main problems faced by every DEM model is validation, where the numerical

model is tested and compared to experiments. Validation of models is becoming easier thanks to the progressive refinement and diffusion of 3D printing technology in recent years, greatly simplifying some formerly used techniques of agglomerate manufacturing for strength testing [135,136]. Clusters with regular [37] and random [39] structures can be 3D printed and used in breakage experiments to gather stress-strain and damage ratio data from both compression and impact tests. These valuable data can be used to calibrate DEM models from the single bond up to the whole cluster meso-scale [38, 40].
The model we present is intended to bridge a gap between simplicity and broad physical behaviour of compressed particulate matter. The fundamental element of the model consists of spherical clusters comprised of monodispersed elementary DEM particles interacting with one another via a linear piecewise elasto-plastic harmonic force. Since the bonds between components are soft, the agglomerates can deform, yet maintain their mechanical stability, before eventually breaking if forces separate their components beyond the breaking point. Partial elastic recovery is also a response of the model thanks to the elastic bounds. The force is stable and attractive for finite overlaps. Therefore, the structure of clusters is naturally porous and the latter can be tuned by properly setting the interaction parameters. A final property is that particle cohesion acts both inter- and intra-clusters, and will be a built-in feature of the model allowing applications of the former to numerical study dry agglomeration and compaction.
In summary, with the approach used we can represent a real-life particle (crystal, agglomerate, pellet, granule) via a cluster (consisting of many DEM particles). The properties of the real-life particle can be emulated by changing the cluster properties (e.g., solid, low-porosity particles or porous granules achieved via fluid-bed granulation). Many such clusters with different size and shape can be considered, and thus, the physics of multiple real-life particles during compaction can be modelled.
Part of this work is devoted to a precise definition and analysis of structural properties of the clusters generated, such as size, mass fraction and density. Tools to numerically measure these mesoscopic properties and the inner components homogeneity and isotropicity are provided as well. Moreover, since the force law used allows the prediction of the final average overlap between particles composing each cluster, cluster size and mass fraction are analytically related to DEM particle properties in a very simple way. This allows the creation of clusters each with a precisely defined structure to properly mimic real-life particle ensembles of arbitrary size distribution and internal void fraction.
The structure of this article is the following. After a brief description of the interaction model used, the final average elementary particle overlap within clusters is computed from the force law. The Clusters' structural parameters are then defined with respect to primary particles properties, details on their formation are provided, and their homogeneity is tested alongside isotropicity. A theoretical part is then following where cluster size and mass fraction are analytically related to number of DEM particles per cluster and their plasticity. These relations are then tested in two different ways by modelling clusters with a broad variety of size and porosity. Finally, future development stages of the model are enumerated, and two examples of future studies adopting this cluster model are provided.
The goal of the present work is to provide the first steps in the development of a plastic and brittle DEM-particle compound model of varying porosity, capable of both deforming and breaking under stress, and agglomerating with others to form stable connected bodies. Thus, compaction of both, plastic and brittle, materials can be studied using a novel

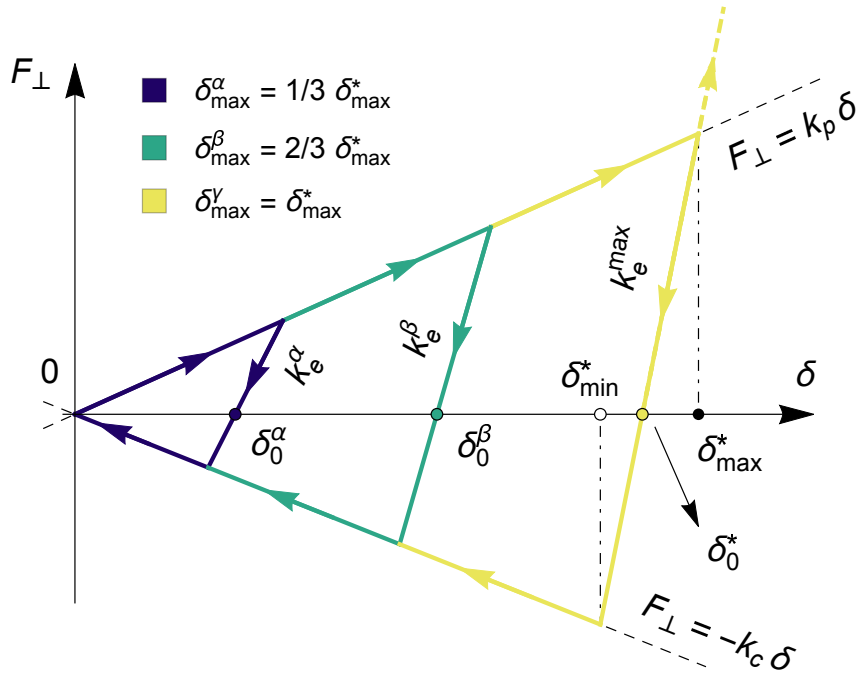

Figure 5.1: Schematic plot of the normal hysteretic force $F_\perp$ as a function of the overlap δ for two colliding particles. Colours indicate the dynamics of particles with increasing maximum overlaps $\delta_{\max}$, leading to proportionally higher elastic stiffnesses k_e and larger equilibrium overlaps δ_0.

approach.

5.2 Elasto-plastic interaction law

Since DEM modelling is widespread in the literature, and in use by the scientific community since years [23], the details on how the technique works are omitted for the sake of brevity. The interaction law used in our model is a linear spring-dashpot model [84], with a linearised piecewise function to determine the normal interaction force [83, 84], which we will briefly introduce. Employing a piecewise function for the normal force to mimic inter-particle cohesion is no novelty [146, 147], and we opted for a linear model to simplify the theoretical formulation of the study. Some objections regarding the asymptotic response of the model have been raised [142], but its simplicity and its valuable predictive capacity [58] justify the choice of the interaction law. In principle, any cohesive interaction model can be used with this framework with the proper adjustments of the algebra. The DEM material parameters used for primary particles and the force integration time step used in the simulations are reported in table 5.1. To perform the simulations used in this study the open-source DEM code MercuryDPM [2, 157] was used.
The piecewise structure of the normal force $F_\perp$ allows to model different behaviours of the particles when colliding, as depicted in figure 5.1. At the moment of contact, two particles have a negative relative velocity, and the overlap between the former (since DEM is a soft-sphere model) increases in time. In this regime the normal force is repulsive and

proportional to the overlap δ, with a proportionality constant k_p defined as plastic stiffness. This harmonic interaction implies that at some point the relative velocity will decrease to zero and become positive, indicating that the distance between the colliding particles is now increasing with time, the maximum penetration depth met by the particles being defined as $\delta_{\max}$. At this stage of the collision, the interaction law switches to its second branch where the elastic spring constant is now the elastic stiffness k_e. Following figure 5.1, the k_e branch will intersect the $F_\perp = 0$ axis at an overlap δ_0, and decreasing the overlap below this value will result in an attractive (negative) normal force. This behaviour is analogous to a plastic contact deformation, where the particles irreversibly deform and stick to one another forming a stable bond, the equilibrium point depending on the history parameter $\delta_{\max}$. Upon further increase of distance the force becomes attractive with a constant slope until a minimum overlap $\delta_{\min}$ is reached. If that is the case the interaction switches to its third and final branch, where the attractive spring stiffness drops to k_c, defined as cohesive stiffness. Multiple reloading instances can happen during a single collision, each one of these characterised by a reloading stiffness k_e. The three branches of the normal force are chosen at any point during the collision according to

$$F_\perp = \begin{cases} k_p\,\delta & \text{if } k_e\left(\delta-\delta_0\right) \geq k_p\,\delta \\ k_e\left(\delta-\delta_0\right) & \text{if } k_p\,\delta > k_e\left(\delta-\delta_0\right) > -k_c\,\delta \\ -k_c\,\delta & \text{if } -k_c\,\delta \geq k_e\left(\delta-\delta_0\right) \end{cases} \tag{5.1}$$

where consistency requires $k_p < k_e$. For the reader's convenience we point out that our notation differs from the original one in [83] to allow a more intuitive interpretation of each spring stiffness role in the interaction. The analytical value of the equilibrium overlap δ_0 will be of particular importance in this study, given by

$$\delta_0 = \left(1 - k_p/k_e\right)\delta_{\max}. \tag{5.2}$$

Real particles undergoing plastic deformations have a more complicated behaviour, becoming stiffer the more they are compressed, and reaching the plastic equilibrium at proportionally smaller overlaps δ_0. The model can be refined by introducing a maximum penetration depth $\delta^*_{\max}$ below which the elastic stiffness is interpolated between k_p and a maximum elastic stiffness $k_e^{\max}$ as

$$k_e\big(\delta_{\max}\big) = \begin{cases} k_p + \left(k_e^{\max} - k_p\right)\frac{\delta_{\max}}{\delta^*_{\max}} & \delta_{\max} < \delta^*_{\max} \\ k_e^{\max} & \delta_{\max} \geq \delta^*_{\max}. \end{cases} \tag{5.3}$$

Figure 5.1 illustrates the force behaviour for 3 increasing maximum overlaps $\delta^\alpha_{\max} < \delta^\beta_{\max} < \delta^\gamma_{\max} = \delta^*_{\max}$ depicted with different colours. According to equation 5.3, the elastic stiffnesses will be proportionally higher, and respectively $k_e^\alpha < k_e^\beta < k_e^\gamma = k_e^{\max}$, leading through equation 5.2 to the increasing equilibrium overlaps $\delta_0^\alpha < \delta_0^\beta < \delta_0^\gamma = \delta_0^*$ respectively. In our notation we mark with $*$ values of the overlaps such that $\delta_{\max} > \delta^*_{\max}$, i.e., collisions that will experience elastic repulsion proportional to $k_e^{\max}$.
The penetration threshold $\delta^*_{\max}$ is defined as a function of spring stiffness and reduced radius of the colliding particles, and proportional to a constitutive model parameter ϕ defined as dimensionless plasticity depth, according to the following relation:

$$\delta^*_{\max}(\phi) = \frac{k_e^{\max}}{k_e^{\max} - k_p}\,\phi\,\frac{2r_i r_j}{r_i + r_j}. \tag{5.4}$$

Table 5.1: DEM parameters used for the model.

Density [kg/m^3]	1500
Restitution coefficient $[\cdot]$	0.5
Dissipation coefficient [Ns/m]	$6.0 \cdot 10^{-3}$
Plastic stiffness [N/m]	500
Maximum elastic stiffness [N/m]	1000
Cohesion stiffness [N/m]	500
Sliding friction coefficient $[\cdot]$	0.5
Rolling friction coefficient $[\cdot]$	0.3
Torsion friction coefficient $[\cdot]$	0.0
Time step [s]	$1.0 \cdot 10^{-6}$

In the former r_i and r_j are the radii of the two colliding particles. The plasticity depth determines at what relative overlap the interaction between colliding particles transitions from plastic to elastic, and ranges between 0 and 1.
From this point onwards we will be working with dimensionless units for the sake of convenience: spring constants will be rescaled as $\hat{k} = k/k_e^{\max}$ and lengths will be rescaled as $\hat{L} = L/r$, where r is the average particle radius.

5.3 The equilibrium overlap

The main relations of the previous section will be now expressed in dimensionless form as a function of $\hat{\delta}_0$. This last quantity is key in our framework, since we want to study the properties of stable clusters after agglomeration, i.e., when the average overlap between particles forming the clusters will satisfy $\langle\hat{\delta}\rangle \to \hat{\delta}_0$. We also consider the primary particles to be mono-disperse with radius r.
Under these assumptions equation (5.4) becomes

$$\hat{\delta}^*_{\max} = \phi/\big(1 - \hat{k}_p\big). \tag{5.5}$$

This is the threshold deformation above which every overlap increment leads to a perfectly elastic response, and therefore have no effect on the final equilibrium deformation. Inserting the latter and equation(5.3) into (5.2) allows us to express the value of $\hat{\delta}_0$ as a function of primary particles properties $\hat{k}_p$ and ϕ:

$$\hat{\delta}_0 = \begin{cases} \dfrac{\big(1-\hat{k}_p\big)^2\,\hat{\delta}^2_{\max}}{\hat{k}_p\phi + \big(1-\hat{k}_p\big)^2\,\hat{\delta}_{\max}} & \hat{\delta}_{\max} < \dfrac{\phi}{1-\hat{k}_p} \\ \phi & \hat{\delta}_{\max} \geq \dfrac{\phi}{1-\hat{k}_p}. \end{cases} \tag{5.6}$$

This relation is plotted as a function of ϕ and $\hat{\delta}_{\max}$ for three different values of $\hat{k}_p$ in figure 5.2, where the variables domain is limited to the physically meaningful values $\phi \in [0;1]$ and $\hat{\delta}_{\max} \in [0;1]$.
A couple of considerations arise from equation (5.6). First of all equation (5.5) defines a critical overlap value above which $\hat{\delta}_0 = \hat{\delta}^*_0 = \phi$. Second a certain final overlap $\hat{\delta}_0$ can be

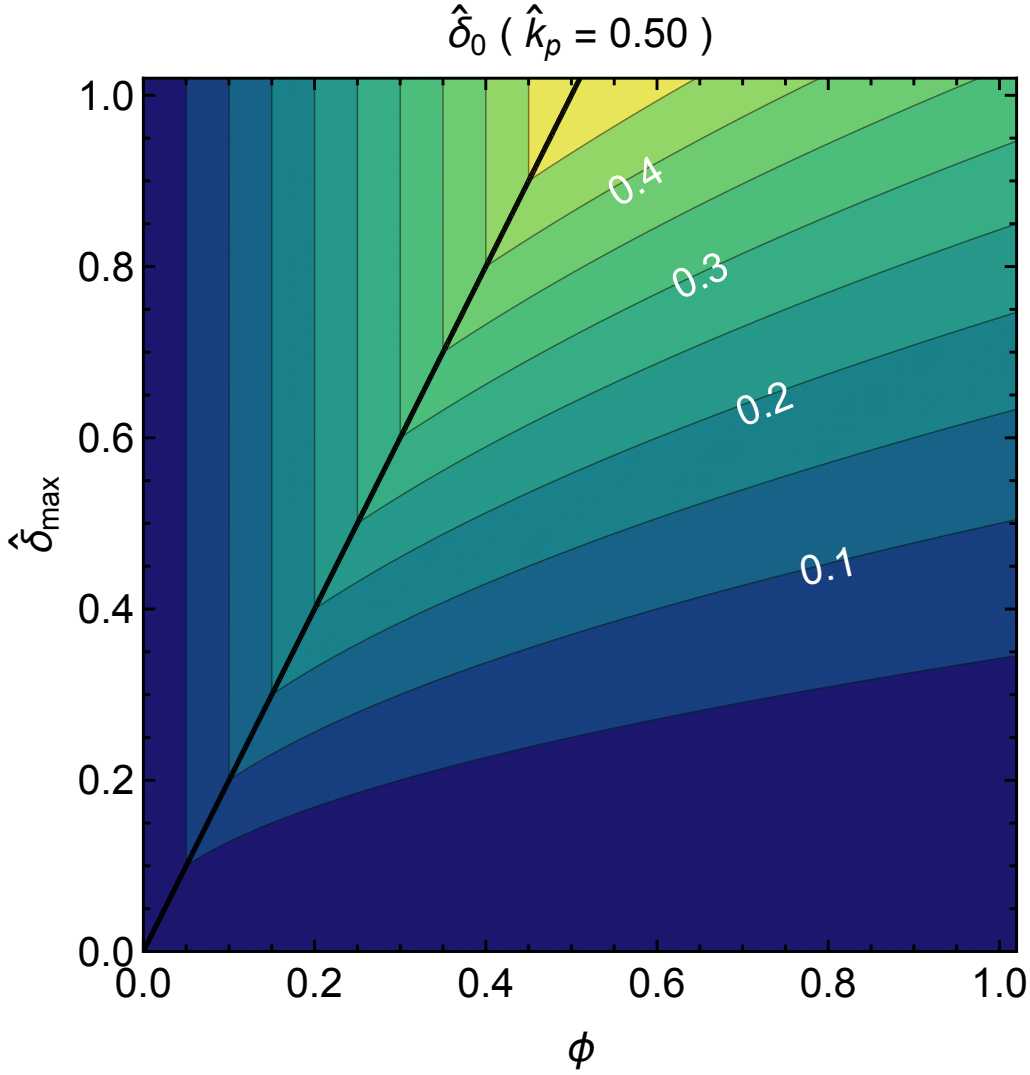

Figure 5.2: Contour plots of final theoretical value of equilibrium particle deformation $\hat{\delta}_0$ (contour values indicated in white on the plots) as a function of ϕ and $\hat{\delta}_{\max}$ for $\hat{k}_p = 0.50$. The diagonal thick line is the critical maximum overlap $\hat{\delta}^*_{\max}$ of equation (5.5): below $\hat{\delta}_0$ is given by the first case of equation (5.6), above by the second.

reached for different values of ϕ, although a higher plasticity will require a higher maximum overlap to be reached during the cluster formation. Finally, the equilibrium overlap only depends on the ratio $\hat{k}_p$ between plastic and maximum elastic particle stiffness, both being model parameters inputs.

These considerations have some practical implications in clusters formation. First of all, the compressive force magnitude needed during the agglomeration to achieve a certain $\hat{\delta}$ does not need to be known a priori. This because equation (5.5) gives us the necessary threshold we need to meet, and all that is needed is to monitor $\langle\hat{\delta}\rangle$ and ensure that it reaches its target value by increasing the compressive force as needed. Secondly, since ϕ is the maximum achievable final overlap, it is convenient to choose both the former and

$\hat{k}_p$ such to minimise the $\langle\hat{\delta}_{\max}\rangle$ needed whenever possible, ensuring numerical stability and reducing computational costs. Lastly, since $\hat{\delta}_0$ depends on the ratio $k_p/k_e^{\max}$, and not simply on k_p, a value of the former suitable for any desired cluster radius can always be found. For instance, since k_p has to be univocally defined to replicate macroscopic cluster properties, such as hardness, $k_e^{\max}$ can be chosen arbitrarily to meet the requirement (5.5) only affecting the computational costs.

5.4 Cluster definition and structural properties

A spherical cluster $\mathcal{C}_N$ is defined as a set of N smaller primary components P_i

$$\mathcal{C}_N = \mathcal{C}_N\left(\vec{o}; R\right) = \bigcup_{i=1}^{N} P_i\big(\vec{o}_i; r\big) \tag{5.7}$$

arranged in a spherical configuration, the latter being bounded together by the attractive branch of the inter-particle interaction force (5.1). Each component i is a common DEM spherical particle of radius r that can follow a certain distribution of choice. For this study we will employ monodisperse particles to simplify the theoretical modelling effort. The use of polydisperse or multi-modal particle size distributions would definitely change structural properties of the agglomerates [88, 134, 155]; the latter most certainly deviating from the theory developed here. The position of each particle is indicated by $\vec{o}_i$, while the cluster centre is found by computing the centre of mass of the particles ensemble

$$\vec{o} = \frac{\sum_{i=1}^{N} m_i\vec{o}_i}{\sum_{i=1}^{N} m_i} = \frac{\sum_{i=1}^{N} \vec{o}_i}{N} \tag{5.8}$$

where $m_i = \frac{4}{3}\pi\, r_i^3\, \rho_i$ is the mass of particle i and ρ_i its density. The second equality follows by assuming constant radius r and density ρ for each particle.
Like in reality, an accurate definition of the cluster size is non trivial [11], especially since the topology of its surface is, by nature, highly irregular. To define the cluster radius R we start by finding the furthest primary particle from $\vec{o}$ and computing its distance $d_{\max} = \max\big(\|\vec{o}_i - \vec{o}\|\big)$ from the latter. This quantity is used to define the subset $M = \big\{P_i\big(\vec{o}_i; r\big)\,\big|\, d_i \geq d_{\max} - r\big\}$ of particles belonging to the cluster external shell such that their distance $d_i = \|\vec{o}_i - \vec{o}\|$ from the centre of mass is larger than $d_{\max} - r$. Now R is defined to be the average distance of the former from the centre of mass:

$$R = \frac{\sum_{i=1}^{M} \|\vec{o}_i - \vec{o}\|}{M}. \tag{5.9}$$

A slice of a cluster $\mathcal{C}_{500}$ passing through its centre is shown at the top of figure 5.3. Primary particles sections are depicted in light green while R is indicated by the thick circle enclosing the former, and is computed according to equation (5.9). The volume enclosed inside this spherical shell and not occupied by particles constitutes the void fraction $\nu = 1 - \zeta$ of the cluster, and is shown in light blue.
It was established [6,17,69,88,91,112,134,155] that the compound internal structure is a key aspect to consider when numerically modelling particle breakage via DEM. In particular, particle porosity is inversely proportional to its structural strength. Since the ability to

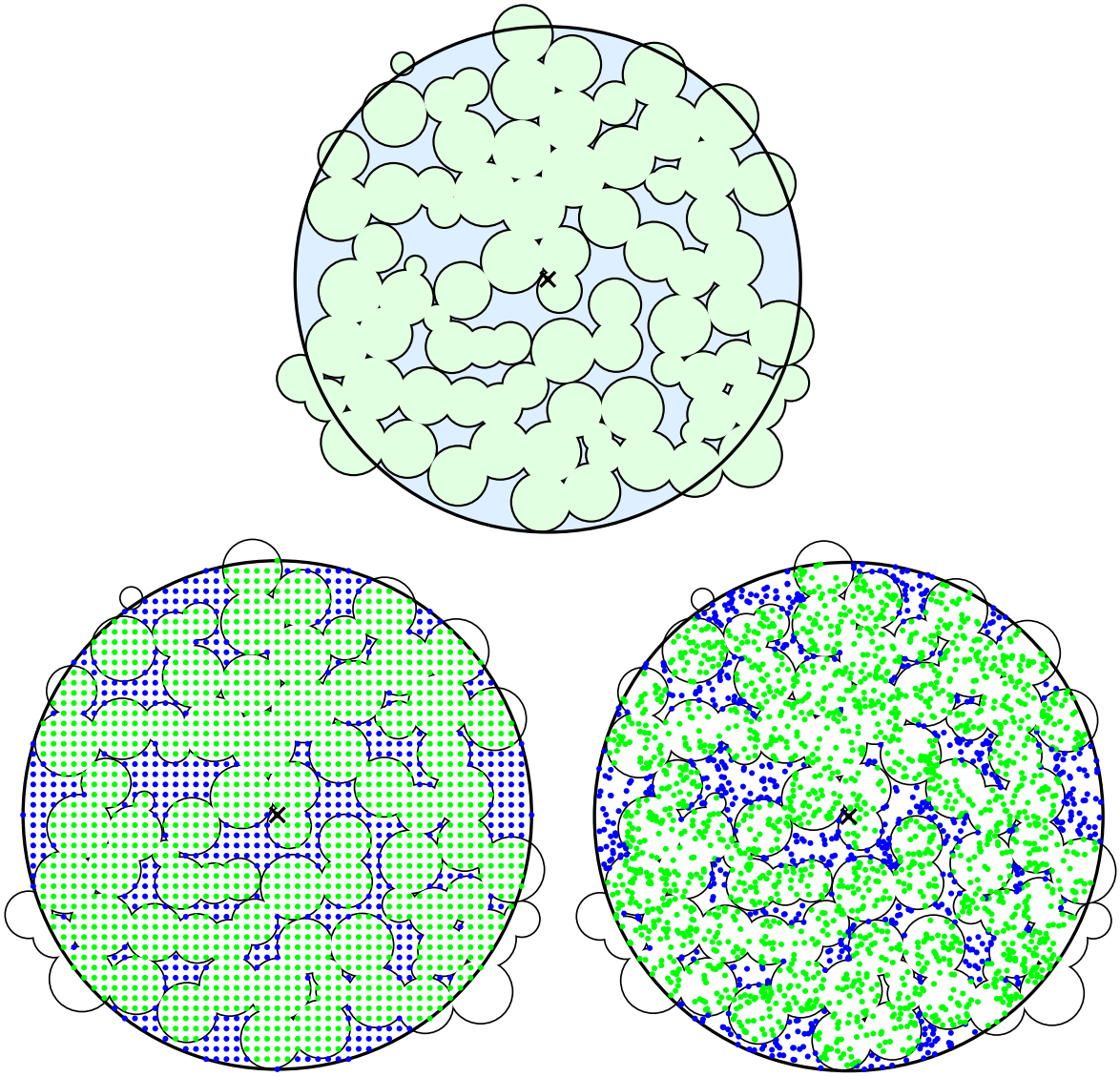

Figure 5.3: Cross-section of a cluster $\mathcal{C}_{500}$ through $\vec{o}$ (indicated by the cross), the thick solid circle representing the cluster radius R. Top: cross-sections of the particles is coloured in light green, while the empty space enclosed in the clusters is in light blue, the latter contributing to the cluster void fraction ν. Bottom left: cluster volume analysis via lattice grid points; points inside cluster volume coloured as above. Bottom right: volume analysis with random Monte Carlo points generated inside the cluster boundary, colours as above.

create a defined internal structure is a key feature of the cluster model, a consistent and precise way to determine the mass fraction ζ must be established. For an ensemble of hard spheres the latter can be easily computed by taking the ratio between particles and cluster volumes. However, the error associated to such measures of ζ increases with the overlap between particles, and since our model consists of soft spheres with appreciably high overlap we must rely on different means for computing the void fraction. Using an analytical method to calculate the mass fraction based on computing the overlapping volume of each spheres cannot be applied if three of the former share some of this volume, and therefore we will rely on statistical numerical methods. In our approach we tested and used two methods, i.e., a grid method and a Monte Carlo approach.

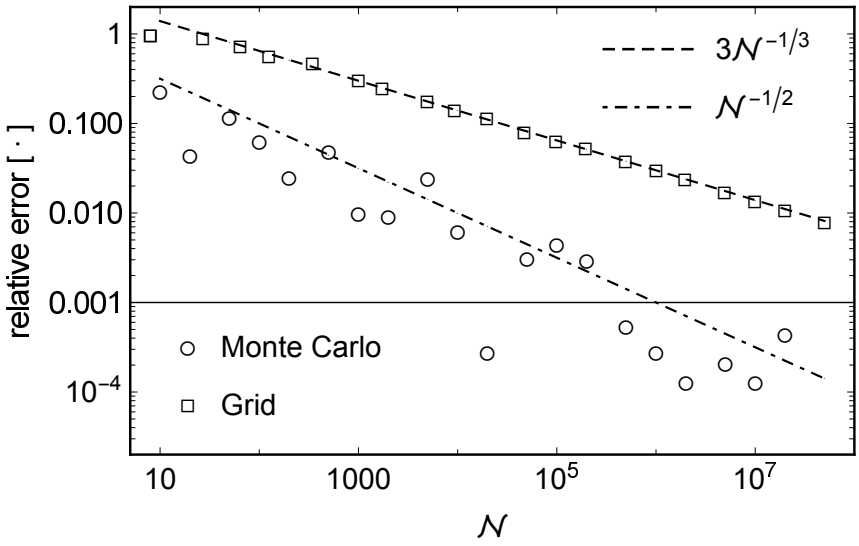

Figure 5.4: Relative error of numerically computed volume ratio from the analytical value of $\pi/6$ for both grid and Monte Carlo approaches. The latter scales significantly better than the former following a $1/\sqrt{\mathcal{N}}$ power law.

The grid method consists in generating a 3D grid of points arranged in a regular cubic lattice of side length $2R$ centred around $\vec{o}$. The number of grid points $\mathcal{N}_{\text{grid}}$ is determined by the grid length $L = (\mathcal{N}_{\text{grid}})^{1/3}$, which in turn gives the grid spatial resolution $\lambda = (L-1)/2R$. If we define the number of grid points contained in the cluster volume as $\mathcal{N}^{\mathcal{C}}_{\text{grid}}$ and, among those, the ones falling inside of at least one of the primary components particles $\mathcal{N}^{\cup P}_{\text{grid}}$, it is obvious that $\mathcal{N}_{\text{grid}} \subset \mathcal{N}^{\mathcal{C}}_{\text{grid}} \subseteq \mathcal{N}^{\cup P}_{\text{grid}}$, and the mass fraction can simply be expressed in this way by $\zeta_{\text{grid}} = \mathcal{N}^{\cup P}_{\text{grid}}/\mathcal{N}^{\mathcal{C}}_{\text{grid}}$. An illustrative example is given in the centre of figure 5.3 where a square grid of $L = 50$ is superimposed to the cluster cross-section. Grid points laying outside of the cluster boundary are not shown, while those belonging to $\mathcal{N}^{\cup P}_{\text{grid}}$ are coloured in green and those not contributing to ζ_{grid} in blue.
The Monte Carlo approach works in a similar fashion: a number of random points $\mathcal{N}_{\text{MC}}$ are chosen inside the cluster volume, and if they are within at least one of the primary components particles they will sum up to $\mathcal{N}^{\cup P}_{\text{MC}}$. The mass fraction computed with this approach is then $\zeta_{\text{MC}} = \mathcal{N}^{\cup P}_{\text{MC}}/\mathcal{N}_{\text{MC}}$. A number $\mathcal{N}_{\text{MC}} = 50^2$ of randomly generated points on the planar cut of the cluster are shown at the bottom of figure 5.3, the colouring

following the same rule as in the previous example. To be noted that in both examples the same number of points are generated $\mathcal{N}_{\text{grid}} = \mathcal{N}_{\text{MC}}$.
Obviously both $\mathcal{N}_{\text{grid}}$ and $\mathcal{N}_{\text{MC}}$ are instrumental in determining how good the estimation of ζ will be for each respective method. To evaluate their computational efficiency both methods are used to compute the volume ratio between a cube of unitary length and its inscribed sphere. The volume ratio between the two is given analytically by $\frac{4}{3}\pi\left(\frac{\ell}{2}\right)^3/\ell^3 = \pi/6$, and the relative error in the numerical computation estimated from the former as $\mathcal{N}$ grows is shown in figure 5.4. Since we are studying a 3-dimensional system the Monte Carlo method performs better since the method is inherently dimensionality-free, with its error scaling as $\mathcal{N}^{-1/2}$ following the central limit theorem, falling below a relative error of 0.1% at $\mathcal{N}_{\text{MC}} > 10^6$. The grid method proves to be less efficient since it scales linearly in every dimension, meaning that in 3D its error will scale like $\mathcal{N}^{-1/3}$, and we managed to fall below 1% only around $\mathcal{N}_{\text{grid}} \approx 2.7 \cdot 10^7$. Thus, analysing the clusters internal structure via random Monte Carlo points has proven to be more efficient. However, according to the application a regular distribution of grid points might be desirable as well, for instance when the topology of the clusters pores is needed. Since this paper will focus on average structure properties we will use the Monte Carlo approach to compute the mass fraction, that will be given by

$$\zeta = \frac{\mathcal{N}_{\text{MC}}^{\cup P}}{\mathcal{N}_{\text{MC}}}. \tag{5.10}$$

where we will use $\mathcal{N}_{\text{MC}} = 10^6$. However, when plotting the clusters internal structure (see figure 5.5 we will rely on the grid technique with a grid length $L = 300$.
Finally, the expression of the cluster radius, given by equation (5.9), will allow us to correctly set the density ρ_P of the cluster's components to meet a target cluster density ρ. To replicate the behaviour of an actual object its inertia must be matched in the model. Let ρ_{true} be the true density of the object, m_{true} its mass and V_{true} its volume. Imposing R to coincide with the radius of the object R_{true}, the real and modelled clusters will have the same mass if $m_{\mathcal{C}} = \rho_{\text{true}} V = N \rho_P V_P$. Simplifying and re-arranging, the value of the components is easily found to be

$$\rho_P = \rho_{\text{true}} \frac{\hat{R}^3}{N}. \tag{5.11}$$

This value for the components density, based on the real mass of the object, is unaffected by their overlap, which is a necessary feature of the model. Because of the random yet homogeneous spatial distribution of the components inside the cluster, the moment of inertia of the latter can be considered to match the one of a constant density sphere. These parameters, alongside with properties determining dynamics and breakage patterns presented in a follow-up to this article, allow the model of agglomerates of arbitrary scale. A softer and highly porous cluster can be used to mimic the behaviour of pharmaceutical granules or pellets, while tighter and harder agglomerates can be used to replicate single real particles or rocks.
Three clusters $\mathcal{C}_{500}$ and different plasticity depths are depicted in figure 5.5. The initial particle position before their formation (explained in the next section) is the same for each set of particles, as well as every other DEM particle parameter with the only exception of ϕ. It is recognisable that there is a different final inter-particle overlap after the agglomeration process, due to different ϕ leading to different equilibrium overlaps δ_0. A higher

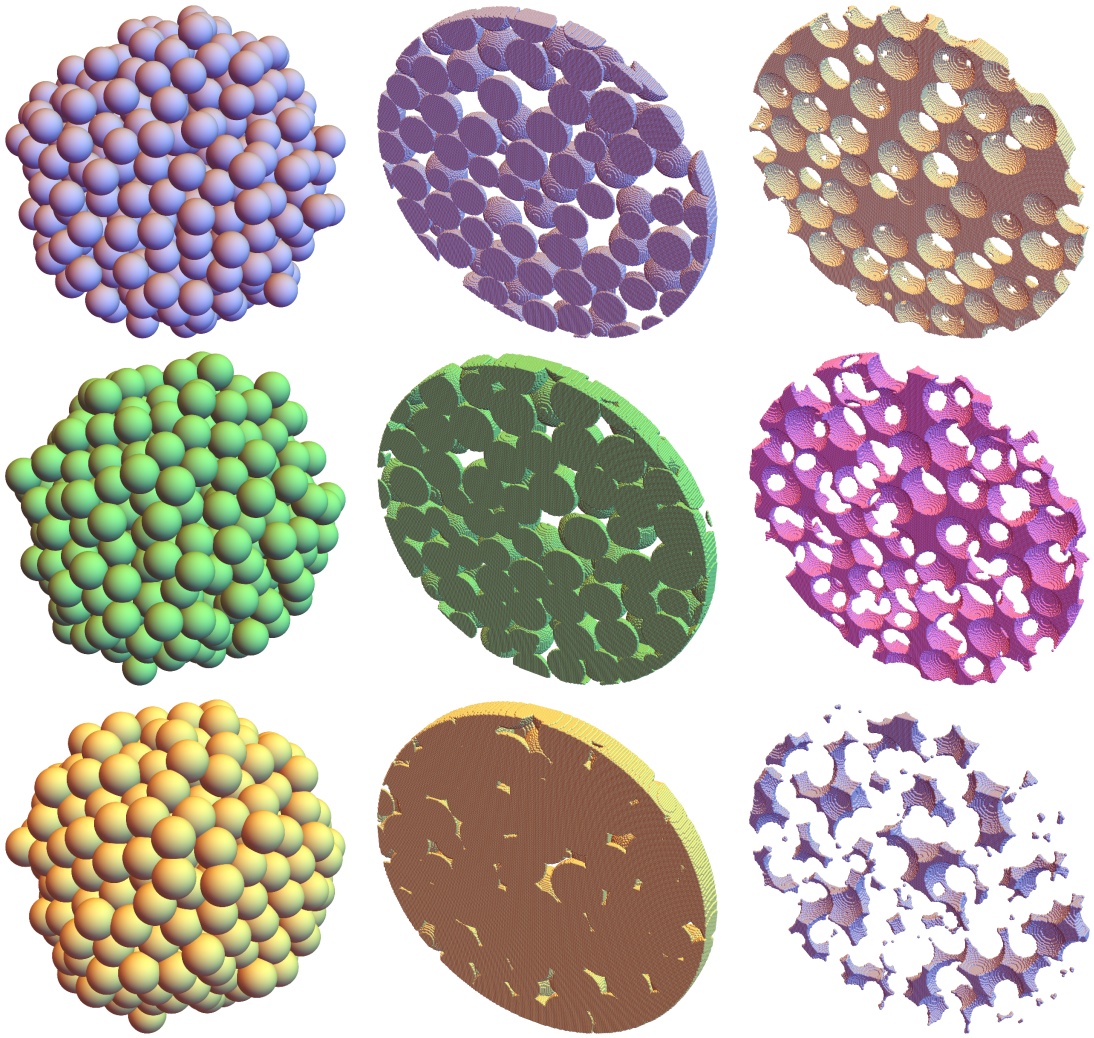

Figure 5.5: 3D representation of clusters $\mathcal{C}_{500}$ after agglomeration with different plasticity depths: top $\phi = 0.01$, middle $\phi = 0.15$ and bottom $\phi = 0.30$. In the left column 3D front view of the cluster. Higher average overlaps are clearly visible for higher ϕ due to the consequently higher δ_0. In the middle and right columns is a 3D section of these clusters of width r centred along a center plane. Similarly to figure 5.3, here spheres of radius $r/20$ are placed at every grid point used for the computation of the mass fraction with the grid method. In the central column only grid points inside of DEM particles are plotted, in the right one only those outside.

average overlap between components naturally leads to a higher mass fraction, computed numerically via (5.10), and equal to $\zeta = 0.60, 0.75$ and 0.91 for the three displayed clusters respectively. To better visualise the clusters internal structure and how it is affected by changing ϕ, a slice of thickness r is cut around the plane $\vec{y} = 0$, and the grid points contained in this volume shown figure 5.5. When a node falls inside of a DEM particle, the corresponding sphere is coloured alike the respective cluster, and displayed in the second column of figure 5.5. Vice versa, nodes laying outside the components are displayed on the right column and colour-reversed. In the first case these points belong to $\mathcal{N}_{\text{grid}}^{\cup P}$ and contribute to the mass fraction computation, in the second they constitute the complementary set $\mathcal{N}_{\text{grid}}^{\mathcal{C}} \cap \mathcal{N}_{\text{grid}}^{\cup P}$ and thus counted for the void fraction. Visualising grid nodes in this way allows a quick but detailed glimpse of the clusters internal structure and topology. Small ϕ results in a high porosity distributed homogeneously inside the cluster's volume, leading to a connected network of pores. Increasing ϕ proportionally decreases the void fraction, eventually leading to isolated hollow regions inside the structure. There are still a few connected paths crossing the cluster interior, but the pores are way narrower and intricate. Given their internal porous structure, clusters can then be used to model systems of porous materials, with useful applications for the study of catalysts or other particulate materials. In all cases the distribution of hollow regions is homogeneous and isotropic, due to the initial homogeneous random distribution of particles and to the isotropic centripetal force. This spatial distribution is instrumental for the theoretical part of the model, and will be discussed in the next session.

5.5 Cluster formation, homogeneity and isotropicity

Clusters formation is composed of 3 stages: initial particle loading, isotropic compression and relaxation. During the loading phase each primary particle is loaded inside a spherical region in a random position, such that none of the former is in contact with another [29, 35, 49, 96, 134, 144, 148, 169, 174]. The radius of this region is chosen to be $2r\sqrt[3]{2N}$, which is twice the radius of a sphere filled with N not overlapping primary particles with a packing fraction of 0.5. This ensures that an initial configuration for loading the particles is likely to be found. Alternatively particles could also be loaded in precise predefined location if the aim is to have a regular crystalline structure [17, 66, 91, 166, 175]. The choice depends on the applications of the model [88]. Since we are interested in modelling pharmaceutical powders and granules, an unstructured internal composition structure is our choice, requiring a random initial distribution of particles. In the second phase a centripetal force directed towards the centre of mass of the loaded ensemble is activated and slowly increased until the average particle overlap satisfies $\langle\hat{\delta}\rangle > \hat{\delta}^*_{\text{max}}$. Finally, the relaxation phase begins, where this force is slowly decreased and the particles' velocity is damped until the system is static and in mechanical equilibrium. Velocity damping is required to prevent the cluster from spinning, which is likely to occur when particles are subjected to central forces.
This procedure ensures the formation of homogeneous and isotropic clusters, in the limit of high N and an initial distribution as random and uniform as possible. As we will see in the upcoming sections, these two properties are key in the formulation of a simple predictive theory of clusters properties. To test these structural properties two quantities

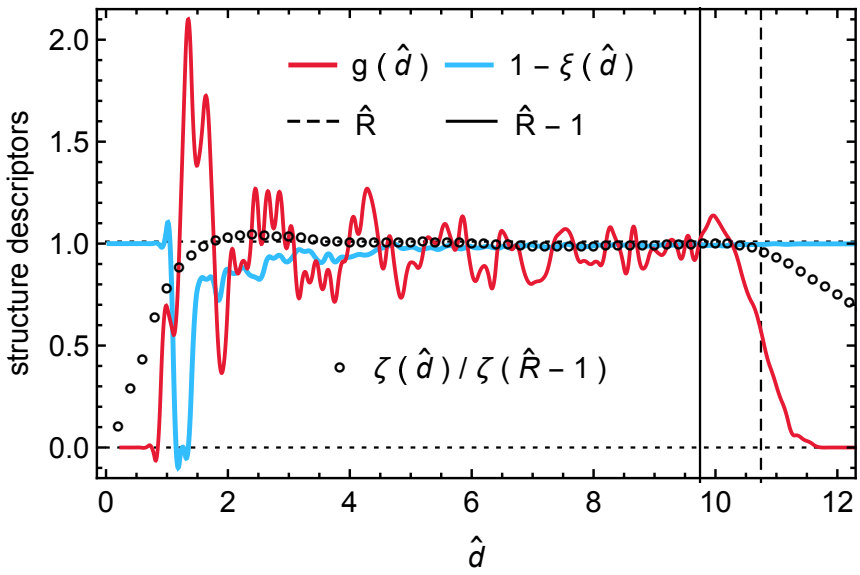

Figure 5.6: Descriptors of cluster homogeneity g and isotropicity ξ as a function of primary particles distance from the centre of mass for a cluster $\mathcal{C}_{1000}$ with $\phi = 0.15$. The circles show the numerically computed mass-fraction ζ inside spheres of radius $\hat{d}$ normalised by the value at $\hat{d} = \hat{R} - 1$ as used in this work. Clusters are homogeneous and isotropic given $\hat{d} > 4$ but show boundary effects for $\hat{d} > \hat{R} - 1$ due to their finite size.

are computed: the radial distribution function g to test the homogeneity [89, 129, 170] and a slightly modified version of the closing vector $\vec{\xi}$ to test the isotropicity [145]. The first is a commonly used tool to test the homogeneity of granular assemblies, and is defined by the ratio between the density of particles inside a spherical shell and the overall particle density, as a function of the distance between the shell and a reference point. In our case we compute the number N_i of particles inside concentric spherical shells S_i of constant thickness $\Delta\hat{R} = 0.1$ centred in $\vec{o}$ and of volume V_i. Defining $\hat{d}_i$ as the distance of S_i from $\vec{o}$ we can write

$$g(\hat{d}_i) = \frac{V}{N}\frac{N_i}{V_i} \approx \frac{N_i\,\hat{R}^3}{3N\hat{d}_i^2\Delta\hat{R}} \tag{5.12}$$

This function oscillates heavily in the neighbourhood of $\hat{d}_i \to 0$, since V_i at such close distance from $\vec{o}$ is of the same order of magnitude of V_P, reaches a plateau $g \approx 1$ when (and if) the cluster bulk is homogeneous, and sharply decreases to zero outside V. The closing vector is instead defined as the sum of the position vector of an ensemble of particles with respect to a reference point. For our study we are interested to verify that for sufficiently large $\hat{R}$ the clusters are isotropic, and therefore will evaluate $\vec{\xi}$ for all particles N_i^- which distance from $\vec{o}$ is below $\hat{d}_i$. In this way we can compare both descriptors of clusters internal structure as a function of the same quantity. Normalising and rescaling results in

$$\xi(\hat{d}_i) = \frac{1}{N_i^-}\left\|\sum_{i=1}^{N_i^-}\frac{(\vec{o}_i - \vec{o})}{d_i}\right\|. \tag{5.13}$$

This function is defined in the interval $[0, 1]$ and tends to zero for isotropic clusters. Every particle that is not "balanced" by counterparts on the opposite side of the centre of mass gives a contribution of up to $1/N_i^-$ regardless of its distance from $\vec{o}$. This means that asymmetric protrusions on the surface of the clusters would increase ξ by an amount proportional to $\hat{R}^{-3}$. This feature is important since asymmetries on the cluster surface due to a single particle can be neglected, in the context of isotropy, for relatively big clusters, while for comparatively small clusters this is not the case. Simply put, ξ numerically quantifies the isotropicity of a granular assembly since particles at the opposite sides of $\vec{o}$ factors one-another out in the sum, while those next to one-another will add a similar contribution.
Both equations (5.12) and (5.13) are plotted in figure 5.6 (the latter translated for the sake of readability) for a cluster $\mathcal{C}_{1000}$ with $\phi = 0.15$. Both descriptors oscillate heavily for $\hat{d} < 4$ and subsequently stabilise around 1 indicating reasonable homogeneity and isotropicity. In case of g we see a sharp decrease towards 0 starting around $\hat{d} \approx \hat{R} - 1$, while the value of ξ remains unchanged and becomes constant for $\hat{d} > \hat{R}$. These behaviours at distances above the cluster size had to be expected: since there are no more particles to be added to the statistics g must vanish due to the factor $\hat{d}^{-2}$, while ξ will only see null increments.
Another important aspect can be deduced from figure 5.6: the range at which clusters can no longer be considered homogeneous due to their finite size. The threshold lies around $\hat{R} - 1$, after which the lack of particles on the outside of the cluster boundary will introduce finite size effects to any statistical measurement. For this reason the boundary for the statistical computation of ζ via equation (5.10) will not be the cluster radius, but only $\hat{R} - 1$.
To demonstrate that $\hat{R} - 1$ is the correct boundary for evaluation of equation (5.10), data from numerically computed ζ are shown in figure 5.6 for linearly increasing spherical boundary radius given by $\hat{d}$. In the plot the former are normalised by the value computed at $\hat{d} = \hat{R} - 1$ and used in the rest of this work, to allow an easier comparison with g and ξ. Like the latter ζ reaches a plateau for $4 \leq \hat{d} \leq \hat{R} - 1$, therefore showing that the upper extremum is indeed the correct distance to consider when measuring clusters internal structure properties. Both tests via g and ξ, as well as the comparison with ζ, have been performed for every cluster simulated and show the same behaviour, but are not plotted here for sake of brevity.

5.6 Analytical model of cluster structure parameters

We now have the definition of clusters structural properties and the tools to numerically measure them, as well as a method to test their inner spatial arrangement. This would be of limited usefulness if these descriptors would not allow us to prescribe structure properties of clusters before their formation. In this section we will then attempt to analytically relate final clusters properties to DEM model parameters via simple geometrical considerations. Since the density is related trivially by equation (5.11) we only have to study $\hat{R}$ and ζ.
By using the normalised cluster radius we do not have to worry about primary particles size: R varies linearly with r, so for fixed N to achieve a target cluster size it is sufficient to only scale primary particles size proportionally. Besides N only ϕ is involved in determining the cluster parameters due to equation (5.6) and to how we perform the agglomeration,

providing us, a priori, the average particle overlap. Only their relative spatial arrangement is the last factor needed for the link. Of the two DEM parameters $\big(N, \phi\big)$ the first is an extensive quantity while the second is intensive, and the same holds true for clusters parameters $\big(\hat{R}, \zeta\big)$. We therefore expect the relation between ζ and ϕ to be independent from both $\hat{R}$ and N.
In the limit of vanishing inter-particle overlaps and for a homogeneous and isotropic bulk, ζ can be calculated numerically as the ratio between total volume of components and cluster

$$\zeta \xrightarrow{\langle\hat{\delta}\rangle\to 0} \zeta_0 = \frac{N\,V_P}{V_0} = \frac{N}{\hat{R}_0^3}. \tag{5.14}$$

For increasing overlaps this volume ratio will increase, and eventually tend to a value greater than unity as soon as $\langle\hat{\delta}\rangle$ surpasses a certain threshold dependent on ζ_0. This relationship also involves the size distribution of particles, a dependency that was circumvented in this work by choosing a mono-disperse size distribution and that will constitute a case of study for future research. With the previous assumptions ζ_0 is constant and independent from the cluster size, i.e. is intensive, and represents the packing of the single particles inside the cluster, and is the link between $\big(N, \phi\big)$ and $\big(\hat{R}, \zeta\big)$ we need. For vanishing $\langle\hat{\delta}\rangle$ the cluster radius will also become independent from the average overlap, and by re-arranging equation (5.14) can be expressed as

$$\hat{R} \xrightarrow{\langle\hat{\delta}\rangle\to 0} \hat{R}_0 = \left(\frac{N}{\zeta_0}\right)^{1/3} \tag{5.15}$$

where $\hat{R}_0$ is the cluster radius as zero overlap.
Given the cluster homogeneity ζ represents the probability to find a particle in any point of the cluster bulk, and the same holds true for ζ_0 for $\langle\hat{\delta}\rangle \to 0$. The number of particles n_D encountered when crossing the cluster diametrically passing through its centre will then be proportional to ζ_0 and to its diameter $2\hat{R}_0$, and does not depend on the direction we choose because clusters are isotropic. Since, during their formation, we compress clusters isotropically along their radius, the radial force will mostly displace particles towards $\vec{o}$ but not away from one another. This means that n_D can roughly be considered constant, so $n_D \approx \zeta_0\hat{R}_0$. Now an isotropic diametral compression $\hat{\Delta} = 2\big(\hat{R}_0 - \hat{R}\big)$ would result in an average particle deformation of $\langle\hat{\delta}\rangle = \hat{\Delta}/2n_D$, where the last factor 2 accounts for each particle being deformed twice along the direction of compression. Putting everything together we finally arrive at the expression for $\hat{R}$ at finite particle overlaps

$$\hat{R} = \hat{R}_0 - \zeta_0\,\hat{R}_0\,\langle\hat{\delta}\rangle. \tag{5.16}$$

The former equation relates, at any point, the radius of the cluster to the spatial arrangement of its components ζ_0, their number N and their average overlap $\langle\hat{\delta}\rangle$.
The way to analytically determine ζ can be carried out only for $\langle\hat{\delta}\rangle \to 0$, i.e. when equation (5.14) is valid. In case of particles overlap the total particle volume should account for the missing ΔV_P contained in the spherical caps originated by each contact, proportional to $\langle\hat{\delta}\rangle^2$ and to the coordination number C of the system. The latter can only be measured numerically, especially in case of polydisperse particle size distributions, and poses a problem in the analytical estimation of ζ. However, since the contributions of ΔV_P to ζ are

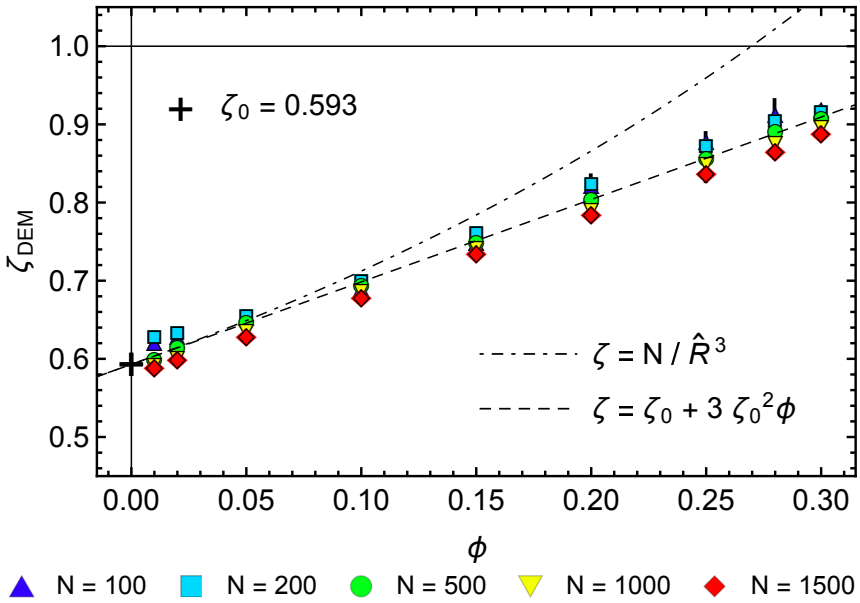

Figure 5.7: Numerically computed cluster mass fraction ζ_{DEM} as a function of ϕ for varying N. The dot-dashed line represents ζ evaluated via equation (5.14), the dashed one via equation (5.17). The asymptotic limits $\phi = 0$ and $\zeta = 1$ are highlighted with black solid lines, the cross (+) indicating the intercept $\zeta = \zeta_0 = 0.593$ computed via linear regression.

quadratic in $\langle\hat{\delta}\rangle$, by taking a first order approximation at small overlaps we get rid of the additional term ΔV_P, and therefore

$$\zeta \approx \zeta_0 + 3\,\zeta_0^2\,\langle\hat{\delta}\rangle. \tag{5.17}$$

Equation (5.17) anyways grows slower than $N/\hat{R}^3$ which is an improvement, from the former, towards the actual behaviour of ζ, since the mass fraction asymptotically tends to 1 for increasing overlaps. When studying clusters structure we are mostly interested in the final cluster radius, rather than its evolution during the formation stage, and given that we impose $\hat{\delta}_{\max} > \hat{\delta}^*_{\max}$, we will from now on implicitly refer to the final radius when writing $\hat{R}$ and assume $\langle\hat{\delta}_0\rangle = \phi$, unless explicitly specified otherwise.
In the previous framework we explicitly neglected the effect of friction during the cluster agglomeration phase [132]. Inter-particle friction forces play a central role in determining the structure of granular assemblies [67], but a systematic study of their effect in the context of this work is beyond the scope of this paper. Both rolling and sliding friction contribute to the initial configuration of primary particles inside the clusters, and consequently ζ_0. Negligible friction coefficients lead to $\zeta_0 \approx 0.66$, i.e. around the value of random tight packing, while with our choice (see table 5.1) we reached packings of $\zeta_0 \approx 0.59$, consistent with random loose packing configurations. This result is expected, since frictionless primary particles can re-arrange freely during clusters agglomeration, therefore reaching higher bulk densities, while frictional ones will interlock due to jamming effects leaving wider interstitial voids. Since ζ_0 depends on friction and initial arrangement of primary particles, it must be computed numerically once the former are set, as explained in the

Table 5.2: List of parameters design space for explicit and implicit numerical testing of clusters theory.

explicit scheme	$N = \{1, 2, 5, 10, 15\} \cdot 10^2$ $\phi = \{1, 2, 5, 10, 15, 20, 25, 28, 30\} \cdot 10^{-2}$
implicit scheme	$\hat{R} = \{4, 6, 8, 10, 12\}$ $\zeta = \{65, 70, 75, 80, 85, 90\} \cdot 10^{-2}$
constant parameters	$r = 5.0 \cdot 10^{-4}\text{m} \quad \hat{k_p} = \hat{k_c} = 0.5$

next section.

5.7 Clusters theory numerical validation

To validate the previous theoretical framework, both equations (5.16) and (5.17) must be validated. To do so, a twofold approach will be followed. In the first, DEM parameters are explicitly set in the models and clusters successively generated. After agglomeration the cluster properties are measured and compared to the predicted values following from the initial DEM particle properties dataset used. The second, implicit, approach requires the initial specifications of desired final clusters properties instead. Here the DEM initial parameters are implicitly determined by inverting (5.16) and (5.17) and automatically set as a function of the desired characteristics. In both cases 3 simulation runs are performed for each setting of parameters, where a different initial spatial distribution of particles is used to add statistical significance to the results. From this point onwards every numerical parameter measured via DEM will be obtained by averaging over these 3 runs. The latter are not explicitly marked with different symbols to avoid cumbersome notations.
Table 5.2 summarizes the parameters used for numerical testing of the previous theory. In case of the explicit validation scheme, N and ϕ are systematically varied throughout this set of simulations. At the end of each simulation both $\hat{R}$ and ζ are evaluated according to equations (5.9) and (5.10) and compared to (5.16) and (5.17) respectively. To compare numerical data of N and ϕ gathered during implicit simulations scheme we need to invert both the former as a function of $\hat{R}$ and ζ to obtain

$$N = \left\lfloor \zeta_0 \left(\frac{3\,\zeta_0\,\hat{R}}{4\,\zeta_0 - \zeta} \right)^3 \right\rfloor \tag{5.18}$$

$$\phi = \frac{\zeta - \zeta_0}{3\,\zeta_0^2} \tag{5.19}$$

where the brackets $\lfloor \cdot \rfloor$ indicate the integer part of the argument. During numerical validations $r = 5 \cdot 10^{-4}$m and $\hat{k_p} = \hat{k_c} = 0.5$ are kept constant to reduce the total number of cases tests needed, but this without loss of generality. In addition, at the end of each test the relative deviation $|\langle\hat{\delta}\rangle - \phi|/\phi$ is computed to ensure that the agglomeration process reached the critical threshold (5.5), resulting in no deviation above 5% for all data sets. In general, a higher amount of particles implies a higher variability of the final $\langle\hat{\delta}\rangle$ from ϕ due to the resulting bigger size.

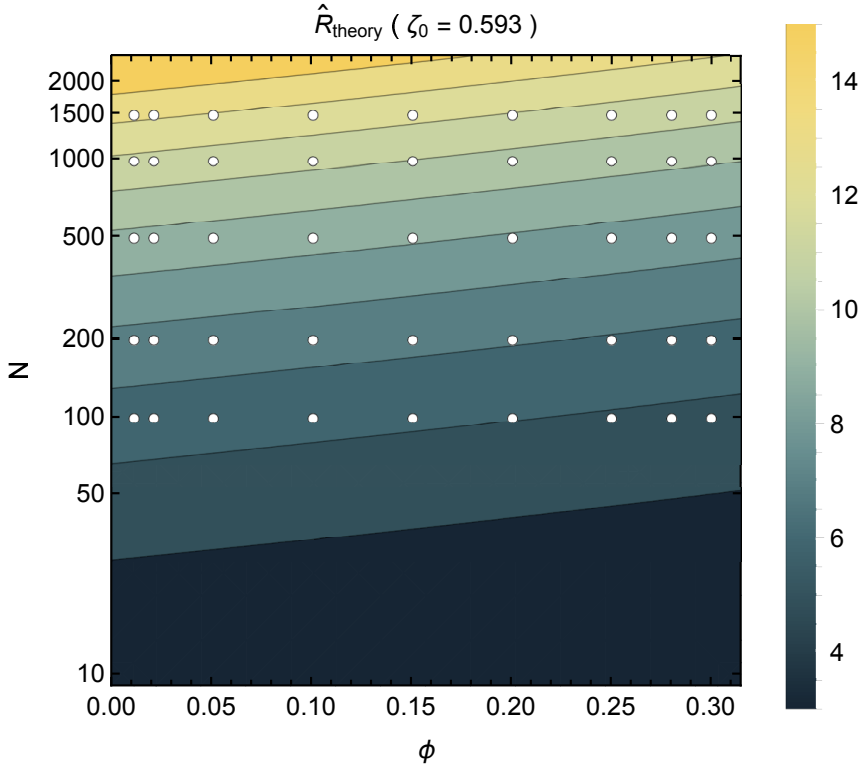

Figure 5.8: Contour plot of cluster radius $\hat{R}$ dependency as a function of DEM particle parameters N and ϕ for $\zeta_0 = 0.593$. Each white dot represents a point in the (N, ϕ) particle properties phase space selected for theory validation in the explicit scheme.

To quantify the agreement between expected values of a parameter x and the corresponding numerical results two descriptors are used: the mean relative deviation $\epsilon(x)$ across the 3 replicate simulation runs and the relative displacement $\iota(x)$ between theoretical or target and measured values. Both are defined respectively as

$$\epsilon(x) = \sum_{i=1,2,3} \frac{\left|x_i - \langle x \rangle\right|}{\langle x \rangle} \tag{5.20}$$

$$\iota(x) = \frac{\left|\langle x \rangle - x_{\text{theory/target}}\right|}{x_{\text{theory/target}}} \tag{5.21}$$

where x_i is the numerical value of parameter x measured in the i-th simulation run and $\langle x \rangle$ is the mean value of all the former. Depending on whether the test is explicit or implicit the mean value of the studied parameters is compared with either the expected theoretical value x_{theory} or with the target one x_{target} respectively. In the upcoming plots of numerical results ϵ is depicted with black vertical bars, while all values of both ϵ and ι computed for each parameter couple tested are reported in appendix for sake of brevity.
Both (5.16) and (5.17) depend on the initial mass fraction ζ_0, inherited by particle size distribution and initial spatial arrangement, which is a key parameter to properly describe the final clusters. Since there is no analytical expression for ζ_0, its value must be computed numerically as follows. According to (5.17) and (5.6) the relationship between ζ and ϕ is

linear for small ϕ, and can be expressed in the form $\zeta = m\phi + q$, where m and q indicate slope and intercept of the linear approximation respectively. By comparing the two it is evident that ζ_0 is simply given by the intercept q of the linear regression line. The numerical data set used to estimate ζ_0 this way is the same used to investigate the theory following the explicit scheme, since the setup variables depend on simple DEM parameters and ζ is computed *a posteriori*.
Figure 5.7 shows the evolution of ζ computed numerically via equation (5.10) for the parameters set indicated in table 5.2. The intercept computed with this numerical dataset gives $q = 0.593$ with a coefficient of determination $R^2 = 0.986$, and is indicated in figure with a cross. Given this result, we set $\zeta_0 = 0.593$, corresponding to a random loose packing configuration [132], that will be used from now on to compute each cluster related parameters. The linear trend in ϕ is clearly visible by comparing the dataset to ζ (dashed line), demonstrating the validity of equation (5.17) in the range of ϕ explored, and its independency on N for values satisfying $\hat{R} \gg 1$. The dot-dashed line shown in figure 5.7 is instead the value of ζ computed via equation (5.14), i.e., without any correction to account for particle overlaps. As it can be seen when comparing with the numerical data the linearised expression for ζ is a way better analytical expression for the cluster mass fraction. In addition the decrease in slope expected for increasing $\langle\hat{\delta}\rangle$ is still negligible in the range of ϕ explored, giving an additional motivation for using the linearised expression (5.17).

5.7.1 Explicit validation tests

Now that we found a numerical value for ζ_0, we can compute the cluster parameters $\left(\hat{R}, \zeta\right)$ as a function of $\left(N, \phi\right)$ according to the previous theoretical framework, and investigate if the former holds by comparing predicted and numerical values obtained via DEM. The parameters design space explored in the explicit validation scheme is illustrated in figure 5.8, where highlighted are the selected trial data points of table 5.2.
The cluster radius estimated according to the theory (5.16) is compared to its counterpart measured via DEM according to (5.9) in figure 5.9a. As expected $\hat{R}$ decreases linearly with ϕ (data for increasing ϕ displaced in the direction of the arrow), since an increase in the latter translates into a higher equilibrium overlap, leading to a higher average particle overlap after agglomeration. Higher number of components N per cluster obviously increase its size, but also determines a better agreement between equation (5.9) and DEM results (as shown in figure 5.14. This has to be expected since increasing N implies a higher R/r ratio, and a consequent more homogeneous distribution of particles into the cluster given the higher size ratio. Conversely, lowering $\hat{R}$ via decreasing N results in a worse fit due to the increasing finite size effect. This is reflected by the displacement $\iota(R)$ being inversely proportional to N (figure 5.14. The mean deviation $\epsilon(R)$ between statistical replicates seems to be relatively unaffected by either N or ϕ, while the latter seems to proportionally lead to an increase in $\iota(R)$.
When comparing the mass fraction, the fine resolution chosen for (5.10) allows us to estimate ζ with great precision, although not giving us information on the internal distribution of the pores. As plotted in figure 5.9b the expected mass fraction ζ is in good accordance with the numerical results. Porosity is independent on N for the range explored, a fact that we not expect to change for even higher number of particles due to the arguments

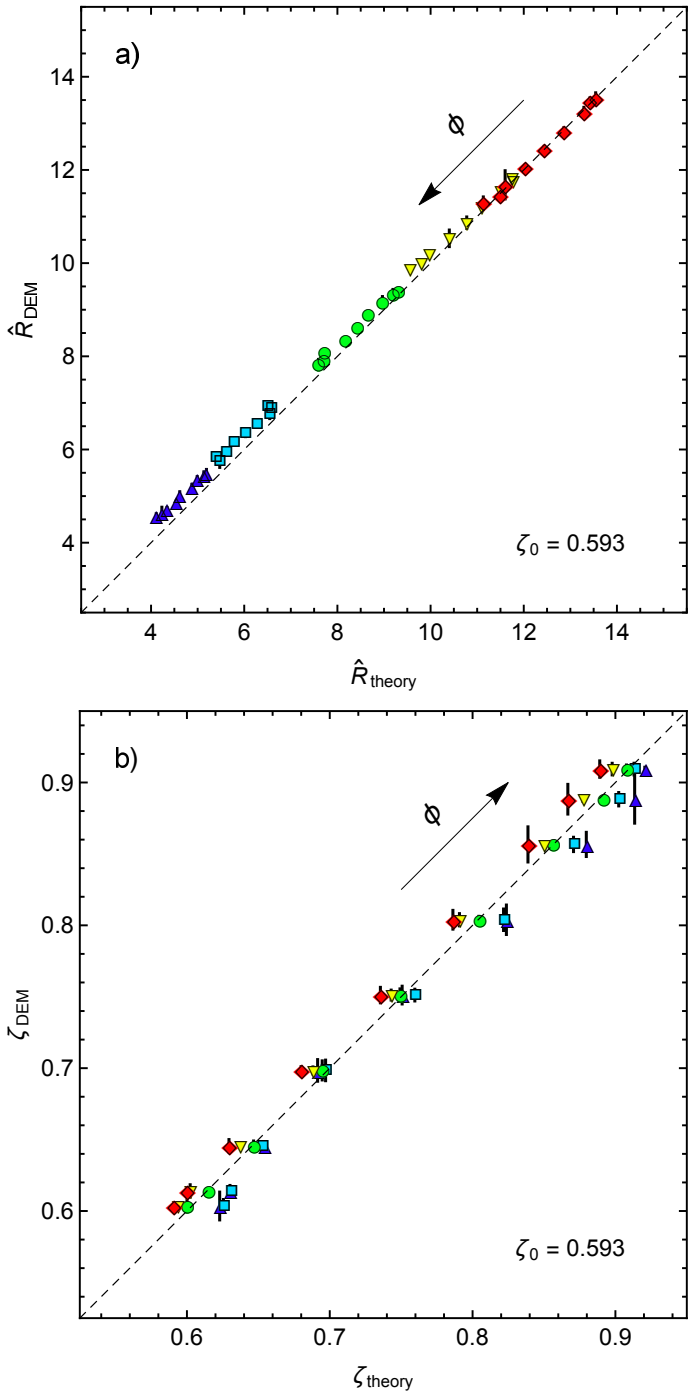

Figure 5.9: Comparison between theoretically expected values $\hat{R}_{\text{theory}}$ and ζ_{theory} and numerically measured counterparts $\hat{R}_{\text{DEM}}$ and ζ_{DEM}, respectively in (a) and (b). Colour refers to particle number per cluster N, with the direction of increasing plasticity depth ϕ indicated by the arrow. In both cases theoretical values agree well with DEM data, with agreement for $\hat{R}$ getting better for increasing N. Since ζ is only function of particle size and initial spatial distributions its value does not change with N for a sufficiently high ratio $\hat{R}$, as confirmed by both ζ_{theory} and ζ_{DEM}.

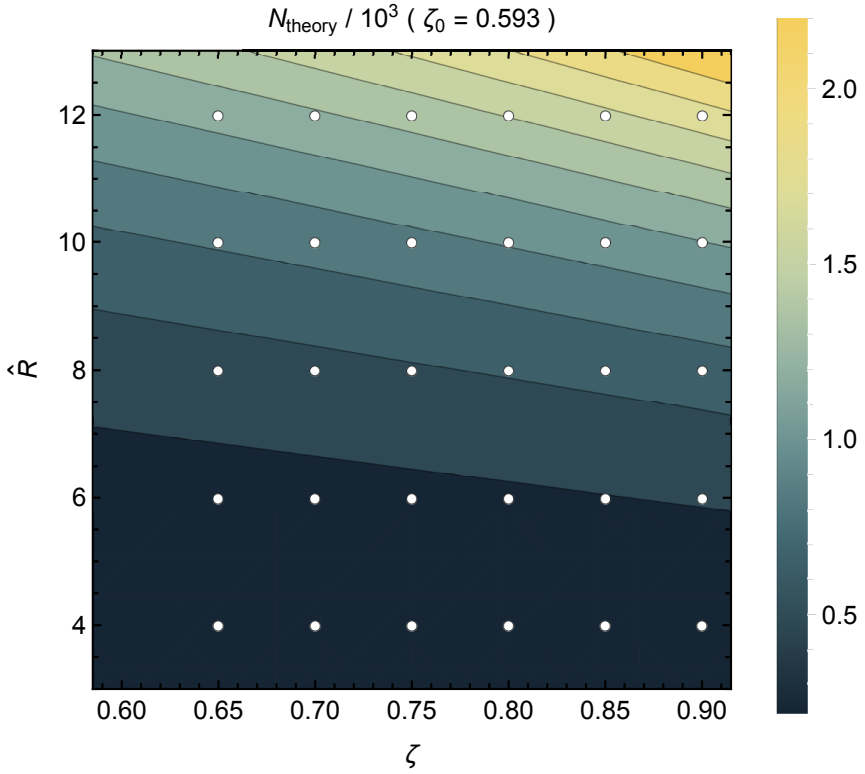

Figure 5.10: Contour plot of particles number N as a function of cluster macroscopic parameters $\hat{R}$ and ζ for $\zeta_0 = 0.593$. Each white dot represents a point in the $\left(\hat{R}, \zeta\right)$ cluster properties phase space selected for theory validation in the implicit scheme.

stated above for the behaviour of $\hat{R}$. Logically increasing ϕ sees a proportional increase of ζ, since the higher the final stable overlap the smaller the pores left within the cluster. As for its counterpart, $\epsilon(\zeta)$ seems to be independent on variations of either N or ϕ, as displayed in figure 5.14. The behaviour of $\iota(\zeta)$ is however more complicated, showing an increase at both ends of the N and ϕ tested. This determines a "sweet spot" where the deviation is at its minimum for $N = 500$ and $\phi \in [0.10; 0.15]$.
Magnitudes of both $\epsilon(\zeta)$ and $\iota(\zeta)$ being below 4% for every tested value in the explicit framework demonstrates how well equation (5.17) agrees with the numerical results for the range of parameters tested. As expected a discrepancy from the theory is found at the lower end of N since finite-size effects start playing a role, given the lower R/r ratio. This seems to affect $\iota(R)$ but not $\epsilon(R)$, an additional proof of the clusters homogeneity and isotropicity. Nevertheless for $N = 500$ and above $\iota(R)$ falls as well below 4%, thus ensuring the validity of the predictive theory.

5.7.2 Implicit validation tests

The implicit validation test works in a similar way: a set of points in the design space is defined, and simulations of cluster agglomeration performed accordingly. This time, however, the final desired cluster properties $\hat{R}$ and ζ are set as input parameters, and the model automatically tunes N and ϕ accordingly via equations (5.18) and (5.19). The set

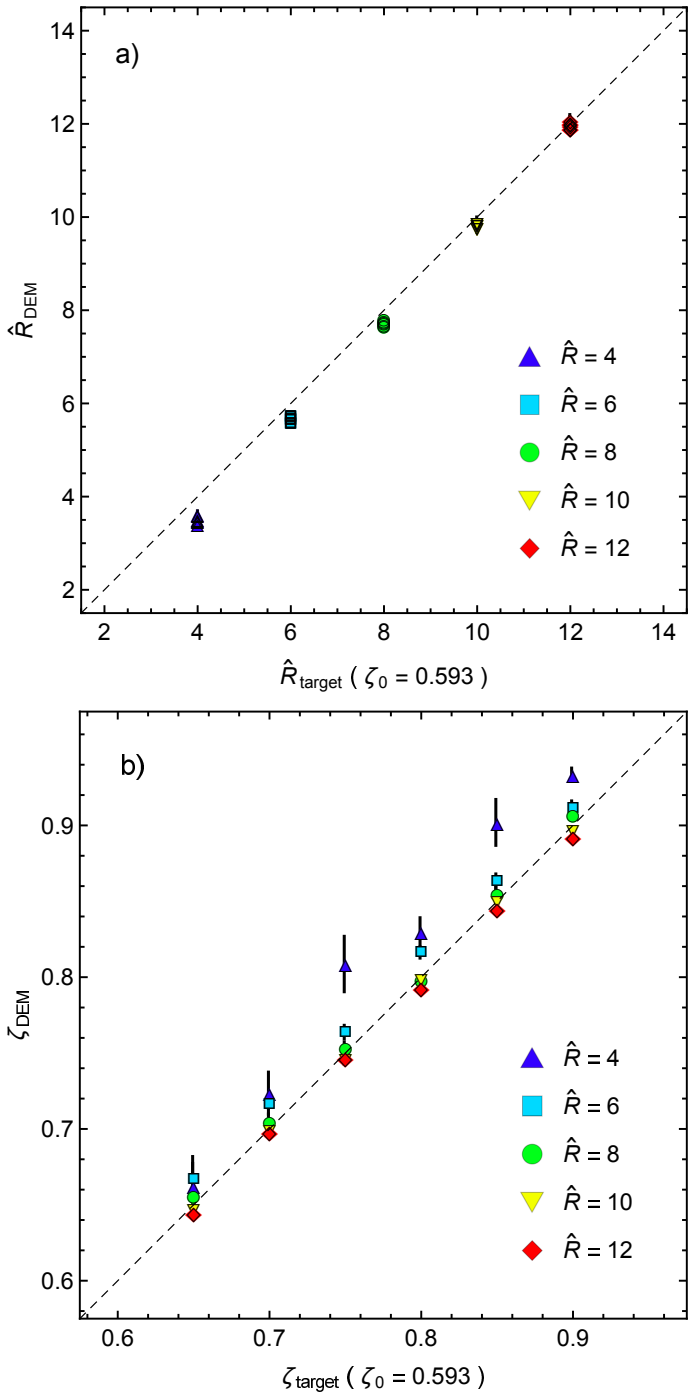

Figure 5.11: Comparison between target values $\hat{R}_{\text{target}}$ and ζ_{target} and numerically measured $\hat{R}_{\text{DEM}}$ and ζ_{DEM}, respectively in (a) and (b). Colour refers to target cluster radius $\hat{R}_{\text{target}}$. In both cases target values agree well with DEM data, with the only exception of a systematic error for $\hat{R}_{\text{target}} = 4$ due to finite size effect. Since ζ is only function of size and spatial distributions of particles, its value does not change with N for a sufficiently high ratio $\hat{R} > \hat{R}_{\text{crit}}$, as confirmed by both ζ_{target} and ζ_{DEM}.

of points chosen for this test is shown in figure 5.10 on top of the contour plot showing N as a function of the implicit particle parameters phase space explored.
The model response to a target final cluster radius $\hat{R}_{\text{target}}$ is very reliable, as shown in figure 5.11a. The predicted values are very close to the measured ones $\hat{R}_{\text{DEM}}$ after agglomeration, and the fitness of the prediction is not substantially affected by different target mass fractions ζ_{target}. This has to be expected, since inspection of equation (5.18) reveals that N depends on ζ only via the term $4\zeta_0 - \zeta$; a very weak dependency given the value of ζ_0 and the range of ζ explored. It is also noticeable how the fit is getting worse for lower $\hat{R}$. As mentioned, the cause of this deviation is due to emerging finite size effect, due to the comparable scale of cluster and its components. For these tests both $\epsilon(R)$ and $\iota(R)$ sharply increase for decreasing target $\hat{R}$ accordingly, with $\epsilon\big(\hat{R} = 4\big) > 10\%$ (see figure 5.14. Because of the aforementioned weak dependence of $\hat{R}$ on ζ, both $\epsilon(R)$ and $\iota(R)$ seem to be unaffected by the tuning of the former except for low $\hat{R}$.

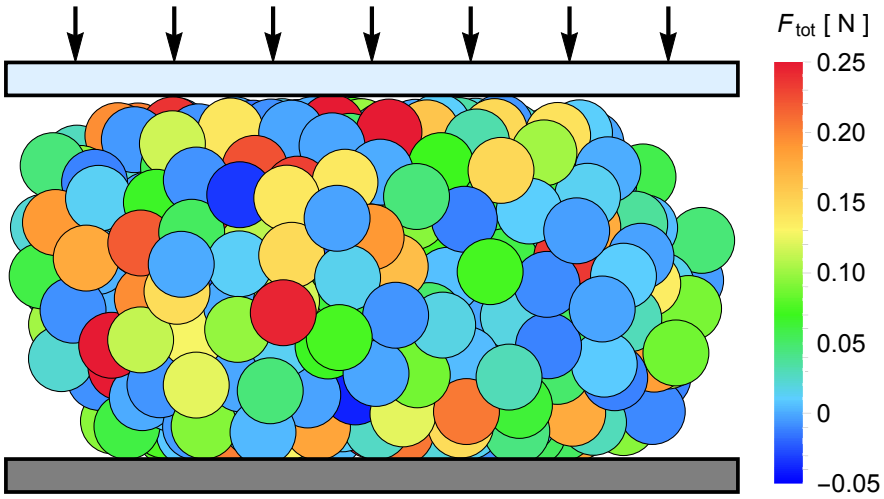

Figure 5.12: Front view of single cluster $\mathcal{C}_{500}$ uniaxial compression between a fixed bottom and a mobile piston on top. Particles are coloured according to the total force they are subject to.

A very good agreement is also found when comparing target and measured mass fractions ζ for the implicit test, sketched in figure 5.11b. Again statistical replicates do not show significant discrepancies from one another, leading to a very small $\epsilon(\zeta)$ for every parameter tested. Variations of target ζ do not affect the quality of the output, since both $\epsilon(\zeta)$ and $\iota(\zeta)$ show no dependency, as it was for the target $\hat{R}$. Again finite size effects are only responsible for the rise in deviation and displacement. The latter reaches values above 5% only for $\hat{R} = 4$, and becomes negligible for $\hat{R} \geq 8$.
Results from the implicit tests show that the model allows a reliable prediction of clusters properties after agglomeration, and precise target structural properties can be met, provided that finite size effects are avoided. According to our results noticeable discrepancies (above 5%) in the modelled clusters properties are found only for $\hat{R}_{\text{target}} < 8$. By interpolating the data shown in figure 5.14, to ensure a reliable formation of clusters with deviations below 5% one must ensure $\hat{R}_{\text{target}} \geq 7.5$, while setting $\hat{R}_{\text{target}} > 5.5$ is sufficient to achieve deviations below 10%. These considerations become important, among many

others, when one has to choose r given the size of the clusters to be modelled.

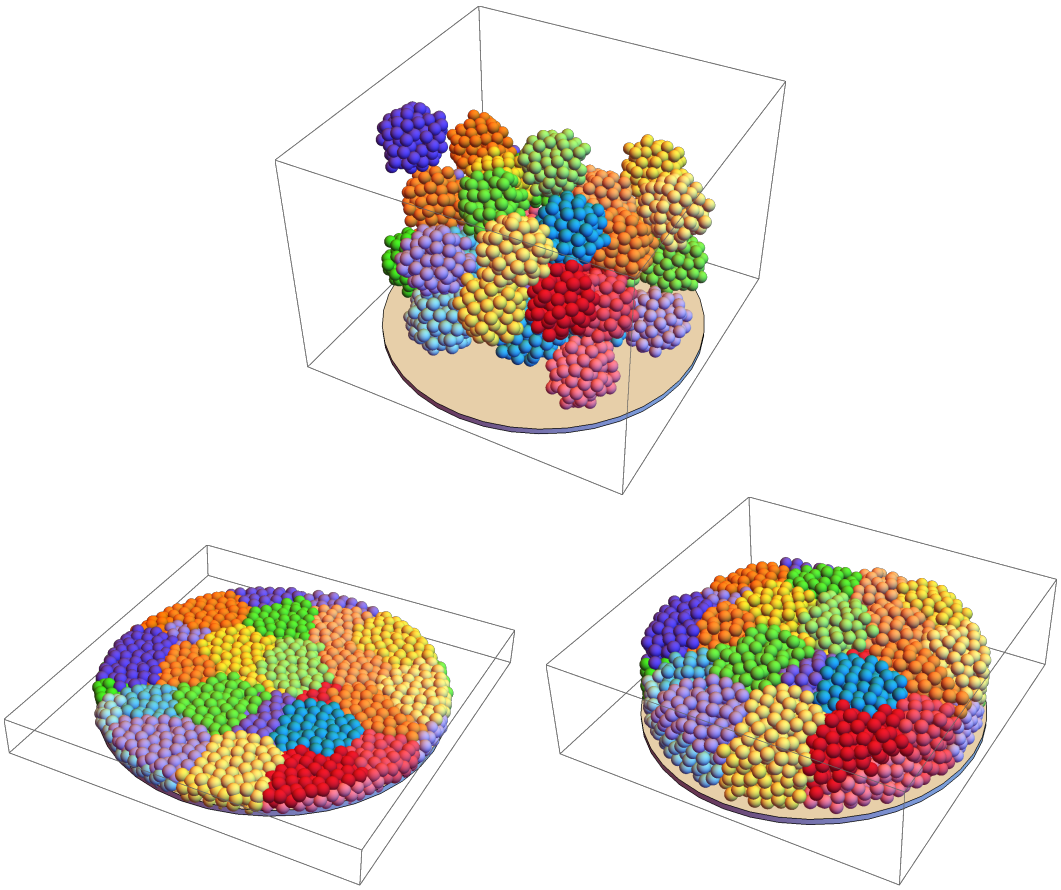

Figure 5.13: Snapshots of die compaction of 40 independent $\mathcal{C}_{100}$ clusters inside a cylindrical barrel (only the bottom shown for sake of clarity). Snapshots are taken before (top), at maximum (bottom left) and after (bottom right) compression. Particles of each cluster have the same colour to easily follow them visually between different compaction stages.

5.8 Future applications

The scope of this paper is to illustrate a new methodology to model particles via agglomerates possessing a plastic behaviour, thus being able to deform and break. For practical reasons it is desirable to infer precise structural properties of the former prior to the model implementation, which constitutes the second part of this paper. Applications for such a model are not illustrated in detail here for sake of brevity, but will be briefly introduced to give context and perspective to this modelling effort. The first step to be taken will be to develop a model for particles and granules breakage [49, 53, 91, 122, 134, 143, 155] in a pharmaceutical context [35, 100]. When compressed, such materials deform plastically during the first instances of the force loading, eventually fracturing when above a certain load. Figure 5.12 shows a uniaxial compression test of a single cluster $\mathcal{C}_{500}$ under a force of 1.5N. The cluster model shown in this paper is suited for modelling particles having

an initial plastic behaviour since the bonds between their elementary components are not rigid, but can re-arrange in response to external forces. Clusters are mechanically stable during each stage of compression, regardless of their eventual deformation.
Since clusters inherit physical properties from equation (5.1) for small stresses applied they will initially deform and then recover their initial configuration once the external perturbation is removed. Moreover, since elementary particles can form stable bonds, clusters are ideal to model particle agglomeration processes such as die compaction [35, 88, 92, 122]. When compressed together particles belonging to different clusters can form stable cohesive bonds, mimicking particles dry agglomeration under compression. In figure 5.13 three snapshots are taken from a die compaction simulation test that was performed to test the model capabilities in capturing the physics of dry agglomeration. Walls composing the boundary geometry are interacting with particles via a linear spring-dashpot interaction, therefore no adhesion between the former is implemented. Here 40 $\mathcal{C}_{100}$ clusters with $\phi = 0.10$ are compressed together with a pressure up to 1.7MPa and then let to slowly recover elastically. After compression, the initially independent clusters now form a stable agglomerated ensemble of cylindrical shape. The model still needs many refinements to properly capture the dynamics of die compaction, but these preliminary results are a step in the right direction.

5.9 Conclusions

We presented a framework for the implementation of deformable and breakable particle clusters in DEM. DEM particles are agglomerated together to form a cluster via a strong centripetal force. After the latter is slowly decreased to zero, elasto-plastic inter-particle forces keep the cluster together, the relative distance between components determined by an input parameter. Details on how to define and numerically measure cluster structural properties are provided and explained.
A theory is then developed, where clusters macroscopic variables, such as radius, mass and mass fraction, are related to DEM particle parameters such as number, density and plasticity. To validate the theory two approaches are followed: explicit and implicit. In the first approach, particle parameters are given as input and expected final clusters properties are compared to numerical results of agglomeration. In the second approach, desired clusters parameters are used as input, the model automatically exploiting the theoretical framework to set the needed DEM parameters. Final cluster properties are then compared to the target ones. Both approaches confirm the theoretical modelling presented, provided the size ratio between cluster and particles to be above $\hat{R} = 5.5$ to avoid high deviations of structural parameters from the expected ones due to finite size effects. This will allow users of this model to design clusters with precise size and porosity to carefully mimic particles or granules of specific structural properties.
Finally two applications of this model are briefly presented: uniaxial compression of single particle of granule and die compaction. Despite still being at the stage of feasibility tests, the simulations performed show this framework to be promising in the presented contexts. In particular, the ability to deform plastically while maintaining mechanical stability is relevant during compression of plastic or semi-plastic materials, such as soil and pharmaceutical powders. Attractive bounds can also be established between particles of different

clusters, paving the way to DEM models of complex particle agglomeration.
The presented framework is going to be developed further in multiple directions. On the one hand we will implement clusters with higher aspect ratios and polyhedral shape, as well as the underlying theory, to allow the modelling of a broader range of particles. On the other hand it is our objective to theoretically relate clusters' dynamic variables to particle properties, such as restitution and friction coefficients, that need collision tests to be measured. Finally, cluster properties relevant to particle breakage, such as hardness and compressibility, will be related to DEM counterparts such as particles stiffnesses, to allow a reliable usage of clusters in the context of particle breakage. All of these aspects will constitute the necessary steps towards the development of a numerical model of die compaction based on the particle clusters presented.

5.10 Appendix: quantification of numerical errors

Error quantifiers ϵ and ι from equations (5.20) and (5.21) respectively, computed for both $\hat{R}$ and ζ, are here displayed in figure 5.14 for each set of parameters tested and type of validation run. Cells are colour-coded depending on the magnitude of the discrepancy: from blue to red for increasing value.
All but two values of $\epsilon(R)$ and $\epsilon(\zeta)$ are below 3%, indicating that a different initial distribution of particles is not altering the final cluster properties. This is consistent with our expectations, and a further confirmation of both the assumption of initial particle homogeneity and isotropy in space. Values of $\iota(R)$ and $\iota(\zeta)$ show a dependency on the cluster size instead: to have values systematically lower than 5% a value of $\hat{R} > 7$ is required. This is not surprising either since the theory developed here relies on the modelling of clusters as continuous, homogeneous and isotropic bodies. These approximations become progressively less accurate the smaller the size ratio between clusters and elementary components. When this is not the case ι rapidly decreases for both cluster structure parameters and the numerical results agree very well with the expected ones, confirming the validity of the theory developed in this work.

Acknowledgements

This work was funded through the Austrian COMET — Competence Centres for Excellent Technologies programme. The COMET programme is operated by the Austrian Research Promotion Agency (FFG) on behalf of the Federal Ministry for Transport, Innovation and Technology (BMVIT) and the Federal Ministry for Digital and Economic Affairs (BMDW). Our projects are also funded by Land Steiermark and the Styrian Business Development Agency (SFG).

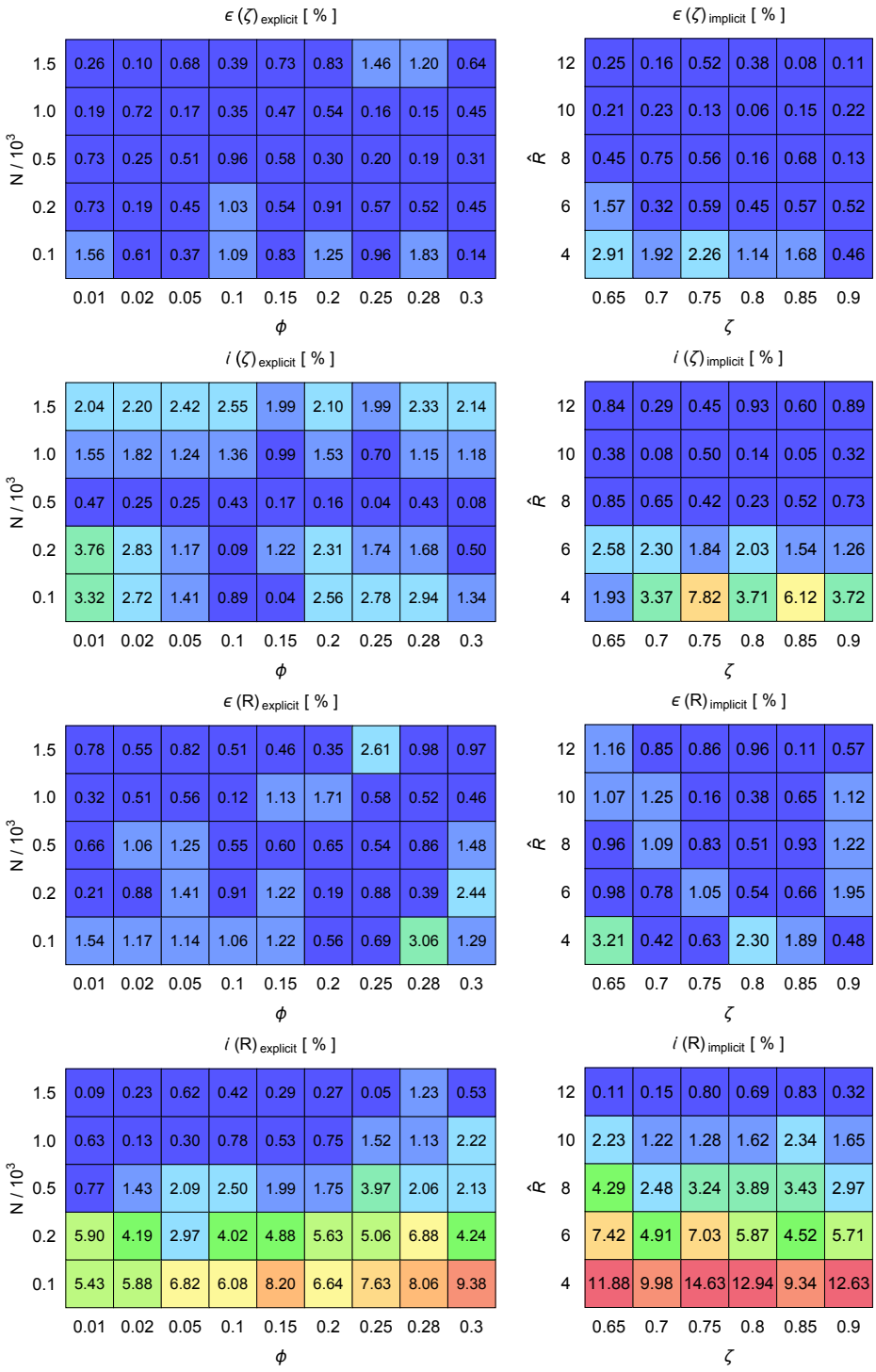

Figure 5.14: Error quantifiers ϵ and ι for tested variables $\hat{R}$ and ζ as a function of input parameters, in both explicit and implicit numerical tests. Cells are coloured according to the magnitude of the deviation from the expected value.

Chapter 6

Conclusion and outlook

"Who we are is but a stepping stone
to what we can become..."

DE:HR

The final part of this thesis is dedicated to a concise recapitulation of the main findings of the works exposed previously, and how they can be exploited to increase our understanding of the of the modelled device and improve the related processes. Since science is mostly made of small steps, the perspective of future research is an important element of the bigger picture. For this reason the continuation of the research topics presented will be briefly illustrated as well.

6.1 Main findings

The numerical investigation of the dynamics of frictional granular materials transported inside a partially filled periodic screw conveyor led to the following insights:

- There is an active interplay between the screw geometry and the fill level, mediated by the particle friction, that affects the transport efficiency of the feeder.

- For certain geometry related filling levels, the motion of the screw actively generates a backward flow of particles, hindering the conveying efficiency but intrinsically improving the mixing during the transport.

- Due to the back-flow mechanism established, the mass flow is not a monotonic function of the filling level, but exhibits an inflection depending on the screw shaft size and on the particle friction.

The DEM-FEM framework for the numerical study of roller compaction provided the following results:

- This newly proposed approach succeeded to model the final compacted ribbon, while at the same time capturing the density distribution periodic anisotropy of the latter

inherited by the complex flow of the material inside the device.

- The coarse graining technique was established to be the ideal tool to transform discrete flow data into continuous fields, while maintaining all the aspects of the dynamics inherited by an intrinsically discrete motion of particles.

- Physical indicators of steady-state granular flow were successfully identified in the context of the studied device, allowing a physically sound and consistent data gathering and averaging in space and time.

Calibration of DEM model parameters for cohesive powders is a topic as important as it is complicated. The work dedicated to this subject gave promising results:

- A rational and fully automatised calibration method has been designed, where the number of parameters to be calibrated has been reduced as much as possible via physical considerations and by exploiting the properties of the cohesive interaction model used.

- Numerical replicates of rheology tests are executed in a precise order to limit the effect of parameters yet to be calibrated on the ongoing calibration cycle, where variables are dynamically tuned during the simulation to save computational time.

- The calibration procedure was validated and the results are mostly in good agreement with the experiments, especially for noncohesive materials or for the unloading branches of compression and shear tests.

The development of a new method to generate deformable and breakable particle compounds opened exciting new perspectives that need further extensive studies. The relevant findings concerning their structure and their properties are listed below:

- By exploiting the properties of linear piecewise elasto-plastic inter-particle interaction laws in DEM, mechanically stable clusters of primary DEM particles can be generated, with the additional feature that their elasto-plastic bonds are both deformable and breakable, while being at the same time way more computationally efficient than usual multi-sphere based models of composite particles.

- Clusters structural parameters such as density, size and mass fraction are defined, and the tools to carefully compute the naturally-inherited clusters porosity are explained and compared.

- Via physical and geometrical considerations, and exploiting the properties of the inter-particle interaction law, the structural parameters of clusters are analytically related to the DEM material parameters of their components, relation then is also validated up to a very high accuracy.

6.2 Future directions

- In the context of screw feeding several directions will be explored, motivated by the importance of such devices and the consequent increasing interest towards their numerical modelling. Given the computational burden due to the size of such devices, the main investigation technique will still rely on DEM modelling of periodic screw sections. Feeding of cohesive materials deserve large interest, especially when it comes to conveying efficiency, mass flow and mean residence time analysis. Single and twin screws will also be compared to identify analogies and differences in the dynamics of the granular flow. Often DEM codes use triangulated geometries to model the mechanical elements of devices, such as the screw. This approximation simplifies the modelling of complicated surfaces, but introduces artifacts such as local roughness and uneven surfaces. Artifacts decrease with a finer triangulation, but this makes the model more computational expensive. An alternative is to model, whenever possible, surfaces as analytically designed screws, i.e. geometries implemented via mathematical equations rather than a discretisation via triangulation. This direction will also be a topic of upcoming study, since it is reasonable to assume that this kind of implementation should be both more precise and computationally faster than the usual one achieved via triangulated surfaces insertion.

- The DEM-related part of the study proved challenging for two main reasons: the computational expense required and the numerical stability. Both issues can be addressed at the same time in two different ways, resulting in possible follow-ups to this study. First and foremost, the whole roller compaction process could be implemented in DEM, including the compaction region. This approach would rely on cohesive particles, eliminating the numerical instability due to over-pressurising purely elastic particles in the compaction region while still achieving a target mass-flow. If successful, the coupling with FEM would become unnecessary, but the reduction in computational costs would be minimal since DEM is, by far, the most expensive of the two methods. On the other side flow fields could be extracted from DEM models of particles with different material properties and analytically related to the latter. This would provide the FEM model with the needed boundary conditions, while making the DEM model non-essential and avoiding most of the computational expenses.

- DEM material properties calibration is of extreme importance, and is a primary focus in modelling effort lately, as demonstrated by recent trends in the related scientific literature. Upcoming efforts in this topic are planned and follow-ups studies are already subject of study. First and foremost the calibration procedure needs improvement: despite the rational approach and the save in computational time there are still discrepancies between numerical results and experiments, especially during the powder rheometer loading stages. A further improvement to the calibration will be to add a dynamic angle of repose tester, such as a rotating tumbler, both in the rheology characterisation experiments and in the numerical

calibration routine. This additional test aims to a more precise measurement and calibration of inter-particle friction and cohesion that should not strongly depend on the particle stiffness, to be added to the standard routine for both experimental material characterisation and DEM numerical calibration. Finally the framework will be extended to the calibration of blends, hopefully allowing the extrapolation of flow properties and parameters for blends with different relative concentration of single components.

- Precise characterisation of clusters interaction parameters such as hardness, ductility, elasticity, fragmentation under compression and many others are yet to be carefully defined, and will be the next step in the study of such model. At the same time an analytical model of single clusters uniaxial breakage will be developed and compared to experimental results of single particles and single granules crushing experiments for validation. Once brittle fracture response has been added, the interplay between two different behaviour under compression, plastic deformation and brittle breakage, will be studied as a function of DEM material input parameters, and compared to breakage and deformation theories for solid matter. As a final aim, such clusters will be used to model die compaction and tableting processes, focusing on the properties of the final mechanically stable compound generated after compaction and how these relate to clusters attributes.

6.3 A personal take

I owe to my former doctorate advisor the addition of a small personal perspective on the modern conception of scientific work, its direction and its role in the university and in the rapidly evolving modern society. However, as much as I wish to honour his legacy, I will only be able to add a small personal take to the conclusion of my thesis work, rather than a whole, more exhaustive and philosophically valuable chapter to the latter.
I think my personal experience in my PhD journey was quite peculiar, as cliché this statement may sounds. Not only I was leaving my Country, but I was also completely changing environment and field of study, transitioning from theoretical physics to process and chemical engineering. From a purely theoretical and fundamental academic background I was switching to a semi-industrial, more practical oriented environment. The topics of my future research were also completely new to me: my background in Bose-Einstein condensation and quantum mechanics was totally useless if applied to classical physics of granular materials or Discrete Element models, of which I was lacking even the most fundamental knowledge. I also had no basic experience in process engineering, nor about the pharmaceutical manufacturing processes I would soon have started to study.
However, I soon realised that despite the new area of study my main obstacle was not understanding the fundamentals, but rather the classification of concepts and ideas. Physics, which, to me, is the most beautiful, intriguing and fundamental discipline of them all, was giving me the basis for understanding problems, but provided me with a very specific lexicon through which to express my ideas. In my new environment there were people with different backgrounds, mostly engineering and pharmacy, each with their own jargon, perspectives and classifications. Some of them had an experienced and exhaustive lexi-

con, and were able to describe every aspect of the problem in a precise technical manner, with terms that were as complicated as meaningless to me. However, despite a complete technical description of the problem, their understanding of the underlying physics was missing, of the "essence" of the problem lacking. This was peculiar to me until I realised that language works in a similar way. To communicate human beings need common terms a selected group of people agreed upon, encoded and transmitted to future generations. These vocabularies constantly evolve and expand, but must be translated to others if people that come from afar, or that share different roots or cultures are to communicate. This reminded me of a brilliant quote from a genius mind: *Richard Feynman* [31]. In an extract from a famous interview in 1981 he explains his point of view about names and understanding:

> Looking at a bird he [my father] says, "Do you know what that bird is? It's a brown throated thrush; but in Portuguese it's a ..., in Italian a ...," he says "in Chinese it's a ..., in Japanese a ...," etcetera. "Now," he says, "you know in all the languages you want to know what the name of that bird is and when you've finished with all that," he says, "you'll know *absolutely nothing* whatever about the bird. You only know about humans in different places and what they call the bird. Now," he says, "let's look at the bird." [...] Now that's a deep understanding — he doesn't give me a name, he knew the difference between *knowing the name* of something and *knowing* something...

This was exactly how I perceived the situation at the beginning of my journey, and how I still experience it whenever people from different backgrounds and experience interact and collaborate. And I feel it to be a recurrent theme embedded in modern society that is but a heavy hollow burden we should learn to get rid of. Science, collaborations and every relationship depend and are based on communication: success is therefore only achieved by bridging through the different ways of expression and connecting to the actual *meaning*.

Publications

Peer-reviewed journal articles part of this thesis (sorted by inverse publication date):

- L. Orefice and J. G. Khinast. Deformable and breakable DEM particle clusters for modelling compression of plastic and brittle porous materials — model and structure properties. *Powder Technology*, in press. DOI: 10.1016/j.powtec.2020.04.035
- L. Orefice and J. G. Khinast. A novel framework for a rational, fully-automatised calibration routine for DEM models of cohesive powders. *Powder Technology*, 361:687-703 (2020). DOI: 10.1016/j.powtec.2019.11.054
- A. Mazor, L. Orefice, A. Michrafy, A. De Ryck and J. G. Khinast. A combined DEM & FEM approach for modelling roll compaction process. *Powder Technology*, 337:3-16 (2018). DOI: 10.1016/j.powtec.2017.04.053
- L. Orefice and J. G. Khinast. DEM study of granular transport in partially filled horizontal screw conveyors. *Powder Technology*, 305:347-356 (2017). DOI: 10.1016/j.powtec.2016.09.067

Peer-reviewed journal articles or archive material not part of this thesis, but authored during the doctorate studies (sorted by inverse publication date):

- T. Weinhart, L. Orefice, M. Post, M. P. van Schrojenstein Lantman, I. F. C. Denissen, D. R. Tunuguntla, J. M. F. Tsang, H. Cheng, M. Y. Shaheen, H. Shi, P. Rapino, E. Grannonio, N. Losacco, J. Barbosa, L. Jing, J. E. Alvarez Naranjo, S. Roy, W. K. den Otter and A. R. Thornton. Fast, flexible particle simulations — An introduction to MercuryDPM. *Computer Physics Communications*, 249:107129 (2020). DOI: 10.1016/j.cpc.2019.107129
- S. González and L. Orefice. Granular Segregation in Tapered Rotating Drums. *arXiv*, 1501.06040 (2015).

Peer-reviewed journal articles not part of this thesis, and not authored during the doctorate studies:

- P. Buonsante, L. Orefice and A. Smerzi. Dynamic phase diagram for the quantum phase model. *Physical Review A*, 87:063620 (2013). DOI: 10.1103/PhysRevA.87.063620

Bibliography

[1] LIGGGHTS. http://www.cfdem.com/.

[2] MercuryDPM: Fast, flexible particle simulations. http://mercurydpm.org/.

[3] Z. A. Al-Ibraheemi, M. S. Anuar, F. S. Taip, M. C. Amin, S. M. Tahir, and A. B. Mahdi. Deformation and mechanical characteristics of compacted binary mixtures of plastic (microcrystalline cellulose), elastic (sodium starch glycolate), and brittle (lactose monohydrate) pharmaceutical excipients. *Particulate Science and Technology*, 31(6):561–567, 2013.

[4] M. Alizadeh, M. Asachi, M. Ghadiri, A. Bayly, and A. Hassanpour. A methodology for calibration of DEM input parameters in simulation of segregation of powder mixtures, a special focus on adhesion. *Powder Technology*, 339:789–800, 2018.

[5] B. Andreotti, Y. Forterre, and O. Pouliquen. *Granular Media: Between Fluid and Solid*. Cambridge University Press, 2013.

[6] S. Antonyuk, M. Khanal, J. Tomas, S. Heinrich, and L. Mörl. Impact breakage of spherical granules: Experimental study and DEM simulation. *Chemical Engineering and Processing: Process Intensification*, 45(10):838–856, 2006.

[7] I. S. Aranson and L. S. Tsimring. Patterns and collective behavior in granular media: Theoretical concepts. *Reviews of Modern Physics*, 78(2):641–692, 2006.

[8] H. M. Beakawi Al-Hashemi and O. S. Baghabra Al-Amoudi. A review on the angle of repose of granular materials. *Powder Technology*, 330:397–417, 2018.

[9] D. J. Benson and S. Okazawa. Contact in a multi-material Eulerian finite element formulation. *Computer Methods in Applied Mechanics and Engineering*, 193:4277–4298, 2004.

[10] M. Bi, F. Alvarez-Nunez, and F. Alvarez. Evaluating and modifying Johanson's rolling model to improve its predictability. *Journal of Pharmaceutical Sciences*, 103(7):2062–2071, 2014.

[11] D. L. Black, M. Q. McQuay, and M. P. Bonin. Laser-based techniques for particle-size measurement: A review of sizing methods and their industrial applications. *Progress in Energy and Combustion Science*, 22(3):267–306, 1996.

[12] C. A. Blackshields and A. M. Crean. Continuous powder feeding for pharmaceutical solid dosage form manufacture: a short review. *Pharmaceutical Development and Technology*, 23(6):554–560, 2018.

[13] P. Boehling, G. Toschkoff, K. Knop, P. Kleinebudde, S. Just, A. Funke, H. Rehbaum, and J. G. Khinast. Analysis of large-scale tablet coating: Modeling, simulation and experiments. *European Journal of Pharmaceutical Sciences*, 90:14–24, 2016.

[14] N. Brilliantov, F. Spahn, J. Hertzsch, and T. Pöschel. A model for collisions in granular gases. *Physical Review E*, 53:5382, 1996.

[15] H. Cheng, T. Shuku, K. Thoeni, P. Tempone, S. Luding, and V. Magnanimo. An iterative Bayesian filtering framework for fast and automated calibration of DEM models. *Computer Methods in Applied Mechanics and Engineering*, 350:268–294, 2019.

[16] Y. P. Cheng, M. D. Bolton, and Y. Nakata. Crushing and plastic deformation of soils simulated using DEM. *Geotechnique*, 54(2):131–141, 2004.

[17] Y. P. Cheng, Y. Nakata, and M. D. Bolton. Discrete element simulation of crushable soil. *Geotechnique*, 53(7):633–641, 2003.

[18] D. Choi, N. Kim, K. Chu, Y. Jung, J. Yoon, and S. Jeong. Material Properties and Compressibility Using Heckel and Kawakita Equation with Commonly Used Pharmaceutical Excipients. *Journal of Pharmaceutical Investigation*, 40(4):237–244, 2010.

[19] P. Cleary. Large scale industrial DEM modelling. *Engineering Computations*, 21(2-4):169–204, 2004.

[20] C. J. Coetzee. Review: Calibration of the discrete element method. *Powder Technology*, 310:104–142, 2017.

[21] C. J. Coetzee. Particle upscaling: Calibration and validation of the discrete element method. *Powder Technology*, 344:487–503, 2019.

[22] G. Combe and J. N. Roux. Strain versus stress in a model granular material: a devil's staircase. *Physical Review Letters*, 85(17):3628–3631, 2000.

[23] P. A. Cundall and O. D. L. Strack. A discrete numerical model for granular assemblies. *Geotechnique*, 29(1):47–65, 1979.

[24] J. C. Cunningham. Experimental studies and modeling of the roller compaction of pharmaceutical powders. *Strain*, (July):267, 2005.

[25] J. C. Cunningham, D. Winstead, and A. Zavaliangos. Understanding variation in roller compaction through finite element-based process modeling. *Computers and Chemical Engineering*, 34(7):1058–1071, 2010.

[26] P. U. Dassault Systems. ABAQUS Documentation. 2014.

[27] P. de Gennes. Granular matter: a tentative view. *Reviews of modern physics*, 71(2):374–382, 1999.

[28] R. Dec, A. Zavaliangos, and J. C. Cunningham. Comparison of various modeling methods for analysis of powder compaction in roller press. *Powder Technology*, 130(1-3):265–271, 2003.

[29] X. Deng and R. N. Davé. Breakage of fractal agglomerates. *Chemical Engineering Science*, 161:117–126, 2017.

[30] J. W. Fernandez, P. W. Cleary, and W. McBride. Effect of screw design on hopper drawdown of spherical particles in a horizontal screw feeder. *Chemical Engineering Science*, 66(22):5585–5601, 2011.

[31] C. Feynman and M. Feynman. *The pleasure of finding things out*, chapter Tyrannosaurus in the window. Perseus Books Group, 1999.

[32] Y. Forterre and O. Pouliquen. Flows of Dense Granular Media. *Annual Review of Fluid Mechanics*, 40(1):1–24, 2008.

[33] R. Freeman. Measuring the flow properties of consolidated, conditioned and aerated powders - A comparative study using a powder rheometer and a rotational shear cell. *Powder Technology*, 174(1-2):25–33, 2007.

[34] R. Fuchs, T. Weinhart, J. Meyer, H. Zhuang, T. Staedler, X. Jiang, and S. Luding. Rolling, sliding and torsion of micron-sized silica particles: Experimental, numerical and theoretical analysis. *Granular Matter*, 16(3):281–297, 2014.

[35] R. Furukawa, K. Kadota, T. Noguchi, A. Shimosaka, and Y. Shirakawa. DEM Modelling of Granule Rearrangement and Fracture Behaviours During a Closed-Die Compaction. *AAPS PharmSciTech*, 18(6):2368–2377, 2017.

[36] GDR MiDi. On dense granular flows. *European Physical Journal E*, 14(4):341–365, 2004.

[37] R. Ge, M. Ghadiri, T. Bonakdar, and K. Hapgood. 3D printed agglomerates for granule breakage tests. *Powder Technology*, 306:103–112, 2017.

[38] R. Ge, M. Ghadiri, T. Bonakdar, Q. Zheng, Z. Zhou, I. Larson, and K. Hapgood. Deformation of 3D printed agglomerates: Multiscale experimental tests and DEM simulation. *Chemical Engineering Science*, 217:115526, 2020.

[39] R. Ge, M. Ghadiri, T. Bonakdar, Z. Zhou, I. Larson, and K. Hapgood. Experimental study of the deformation and breakage of 3D printed agglomerates: Effects of packing density and inter-particle bond strength. *Powder Technology*, 340:299–310, 2018.

[40] R. Ge, L. Wang, and Z. Zhou. DEM analysis of compression breakage of 3D printed agglomerates with different structures. *Powder Technology*, 356:1045–1058, 2019.

[41] D. Geldart, E. C. Abdullah, and A. Verlinden. Characterisation of dry powders. *Powder Technology*, 190(1-2):70–74, 2009.

[42] D. J. Golchert, R. Moreno, M. Ghadiri, J. Litster, and R. Williams. Application of X-ray microtomography to numerical simulations of agglomerate breakage by distinct element method. *Advanced Powder Technology*, 15(4):447–457, 2004.

[43] I. Goldhirsch. Rapid granular flows. *Annual Review of Fluid Mechanics*, 35(1):267–293, 2003.

[44] I. Goldhirsch. Stress, stress asymmetry and couple stress: From discrete particles to continuous fields. *Granular Matter*, 12(3):239–252, 2010.

[45] N. Govender, R. K. Rajamani, S. Kok, and D. N. Wilke. Discrete element simulation of mill charge in 3D using the BLAZE-DEM GPU framework. *Minerals Engineering*, 79:152–168, 2015.

[46] N. Govender, D. N. Wilke, C. Y. Wu, J. Khinast, P. Pizette, and W. Xu. Hopper flow of irregularly shaped particles (non-convex polyhedra): GPU-based DEM simulation and experimental validation. *Chemical Engineering Science*, 188:34–51, 2018.

[47] A. P. Grima and P. W. Wypych. Development and validation of calibration methods for discrete element modelling. *Granular Matter*, 13(2):127–132, 2011.

[48] P. Guigon and O. Simon. Roll press design - Influence of force feed systems on compaction. *Powder Technology*, 130(1-3):41–48, 2003.

[49] V. Gupta, X. Sun, W. Xu, H. Sarv, and H. Farzan. A discrete element method-based approach to predict the breakage of coal. *Advanced Powder Technology*, 28(10):2665–2677, 2017.

[50] S. K. Haigh, P. J. Vardanega, and M. D. Bolton. The plastic limit of clays. *Geotechnique*, 63(6):435–440, 2013.

[51] L. H. Han, J. a. Elliott, a. C. Bentham, a. Mills, G. E. Amidon, and B. C. Hancock. A modified Drucker-Prager Cap model for die compaction simulation of pharmaceutical powders. *International Journal of Solids and Structures*, 45:3088–3106, 2008.

[52] B. Hancock, S. Clas, and K. Christensen. Micro-scale measurement of the mechanical properties of compressed pharmaceutical powders. 1: The elasticity and fracture behavior of microcrystalline cellulose. *International Journal of Pharmaceutics*, 209:27–35, 2000.

[53] K. J. Hanley, C. O'Sullivan, J. C. Oliveira, K. Cronin, and E. P. Byrne. Application of Taguchi methods to DEM calibration of bonded agglomerates. *Powder Technology*, 210(3):230–240, 2011.

[54] S. Helwany. *Applied Soil Mechanics with ABAQUS*. 2007.

[55] H. Hertz. Über die Berührung fester elastischer Körper. *Journal Für Die Reine Und Angewandte Matematik*, 92:156–171, 1882.

[56] H. Hiestand and D. Smith. Indices of tableting performance. *Powder Technology*, 38(2):145–159, 1984.

[57] Q. F. Hou, K. J. Dong, and A. B. Yu. DEM study of the flow of cohesive particles in a screw feeder. *Powder Technology*, 256:529–539, 2014.

[58] O. I. Imole, D. Krijgsman, T. Weinhart, V. Magnanimo, B. E. Chávez Montes, M. Ramaioli, and S. Luding. Experiments and discrete element simulation of the dosing of cohesive powders in a simplified geometry. *Powder Technology*, 287:108–120, 2016.

[59] S. M. Iveson and N. W. Page. Brittle to Plastic Transition in the Dynamic Mechanical Behavior of Partially Saturated Granular Materials. *Journal of Applied Mechanics, Transactions ASME*, 71(4):470–475, 2004.

[60] H. M. Jaeger, S. R. Nagel, and R. P. Behringer. Granular solids, liquids, and gases. *Reviews of Modern Physics*, 68(4):1259–1273, 1996.

[61] D. Jajcevic, E. Siegmann, C. Radeke, and J. G. Khinast. Large-scale CFD-DEM simulations of fluidized granular systems. *Chemical Engineering Science*, 98:298–310, 2013.

[62] R. P. Jensen, P. J. Bosscher, M. E. Plesha, and T. B. Edil. DEM simulation of granular media-structure interface: Effects of surface roughness and particle shape. *International Journal for Numerical and Analytical Methods in Geomechanics*, 23(6):531–547, 1999.

[63] J. R. Johanson. A rolling theory for granular solids. *Journal of Applied Mechanics*, pages 842–848, 1965.

[64] K. L. Johnson, K. Kendall, and A. D. Roberts. Surface Energy and the Contact of Elastic Solids. *Proceedings of the Royal Society A: Mathematical, Physical and Engineering Sciences*, 324(1558):301–313, 1971.

[65] D. D. Jones and M. F. Kocher. Auger Design for Uniform Unloading of Granular Material: I. Rectangular Cross-Section Containers. *Transactions of the American Society of Agricoltural Engineers*, 38(4):1157–1162, 1995.

[66] K. D. Kafui and C. Thornton. Numerical simulations of impact breakage of a spherical crystalline agglomerate. *Powder Technology*, 109(1-3):113–132, 2000.

[67] K. Kendall and C. Stainton. Adhesion and aggregation of fine particles. *Powder Technology*, 121(2-3):223–229, 2001.

[68] R. G. Keys. Cubic Convolution Interpolation for Digital Image Processing. *IEEE Transactions on Acoustics, Speech and Signal Processing*, 29(6):1153–1160, 1981.

[69] M. Khanal, W. Schubert, and J. Tomas. Ball Impact and Crack Propagation - Simulations of Particle Compound Material. *Granular Matter*, 5(4):177–184, 2004.

[70] J. G. Khinast and D. Luss. Efficient bifurcation analysis of periodically-forced distributed parameter systems. *Computers and Chemical Engineering*, 24(1):139–152, 2000.

[71] C. Kloss, C. Goniva, A. Hager, S. Amberger, and S. Pirker. Models, algorithms and validation for opensource DEM and CFD-DEM. *Progress in Computational Fluid Dynamics*, 12(2-3):140–152, 2012.

[72] G. Koval, J. N. Roux, A. Corfdir, and F. Chevoir. Annular shear of cohesionless granular materials: From the inertial to quasistatic regime. *Physical Review E - Statistical, Nonlinear, and Soft Matter Physics*, 79(2):1–16, 2009.

[73] H. Kureck, N. Govender, E. Siegmann, P. Boehling, C. Radeke, and J. G. Khinast. Industrial scale simulations of tablet coating using GPU based DEM: A validation study. *Chemical Engineering Science*, 202:462–480, 2019.

[74] L. D. Landau and E. M. Lifshitz. *Theory of Elasticity*. Pergamon Press, 1970.

[75] B. Latella and S. Humphries. Young's modulus of a 2.25cr–1mo steel at elevated temperature. *Scripta Materialia*, 51:635–639, 2004.

[76] H. Ledbetter. Stainless-steel elastic constants at low temperatures. *Journal of applied Physics*, 52:1587(3), 1981.

[77] Q. Li, M. Feng, and Z. Zou. Validation and Calibration Approach for Discrete Element Simulation of Burden Charging in Pre-reduction Shaft Furnace of COREX Process. *ISIJ International*, 53(8):1365–1371, 2013.

[78] C. C. Liao, S. S. Hsiau, T. H. Tsai, and C. H. Tai. Segregation to mixing in wet granular matter under vibration. *Chemical Engineering Science*, 65(3):1109–1116, 2010.

[79] L. Liu, C. Thornton, S. J. Shaw, and E. M. Tadjouddine. Discrete element modelling of agglomerate impact using autoadhesive elastic-plastic particles. *Powder Technology*, 297:81–88, 2016.

[80] Y. Liu and C. Wassgren. Modifications to Johanson's roll compaction model for improved relative density predictions. *Powder Technology*, 297:294–302, 2016.

[81] S. Lommen, D. Schott, and G. Lodewijks. DEM speedup: Stiffness effects on behavior of bulk material. *Particuology*, 12(1):107–112, 2014.

[82] L. B. Lucy. A numerical approach to the testing of the fission hypothesis. *The Astronomical Journal*, 82(12):1013–1024, 1977.

[83] S. Luding. Cohesive, frictional powders: Contact models for tension. *Granular Matter*, 10(4):235–246, 2008.

[84] S. Luding. Introduction to discrete element methods: Basic of contact force models and how to perform the micro-macro transition to continuum theory. *European Journal of Environmental and Civil Engineering*, 12(7-8):785–826, 2008.

[85] S. Luding, K. Manetsberger, and J. Müllers. A discrete model for long time sintering. *Journal of the Mechanics and Physics of Solids*, 53(2):455–491, 2005.

[86] M. Marigo and E. H. Stitt. Discrete element method (DEM) for industrial applications: Comments on calibration and validation for the modelling of cylindrical pellets. *KONA Powder and Particle Journal*, 32(32):236–252, 2015.

[87] D. Markauskas, R. Kačianauskas, A. Džiugys, and R. Navakas. Investigation of adequacy of multi-sphere approximation of elliptical particles for DEM simulations. *Granular Matter*, 12(1):107–123, 2010.

[88] C. L. Martin, D. Bouvard, and G. Delette. Discrete element simulations of the compaction of aggregated ceramic powders. *Journal of the American Ceramic Society*, 89(11):3379–3387, 2006.

[89] G. Mason. Radial distribution functions from small packings of spheres. *Nature*, 217(5130):733–735, 1968.

[90] A. Mazor, L. Perez-Gandarillas, A. de Ryck, and A. Michrafy. Effect of roll compactor sealing system designs: A finite element analysis. *Powder Technology*, 289:21–30, 2016.

[91] G. R. McDowell and O. Harireche. Discrete element modelling of soil particle fracture. *Geotechnique*, 52(2):131–135, 2002.

[92] G. R. McDowell and O. Harireche. Discrete element modelling of yielding and normal compression of sand. *Geotechnique*, 52(4):299–304, 2002.

[93] D. McGlinchey. *Bulk Solids Handling: Equipment Selection and Operation*. Blackwell Publishing Ltd., 2008.

[94] A. Michrafy, H. Diarra, J. A. Dodds, and M. Michrafy. Experimental and numerical analyses of homogeneity over strip width in roll compaction. *Powder Technology*, 206(1-2):154–160, 2011.

[95] A. Michrafy, H. Diarra, J. A. Dodds, M. Michrafy, and L. Penazzi. Analysis of strain stress state in roller compaction process. *Powder Technology*, 208(2):417–422, 2011.

[96] R. Moreno, M. Ghadiri, and S. J. Antony. Effect of the impact angle on the breakage of agglomerates: A numerical study using DEM. *Powder Technology*, 130(1-3):132–137, 2003.

[97] P. A. Moysey and M. R. Thompson. Modelling the solids inflow and solids conveying of single-screw extruders using the discrete element method. *Powder Technology*, 153(2):95–107, 2005.

[98] A. R. Muliadi, J. D. Litster, and C. R. Wassgren. Modeling the powder roll compaction process: Comparison of 2-D finite element method and the rolling theory for granular solids (Johanson's model). *Powder Technology*, 221:90–100, 2012.

[99] A. R. Muliadi, J. D. Litster, and C. R. Wassgren. Validation of 3-D finite element analysis for predicting the density distribution of roll compacted pharmaceutical powder. *Powder Technology*, 237:386–399, 2013.

[100] Z. Ning, R. Boerefijn, M. Ghadiri, and C. Thornton. Distinct element simulation of impact breakage of lactose agglomerates. *Advanced Powder Technology*, 8(1):15–37, 1997.

[101] J. M. Ottino and D. V. Khakhar. Mixing and segregation of granular materials. *Annual Review of Fluid Mechanics*, 32:55–91, 2000.

[102] P. J. Owen and P. W. Cleary. Prediction of screw conveyor performance using the Discrete Element Method (DEM). *Powder Technology*, 193(3):274–288, 2009.

[103] P. Pandey, R. Bharadwaj, and X. Chen. 1 - modeling of drug product manufacturing processes in the pharmaceutical industry. In P. Pandey and R. Bharadwaj, editors, *Predictive Modeling of Pharmaceutical Unit Operations*, pages 1 – 13. Woodhead Publishing, 2017.

[104] J. A. Parker, R. V. Kenyon, and D. E. Troxel. Comparison of interpolating methods for image resampling. *IEEE Transactions on Medical Imaging*, 2(1):31–39, March 1983.

[105] S. Patel, A. M. Kaushal, and A. K. Bansal. Compression physics in the formulation development of tablets. *Critical Reviews in Therapeutic Drug Carrier Systems*, 23(1):1–65, 2006.

[106] L. Pezo, A. Jovanović, M. Pezo, R. Čolović, and B. Lončar. Modified screw conveyor-mixers - Discrete element modeling approach. *Advanced Powder Technology*, 26(5):1391–1399, 2015.

[107] M. Rackl and K. J. Hanley. A methodical calibration procedure for discrete element models. *Powder Technology*, 307:73–83, 2017.

[108] C. A. Radeke, B. J. Glasser, and J. G. Khinast. Large-scale powder mixer simulations using massively parallel GPUarchitectures. *Chemical Engineering Science*, 65(24):6435–6442, 2010.

[109] F. J. C. Rademacher. On Seed Damage in Grain Augers. *Journal Of Agricultural Engineering Research*, 26:87–96, 1981.

[110] G. E. Rehkugler and L. L. Boyd. Dimensional Analysis of Auger Conveyor Operation. *Transactions of the American Society of Agricoltural Engineers*, 5(1):98–102, 1962.

[111] G. Reynolds, R. Ingale, R. Roberts, S. Kothari, and B. Gururajan. Practical application of roller compaction process modeling. *Computers and Chemical Engineering*, 34(7):1049–1057, 2010.

[112] G. K. Reynolds, J. S. Fu, Y. S. Cheong, M. J. Hounslow, and A. D. Salman. Breakage in granulation: A review. *Chemical Engineering Science*, 60(14):3969–3992, 2005.

[113] A. W. Roberts. The influence of granular vortex motion on the volumetric performance of enclosed screw conveyors. *Powder Technology*, 104(1):56–67, 1999.

[114] A. W. Roberts and A. H. Willis. Performance of grain augers. *Proceedings of the Institution of Mechanical Engineers*, 176(8):165–194, 1962.

[115] R. J. Roberts and R. C. Rowe. Brittle/ductile behaviour in pharmaceutical materials used in tabletting. *International Journal of Pharmaceutics*, 36(2-3):205–209, 1987.

[116] R. J. Roberts, R. C. Rowe, and P. York. The Poisson's ratio of microcrystalline cellulose. *International Journal of Pharmaceutics*, 105(2):177–180, 1994.

[117] T. Roessler and A. Katterfeld. Scaling of the angle of repose test and its influence on the calibration of DEM parameters using upscaled particles. *Powder Technology*, 330:58–66, 2018.

[118] T. Roessler, C. Richter, A. Katterfeld, and F. Will. Development of a standard calibration procedure for the DEM parameters of cohesionless bulk materials – part I: Solving the problem of ambiguous parameter combinations. *Powder Technology*, 343:803–812, 2019.

[119] R. C. Rowe, P. J. Sheskey, and M. E. Quinn. *Handbook of Pharmaceutical Excipients, 6th. ed.* Pharmaceutical Press, 2009.

[120] M. Sakai and S. Koshizuka. Large-scale discrete element modeling in pneumatic conveying. *Chemical Engineering Science*, 64(3):533–539, 2009.

[121] A. Samadani and A. Kudrolli. Segregation transitions in wet granular matter. *Physical Review Letters*, 85(24):5102–5105, 2000.

[122] A. Samimi, A. Hassanpour, and M. Ghadiri. Single and bulk compressions of soft granules: Experimental study and DEM evaluation. *Chemical Engineering Science*, 60(14):3993–4004, 2005.

[123] R. Sánchez, I. C. Romero-Sánchez, S. Santos-Toledano, and A. Huerta. Polydispersity and structure: A qualitative comparison between simulations and granular systems data. *Revista Mexicana de Fisica*, 60(2):136–141, 2014.

[124] U. Sander and K. Schönert. Operational conditions of a screw-feeder-equipped high-pressure roller mill. *Powder Technology*, 105(1-3):282–287, 1999.

[125] D. A. Santos, M. A. Barrozo, C. R. Duarte, F. Weigler, and J. Mellmann. Investigation of particle dynamics in a rotary drum by means of experiments and numerical simulations using DEM. *Advanced Powder Technology*, 27(2):692–703, 2016.

[126] Z. Shen, M. Jiang, and C. Thornton. DEM simulation of bonded granular material. Part I: Contact model and application to cemented sand. *Computers and Geotechnics*, 75:192–209, 2016.

[127] Y. Shimizu and P. A. Cundall. Three-dimensional DEM simulations of bilk handling by screw conveyors. *Journal of Engineering Mechanics*, 127(9):864–872, 2001.

[128] E. Siegmann, D. Jajcevic, C. Radeke, D. Strube, K. Friedrich, and J. G. Khinast. Efficient Discrete Element Method Simulation Strategy for Analyzing Large-Scale Agitated Powder Mixers. *Chemie-Ingenieur-Technik*, 89(8):995–1005, 2017.

[129] L. E. Silbert, D. Ertaş, G. S. Grest, T. C. Halsey, and D. Levine. Geometry of frictionless and frictional sphere packings. *Physical Review E - Statistical Physics, Plasmas, Fluids, and Related Interdisciplinary Topics*, 65(3):1–6, 2002.

[130] O. Simon and P. Guigon. Correlation between powder-packing properties and roll press compact heterogeneity. *Powder Technology*, 130(1-3):257–264, 2003.

[131] A. Skelbæk-Pedersen, T. Vilhelmsen, V. Wallaert, and J. Rantanen. Quantification of fragmentation of pharmaceutical materials after tableting. *Journal of Pharmaceutical Sciences*, 108(3):1246 – 1253, 2019.

[132] C. Song, P. Wang, and H. A. Makse. A phase diagram for jammed matter. *Nature*, 453(7195):629–632, 2008.

[133] Y. Song, R. Turton, and F. Kayihan. Contact detection algorithms for DEM simulations of tablet-shaped particles. *Powder Technology*, 161(1):32–40, 2006.

[134] A. Spettl, M. Dosta, S. Antonyuk, S. Heinrich, and V. Schmidt. Statistical investigation of agglomerate breakage based on combined stochastic microstructure modeling and DEM simulations. *Advanced Powder Technology*, 26(3):1021–1030, 2015.

[135] J. Subero and M. Ghadiri. Breakage patterns of agglomerates. *Powder Technology*, 120(3):232–243, 2001.

[136] J. Subero, D. Pascual, and M. Ghadiri. Production of agglomerates of well-defined structures and bond properties using a novel technique. *Chemical Engineering Research and Design*, 78(1):55–60, 2000.

[137] B. Suhr, S. Marschnig, and K. Six. Comparison of two different types of railway ballast in compression and direct shear tests: experimental results and DEM model validation. *Granular Matter*, 20(4), 2018.

[138] C. C. Sun and P. Kleinebudde. Mini review: Mechanisms to the loss of tabletability by dry granulation. *European Journal of Pharmaceutics and Biopharmaceutics*, 106:9–14, 2016.

[139] S. C. Thakur, J. P. Morrissey, J. Sun, J. F. Chen, and J. Y. Ooi. Micromechanical analysis of cohesive granular materials using the discrete element method with an adhesive elasto-plastic contact model. *Granular Matter*, 16(3):383–400, 2014.

[140] A. Thornton, T. Weinhart, S. Luding, and O. Bokhove. Modeling of particle size segregation: calibration using the discrete particle method. *International Journal of Modern Physics C*, 23(08):1240014, 2012.

[141] C. Thornton, M. T. Ciomocos, and M. J. Adams. Numerical simulations of diametrical compression tests on agglomerates. *Powder Technology*, 140(3):258–267, 2004.

[142] C. Thornton, S. J. Cummins, and P. W. Cleary. On elastic-plastic normal contact force models, with and without adhesion. *Powder Technology*, 315:339–346, 2017.

[143] C. Thornton and L. Liu. How do agglomerates break? *Powder Technology*, 143-144:110–116, 2004.

[144] C. Thornton, K. K. Yin, and M. J. Adams. Numerical simulation of the impact fracture and fragmentation of agglomerates. *Journal of Physics D: Applied Physics*, 29(2):424–435, 1996.

[145] L. T. To, D. J. Daley, and Z. H. Stachurski. On the definition of an ideal amorphous solid of uniform hard spheres. *Solid State Sciences*, 8(8):868–879, 2006.

[146] J. Tomas. Particle adhesion fundamentals and bulk powder consolidation. *KONA Powder and Particle Journal*, 18(May):157–169, 2000.

[147] J. Tomas. Fundamentals of cohesive powder consolidation and flow. *Granular Matter*, 6(2-3):75–86, 2004.

[148] Z. B. Tong, R. Y. Yang, A. B. Yu, S. Adi, and H. K. Chan. Numerical modelling of the breakage of loose agglomerates of fine particles. *Powder Technology*, 196(2):213–221, 2009.

[149] P. Toson, E. Siegmann, M. Trogrlic, H. Kureck, J. Khinast, D. Jajcevic, P. Doshi, D. Blackwood, A. Bonnassieux, P. D. Daugherity, and M. T. am Ende. Detailed modeling and process design of an advanced continuous powder mixer. *International Journal of Pharmaceutics*, 552(1-2):288–300, 2018.

[150] K. Uchida and K. Okamoto. Measurement of powder flow in a screw feeder by x-ray penetration image analysis. *Measurement Science and Technology*, 17:419–426, 2006.

[151] T. Uematu and S. Nakamura. A study of the screw conveyor. *Bulletin Of The Japan Society Of Mechanical Engineers*, 3(12):449–455, 1960.

[152] K. Van Der Weele, D. Van Der Meer, M. Versluis, and D. Lohse. Hysteretic clustering in granular gas. *Europhysics Letters*, 53(3):328–334, 2001.

[153] A. Vasilenko, B. J. Glasser, and F. J. Muzzio. Shear and flow behavior of pharmaceutical blends - Method comparison study. *Powder Technology*, 208(3):628–636, 2011.

[154] K. Watanabe and H. Tanaka. Direct observation of medium-range crystalline order in granular liquids near the glass transition. *Physical Review Letters*, 100(15):4–7, 2008.

[155] M. Weber, A. Spettl, M. Dosta, S. Heinrich, and V. Schmidt. Simulation-based investigation of core-shell agglomerates: Influence of spatial heterogeneity in particle sizes on breakage characteristics. *Computational Materials Science*, 137:100–106, 2017.

[156] T. Weinhart, R. Hartkamp, A. Thornton, and S. Luding. Coarse-grained local and objective continuum description of three-dimensional granular flows down an inclined surface. *Physics of Fluids*, 25:070605(26), 2013.

[157] T. Weinhart, L. Orefice, M. Post, M. P. van Schrojenstein Lantman, I. F. Denissen, D. R. Tunuguntla, J. Tsang, H. Cheng, M. Y. Shaheen, H. Shi, P. Rapino, E. Grannonio, N. Losacco, J. Barbosa, L. Jing, J. E. A. Naranjo, S. Roy, W. K. den Otter, and A. R. Thornton. Fast, flexible particle simulations — an introduction to mercurydpm. *Computer Physics Communications*, page 107129, 2019.

[158] T. Weinhart, A. R. Thornton, S. Luding, and O. Bokhove. Closure relations for shallow granular flows from particle simulations. *Granular Matter*, 14(4):531–552, 2012.

[159] T. Weinhart, A. R. Thornton, S. Luding, and O. Bokhove. From discrete particles to continuum fields near a boundary. *Granular Matter*, 14(2):289–294, 2012.

[160] C. M. Wensrich and A. Katterfeld. Rolling friction as a technique for modelling particle shape in DEM. *Powder Technology*, 217:409–417, 2012.

[161] S. K. Wilkinson, S. A. Turnbull, Z. Yan, E. H. Stitt, and M. Marigo. A parametric evaluation of powder flowability using a Freeman rheometer through statistical and sensitivity analysis: A discrete element method (DEM) study. *Computers and Chemical Engineering*, 97:161–174, 2017.

[162] C. D. Willett, M. J. Adams, S. A. Johnson, and J. P. K. Seville. Capillary bridges between two spherical bodies. *Langmuir*, 16(24):9396–9405, 2000.

[163] T. F. Wong and P. Baud. The brittle-ductile transition in porous rock: A review. *Journal of Structural Geology*, 44:25–53, 2012.

[164] H. Wu, N. Gui, X. Yang, J. Tu, and S. Jiang. A smoothed void fraction method for CFD-DEM simulation of packed pebble beds with particle thermal radiation. *International Journal of Heat and Mass Transfer*, 118:275–288, 2018.

[165] B. Xavier, M. Sylvain, N. Abibatou, P. Veronique, and B. Olivier. Calibration of DEM parameters on shear test experiments using Kriging method. *EPJ Web of Conferences*, 14(1):15016, 2017.

[166] M. Xu, J. Hong, and E. Song. DEM study on the macro- and micro-responses of granular materials subjected to creep and stress relaxation. *Computers and Geotechnics*, 102(January):111–124, 2018.

[167] B. Yan and R. Regueiro. Large-scale dynamic and static simulations of complex-shaped granular materials using parallel three-dimensional discrete element method (DEM) on DoD supercomputers. *Engineering Computations*, 35(2):1049–1084, 2018.

[168] Z. Yan, S. K. Wilkinson, E. H. Stitt, and M. Marigo. Discrete element modelling (DEM) input parameters: understanding their impact on model predictions using statistical analysis. *Computational Particle Mechanics*, 2(3):283–299, 2015.

[169] R. Y. Yang, A. B. Yu, S. K. Choi, M. S. Coates, and H. K. Chan. Agglomeration of fine particles subjected to centripetal compaction. *Powder Technology*, 184(1):122–129, 2008.

[170] R. Y. Yang, R. P. Zou, and A. B. Yu. Computer simulation of the packing of fine particles. *Physical Review E*, 62(3):3900–3908, sep 2000.

[171] F. Ye, C. Wheeler, B. Chen, J. Hu, K. Chen, and W. Chen. Calibration and verification of DEM parameters for dynamic particle flow conditions using a backpropagation neural network. *Advanced Powder Technology*, 30(2):292–301, 2019.

[172] A. B. Yu. Discrete element method: An effective way for particle scale research of particulate matter. *Engineering Computations*, 21(2-4):205–214, 2004.

[173] Y. Yu and P. C. Arnold. The influence of screw feeders on bin flow patterns. *Powder Technology*, 88(1):81–87, 1996.

[174] K. Zheng, C. Du, J. Li, B. Qiu, L. Fu, and J. Dong. Numerical simulation of the impact-breakage behavior of non-spherical agglomerates. *Powder Technology*, 286:582–591, 2015.

[175] W. Zhou, L. Yang, G. Ma, K. Xu, Z. Lai, and X. Chang. DEM modeling of shear bands in crushable and irregularly shaped granular materials. *Granular Matter*, 19(2):1–12, 2017.

[176] Y. Zhou, B. Xu, and A. Yu. Numerical investigation of the angle of repose of monosized spheres. *Physical Review E*, 64:021301, 2001.

[177] Y. C. Zhou, B. H. Xu, A. B. Yu, and P. Zulli. Numerical investigation of the angle of repose of monosized spheres. *Physical Review E - Statistical Physics, Plasmas, Fluids, and Related Interdisciplinary Topics*, 64(2):8, 2001.